# Sharing the Baryons: Stars and Gas in Local Volume Galaxies

Emma Marie Kirby

A thesis submitted for the degree of

Doctor of Philosophy

of The Australian National University

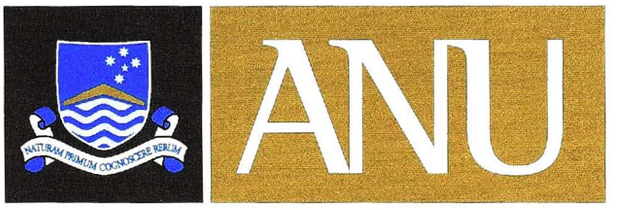


THE AUSTRALIAN NATIONAL UNIVERSITY



Research School of Astronomy and Astrophysics

The Australian National University

February 2010

# Disclaimer

I hereby declare that the work in this thesis is that of the candidate alone, except where indicated below or in the text of the thesis.

*Chapter (2).* – This chapter presents the paper Kirby et al. (2008) which was co-authored by Dr. Helmut Jerjen, Dr. Stuart Ryder and Dr. Simon Driver. The majority of the work is that of the candidate except for paragraphs 2 to 5 of section 2.3 which is that of Dr. Ryder. The majority of the observing for the LSI survey was carried out by Dr. Ryder. The candidate accompanied Dr. Ryder for 4 nights of observing and obtained the imaging data for 10 of the 68 galaxies presented in this chapter. Figure 2.1 was made by Dr. Jerjen.

*Chapter (3).* – This chapter presents the paper Kirby et al. (2010) which is co-authored by Dr. Bärbel Koribalski and Dr. Helmut Jerjen who have contributed to the text. The majority of the work is that of the candidate.

*Chapter (4).* – This chapter presents the paper Kirby & Jerjen (2010) which is co-authored by Dr. Helmut Jerjen who has contributed to the text. The majority of the work is that of the candidate.

*Appendix (A).* – This appendix introduces the Local Volume H I Survey (LVHIS). LVHIS is a large project being carried out by a team of 10 collaborators (Principal Investigator Dr. Bärbel Koribalski). The candidate joined the LVHIS team in 2006 and obtained data for approximately 470 hours of observing (out of the total 2200 hours for the survey). The candidate reduced and calibrated all data collected during their observing runs as well as contributed to the overall data reduction effort for the survey. Tables A.1 to A.3 were initially created by Dr. Koribalski and were updated by the candidate.

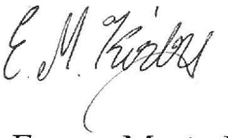

Emma Marie Kirby

February 2010

# Acknowledgments

I would first like to start off by acknowledging my supervisors Helmut Jerjen and Bärbel Koribalski. My main supervisor, Helmut provided guidance throughout these four years, the quality of which was nothing short of amazing. He has always been there to help me work through any problems, and has always made time for long helpful discussions. My co-supervisor Bärbel was always willing to lend her talents and provide thorough, meaningful insights to make the project and my thesis a reality. Bärbel always welcomed me to visit her in Sydney and would take time out of her busy schedule during these visits.

I am grateful for the assistance of Stuart Ryder for his help and expertise in near-IR photometry, and for welcoming me on an observing trip. I am also grateful to Jeremy Bailin who devoted many hours introducing me to the world of n-body simulations. Despite my project evolving in a different direction, I enjoyed this work and appreciate your efforts.

I would also like to personally thank the following friends and family: With the deepest of hearts, I would like to thank two people, without whom this thesis would have not been possible, my parents Diana and Mac. Their tremendous support and encouragement has given me the confidence to finish this monumental task. My two closest friends Aimee and Melissa have been constant support since the beginning of this PhD and have put up with my lack of communication. Finally, Bradley, for his unending patience during the most trying of hours and making the last few years the best ones of my life. Your ability to always bring a smile to my face and believe in myself has made these years a truly remarkable journey.

Chapter 2 is based on the paper Kirby et al. (2008); the authors of which thank the referee of the paper for the useful comments. Chapter 2 is based on data obtained with the Anglo-Australian Telescope. Chapters A and 3 are based on observations were obtained with the Australia Telescope which is funded by the Commonwealth of Australia for operations as a National Facility managed by CSIRO. Chapter 4 includes data for 789 galaxies kindly provided Bradley Warren.

The candidate acknowledges financial support from the Australian Research Council Discovery Project Grant DP0451426. The study made use of data products from the Two Micron All Sky Survey (2MASS), which is a joint project of the University of Massachusetts and the Infrared Processing and Analysis Center/California Institute of Technology, funded by the National Aeronautics and Space Administration and the National Science Foundation. Support for IRIS2 data reduction within ORAC-DR is provided by the Joint Astronomy Centre. This research has made use of the GOLD Mine Database. This research has made use of the NASA/IPAC Extragalactic Database (NED) which is operated by the Jet Propulsion Laboratory, California Institute of Technology, under contract with

the National Aeronautics and Space Administration. This research has made use of NASA's Astrophysics Data System. This research was done with the support of the Australia Telescope National Facility, CSIRO.

# Abstract

The baryonic content of a galaxy is divided into two distinct, albeit related, components; the stellar component and the gaseous component. Although many individual galaxies have had their stars and gas studied in great detail, overall the relation between these two baryonic components is poorly understood. This thesis presents a study of the stellar and gas properties of galaxies in the Local Volume ($D < 10$ Mpc) and investigates the relation between the atomic hydrogen and stellar components of a galaxy.

We present $H$-band (1.65$\mu$m) surface photometry of 57 galaxies drawn from the Local Sphere of Influence (LSI) with distances of less than 10 Mpc from the Milky Way. The images with a typical surface brightness limit 4 mag fainter than 2MASS (24.5 mag arcsec$^{-2}$ < $\mu_{lim}$ < 26 mag arcsec$^{-2}$ ) have been obtained with IRIS2 on the 3.9 m Anglo-Australian Telescope. A total of 22 galaxies that remained previously undetected in the near-IR and potentially could have been genuinely young galaxies were found to have an old stellar population with a star density 1 – 2 magnitudes below the 2MASS detection threshold. The cleaned near-IR images reveal the morphology and extent of many of the galaxies for the first time. For all program galaxies, we derive radial luminosity profiles, ellipticities, and position angles, together with global parameters such as total magnitude, mean effective surface brightness and half-light radius. Our results show that 2MASS underestimates the total magnitude of galaxies with $\langle\mu_H\rangle_{eff}$ between 18 – 21 mag arcsec$^{-2}$ by up to 2.5 mag. The Sérsic parameters best describing the observed surface brightness profiles are also presented. Adopting accurate galaxy distances and a $H$-band mass-to-light ratio of $\Upsilon_*^H = 1.0 \pm 0.4$, the LSI galaxies are found to cover a stellar mass range of $5.6 < \log_{10}(\mathcal{M}_{\rm stars}) < 11.1$. The results are discussed along with previously obtained optical data. Our sample of low luminosity galaxies is found to follow closely the optical-infrared $B$ versus $H$ luminosity relation defined by brighter galaxies with a slope of $1.14 \pm 0.02$ and scatter of 0.3 magnitudes. Finally we analyse the luminosity – surface brightness relation to determine an empirical mass-to-light ratio of $\Upsilon_*^H = 0.78 \pm 0.08$ for late-type galaxies in the $H$-band.

The atomic hydrogen distribution and kinematics for Local Volume galaxies have been obtained as part of the 'Local Volume H I Survey' (LVHIS). We use the new, high resolution, H I line data obtained with the Australia Telescope Compact Array for a kinematical analysis of 12 nearby galaxies. For six galaxies in our sample we present the only resolved H I imaging available to date which reveals the atomic hydrogen distribution for the first time. Detailed kinematic information is presented as global H I line profiles and rotation curves. The rotation parameters obtained from the H I line profile are shown to be an accurate measure of the true rotation derived via rotation curve analysis. The kinematics of the 12 galaxies are analysed in detail and the classical and baryonic Tully-Fisher

relations determined.

Near-IR and 21cm data for 1394 nearby galaxies are analysed to investigate the relation between the atomic hydrogen and stellar components of a galaxy. We show that there is an upper limit for the H I mass in a galaxy, a quantity that correlates with its stellar mass. We examine the relation between the stellar and baryonic mass and find that the minimum stellar mass fraction $(\mathcal{M}_*/\mathcal{M}_{bary})_{min}$ for galaxies increases systematically to unity as their baryonic mass goes from $10^8$ to $10^{12}\mathcal{M}_\odot$. This result suggests that there is a physical limit to the maximum baryonic mass a galaxy has at the current epoch with giant cluster ellipticals being the most extreme systems. A similar mass limit has been proposed on theoretical grounds by Rees & Ostriker (1977) and Silk (1977).

# CONTENTS

# LIST OF FIGURES

# LIST OF TABLES

# CHAPTER 1

# Introduction

Galaxies are the largest and most abundant laboratories throughout the universe, and are the key to unlocking the mysteries of the cosmos. Obtaining a complete and coherent understanding of the physical processes that regulate the formation and evolution of galaxies has been an ongoing effort in astrophysics. While there has been a tremendous amount of work into analysing individual galaxies, a broader understanding of the interactions and process involved and thus the subsequent cosmological implications has not yet been achieved.

Traditionally, cosmological problems are approached by studying distant objects, wherein large samples of galaxies are studied at varying redshift giving a proxy for the evolution of these systems. While traditional cosmology has enjoyed enormous success, particularly in furthering our understanding of the formation of large scale structures, it faces obvious difficulties imposed by the high redshifts of the objects. In the distant universe, Malmquist bias has a significant impact which leads to only the most luminous galaxies being studied. This, compounded with the fact that at high redshift the wavelength coverage is limited, results in only a fraction of the total information being observed. Moreover, the large distances to the targets dictate that the angular resolution is low, meaning that only global properties of the targets can be derived.

More recently, the expanding discipline of near-field cosmology has allowed astronomers to tackle the question of galaxy formation and evolution from a different angle, in which fossil evidence remaining from the evolution is pursued (leading to the alternative name galactic archeology). In the nearby Universe, galaxies of all morphological types can be studied in tremendous detail; most notably, hundreds of dwarf galaxies can be observed. Dwarfs, the smallest of all galaxies, are an important cosmological probe as they are the basic building blocks of larger galaxies in the commonly accepted paradigm of hierarchical assembly. While the near-field offers a high angular resolution view of the Universe today, traditional cosmology enjoys large sample sizes

and time resolution. Therefore, these two approaches provide a different but complementary route to examining the evolution of galaxies.

Near-field cosmologists use several different techniques to hunt for evidence of the evolution galaxies remaining in present day systems. Usually individual galaxies are studied in immense detail to find the elusive clues of their past. Early work consisted of the investigation of individual stars in the Milky Way for stellar systems which may have merged. One of the most significant early results was the detection of Sagittarius dwarf spheroidal by Ibata et al. (1994) and the evidence of its tidal disruption as it merges with our Galaxy. This detection has served as the inspiration for many current and future surveys to measure the motions, metallicities and abundance ratios for millions of Galactic stars such as the Radial Velocity Experiment (RAVE; Steinmetz et al. 2006) and Gaia (Perryman et al., 2001). Extra-Galactic objects have also been targeted for detailed studies (eg., see Mateo 1998 for a review of Local Group dwarf galaxies as well as Tolstoy 1999; Grebel & Gallagher 2004; Warren et al. 2004; Bouchard et al. 2007, amongst others). Most recently, with the aid of the Sloan Digital Sky Survey (SDSS; York et al. 2000) searches for new ultra-faint companions to the Milky Way has begun in an effort to investigate the discrepancy between cold dark matter simulations and the observed matter distribution of the halo (Martin et al., 2004; Willman et al., 2005a,b; Sakamoto & Hasegawa, 2006; Zucker et al., 2006; Belokurov et al., 2006, 2007; Walsh et al., 2007).

High redshift studies of galaxy evolution have always had the luxury of large sample sizes allowing for the analysis of general galaxy properties rather than those on a case by case basis. However, in the last decade many new large scale surveys have provided homogenous catalogues which are complete (to the limiting magnitude of the surveys) and contain information on large numbers of nearby galaxies. For the first time it has been possible to carry out an investigation of the general properties of $z \approx 0$ galaxies using statistically complete and significant sample sizes (see for example Karachentsev et al. 2004; Warren et al. 2007).

The two main visible components of a galaxy are the stellar component and the atomic hydrogen component. These distinct, albeit intimately related constituents make up the majority of baryonic mass in galaxies and their ratio offers an observational quantity that describes the integral evolutionary status of a galaxy by comparing the available amounts of unprocessed to processed baryons (hydrogen gas versus stars). The main aim of this thesis is to provide high quality, deep imaging of large numbers of nearby galaxies to determine the properties of their stellar and neutral hydrogen content, and to use these data to assess the status quo of galaxy evolution by investigating the baryon mixture of current-day galaxies of different morphological types.

## 1.1. The Local Volume

The Local Volume is defined as the region of space inside a sphere with a radius of 10 Mpc, which is centred on the Local Group. The Local Volume is the premier location for studying large numbers of galaxies with superb angular resolution. Most noteworthy is that the Local Volume is the only location where it is possible to analyse in detail the properties of numerous dwarf (irregular and elliptical) galaxies.

The first attempt at compiling a distance limited catalogue for the Local Volume was undertaken by Kraan-Korteweg & Tammann (1979) who published a list of 179 nearby galaxies satisfying the condition $v_{LG} < 500$ km s$^{-1}$, where $v_{LG}$ is heliocentric velocity corrected for the peculiar motion of the Galaxy within the Local Group. They used the definition $H_0 = 50$ km s$^{-1}$ Mpc$^{-1}$ providing the first census of the Local Volume population. Kraan-Korteweg & Tammann highlighted the need for caution using distances from radial velocities alone. They noted that the Virgo cluster had a systemic velocity of 1050 km s$^{-1}$ and a velocity dispersion of 690 km s$^{-1}$ and that the cluster members populating the low velocity tail would enter their catalogue. Therefore all galaxies within a radius of 5 degrees from the cluster centre were excluded.

Over the following decades, various updates have been made to Local Volume catalogue. Visual inspection of the POSS-II/ESO/SERC plates found more than 500 nearby dwarf galaxy candidates (see Karachentseva & Karachentsev 1998; Karachentseva et al. 1999; Karachentseva & Karachentsev 2000; Karachentsev et al. 2000, 2001 for a compilation of candidates), with approximately 100 being confirmed as new galaxies with radial velocities less than 500 km s$^{-1}$ (Huchtmeier et al., 1997, 2000, 2001; Makarov et al., 2003). Dedicated searches for dwarf companions of nearby galaxies have also revealed new Local Volume galaxies (Kraan-Korteweg et al., 1994; Huchtmeier et al., 1995; McCall & Buta, 1995, 1997; Côté et al., 1997; Armandroff et al., 1998; Jerjen et al., 1998; Armandroff et al., 1999; Jerjen et al., 2000), with more discovered through the use of "blind" H I surveys (Zwaan et al., 1997; Staveley-Smith et al., 1998; Henning et al., 1998, 2000; Rosenberg & Schneider, 2000; Kilborn et al., 2002; Minchin et al., 2003; Donley et al., 2005). Most recently, the search for ultra-faint companions to the Milky Way has begun identifying new Local Group members (Martin et al., 2004; Willman et al., 2005a,b; Sakamoto & Hasegawa, 2006; Zucker et al., 2006; Belokurov et al., 2006, 2007; Walsh et al., 2007).

While searches for new Local Volume galaxies has been increasing the sample size, other factors have been causing it to decrease. Many candidates have been identified by visual inspection of photographic plates, some of which have never had follow up observations to confirm their detection (see section 2.5 of this thesis for an analysis of several galaxies which we hypothesise are incorrectly listed). Moreover, as accurate modern distance estimates are obtained for nearby

galaxies, those located nearby the boundary of the 10 Mpc sphere are either included or excluded from the Local Volume reliably, which was ambiguous using a radial velocity based distance alone. Thus, the census of galaxies in the Local Volume ($D < 10$ Mpc) is constantly evolving and updating as new nearby galaxies are discovered and accurate distance estimates are obtained. The current catalogue of Local Volume galaxies contains 451 galaxies (Karachentsev et al., 2004) and was estimated to be 70% – 80% complete within 8 Mpc. However, this estimate assumes that the sample within $D = 2$ Mpc is complete to nearly 100%. The newly discovered ultra-faint population of Local Group galaxies shows that the completeness is overestimated. A recent update presented at the 'Galaxies in the Local Volume' conference (Koribalski & Jerjen, 2008) puts the number of known Local Volume galaxies at 550 (Karachentsev et al., 2008).

Throughout this thesis, the 2004 catalogue of Karachentsev et al. is used to define our Local Volume galaxy sample, except where stated otherwise.

## 1.2. Multiwavelength Properties of Nearby Galaxies

Over the past several decades the possibilities available in observational astronomy have increased dramatically. As a result, astronomers now have access to almost the entire electromagnetic spectrum; from Gamma ray through to radio wavelengths, to observe and study the Universe. Different physical processes can be observed at different wavelengths which allows a more complete understanding to be obtained.

In this thesis, the stellar and the neutral hydrogen components of galaxies will be analysed and compared. Stars are most commonly observed at the visible wavelengths whereas the neutral hydrogen is detection at radio wavelengths. These two observing regimes will therefore be discussed in detail.

### 1.2.1. Visible and Near Infrared Wavelengths

Astronomy is one of the oldest sciences. In early times, astronomy comprised only the observation and predictions of the motions of objects visible to the naked eye. Although new technologies have made available most of the electromagnetic spectrum, much of our knowledge of galaxies is still obtained observing at the visible wavelengths (approximately 400 – 700 nm).

The overwhelming contributor to the visible light emitted by galaxies is the stellar population. In the nearest of galaxies, this stellar component can often be resolved into individual stars in optical images. Traditionally, almost all catalogues of nearby galaxies have been made using optical $B$-band (390 – 480 nm) measurements due to technical necessity. Much of the light observed in the $B$-band is emitted by hot massive O and B stars. Some of the blue light of

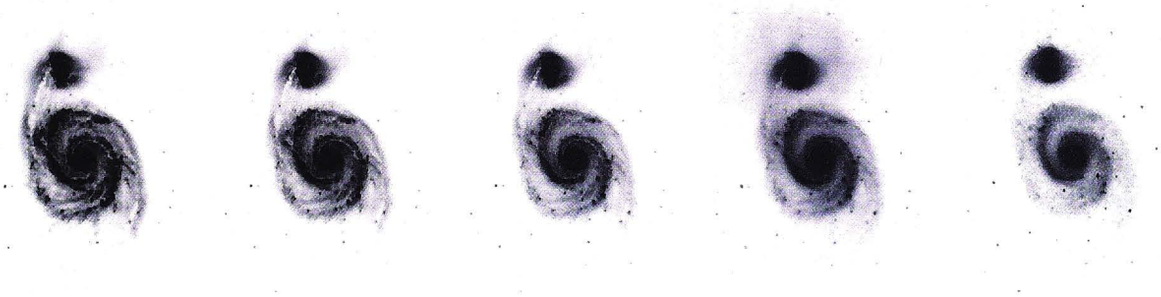

**Figure 1.1** An illustrative example of the differences between the visible and the near-IR. The galaxy M51 and its companion NGC 5195 images in *B*, *V*, *R*, *I*, and *H*-bands from left to right. The *B*-band image is dominated by emission from young massive stars. At longer wavelengths (right hand panels) images are dominated by emission from the old stellar population and are less affected by dust and star formation. – *B*, *V*, *R* and *I* images obtained from Engelbracht et al. (2005), *H* image from Jarrett et al. (2003)

these short-lived giants is absorbed by surrounding dust and re-radiated in the far-infrared at wavelengths greater than approximately 10 $\mu$m. Therefore, *B*-band images of galaxies emphasise where the young massive stars are born, i.e. the spiral arm features, and also have areas of reduced emission indicating absorption of the light due to dust.

As we move away from visible light towards longer wavelengths, we enter the infrared (IR) region of the spectrum. The near-IR emission of Local Volume galaxies is dominated by the quiescent old stellar population. This long lived, low mass, dynamically relaxed stellar population dominates a galaxy's stellar mass and is therefore the most reliable tracer of the galaxy's underlying gravitational potential. Dust attenuation is also vastly reduced at near-IR wavelengths and hence the near-infrared provides a more accurate, unaltered view of the stellar component of a galaxy. The differences between the visible and near-IR is most clearly demonstrated visually. Figure 1.1 shows a sequence of images of M51 in a variety of filters is given. In this figure, shorter wavelength (bluer) are on the left with longer wavelengths (near-IR) on the right. The images show a progressive change towards a smoother appearance at longer wavelengths. Figure 1.2 shows the location of the *B* and *H*-band (1.65 $\mu$m) filters superimposed on the night sky spectrum (dotted line), a galaxy's continuum before and after star burst (solid lines), and the dust attenuation curve (dashed line) (Driver, 2004). This shows the impact of star formation (the difference between the two solid lines) and dust attenuation is reduced in the near-IR and that the *H*-band offers the optimal spectral regime for studies of the stellar content of nearby galaxies.

The stellar mass of a galaxy can be infered from its luminosity, $L_H$:

$$L_H = 10^{0.4(M_{H,\odot}-M_{H,0})}, \quad \text{and} \quad M_{H,0} = m_H - 5\log_{10} D - 25 - A_H \tag{1.1}$$

where $D$ is the galaxy distance in Mpc, $m_H$ is the *H*-band apparent magnitude, $A_H$ is the *H*-band Galactic extinction and $M_{H,\odot} = 3.35$ mag is the *H*-band luminosity

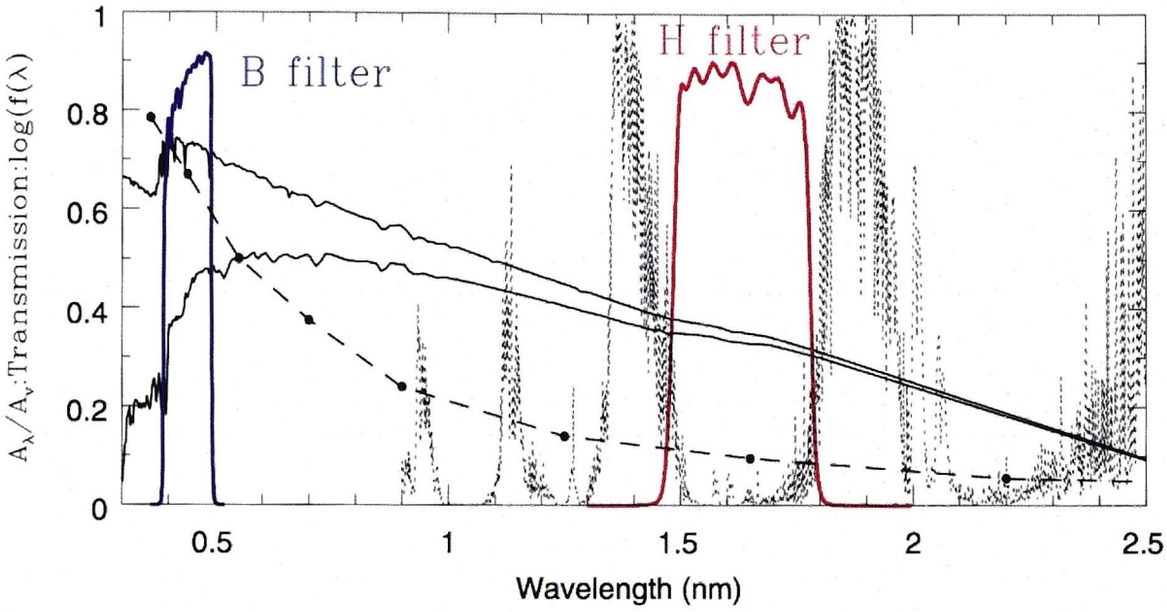


**Figure 1.2** An illustration of the advantages of the near-IR, showing a spectrum of the night sky (dotted line), a spectrum of a galaxy before and after star burst (solid lines), the location of the *B* and *H* filters and the extinction curve (dashed line). – Figure from Driver (2004)

of the sun (Colina et al., 1996). To obtain a measure of the stellar mass a mass-to-light ratio must be applied. This is a source of considerable uncertainty which will be discussed in detail in Chapter 2 of this thesis.

The earliest large-area near-IR survey of the sky was the Two Micron Sky Survey (Neugebauer & Leighton, 1969) which surveyed approximately 70% of the sky and detected ~ 5700 sources. This was vastly improved upon by the Two Micron All Sky Survey (2MASS; Skrutskie et al. 2006) which surveyed 99.998% of the sky and detected 470,992,970 point sources and 1,647,599 extended sources. 2MASS is the current benchmark for near-IR photometry of galaxies and represents the first uniform, all-sky, dust-penetrated view of galaxies of every type (Jarrett et al., 2003). It was the first survey to define the near-IR Hubble galaxy morphology classification sequence providing a qualitative guide to the appearance of galaxies at dust penetrating wavelengths (Jarrett, 2000). However the short integration time of 2MASS observations (7.8 seconds) resulted in most of the low surface brightness (LSB) dwarfs remaining undetected, and if they were detected, 2MASS underestimated the fluxes by as much as 70% (Andreon, 2002). Although targeted near-IR observations were inherently deeper (eg, Gavazzi et al. 1996a,c, 2000; Boselli et al. 2000), the samples included few LSB dwarfs. Therefore, there is a clear need for a deeper and higher resolution study to investigate those galaxies that were beyond the reach of photometric near-IR studies to date.

### 1.2.2. The 21 cm Line

The spectral line at 21 cm (or a frequency of 1420.4 MHz) is created by the transition between the two hyperfine levels of the neutral hydrogen 1s ground state. The two energy levels result from the magnetic interaction between the quantised electron and proton spins. When the relative spins change from parallel to antiparallel, a photon with a wavelength of 21 cm is emitted. This line falls within the radio region (wavelengths longer than 10 cm) of the electromagnetic spectrum and is used extensively in astronomy to observe neutral hydrogen. The atmospheric opacity and attenuation by interstellar dust is low at the hydrogen line (H I line) wavelengths and hence it provides a clear view of the majority of unprocessed baryons in the Local Volume.

Neutral hydrogen is the major component of the interstellar medium in galaxies. The H I line is used to obtained the total mass of the neutral hydrogen component of a galaxy as:

$$M_{HI} = 2.36 \times 10^5 \, D^2 \, F_{HI} \quad M_\odot \tag{1.2}$$

where $F_{HI}$ is the integrated flux density in Jy km s$^{-1}$, and $D$ is the galaxy distance in Mpc (Roberts, 1975). However, H I line observations have proven to be particularly useful not only to determine the atomic hydrogen distribution but also galaxy kinematics. The observed central frequency of the H I line can be used to measure the radial velocity of a galaxy. Moreover, the H I line is Doppler broadened due to the receding and approaching sides of a galaxy disk. Therefore, the width of the H I line can be used to measure a galaxy's rotational velocity (although it is important to note that the line is further broadened due to turbulent motions of the gas). The H I disk frequently extends well outside the stellar radius (eg., Broeils & van Woerden 1994; Meurer et al. 1996; Salpeter & Hoffman 1996; Broeils & Rhee 1997) and therefore the H I rotation is often the best measure of a galaxy's total (or dynamic) mass.

The 21 cm line was first observed from Galactic hydrogen emission by Ewen & Purcell in 1951. Since this time, many H I surveys have targeted catalogued galaxies, galaxy groups and galaxy clusters (see Koribalski et al. 2004 for a summary). The arrival of a 21 cm multibeam system on the 64 m Parkes Telescope (Staveley-Smith et al., 1996) provided the opportunity for a blind southern hemisphere all-sky survey which could easily detect many LSB and late type dwarfs which are often missing in optical surveys. The H I Parkes All-Sky Survey (HIPASS; Barnes et al. 2001) mapped the entire southern sky ($\delta < 2°$) over a velocity range of $-1280$ km s$^{-1} < cz < 12,700$ km s$^{-1}$and currently represents the only H I detection of many dwarf galaxies. It provides important information on the H I mass, rotational velocity and dynamical mass of many nearby galaxies. To supplement this shallow, wide field survey (450 s beam$^{-1}$), the much deeper blind survey, HIDEEP (Minchin et al., 2003), was carried out over a small area of sky ($4 \times 8$ deg$^2$ with an integration time of 9000 s beam$^{-1}$). The major conclusion of HIPASS and HIDEEP was that all H I sources appeared to be associated with

an optical counterpart. Minchin et al. (2003) were able to reach an H I column density limit of $4.2 \times 10^{18}$ cm$^{-2}$, and yet found no galaxies with a column density less than $N_{HI} = 10^{20.65 \pm 0.38}$ which is at least an order of magnitude above the sensitivity limit. This suggests that there are no large gas rich, low surface brightness galaxies, a result that will be discussed further in Chapter 4.

HIPASS was carried out with the single dish Parkes Telescope. Most galaxies are point sources in HIPASS with angular sizes less than the 15.5 arcmin angular resolution (Koribalski et al., 2004). Therefore the H I line width is the only measure of their rotation and no information on the atomic hydrogen distribution is available. The situation is similar in the northern hemisphere with single dish telescopes often providing the only H I detection of many galaxies (eg., the Arecibo H I strip survey; Sorar 1994, the H I Jodrell All-Sky Survey, HIJASS; Kilborn 2002). Therefore, there is a need to follow up on many of the sources with radio interferometer telescopes to provide detailed H I synthesis imaging. Many new targeted H I surveys are currently been carried out using the Giant Metrewave Radio Telescope (FIGGS: Faint Irregular Galaxies GMRT Survey; Begum et al. 2008b), the Very Large Array (including THINGS: The HI Nearby Galaxy Survey; Walter et al. 2005, Little THINGS; Hunter et al. 2007 and VLA-ANGST; Ott et al. 2010), and the Westerbork Synthesis Radio Telescope (WHISP: Westerbork observations of neutral Hydrogen in Irregular and SPiral galaxies; van der Hulst et al. 2001 and WSRT-LVHIS: Westerbork Synthesis Radio Telescope - Local Volume HI Survey; PI = Eva Manthey). In this thesis the new "Local Volume H I Survey" (LVHIS; Koribalski et al. 2010) from the Australia Telescope Compact Array (ATCA) is discussed. It provides deep H I line and 20 cm continuum observations for all nearby, southern hemisphere ($\delta < -30°$), gas rich galaxies allowing for a detailed investigation of the atomic hydrogen distribution and kinematics.

## 1.3. Thesis Overview

This PhD thesis presents an observational study of the stellar and gas properties of galaxies in the Local Volume ($D < 10$ Mpc) and investigates the relation between the atomic hydrogen and stellar components of a galaxy based on a new ultra-deep near-IR survey and the new LVHIS 21 cm survey.

Chapter 2 presents an analysis of the stellar component of 57 galaxies. There we describe the new near-IR "Local Sphere of Influence" (LSI) Survey and investigate the photometric and physical properties of the stellar component of the sample galaxies. The question of whether any genuinely young galaxies exists is addressed and the limitations of 2MASS examined. A optical-infrared $B$ versus $H$ luminosity relation is defined. The $H$-band mass-to-light ratio is discussed in detail and a new empirical ratio determined from the luminosity – surface brightness relation. Finally interesting galaxies are discussed individually.

In Chapter 3 we introduce the new "Local Volume H I Survey" (LVHIS) which provides a high quality data set to investigate the atomic hydrogen component of nearby galaxies. The LVHIS data is used to analyse the kinematics of 12 Local Volume galaxies. In this chapter, the new ATCA spectra are compared to HIPASS spectra and rotation curves presented for each galaxy. The spectral properties are compared to the derived rotation curve parameters and the (baryonic) Tully-Fisher relation is determined. The kinematics of the individual galaxies are discussed in detail.

Chapter 4 presents an investigation into the relation between the two baryonic components; the stellar and the atomic hydrogen components of galaxies in the Local Volume. We examine how well gas and stellar masses correlate in Local Volume galaxies and investigate the H I mass-to-light ratio, $\mathcal{M}_{HI}/L$, which provides a measure of the integral evolutionary status of a galaxy. This is explored further through the relationship between the stellar mass fraction and the total baryonic mass of the sample galaxies

Finally, Chapter 5 summarises the major conclusions and identifies future work in this area.

Chapter 2 of this thesis is published in *The Astronomical Journal*. Chapter 3 is to be submitted to *Monthly Notices of the Royal Astronomical Society* and Chapter 4 to *The Astrophysical Journal*. In accordance with journal style, each chapter contains an abstract, introduction and conclusion. However, the bibliographic details have been collated at the end of the thesis to avoid duplication.

# CHAPTER 2

# Deep Near-IR Surface Photometry of 57 Galaxies in the Local Sphere of Influence

*Published in the Astronomical Journal*
*Kirby, Jerjen, Ryder, & Driver 2008*

**Abstract:**
We present $H$-band (1.65$\mu$m) surface photometry of 57 galaxies drawn from the Local Sphere of Influence (LSI) with distances of less than 10 Mpc from the Milky Way. The images with a typical surface brightness limit 4 mag fainter than 2MASS (24.5 mag arcsec$^{-2}$ < $\mu_{lim}$ < 26 mag arcsec$^{-2}$ ) have been obtained with IRIS2 on the 3.9 m Anglo-Australian Telescope. A total of 22 galaxies that remained previously undetected in the near-IR and potentially could have been genuinely young galaxies were found to have an old stellar population with a star density 1 – 2 magnitudes below the 2MASS detection threshold. The cleaned near-IR images reveal the morphology and extent of many of the galaxies for the first time. For all program galaxies, we derive radial luminosity profiles, ellipticities, and position angles, together with global parameters such as total magnitude, mean effective surface brightness and half-light radius. Our results show that 2MASS underestimates the total magnitude of galaxies with $\langle\mu_H\rangle_{eff}$ between 18 – 21 mag arcsec$^{-2}$ by up to 2.5 mag. The Sérsic parameters best describing the observed surface brightness profiles are also presented. Adopting accurate galaxy distances and a $H$-band mass-to-light ratio of $\Upsilon_*^H = 1.0 \pm 0.4$, the LSI galaxies are found to cover a stellar mass range of $5.6 < \log_{10}(\mathcal{M}_{\rm stars}) < 11.1$. The results are discussed along with previously obtained optical data. Our sample of

low luminosity galaxies is found to follow closely the optical-infrared $B$ versus $H$ luminosity relation defined by brighter galaxies with a slope of $1.14 \pm 0.02$ and scatter of 0.3 magnitudes. Finally we analyse the luminosity – surface brightness relation to determine an empirical mass-to-light ratio of $\Upsilon_*^H = 0.78 \pm 0.08$ for late-type galaxies in the $H$-band.

## 2.1. Introduction

The observational properties of nearby galaxies such as fluxes, colours, morphologies and sizes reflect their underlying physical properties (stellar/baryonic and dark matter content, star formation rates, formation history and angular momenta). Exactly how these observational and physical properties are related is still poorly understood. By technical necessity, the observational quantities are mainly based on the optical $B$-band (390 – 480 nm). However galaxies evolving in low density environments with little external stimulation for star formation often contain significant quantities of dust (eg. see Driver et al. 2007) which can attenuate and distort their optical light profiles. In contrast, dust attenuation is vastly reduced at near-IR wavelengths and hence the near-IR provides a spectral regime where a more accurate, unaltered representation of a galaxy's underlying stellar distribution can be obtained (Gavazzi et al., 1996b). Furthermore, the stellar mass of most galaxies is dominated by the quiescent old stellar component whose energy output peaks at near-IR wavelengths. Even in the extreme case of Blue Compact Dwarf (BCD) galaxies, previously thought to be primeval galaxies forming their first stars at the present epoch (Thuan & Izotov, 1997), the analysis of their resolved stellar populations has revealed the presence of stars at least a few Gyrs of age (Schulte-Ladbeck et al. eg. the BCD galaxies: VII Zw 403, Mrk 178 and I Zw 36 as discussed by 1998, 2000, 2001, respectively; SBS 1415+437 discussed by Aloisi et al. 2005; I Zw 18 by Aloisi et al. 2007; and CGCG 269-049 by Corbin et al. 2008).

In order to obtain a deeper understanding of the connection between the light and matter distribution in galaxies, a representative sample of nearby stellar systems needs to be studied in detail. The Local Sphere of Influence (LSI, $D < 10$ Mpc) contains large numbers of early (dE) and late-type (dIrr) dwarf galaxies that make up about 85% of the local galaxy population (Kraan-Korteweg & Tammann, 1979; Schmidt & Boller, 1992; Karachentsev et al., 2004). Dwarf galaxies contribute about 4% to the local luminosity density and about 10-15% to the local H I mass density (Karachentsev et al., 2004). Due to their proximity to the Milky Way, LSI galaxies are ideal for a near-IR study which includes significant numbers of dwarf systems.

Previous near-IR surveys include the Two Micron All Sky Survey (2MASS, Skrutskie et al., 2006) as well as deeper targeted galaxy surveys (Gavazzi et al., 1996a,c, 2000; Boselli et al., 2000). 2MASS photometry for galaxies suffers from a

number of important drawbacks that are becoming more evident as the samples of independently investigated galaxies become larger. The short integration time of 2MASS observations resulted in most of the low surface brightness (LSB) dwarfs in the LSI remaining undetected, and if they were detected, 2MASS underestimated the fluxes by as much as 70% (Andreon, 2002). The targeted *H*-band observations of Gavazzi et al. (1996a,c, 2000) and Boselli et al. (2000) were inherently deeper however the samples included few LSB dwarfs. This serious limitation demands a deeper and higher resolution study to investigate those galaxies that were beyond the reach of photometric near-IR studies to date.

A reference atlas of images needs to have the necessary spatial resolution to probe the morphological fine-structure of these nearby galaxies and contain a significant number of dwarf galaxies that are generally overlooked. A LSI sample has the additional advantage that an increasingly large number of nearby galaxies have accurately known distances. Karachentsev et al. (2006) report that 214 out of 451 LSI galaxies have distance estimates (with less than 10% uncertainty) by means of the tip magnitude of the red giant branch (TRGB), the Tully-Fisher relation, and the surface brightness fluctuations (SBF) method (see for example Jerjen et al. 1998, 2001 and Karachentsev et al. 2004). The remaining galaxies have rough distance estimates from the luminosity of their brightest stars, radial velocities or their suspected membership to a known galaxy group.

The purpose of this paper is to present a near-IR *H*-band (1.65$\mu$m) atlas of 57 LSI galaxies, probing to flux levels approximately 4 mag arcsec$^{-2}$ or 40 times fainter than 2MASS. The majority of the galaxies presented here are much fainter than those in previous targeted surveys. We derive photometric parameters for each object such as the total magnitude, the effective radius and effective surface brightness, Sérsic fitting parameters, etc. Using the best distances currently available in the literature allows us to derive physical parameters such as their luminosities and stellar masses.

The paper is organised as follows: we describe the sample selection in section 2.2. In section 2.3 and section 2.4 we discuss the observing strategies, the data reduction, and the photometric calibration of the images. The 11 galaxies in the sample which remained undetected at our faint detection limit or had images which could not be usefully analysed are discussed in section 2.5. The new data is compared to 2MASS photometry and optical (*B*-band) data in section 2.6 and the luminosity - surface brightness relation discussed. Interesting properties of individual galaxies are described in section 2.7. Finally, the results are summarised in section 2.8.

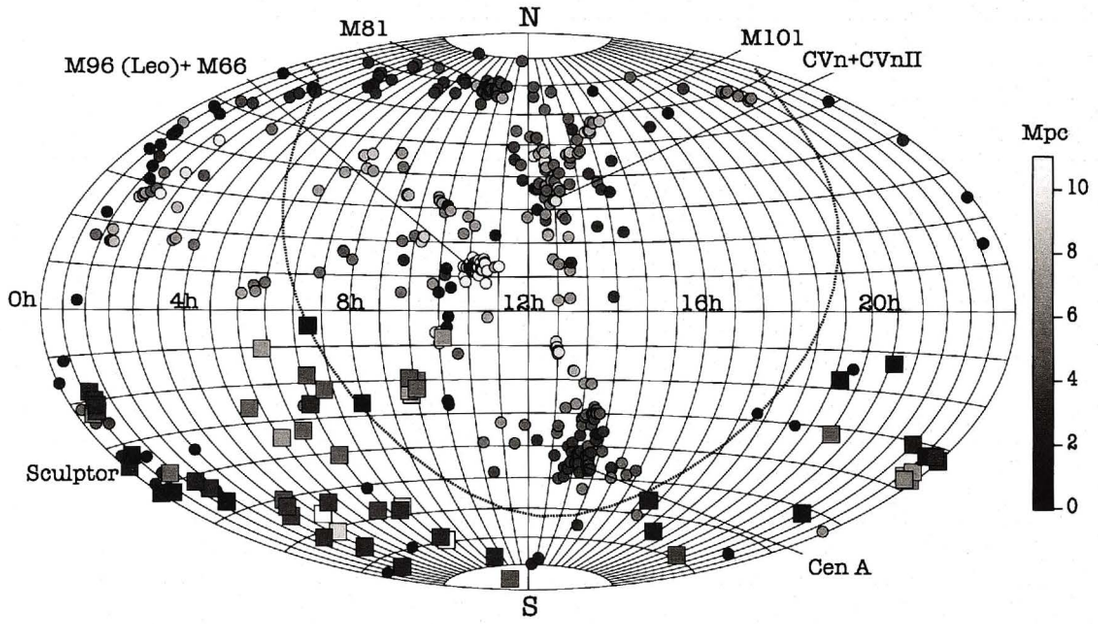


**Figure 2.1** The distribution of galaxies within the Local Sphere of Influence. The circles represent the 451 galaxies listed in Karachentsev et al. (2004) plus 19 from other catalogues, and the squares are the 68 galaxies investigated in our study. The greyscale reflects a galaxy's distance. The curved line shows the location of the Galactic plane.

## 2.2. Sample selection

We have compiled a list of 470 galaxies with estimated distances less than 10 Mpc from the Milky Way[1], from the catalogues of Schmidt & Boller (1992), Côté et al. (1997), Jerjen et al. (2000), and Karachentsev et al. (2004). Approximately 70% of LSI galaxies are members of seven nearby galaxy groups including the Local Group (LG). Each group contains one or more massive spiral or elliptical galaxies accompanied by a population of dwarf satellites which tend to be dwarf ellipticals (dE). The southern hemisphere contains 174 LSI galaxies, 113 of which are members of a nearby group. We randomly selected 68 program galaxies with a range of total apparent $B$-band magnitude (between $m_B = 9$ and 18 mag, as well as several with no optical detection to date) and morphology (Hubble types E3 through to Sc, including many irregular and dwarf galaxies), 19 of which were members of a nearby group. Therefore, our sample contains 80% ($= \frac{68-19}{174-113}$) of southern hemisphere field galaxies and 17% (= 19/113) of group members. The distribution of these Local Sphere of Influence galaxies is shown in Figure 2.1.

The selected galaxies further provide a complementary data set to the Local Volume H I Survey (LVHIS; Koribalski, 2007) which is a H I imaging survey of all LSI galaxies south of declination $\delta = -30°$ that were detected by the H I Parkes

[1]Note that five galaxies have had their distance estimates revised since their inclusion in the sample and have a distance greater than 10 Mpc.

All-Sky Survey (HIPASS, Barnes et al., 2001). The former H I survey is currently been carried out at the Australia Telescope Compact Array. The basic properties of our sample galaxies have been listed in Table 2.1 which is organised as follows:

*Column* (1). - Galaxy name.

*Column* (2). - Morphological type in the Hubble (1936), Sandage (1961), and Sandage & Binggeli (1984) classification scheme.

*Columns* (3) and (4). - Equatorial coordinates for the epoch J2000.

*Column* (5). - Total $B$-band magnitude and its source. When the uncertainty associated with this value is not provided, an error of 0.2 mag has been adopted.

*Columns* (6) and (7) - Distance to the galaxy (from Karachentsev et al. 2004, 2006; Seth et al. 2005; Carrasco et al. 2001) with an indication of the method used: (TRGB) tip magnitude of the red giant branch; (SBF) surface brightness fluctuations; (MEM) group membership; (H) Hubble flow distance $D = v_{LG}/H_0$ where $H_0 = 73$km s$^{-1}$Mpc$^{-1}$ is adopted (WMAP, Spergel et al., 2007).

*Column* (8). - Heliocentric radial velocity, $v_\odot$, from the NASA Extragalactic Database (NED).

*Column* (9). - Local Group velocity, $v_{LG}$, from NED.

*Column* (10). - Reddening estimate, $E(B-V)$ from Schlegel et al. (1998). The associated error is 16%.

*Columns* (11), (12), (13) and (14). - The observing log. The observation date, strategy, total exposure time and seeing is listed.

**Table 2.1** Basic Properties of Sample Galaxies and Observing Log.

| Name | Type | R.A. J(2000.0) | Decl. (J2000.0) | $v_\odot$ (km s$^{-1}$) | $v_{LG}$ (km s$^{-1}$) | $D$ (Mpc) | Method | $m_B$ (mag) | $E(B-V)$ (mag) | Obs. date | Method | $t_{tot}$ (sec) | Seeing (arcsec) |
|---|---|---|---|---|---|---|---|---|---|---|---|---|---|
| (1) | (2) | (3) | (4) | (5) | (6) | (7) | (8) | (9) | (10) | (11) | (12) | (13) | (14) |
| SC18 | LSB | 00:00:59.12 | -41:09:19.6 | 151 | 129 | 1.8 | H | 17.30[j] | 0.013 | 2004-10-22 | JSF | 1620 | 1.2 |
| ESO349-G031 | Irr | 00:08:13.36 | -34:34:42.0 | 207 | 216 | 3.21 | TRGB[b] | 15.48[a] | 0.012 | 2005-01-11 | JSF | 1620 | 1.5 |
| ESO294-G010 | dS0 | 00:26:33.37 | -41:51:19.0 | – | – | 1.92 | TRGB[a] | 15.53[a] | 0.006 | 2006-01-02 | JSF | 1620 | 1.3 |
| ESO473-G024 | Irr | 00:31:22.51 | -22:45:57.5 | 541 | 596 | 8.2 | H | 16.11[e] | 0.019 | 2004-10-23 | JSF | 1620 | 1.3 |
| SC24 | LSB | 00:36:38.31 | -32:34:25.2 | 79 | 83 | 1.1 | H | 17.98[j] | 0.015 | 2006-01-02 | JSF | 1620 | 1.3 |
| IC1574 | Irr | 00:43:03.82 | -22:14:48.7 | 363 | 413 | 4.92 | TRGB[a] | 14.36[a] | 0.015 | 2005-01-11 | JSF | 1350 | 1.9 |
| ESO540-G030 | Irr | 00:49:20.96 | -18:04:31.5 | – | – | 3.4 | TRGB[a] | 16.37[a] | 0.023 | 2005-01-10 | JSF | 1728 | 1.6 |
| UGCA15 | Irr | 00:49:49.20 | -21:00:54.0 | 294 | 346 | 3.34 | TRGB[a] | 15.19[a] | 0.017 | 2004-10-22 | JSF | 1620 | 1.3 |
| ESO540-G032 | Irr | 00:50:24.32 | -19:54:24.2 | – | – | 3.42 | TRGB[a] | 16.44[a] | 0.020 | 2006-01-02 | JSF | 1620 | 1.4 |
| AM0106-382 | dIrr | 01:08:21.93 | -38:12:34.5 | 645 | 605 | 8.3 | H | 16.61[f] | 0.012 | 2004-10-22 | JSF | 1350 | 1.1 |
| NGC0625 | Sb | 01:35:04.63 | -41:26:10.3 | 396 | 309 | 4.07 | TRGB[a] | 11.59[a] | 0.016 | 2006-01-02 | JSF | 1620 | 1.3 |
| SC42 | LSB | 01:39:15.92 | -47:17:51.4 | 162 | 64 | 0.9 | H | 16.66[j] | 0.015 | 2004-10-22 | JSF | 1620 | 1.1 |
| ESO245-G005 | Irr | 01:45:03.74 | -43:35:52.9 | 394 | 308 | 4.43 | TRGB[a] | 12.73[a] | 0.016 | 2005-12-29 | JSF | 1350 | 1.4 |
| KK2000-03** | dE | 02:24:44.58 | -73:30:49.20 | – | – | 4.1 | MEM[a] | 16.0[a] | 0.051 | 2006-01-01 | JSF | 1620 | 1.9 |
| ESO115-G021 | Sc | 02:37:48.10 | -61:20:18.0 | 513 | 337 | 4.66 | TRGB[a] | 13.34[a] | 0.026 | 2005-12-29 | JSF | 1350 | 1.4 |
| ESO154-G023 | Sb | 02:56:50.38 | -54:34:17.1 | 578 | 412 | 5.6 | H | 12.69[a] | 0.017 | 2004-10-23 | CSJ | 1800 | 1.1 |
| KK2000-04** | Irr | 03:12:46.14 | -66:16:12.5 | – | – | 4.2*** | MEM[i] | 17.8[i] | 0.032 | 2006-01-01 | JSF | 810 | 1.8 |
| KK2000-06** | Irr | 03:14:26.14 | -66:23:27.9 | – | – | 4.2*** | MEM[i] | 17.0[i] | 0.055 | 2006-01-01 | JSF | 810 | 1.8 |
| NGC1313 | Sd | 03:18:16.05 | -66:29:53.7 | 475 | 270 | 4.15 | TRGB[a] | 9.66[a] | 0.109 | 2005-12-30 | CSJ | 750 | 1.4 |
| NGC1311 | Sb | 03:20:06.96 | -52:11:07.9 | 570 | 398 | 5.5 | H | 13.18[a] | 0.021 | 2005-12-30 | JSF | 540 | 1.5 |
| AM0319-662 | dIrr | 03:21:02.40 | -66:19:09.0 | 232 | 26 | 4.07 | TRGB[a] | 16.5[a] | 0.077 | 2005-12-30 | JSF | 810 | 1.3 |
| IC1959 | Sb | 03:33:12.59 | -50:24:51.3 | 639 | 464 | 6.4 | H | 13.26[a] | 0.011 | 2005-12-31 | JSF | 1620 | 1.3 |
| AM0333-611 | Irr | 03:34:15.34 | -61:05:47.6 | 1172 | 971 | 13.3 | H | 16.47[j] | 0.032 | 2004-10-24 | JSF | 1080 | 1.2 |
| IC2038 | Sd | 04:08:53.75 | -55:59:22.4 | 712 | 505 | 16.5 | MEM[d] | 14.98[a] | 0.011 | 2005-12-31 | JSF | 1620 | 1.3 |
| IC2039 | S0 | 04:09:02.37 | -56:00:42.1 | 857 | 649 | 16.5 | MEM[d] | 14.97[e] | 0.012 | 2005-12-31 | JSF | 1620 | 1.3 |
| NGC1705 | S0 | 04:54:13.50 | -53:21:39.8 | 627 | 400 | 5.1 | TRGB[a] | 12.76[a] | 0.008 | 2004-10-21 | JSF | 1620 | 1.1 |
| NGC1744 | Sb | 04:59:57.80 | -26:01:20.0 | 741 | 574 | 7.9 | H | 11.94[e] | 0.041 | 2006-01-02 | JSF | 1620 | 1.2 |

Continued on next page

**Table 2.1 – continued from previous page**

| Name | Type | R.A. J(2000.0) | Decl. (J2000.0) | $v_\odot$ (km s$^{-1}$) | $v_{LG}$ (km s$^{-1}$) | $D$ (Mpc) | Method | $m_B$ (mag) | $E(B-V)$ (mag) | Obs. date | Method | $t_{\rm tot}$ (sec) | Seeing (arcsec) |
|---|---|---|---|---|---|---|---|---|---|---|---|---|---|
| (1) | (2) | (3) | (4) | (5) | (6) | (7) | (8) | (9) | (10) | (11) | (12) | (13) | (14) |
| AM0521-343 | dIrr | 05:23:23.72 | -34:34:29.5 | 963 | 756 | 10.4 | H | 15.74[g] | 0.028 | 2004-10-21 | JSF | 1620 | 1.1 |
| KKS2000-55** | Sb | 05:50:17.71 | -10:17:51.6 | 901 | 736 | 10.1 | H | – | 0.827 | 2005-12-31 | JSF | 1620 | 1.4 |
| ESO364-G029 | Irr | 06:05:45.22 | -33:04:51.0 | 787 | 549 | 7.5 | H | 13.58 [a] | 0.044 | 2005-12-29 | JSF | 1620 | 1.2 |
| ESO121-G020 | Irr | 06:15:54.19 | -57:43:31.6 | 575 | 311 | 6.05 | TRGB[b] | 15.85[a] | 0.040 | 2004-10-21 | JSF | 1620 | 1.1 |
| ESO490-G017 | Irr | 06:37:57.09 | -26:00:03.10 | 503 | 264 | 4.23 | TRGB[b] | 14.01[a] | 0.078 | 2004-10-22 | JSF | 1080 | 1.3 |
| ESO308-G022 | dIrr | 06:39:32.70 | -40:43:15.0 | 821 | 556 | 7.6 | H | 16.05[a] | 0.089 | 2005-12-30 | JSF | 810 | 1.2 |
| KKS2000-09** | S | 06:46:56.63 | -17:56:27.2 | 693 | 471 | 6.5 | H | 17.2[a] | 0.443 | 2006-01-01 | JSF | 1620 | 1.2 |
| HIZSS003 | – | 07:00:29.3 | -04:12:30 | 280 | 101 | 1.4 | H | 18[a] | 1.032 | 2005-12-29 | JSF | 1620 | 1.4 |
| Argo | dIrr | 07:05:18.80 | -58:31:13.0 | 564 | 284 | 4.9 | TRGB[a] | 14.95[a] | 0.119 | 2005-12-30 | JSF | 810 | 1.2 |
| ESO558-PN011 | Irr | 07:06:56.80 | -22:02:26.0 | 731 | 489 | 6.7 | H | 14.43[a] | 0.372 | 2004-10-23 | JSF | 1620 | 1.2 |
| AM0717-571 | Irr | 07:18:37.90 | -57:24:46.5 | 1148 | 865 | 11.8 | H | – | 0.165 | 2006-01-02 | JSF | 1620 | 1.2 |
| ESO059-G001 | Irr | 07:31:18.20 | -68:11:16.8 | 530 | 255 | 4.57 | TRGB[b] | 13.98[a] | 0.147 | 2005-12-31 | JSF | 1620 | 1.3 |
| AM0737-691 | Irr | 07:37:12.6 | -69:20:31 | 1456 | 1174 | 16.1 | H | 16.82[h] | 0.213 | 2004-10-24 | JSF | 1080 | 1.1 |
| KK2000-25** | Irr | 07:56:38.48 | -26:15:01.9 | 241 | -34 | 0.5*** | H | 17.7[a] | 0.335 | 2006-01-02 | JSF | 810 | 1.0 |
| ESO006-G001 | Sb | 08:19:22.14 | -85:08:35.9 | 738 | 488 | 6.7 | H | 15.13[a] | 0.193 | 2006-01-01 | JSF | 1620 | 1.8 |
| UGCA148 | Irr | 09:09:46.54 | -23:00:33.0 | 725 | 439 | 9.8 | MEM[a] | 15.63[a] | 0.167 | 2006-01-02 | JSF | 1620 | 1.1 |
| NGC2784 DW1 | dE | 09:12:18.5 | -24:12:41 | – | – | 9.8 | MEM[a] | 17.27[a] | 0.206 | 2006-01-01 | CSJ | 900 | 1.3 |
| NGC2784 | S0 | 09:12:19.50 | -24:10:21.4 | 697 | 402 | 9.82 | SBF[k] | 11.17[a] | 0.214 | 2006-01-01 | CSJ | 900 | 1.3 |
| KK98-73 | dE | 09:12:29.30 | -24:14:28.0 | – | – | 9.8 | MEM[a] | 16.35[a] | 0.197 | 2006-01-01 | CSJ | 900 | 1.3 |
| UGCA153 | Irr | 09:13:12.08 | -19:24:31.0 | 768 | 491 | 6.7 | H | 15.40[a] | 0.088 | 2006-01-02 | JSF | 1620 | 1.1 |
| NGC2835 | Sc | 09:17:52.91 | -22:21:16.8 | 886 | 601 | 8.2 | H | 11.03[e] | 0.101 | 2006-01-01 | CSJ | 600 | 1.3 |
| UGCA162 | Irr | 09:21:28.07 | -22:30:06.8 | 846 | 560 | 7.7 | H | 14.87[e] | 0.067 | 2006-01-01 | JSF | 1620 | 1.2 |
| ESO565-G003 | Irr | 09:23:10.00 | -20:10:03.2 | 829 | 549 | 7.5 | H | 15.53[a] | 0.062 | 2006-01-02 | JSF | 1620 | 1.2 |
| NGC2915 | Irr | 09:26:11.53 | -76:37:34.8 | 468 | 192 | 3.78 | TRGB[a] | 13.20[a] | 0.275 | 2005-01-10 | JSF | 1728 | 1.5 |
| NGC3115 | S0 | 10:05:13.98 | -07:43:06.9 | 720 | 478 | 9.86 | SBF[k] | 9.86[a] | 0.047 | 2006-01-01 | CSJ | 900 | 1.4 |
| SJK98 J1616-55 | – | 16:16:49.0 | -55:44:57 | 421 | 247 | 3.4 | H | – | 0.633 | 2006-05-14 | JSF | 810 | 1.4 |
| HIZOAJ1616-55* | – | 16:18:46 | -55:37:30 | 409 | 236 | 3.2 | H | – | 0.616 | 2006-05-04 | JSF | 810 | 1.5 |
| IC4662 | Irr | 17:47:08.86 | -64:38:30.3 | 302 | 153 | 2.44 | TRGB[b] | 11.74[a] | 0.070 | 2006-05-14 | JSF | 1620 | 1.3 |

Continued on next page

**Table 2.1 – continued from previous page**

| Name | Type | R.A. J(2000.0) | Decl. (J2000.0) | $v_\odot$ (km s$^{-1}$) | $v_{LG}$ (km s$^{-1}$) | $D$ (Mpc) | Method | $m_B$ (mag) | $E(B-V)$ (mag) | Obs. date | Method | $t_{\rm tot}$ (sec) | Seeing (arcsec) |
|---|---|---|---|---|---|---|---|---|---|---|---|---|---|
| (1) | (2) | (3) | (4) | (5) | (6) | (7) | (8) | (9) | (10) | (11) | (12) | (13) | (14) |
| ESO594-G004 | Irr | 19:29:58.97 | -17:40:41.3 | -79 | 24 | 1.04 | TRGB[a] | 14.12[a] | 0.070 | 2006-05-14 | JSF | 1620 | 1.3 |
| ESO461-G036 | dIrr | 20:03:57.38 | -31:40:53.8 | 427 | 470 | 7.83 | TRGB[b] | 17.06[a] | 0.296 | 2006-09-01 | JSF | 1620 | 1.2 |
| DDO210 | Irr | 20:46:51.80 | -12:50:52.5 | -141 | 3 | 0.94 | TRGB[a] | 14.0[a] | 0.051 | 2006-05-14 | JSF | 1620 | 1.3 |
| IC5052 | Sb | 20:52:01.63 | -69:11:35.9 | 584 | 445 | 6.03 | TRGB[c] | 11.68[a] | 0.051 | 2006-09-01 | CSJ | 450 | 1.1 |
| IC5152 | Irr | 22:02:41.51 | -51:17:47.2 | 122 | 69 | 2.07 | TRGB[a] | 11.06[a] | 0.025 | 2006-09-01 | CSJ | 750 | 1.2 |
| ESO468-G020 | E3 | 22:40:43.93 | -30:48:00.2 | – | – | 3.9 | MEM[a] | 17.36[a] | 0.013 | 2006-09-02 | JSF | 1620 | 1.0 |
| UGCA438 | Irr | 23:26:27.52 | -32:23:19.5 | 62 | 99 | 2.23 | TRGB[a] | 13.86[a] | 0.015 | 2004-10-21 | JSF | 1620 | 1.1 |
| ESO347-G017 | Sb | 23:26:56.21 | -37:20:48.9 | 692 | 688 | 9.4 | H | 15.77[e] | 0.017 | 2006-09-02 | JSF | 1620 | 1.0 |
| IC5332 | Sa | 23:34:27.49 | -36:06:03.9 | 701 | 700 | 9.6 | H | 11.00[e] | 0.017 | 2006-09-01 | CSJ | 900 | 1.3 |
| NGC7713 | Sb | 23:36:14.99 | -37:56:17.1 | 692 | 681 | 9.3 | H | 11.66[e] | 0.017 | 2006-09-04 | CSJ | 900 | 1.5 |
| UGCA442 | Sb | 23:43:45.55 | -31:57:24.4 | 267 | 282 | 4.27 | TRGB[a] | 13.58[a] | 0.017 | 2006-09-04 | CSJ | 900 | 1.7 |
| ESO348-G009 | Irr | 23:49:23.47 | -37:46:18.9 | 648 | 633 | 8.7 | H | 15.83[j] | 0.013 | 2006-09-03 | JSF | 1620 | 2.9 |
| NGC7793 | S0 | 23:57:49.83 | -32:35:27.7 | 229 | 252 | 3.91 | TRGB[a] | 9.70[a] | 0.019 | 2004-10-24 | CSJ | 900 | 2.3 |

(a) Karachentsev et al. 2004; (b) Karachentsev et al. 2006; (c) Seth et al. 2005; (d) Carrasco et al. 2001; (e) ESO-LV catalogue, Lauberts & Valentijn 1989; (f) Makarova et al. 2005; (g) Parodi et al. 2002; (h) Vader & Chaboyer 1994; (i) Karachentseva & Karachentsev 2000; (j) Maddox et al. 1990; (k) Tonry et al. 2001.

(*) This galaxy is listed as HIZOAJ1618-55 in the NASA Extragalactic Database (NED). We use the name of HIZOAJ1616-55 which is the original name listed in Juraszek et al. (2000).

(**) We use KK2000 to indicate that the original listing of this galaxy was in the Karachentseva & Karachentsev (2000) paper and KKS2000 to indicate that it was originally listed in the Karachentsev et al. (2000) paper. This is consistent with the names listed in NED.

(***) The distance estimate for KK2000-04 and KK2000-06 is based on a group membership listed by Karachentseva & Karachentsev (2000). These values are discussed in detail in section 2.5. The distance estimate for KK2000-25 is based on a H I spectra obtained by Huchtmeier et al. (2001). Our new data clearly shows that this value is incorrect.

## 2.3. Observations and Reduction

Near-infrared $H$-band images were obtained for the 68 program galaxies during five observing runs between October 2004 and September 2006, using the Infrared Imager and Spectrograph 2 (IRIS2; Tinney et al. 2004) at the 3.9 m Anglo-Australian Telescope (AAT). Table 2.1 lists the observing log of the observations. Atmospheric conditions were clear if not always photometric, and the seeing ranged from 1.″0 to 2.″9 with a mean of 1.″3. The IRIS2 detector is a $1024 \times 1024$ Rockwell HAWAII–1 HgCdTe array with a pixel scale of 0.″45 pixel$^{-1}$, resulting in an instantaneous field-of-view (FoV) of $7.'7 \times 7.'7$.

Two different observing strategies were employed, depending on the anticipated angular extent of the target compared to the IRIS2 FoV:

- Jitter Self Flat (JSF) – The majority of our sample have optical diameters $< 2'$ and, given the sky is typically $7-8$ mag arcsec$^{-2}$ brighter in the $H$-band than the $B$-band, we anticipate these objects filling barely $10-20\%$ of the array in the infrared. These targets were observed in a $3 \times 3$ grid pattern with a spacing of 90″, resulting in a $4.'7 \times 4.'7$ overlap region common to all pointings that encompasses not just the target galaxy but also a substantial amount of the background sky. A maximum of ~30 seconds was spent on any one pointing, consisting of multiple 5–10 s integrations (depending on the sky brightness at the time while aiming to keep the combined object + sky counts well within the linear regime) which were then averaged before being stored. This 9-point jitter pattern was repeated up to 6 times, leading to a total on-source exposure time of just under half an hour per galaxy. This method was also employed on larger, but well-resolved targets such as the Argo Dwarf Irregular galaxy.

- Chop Sky Jitter (CSJ) – In accordance with the recommendations of Vaduvescu & McCall (2004), objects filling $\gtrsim 40\%$ of the array FoV require matching observations of adjacent blank sky to track changes in the background level and illumination pattern. Five jittered observations (10″ offsets) of the target galaxy were bracketed and interleaved with six jittered observations of the (relatively blank) sky 10′ north or south. At each object or sky jitter position, $3 \times 10$ s or $6 \times 5$ s integrations were averaged. This pattern was repeated between 5 and 12 times, for a total on-source exposure time of up to half an hour per galaxy.

The data reduction was carried out using the ORAC-DR[2] pipeline within the starlink package. Observations made with the JSF method employed the JITTER_SELF_FLAT recipe, while those with the CSJ method used the

[2]http://www.oracdr.org/

CHOP_SKY_JITTER recipe. Pre-processing of all raw frames included subtraction of a matching dark frame; linearity and inter-quadrant crosstalk correction; and bad pixel masking.

Considerable care was taken to ensure accurate flat-fielding over the entire field of the array. For JSF observations, an interim flatfield is created by taking the median at each pixel of the nine normalised object frames, then each of the nine images is divided by this interim flatfield. Extended sources within these flatfielded object frames are automatically detected and masked, and an improved flatfield created from masked versions of the nine normalised object frames. A correction for astrometric distortion internal to IRIS2 is applied by resampling the properly flatfielded images, then spatial additive offsets between images are computed using point sources common to all images. The nine images are mosaiced together by applying offsets in intensity to the registered images to produce the most consistent sky value possible in the overlap regions. A new flatfield and mosaic is constructed for each set of nine jittered frames, then all the mosaics registered and co-added to form a master mosaic. Occasionally, significant variations in the level and/or structure of the background sky on a temporal or spatial scale smaller than that sampled by the array within the ~5 minute period of the nine jittered frames resulted in noticeable residual structure in the ensuing mosaic, forcing us to exclude that mosaic from the master mosaic. The total on-source exposure time, after discarding such data, is shown in Table 2.1.

For CSJ observations, the six sky frames are first offset in intensity to a common modal value, then a flatfield formed from the median value at each pixel. All six sky frames, and five object frames are flatfielded, then the modal pixel values of the two sky frames bracketing each object frame are averaged and subtracted from that object frame. Image registration and mosaicing is then performed on each set of five sky-subtracted object frames just as for the JSF observations. These mosaics are registered and co-added to form a master mosaic, with the exception of any showing residual sky structure as described above, yielding the on-source exposure times shown in Table 2.1.

Of the 68 galaxies observed, 11 remained undetected or could not be usefully analysed. This was either because our $H$-band surface brightness limit of $\mu_{lim} \approx 25\,\mathrm{mag\,arcsec^{-2}}$ or $20\,L_{\odot}\,\mathrm{arcsec^{-2}}$ at a distance of 1 Mpc (adopting $M_{H,\odot} = 3.35$ mag, Colina et al. 1996) was not low enough or the galaxy light was heavily contaminated by Galactic foreground stars (see Table 2.4). In both situations the data was not processed further. For instance, the companion galaxies NGC2784 DW1 and KK98-73 were observed parallel to NGC2784. While NGC2784 and KK98-73 can be seen, NGC2784 DW1, located between NGC2784 and KK98-73, is barely visible (see Figure 2.5, second row, middle panel where KK98-73 is visible to the bottom left of the image). The images of the other 57 galaxies are shown in Figures 2.2 to 2.6.

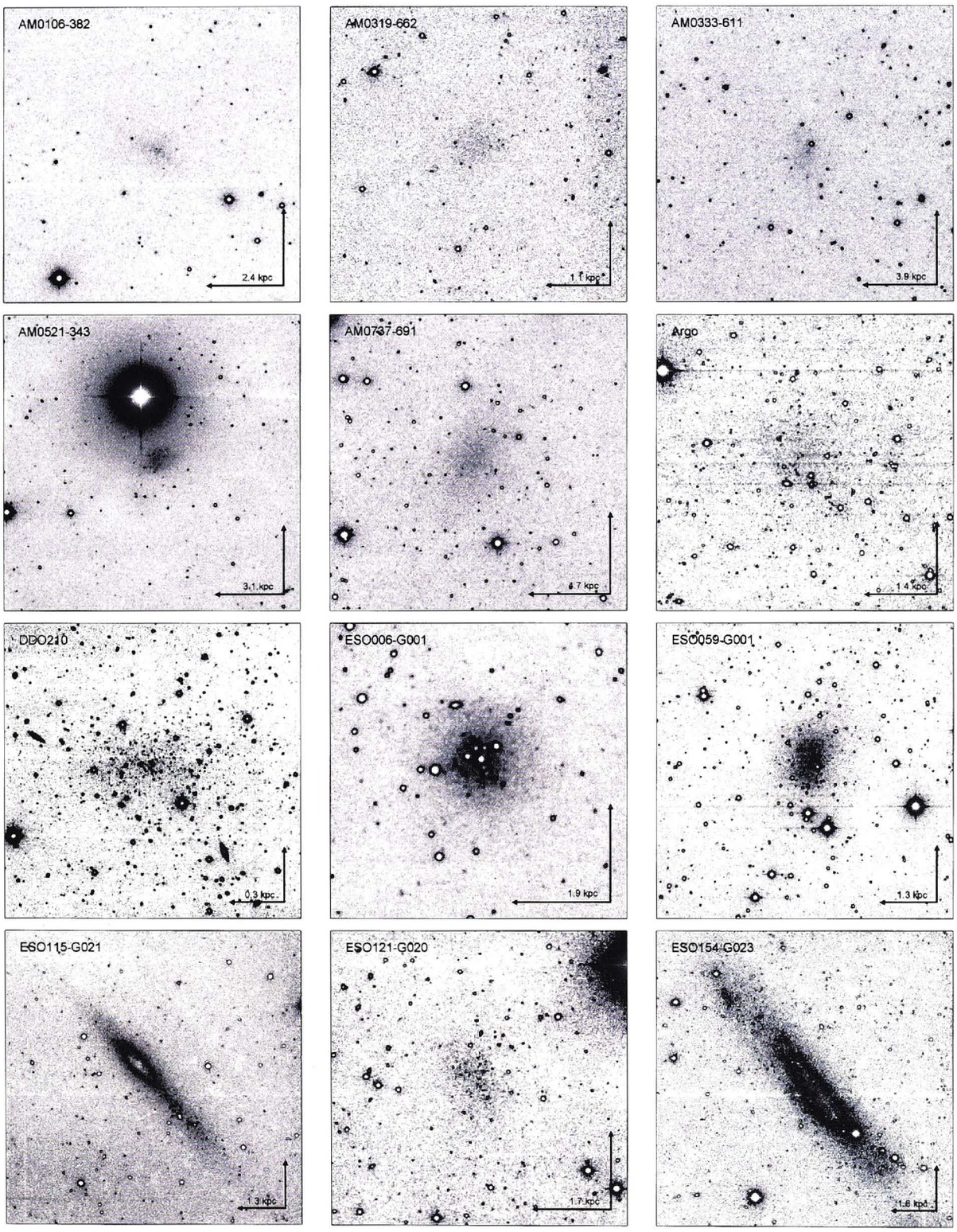


**Figure 2.2** LSI deep *H*-band images from the 3.9m Anglo-Australian Telescope. Here the scale represents 1 arcmin. The corresponding linear scale is also indicated. North is up and East is to the left. The intensity is represented by a greyscale which goes from white (low intensity) to black (medium intensity) and then back to white (high intensity).

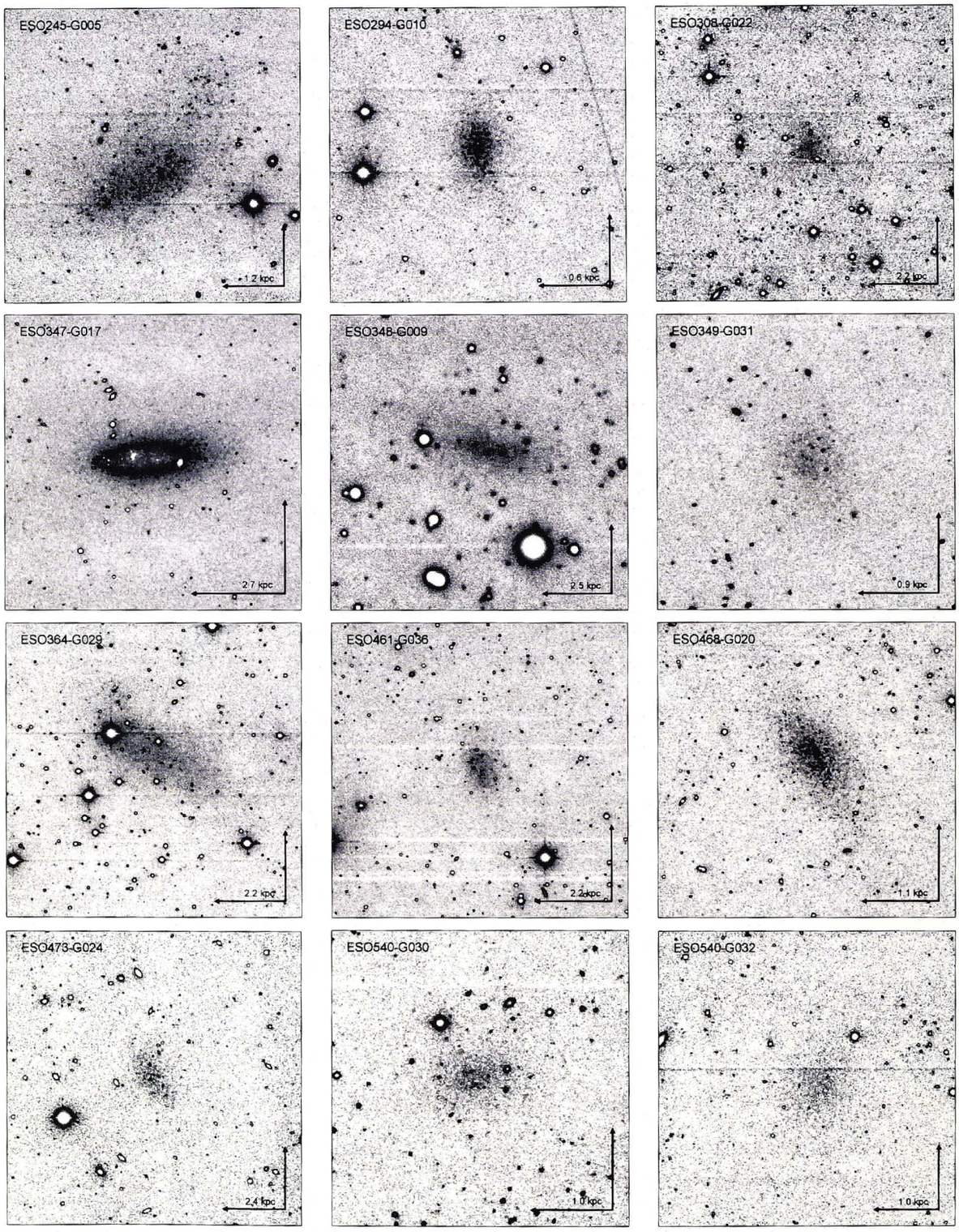


**Figure 2.3** LSI deep $H$-band images from the 3.9m Anglo-Australian Telescope. Here the scale represents 1 arcmin. The corresponding linear scale is also indicated. North is up and East is to the left. The intensity is represented by a greyscale which goes from white (low intensity) to black (medium intensity) and then back to white (high intensity).

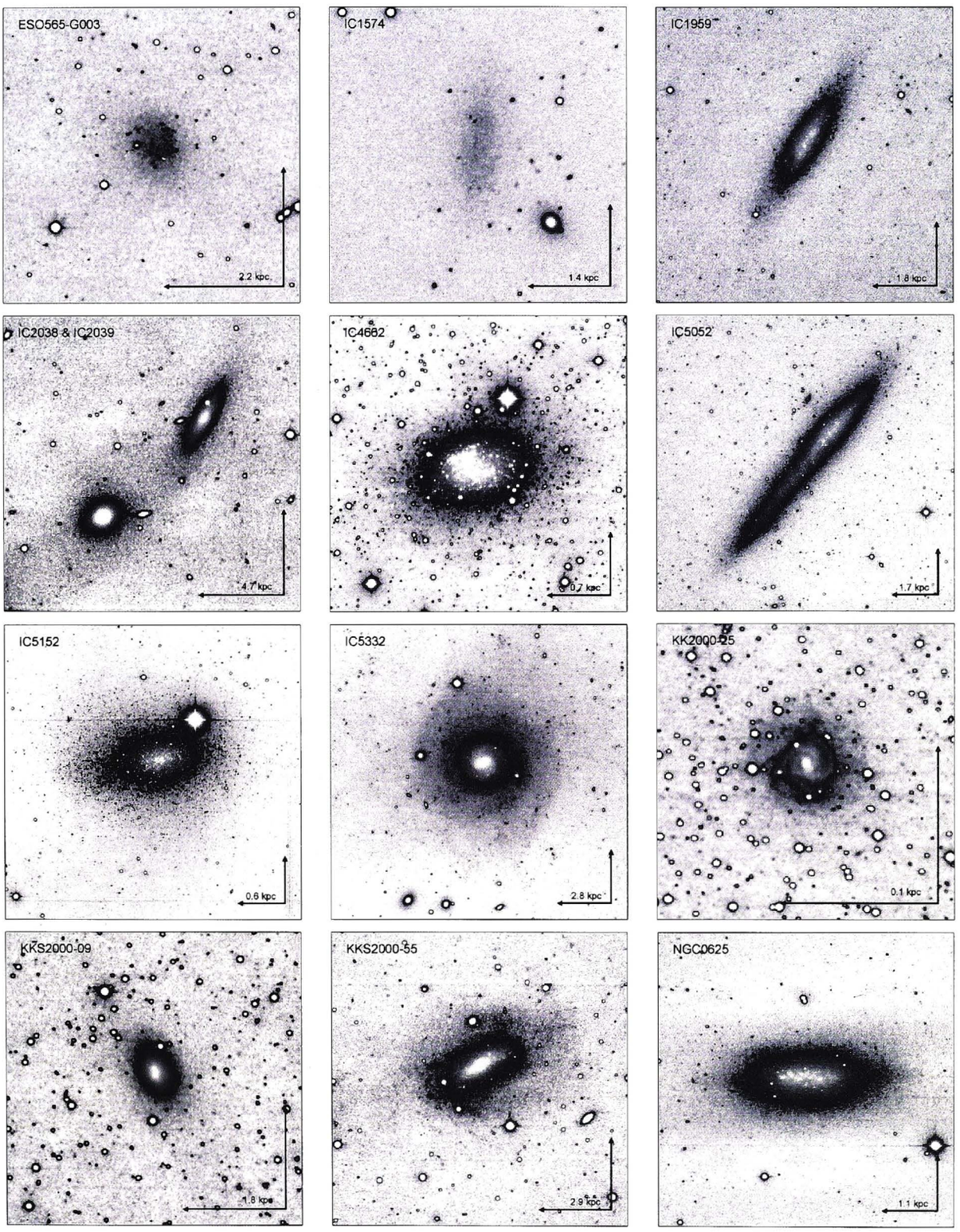


**Figure 2.4** LSI deep $H$-band images from the 3.9m Anglo-Australian Telescope. Here the scale represents 1 arcmin. The corresponding linear scale is also indicated. North is up and East is to the left. The intensity is represented by a greyscale which goes from white (low intensity) to black (medium intensity) and then back to white (high intensity).

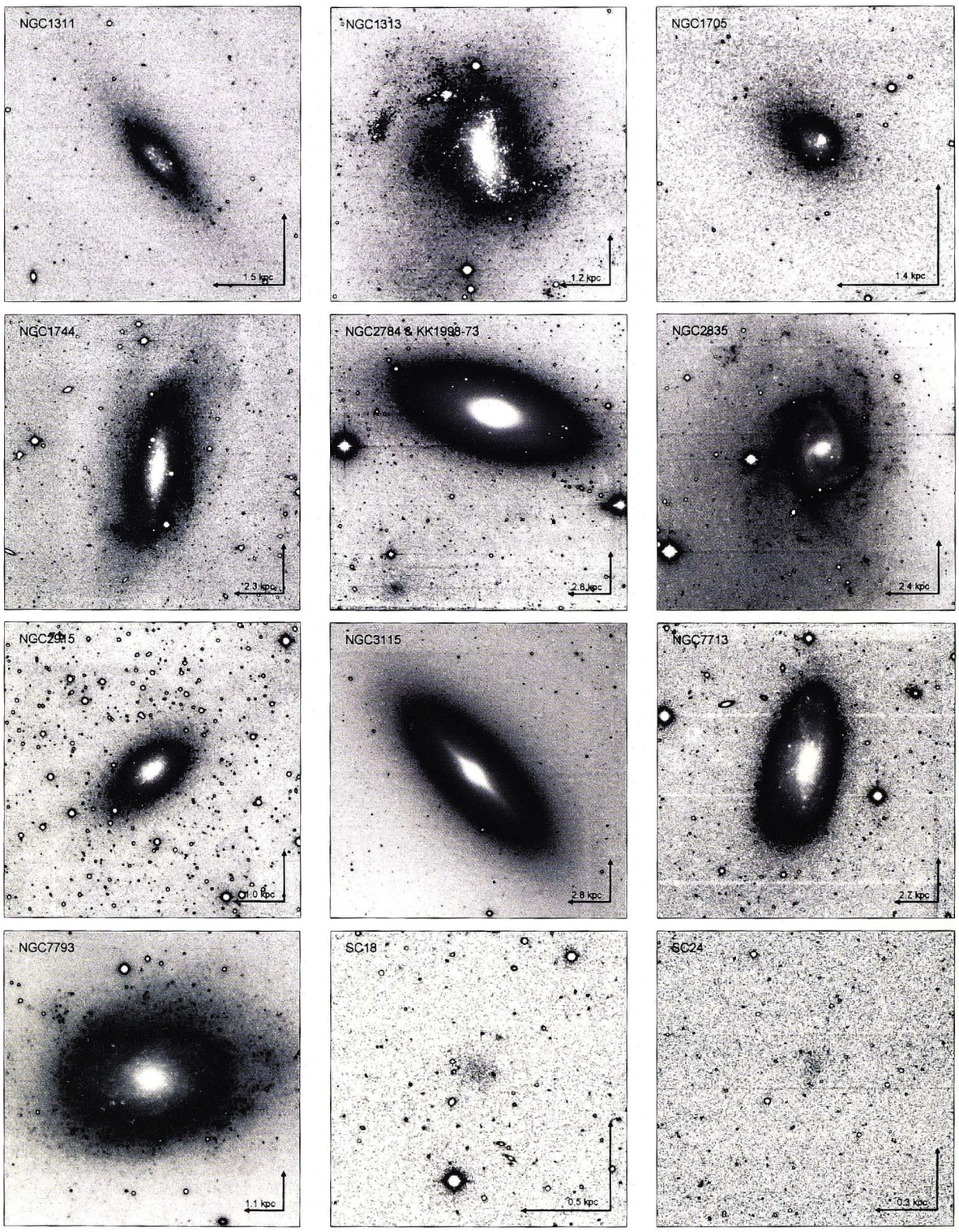


**Figure 2.5** LSI deep *H*-band images from the 3.9m Anglo-Australian Telescope. Here the scale represents 1 arcmin. The corresponding linear scale is also indicated. North is up and East is to the left. The intensity is represented by a greyscale which goes from white (low intensity) to black (medium intensity) and then back to white (high intensity).

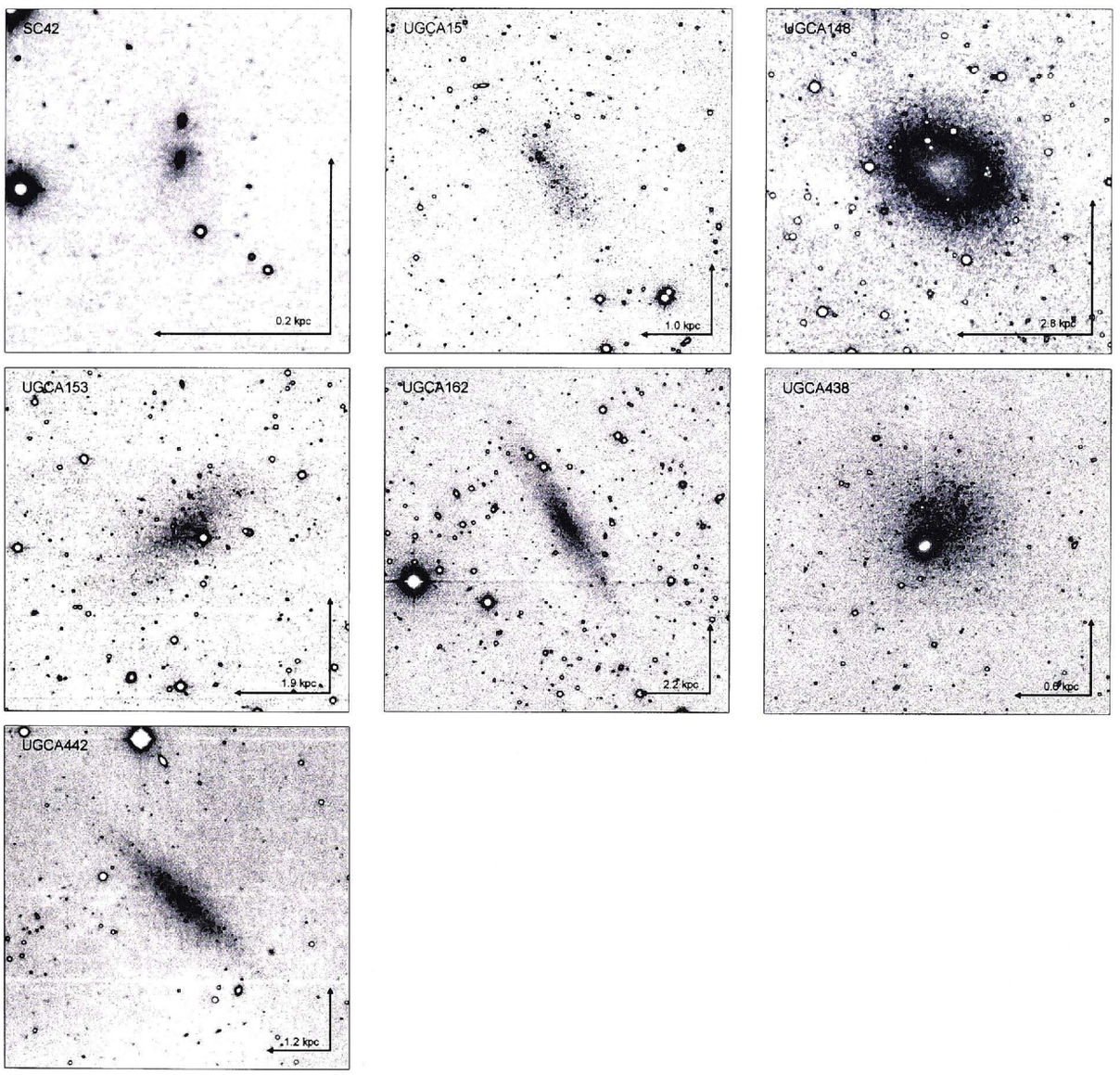


**Figure 2.6** LSI deep $H$-band images from the 3.9m Anglo-Australian Telescope. Here the scale represents 1 arcmin. The corresponding linear scale is also indicated. North is up and East is to the left. The intensity is represented by a greyscale which goes from white (low intensity) to black (medium intensity) and then back to white (high intensity).

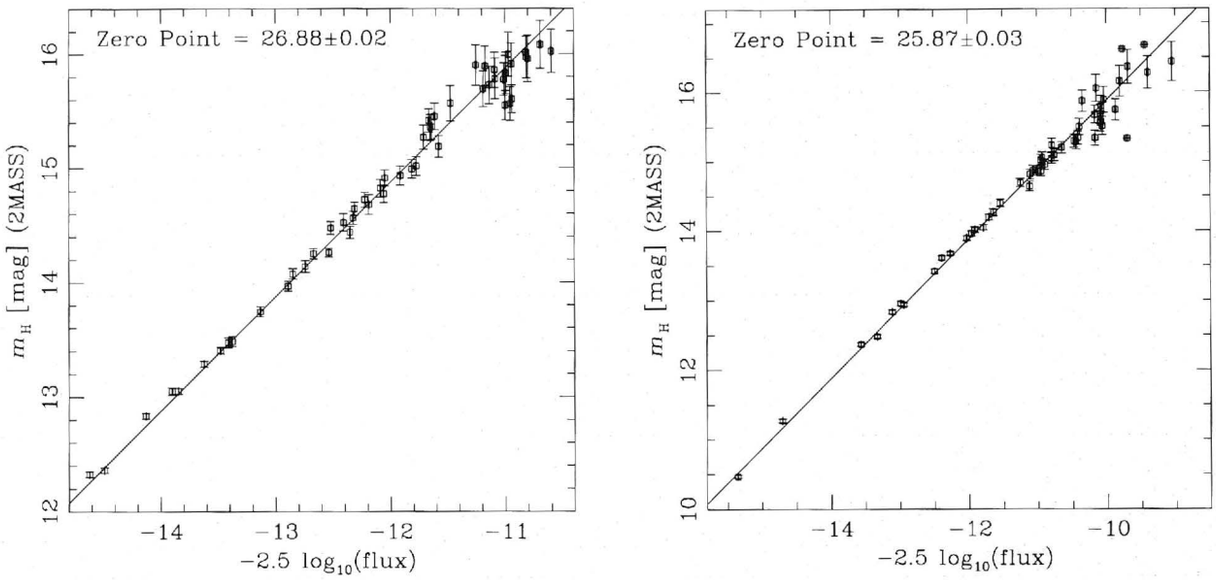


**Figure 2.7** Instrumental versus 2MASS *H*-band magnitudes for foreground stars around the galaxies ESO121-G020 (left) and UGCA153 (right). Both galaxies were observed for the same amount of time and the difference of one mag in zero-point is due to the presence of thin clouds when UGCA153 was observed.

On each image, instrumental magnitudes for 50–100 field stars were measured employing standard IRAF PSF fitting routines. Cross-correlating the stellar positions with the 2MASS Point Source Catalog provided *H*-band magnitudes and allowed the photometric calibration of each field (see Figure 2.7). The stars which deviate from the 45 degree line were usually either extremely red or blue where the transformation between 2MASS and IRIS2 *H*-bands (Ryder, 2007) breaks down. The $1\sigma$ uncertainty in the zero point was calculated to be between 0.01 and 0.04 mag depending on the number of stars used for the calibration.

To ensure accurate galaxy surface photometry down to the faintest possible isophotes, the images were cleaned of foreground stars using procedures written within the IRAF package. Thereby, stars in the field around a galaxy were carefully replaced with nearby patches of plain sky. If superposed on the galaxy, the galaxy light under the star was restored by replacing the contaminated area with its mirror image with respect to the galaxy center. The galaxy center was defined as the center of the luminosity-weighted light distribution. The star removal process was monitored visually to identify small-scale structures and asymmetries, and to ensure accurate removal of foreground stars whilst not removing sources associated with the galaxy itself. The effectiveness of the cleaning procedure is illustrated in Figure 2.8 where pre- and post- cleaning images are shown for the two galaxies ESO468-G020 and IC1959.

The fields of IC5152 (Figure 2.4) and UGCA438 (Figure 2.6) both have a bright foreground star which obscures a large portion of the galaxy. To obtain rough photometric parameters for these objects, the contribution of the bright stars

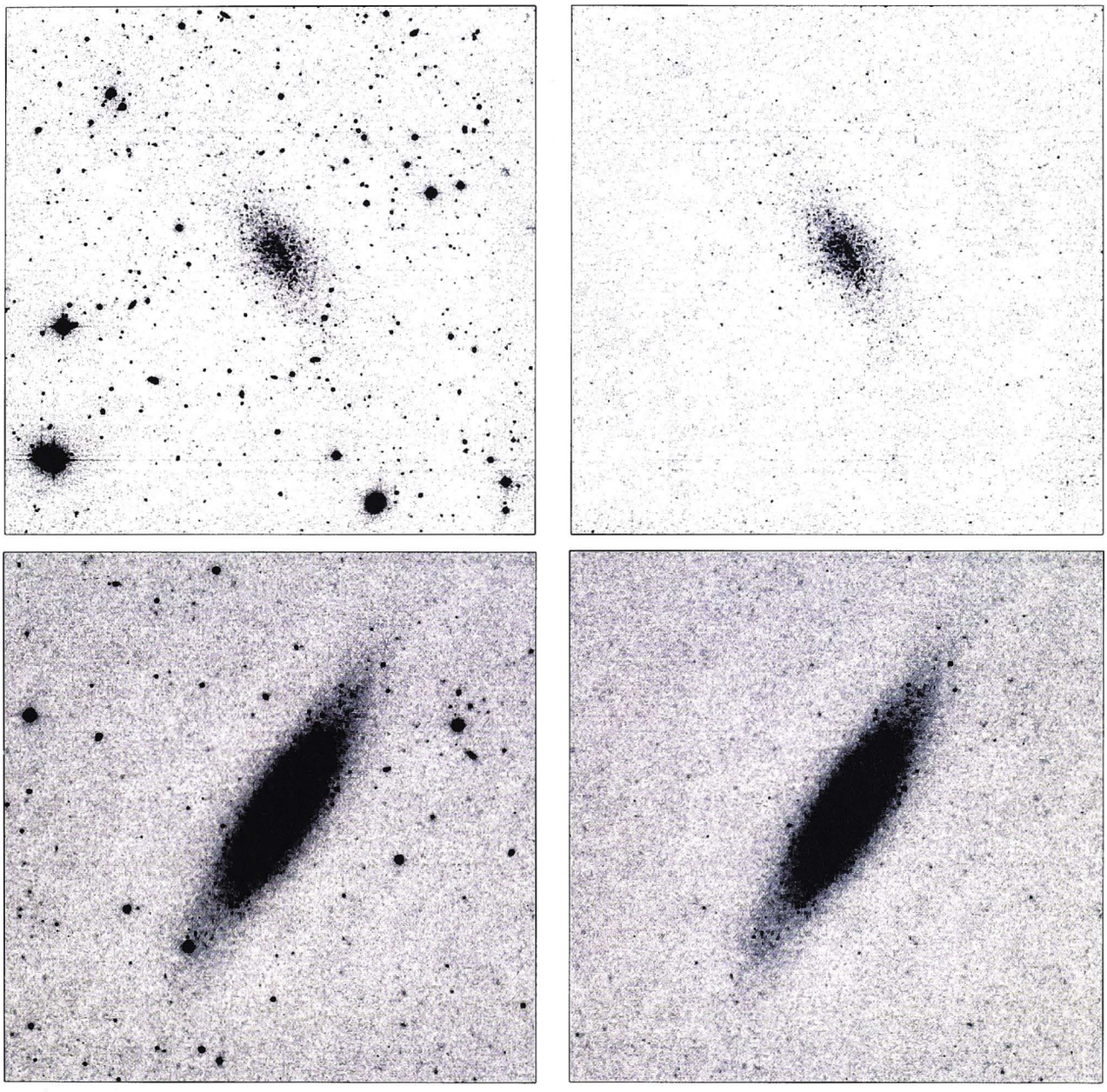

**Figure 2.8** Two examples of the effectiveness of the foreground cleaning process. Shown are the before and after cleaning images of ESO468-G020 [upper panel] and IC1959 [lower panel].

to the total flux needed to be removed. Because such a large portion of both the galaxies is obscured, it was necessary to remove the affected quarter of the image and replace it with the opposite quarter, which was rotated by 180 degrees (i.e., in the case of IC5152, the top-right quarter was replaced with the rotated bottom-left quarter of the image). This method failed in the case of the dIrr galaxy AM0521-343, where an even brighter star (CD-34 2225, $m_H$ = 7.1) near the faint dwarf galaxy prevented proper cleaning (see Figure 2.2).

## 2.4. Surface Photometry

Simulated circular aperture photometry of the star-subtracted $H$-band images produced a growth curve as a function of the geometric mean radius $\sqrt{ab}$ (where $a$ and $b$ are the galaxy's major and minor axes). The asymptotic intensity corresponds to the total apparent magnitude, $m_H$, that can be recovered down to the background noise level of the image. The largest source of uncertainty is the sky level. By systematically varying the sky brightness we determined which growth curve converges best to a plateau as far as possible from the center of the galaxy. We measure the half-light geometric mean radius, $r_{eff}$, at half the asymptotic intensity and calculated the mean surface brightness within that radius: $\langle\mu_H\rangle_{eff}$. The overall uncertainty for the total magnitude, $m_H$, is between 0.05 and 0.30 mag; for the mean effective surface brightness, $\langle\mu_H\rangle_{eff}$, less than 0.2 mag arcsec$^{-2}$, and for the half-light radius, $r_{eff}$, is of the order of five percent. The image of AM0521-343 (Figure 2.2), contains a bright foreground star and thus, the sky brightness plus the contribution from the stellar halo was estimated at the galaxy's position and simulated aperture photometry performed out to the radius of asymptotic intensity (defined on side of the galaxy opposite to the contaminating star).

The radial surface brightness profile of a sample galaxy was determined by differentiating the growth curves with respect to radius. Depending on the total integration time of the image, the profiles could be reconstructed down to a surface brightness limit between 24.5 mag arcsec$^{-2}$ $< \mu_{lim} <$ 26 mag arcsec$^{-2}$. They are shown, with a linear radius scale in Figures 2.9, 2.10 and 2.11. The error bars are calculated as the rms scatter of the intensity along each isophote. The position angle and ellipticity for each isophote, with the galaxy center fixed, were calculated with IRAF's ELLIPSE package as a function of radius. The ellipticity and position angle were, in general, settled in the outer regions of the galaxies, however, in some cases they varied significantly in the inner regions.

Table 2.2 lists the measured properties of the 57 sample galaxies as follows:

*Column* (1). – galaxy name.

*Column* (2). – observed integrated apparent magnitude, $m_{H,obs}$.

*Column* (3). – effective radius, $r_{eff}$

*Column* (4). – mean effective surface brightness, $\langle\mu_H\rangle_{eff}$.

*Column* (5). – ellipticity, $e$.

*Column* (6). – position angle of the major axis measured in degrees from North through East (PA= 90°).

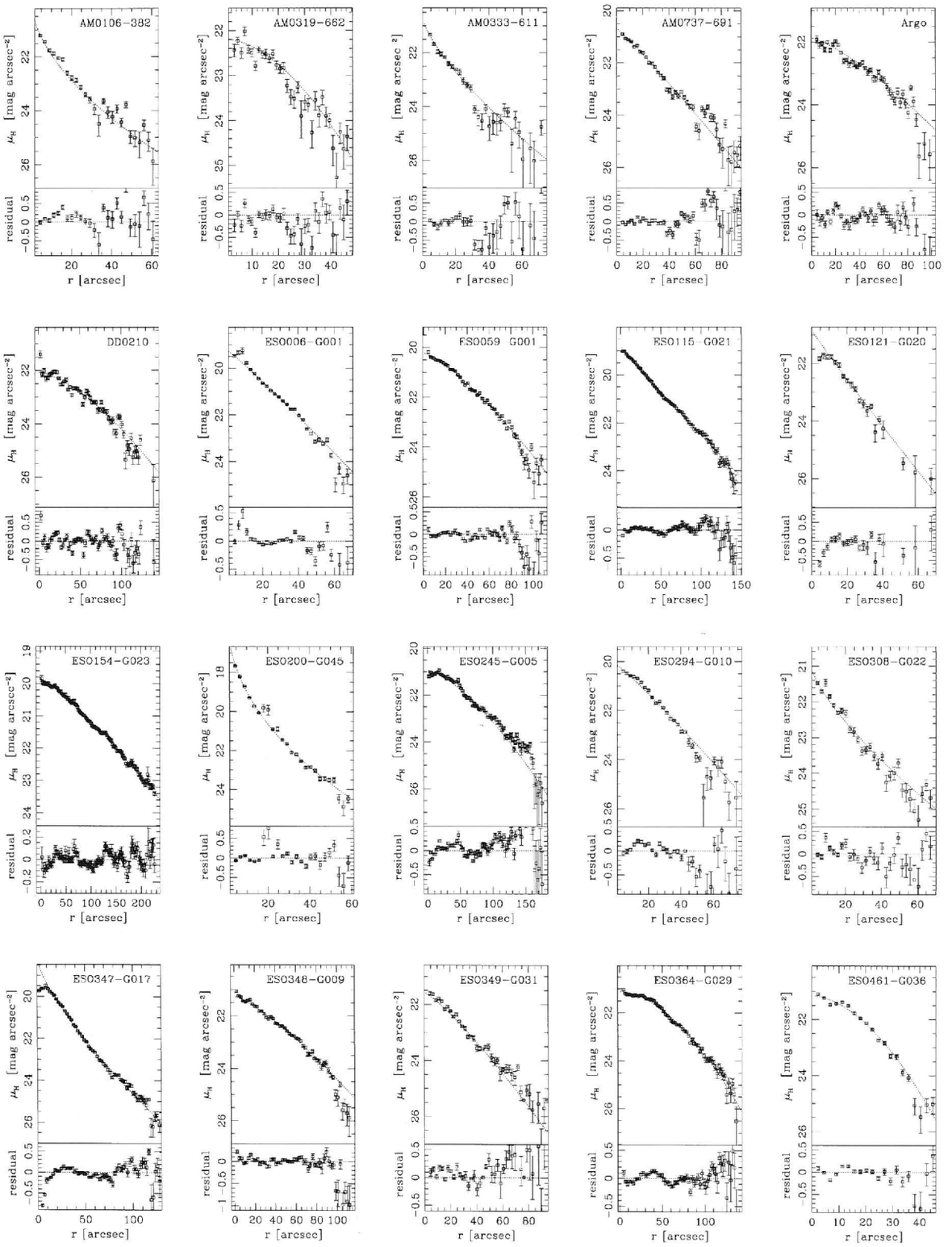


**Figure 2.9** *H*-band surface brightness profiles for all program galaxies except AM0521-343 (see text). The best fitting Sérsic profile is shown as dotted line together with the residuals.

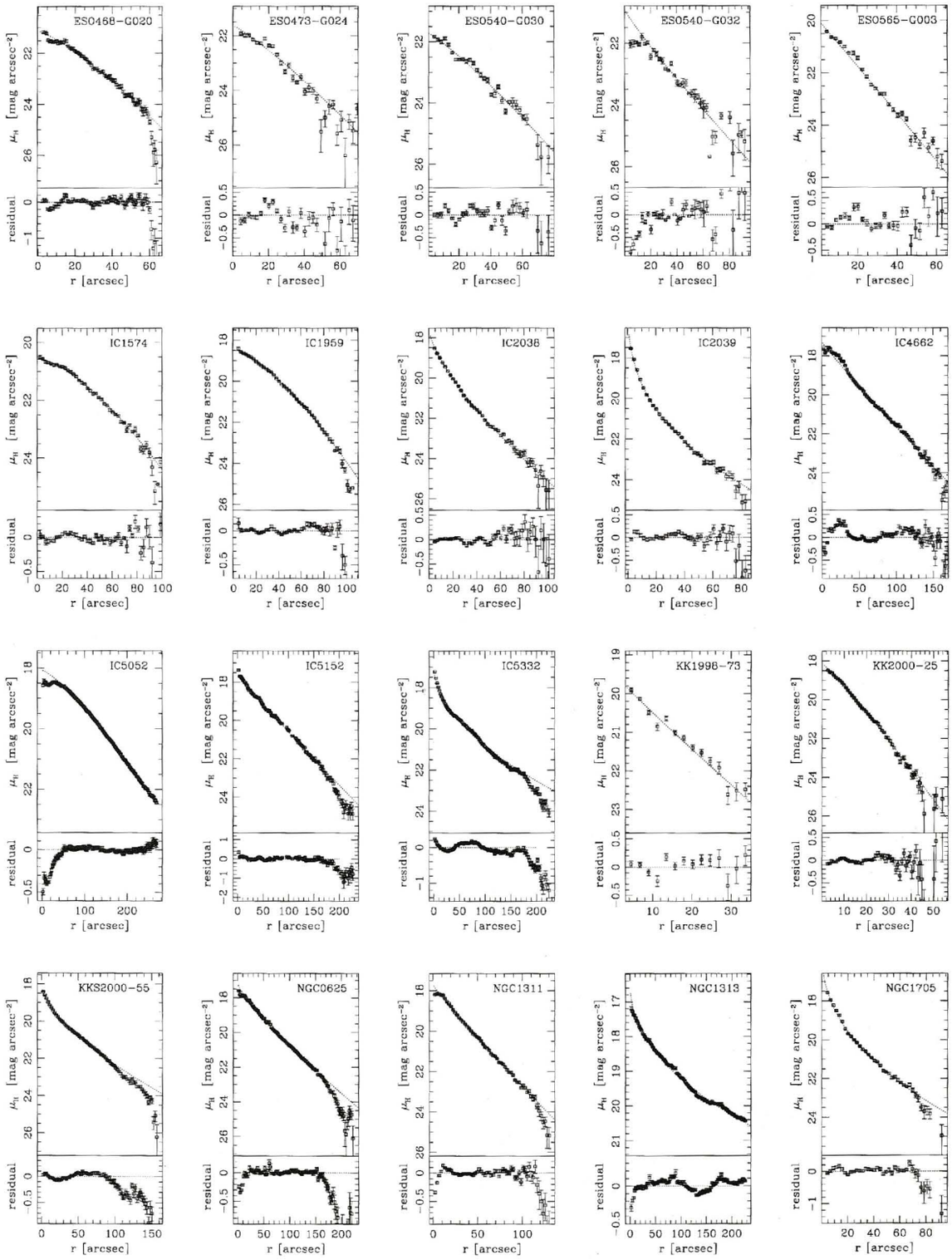


**Figure 2.10** *H*-band surface brightness profiles for all program galaxies except AM0521-343 (see text). The best fitting Sérsic profile is shown as dotted line together with the residuals.

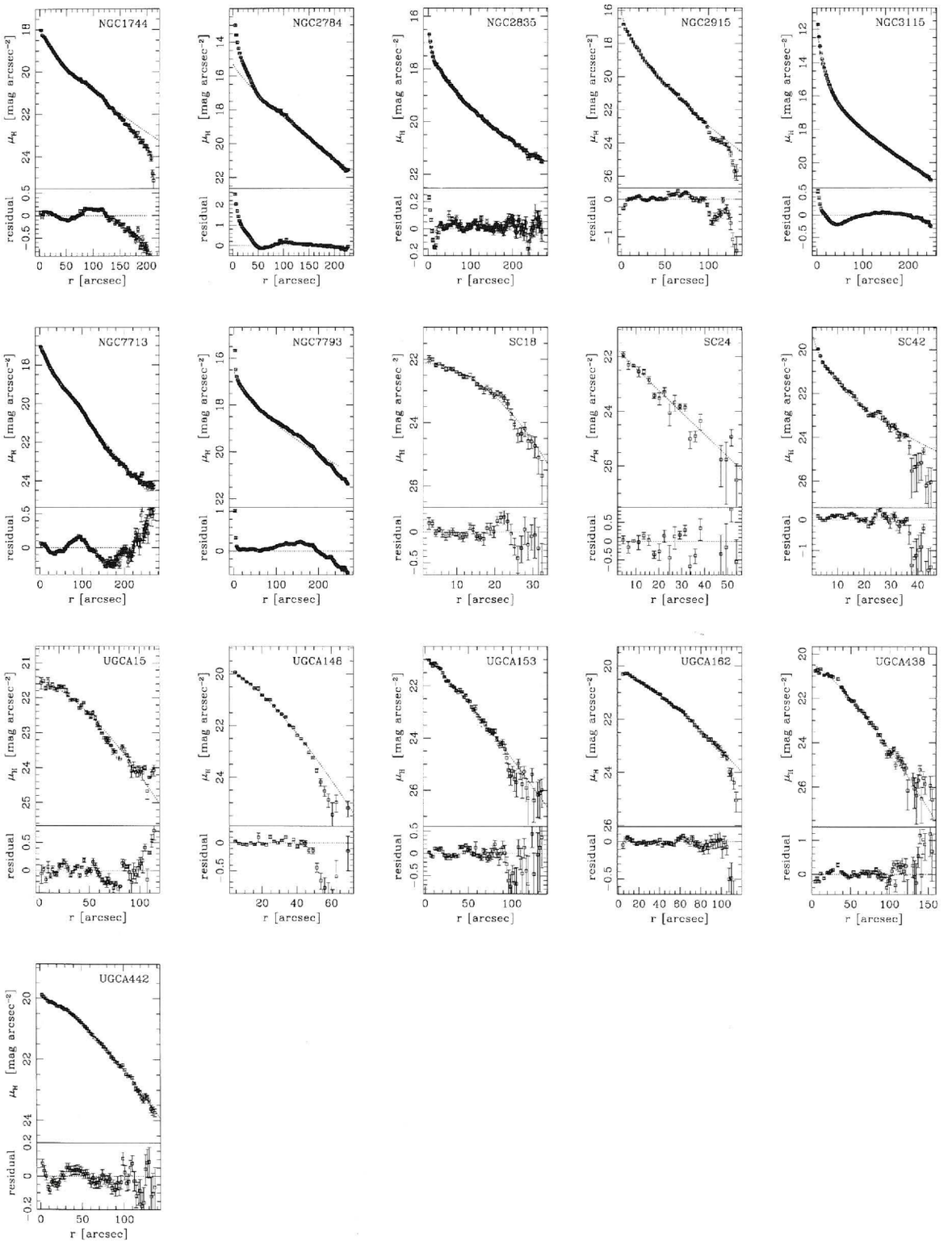


**Figure 2.11** *H*-band surface brightness profiles for all program galaxies except AM0521-343 (see text). The best fitting Sérsic profile is shown as dotted line together with the residuals.

**Table 2.2** Galaxy Parameters: Measured

| Name | $m_{H,obs}$ (mag) | $r_{eff}$ (arcsec) | $\langle\mu_H\rangle_{eff}$ mag arcsec$^{-2}$ | e (degrees) | PA (degrees) |
|---|---|---|---|---|---|
| (1) | (2) | (3) | (4) | (5) | (6) |
| SC18 | 14.94 ± 0.05 | 12.9 ± 0.5 | 22.50 ± 0.02 | 0.5 | 50 |
| ESO349-G031 | 12.96 ± 0.06 | 29.4 ± 1.6 | 22.29 ± 0.04 | 0.05 | 0 |
| ESO294-G010 | 12.4 ± 0.1 | 19.7 ± 1.4 | 20.84 ± 0.06 | 0.3 | 5 |
| ESO473-G024 | 13.7 ± 0.1 | 24.0 ± 2.7 | 22.6 ± 0.1 | 0.5 | 30 |
| SC24 | 14.8 ± 0.2 | 16.8 ± 2.6 | 22.88 ± 0.08 | 0.5 | -5 |
| IC1574 | 11.89 ± 0.08 | 30.1 ± 1.7 | 21.28 ± 0.04 | 0.6 | -10 |
| ESO540-G030 | 13.0 ± 0.1 | 30.5 ± 1.7 | 22.40 ± 0.02 | 0.05 | 0 |
| UGCA15 | 12.73 ± 0.09 | 32.2 ± 1.6 | 22.26 ± 0.02 | 0.7 | 30 |
| ESO540-G032 | 13.10 ± 0.08 | 28.8 ± 1.4 | 22.39 ± 0.03 | 0.4 | -45 |
| AM0106-382 | 13.4 ± 0.1 | 25.0 ± 3.5 | 22.4 ± 0.2 | 0.2 | 45 |
| NGC0625 | 8.94 ± 0.04 | 36.3 ± 1.1 | 18.74 ± 0.03 | 0.58 | -89 |
| SC42 | 14.13 ± 0.08 | 10.4 ± 0.9 | 21.2 ± 0.1 | 0.5 | -5 |
| ESO245-G005 | 11.1 ± 0.1 | 49.7 ± 3.4 | 21.55 ± 0.03 | 0.38 | -53 |
| ESO115-G021 | 10.71 ± 0.06 | 33.6 ± 2.0 | 20.34 ± 0.07 | 0.7 | 42 |
| ESO154-G023 | 10.37 ± 0.07 | 50.9 ± 2.7 | 20.90 ± 0.05 | 0.77 | 39 |
| NGC1313 | 6.7 ± 0.3 | 101.6 ± 15.5 | 18.74 ± 0.09 | 0.3 | 15 |
| NGC1311 | 10.28 ± 0.08 | 23.0 ± 1.6 | 19.09 ± 0.08 | 0.62 | 39 |
| AM0319-662 | 14.00 ± 0.05 | 21.8 ± 0.7 | 22.70 ± 0.02 | 0.1 | -50 |
| IC1959 | 10.84 ± 0.05 | 20.5 ± 0.7 | 19.39 ± 0.03 | 0.7 | -30 |
| AM0333-611 | 13.65 ± 0.08 | 20.9 ± 1.3 | 22.26 ± 0.05 | 0.25 | 5 |
| IC2038 | 11.8 ± 0.09 | 15.8 ± 1.3 | 19.8 ± 0.1 | 0.65 | -28 |
| IC2039 | 11.43 ± 0.04 | 14.1 ± 0.6 | 19.17 ± 0.06 | 0.2 | -57 |
| NGC1705 | 10.16 ± 0.07 | 15.1 ± 1.5 | 18.1 ± 0.1 | 0.2 | 60 |
| NGC1744 | 9.31 ± 0.09 | 47.9 ± 3.0 | 19.70 ± 0.06 | 0.6 | -10 |
| AM0521-343 | 14.2 ± 0.4 | 7.1 ± 0.2 | 20.5 ± 0.4 | 0.3 | -45 |
| KKS2000-55 | 10.44 ± 0.05 | 32.5 ± 0.7 | 20 ± 0.03 | 0.55 | -60 |
| ESO364-G029 | 11.92 ± 0.08 | 35.1 ± 1.8 | 21.64 ± 0.02 | 0.6 | 57 |
| ESO121-G020 | 13.87 ± 0.09 | 17.6 ± 1.2 | 22.10 ± 0.05 | 0.25 | 45 |
| ESO308-G022 | 13.4 ± 0.1 | 25.0 ± 1.9 | 22.32 ± 0.07 | 0.2 | -50 |
| KKS2000-09 | 11.48 ± 0.07 | 8.4 ± 0.9 | 18.3 ± 0.1 | 0.35 | 25 |
| Argo | 12.72 ± 0.08 | 37.3 ± 1.7 | 22.57 ± 0.02 | 0.5 | 45 |
| ESO059-G001 | 11.28 ± 0.06 | 34.4 ± 1.4 | 20.96 ± 0.03 | 0.3 | -20 |
| AM0737-691 | 12.2 ± 0.1 | 32.1 ± 3.3 | 21.94 ± 0.08 | 0.2 | -30 |
| KK2000-25 | 11.66 ± 0.05 | 11.9 ± 0.5 | 19.03 ± 0.03 | 0.15 | 60 |
| ESO006-G001 | 11.37 ± 0.06 | 20.0 ± 1.1 | 19.87 ± 0.06 | 0.12 | -13 |
| UGCA148 | 12.14 ± 0.05 | 19.0 ± 0.6 | 20.53 ± 0.02 | 0.35 | 60 |
| NGC2784 | 6.16 ± 0.07 | 27.2 ± 2.9 | 15.3 ± 0.2 | 0.56 | 73 |
| KK98-73 | 13.0 ± 0.1 | 13.0 ± 0.8 | 20.57 ± 0.01 | 0.4 | 45 |
| UGCA153 | 12.6 ± 0.2 | 30.9 ± 3.8 | 22.0 ± 0.1 | 0.6 | -48 |
| NGC2835 | 7.1 ± 0.2 | 88.0 ± 10.2 | 18.8 ± 0.1 | 0.3 | -20 |
| UGCA162 | 12.49 ± 0.09 | 20.8 ± 1.4 | 21.08 ± 0.06 | 0.8 | 30 |
| ESO565-G003 | 12.79 ± 0.07 | 16.4 ± 0.8 | 20.85 ± 0.05 | 0.25 | 30 |
| NGC2915 | 9.53 ± 0.05 | 21.3 ± 1.1 | 18.17 ± 0.06 | 0.4 | -53 |
| NGC3115 | 5.70 ± 0.07 | 27.3 ± 2.8 | 14.9 ± 0.2 | 0.6 | 44 |
| IC4662 | 8.71 ± 0.03 | 33.1 ± 0.7 | 18.31 ± 0.03 | 0.34 | -80 |
| ESO461-G036 | 13.9 ± 0.2 | 14.7 ± 2.2 | 21.7 ± 0.1 | 0.4 | 25 |

Continued on next page

**Table 2.2 – continued from previous page**

| Name | $m_{H,obs}$ (mag) | $r_{eff}$ (arcsec) | $\langle\mu_H\rangle_{eff}$ mag arcsec$^{-2}$ | e (degrees) | PA (degrees) |
|---|---|---|---|---|---|
| (1) | (2) | (3) | (4) | (5) | (6) |
| DDO210 | 12.30 ± 0.09 | 47.0 ± 1.7 | 22.65 ± 0.01 | 0.4 | -80 |
| IC5052 | 8.89 ± 0.05 | 54.9 ± 1.8 | 19.6 ± 0.03 | 0.85 | -40 |
| IC5152 | 8.26 ± 0.03 | 53.5 ± 1.5 | 18.90 ± 0.03 | 0.35 | -85 |
| ESO468-G020 | 13.2 ± 0.1 | 21.4 ± 1.0 | 21.85 ± 0.04 | 0.4 | 25 |
| UGCA438 | 11.2 ± 0.1 | 36.1 ± 2.5 | 20.96 ± 0.05 | 0.2 | -40 |
| IC5332 | 8.14 ± 0.03 | 68.62 ± 1.5 | 19.32 ± 0.02 | 0.05 | 0 |
| ESO347-G017 | 11.78 ± 0.08 | 21.8 ± 1.6 | 20.47 ± 0.09 | 0.65 | -85 |
| NGC7713 | 8.45 ± 0.06 | 44.0 ± 2.3 | 18.66 ± 0.06 | 0.55 | -10 |
| UGCA442 | 11.27 ± 0.07 | 32.5 ± 1.8 | 20.82 ± 0.05 | 0.75 | 53 |
| ESO348-G009 | 12.66 ± 0.09 | 30.5 ± 1.7 | 22.08 ± 0.03 | 0.6 | 75 |
| NGC7793 | 6.5 ± 0.1 | 88.9 ± 5.5 | 18.27 ± 0.04 | 0.4 | -80 |

The listed ellipticity and position angle is that of the outermost isophote fitted.

The surface brightness profile for each galaxy was fitted with the Sérsic function, $\mu(r) = \mu_0 + 1.086(r/\alpha)^n$ (or $I(r) = I_0 \exp(-(r/\alpha)^n)$), using IRAF's NFIT1D procedure. Extrapolation of the surface brightness profile to infinity with the help of the Sérsic function allows us to make an accurate estimate of the amount of flux that remained undetected in the sky background noise. Using the Sérsic parameter, $n$, the scale length, $\alpha$, and the central surface brightness, $\mu_0$, we calculated the magnitude of the galaxy between the maximum radius and the limit $r = \infty$:

$$\begin{aligned} \Delta m &= -2.5 \log_{10}(I_{\text{missing}}/I_{\text{tot}}) \\ &= -2.5 \log_{10}(\Gamma[2/n, (r_{max}/\alpha)^n]/\Gamma[2/n]) \end{aligned}$$

where:

$$\begin{aligned} I_{\text{missing}} &= \int_{r_{max}}^{\infty} 2\pi I_0 \exp[-(r/\alpha)^n] r dr \\ &= \frac{2\pi I_0 \alpha^2}{n} \Gamma[2/n, (r_{max}/\alpha)^n] \end{aligned} \tag{2.1}$$

and

$$\begin{aligned} I_{\text{tot}} &= \int_{0}^{\infty} 2\pi I_0 \exp[-(r/\alpha)^n] r dr \\ &= \frac{2\pi I_0 \alpha^2}{n} \Gamma[2/n]. \end{aligned} \tag{2.2}$$

Thereby $\Gamma(a, x)$ is the upper incomplete gamma function and $r_{max}$ was taken to be the radius at which the growth curve reaches within 5% of the asymptotic intensity. The missing flux introduces a systematic error to the total magnitude

$m_{H,obs}$. This correction $\Delta m$ was typically less than 0.2 mag (see Table 2.3), except in the few cases, e.g. NGC3115, where the galaxy's angular size extends beyond the IRIS2 FoV. We note that those galaxies have been observed in the CSJ mode to estimate the sky level from dedicated blank sky observations. AM0521-343 was not corrected for missing flux as the bright foreground star prevented the fitting of its surface brightness profile.

The corrected total apparent magnitude, $m_H = m_{H,obs} - \Delta m$, was converted into a luminosity using the standard equations

$$M_{H,0} = m_H - 5\log_{10} D - 25 - A_H$$

and

$$L = 10^{0.4(M_{H,\odot} - M_{H,0})}$$

where $M_{H,\odot} = 3.35$ mag is the $H$-band luminosity of the sun (Colina et al., 1996) and $A_H = 0.576 \cdot E(B-V)$ is the Galactic extinction (Schlegel et al., 1998). The accuracy of the reddening-corrected absolute magnitude, $M_{H,0}$, is dominated by the accuracy of the distance.

The effective radius, $r_{eff}$, is the aperture radius which encloses half the total light of a galaxy. This quantity is systematically underestimated unless corrected for the amount of undetected flux. The corrected effective radius, $R_{eff}$ is defined implicitly by the equation

$$\frac{I_{\rm tot}}{2} = \frac{2\pi I_0 \alpha^2}{n} \cdot \Gamma\left[\frac{2}{n}, \left(\frac{R_{eff}}{\alpha}\right)^n\right] \tag{2.3}$$

where $I_0$, $\alpha$, and $n$ are the Sérsic parameters for a particular galaxy. The solution for all $n \in [0.25, 2]$ can be approximated by the equation

$$R_{eff} \approx \alpha\left(\frac{2}{n} - 0.33211\right)^{1/n}. \tag{2.4}$$

Within the quoted uncertainties, there is no deviation between the approximate analytic solution (equation 2.4) and the numerical solution of equation 2.3.

The $H$-band luminosity of each galaxy was converted into a stellar mass using a mass-to-light ratio of $\Upsilon_*^H = 1.0 \pm 0.4$. This conversion factor is discussed in detail in Section 2.4.2. The derived parameters are listed in Table 2.3 for the 57 LSI galaxies as follows:

*Column* (1). – galaxy name.

*Column* (2). – effective radius, $r_{eff}$, in kpc.

*Columns* (3), (4) and (5). – the Sérsic parameters $\mu_0$, $n$ and $\alpha$ respectively.

*Column* (6). – the missing flux, $\Delta m$.

*Columns* (7) and (8). – the corrected effective radius, $R_{eff}$, in arcsec and kpc.

*Column* (9). – absolute H magnitude, $M_{H,0}$.

*Column* (10). – the total stellar mass, $\log_{10} \mathcal{M}_*$.

**Table 2.3** Galaxy Parameters: Derived

| Name | $r_{eff}$ (kpc) | $\mu_0$ (mag arcsec$^{-2}$) | $n$ | $\alpha$ (arcsec) | $\Delta m$ (mag) | $R_{eff}$ (arcsec) | $R_{eff}$ (kpc) | $M_{H,0}$ (mag) | $\log_{10}(\mathcal{M}_*)$ ($\log_{10}(\mathcal{M}_\odot)$) |
|---|---|---|---|---|---|---|---|---|---|
| (1) | (2) | (3) | (4) | (5) | (6) | (7) | (8) | (9) | (10) |
| SC18 | 0.11 ± 0.01 | 22.11 ± 0.09 | 2.08 ± 0.3 | 20.15 ± 1.0 | 0.18 | 16.1 ± 1.3 | 0.14 ± 0.01 | -11.5 ± 0.2 | 5.9 ± 0.2 |
| ESO349-G031 | 0.46 ± 0.03 | 21.57 ± 0.4 | 1.21 ± 0.2 | 26.80 ± 4.0 | 0.05 | 33.7 ± 6.6 | 0.52 ± 0.09 | -14.6 ± 0.2 | 7.2 ± 0.2 |
| ESO294-G010 | 0.18 ± 0.02 | 20.11 ± 0.4 | 1.10 ± 0.5 | 18.20 ± 5.8 | 0.14 | 26.1 ± 13.1 | 0.24 ± 0.09 | -14.2 ± 0.2 | 7.0 ± 0.2 |
| ESO473-G024 | 1.0 ± 0.1 | 21.63 ± 0.3 | 1.17 ± 0.3 | 23.41 ± 6.5 | 0.28 | 30.8 ± 11.0 | 1.2 ± 0.3 | -16.1 ± 0.3 | 7.8 ± 0.2 |
| SC24 | 0.09 ± 0.02 | 21.58 ± 0.4 | 0.98 ± 0.2 | 12.97 ± 4.6 | 0.18 | 22.4 ± 9.6 | 0.12 ± 0.04 | -10.7 ± 0.3 | 5.6 ± 0.2 |
| IC1574 | 0.72 ± 0.04 | 20.54 ± 0.08 | 1.50 ± 0.1 | 42.91 ± 2.3 | 0.01 | 42.9 ± 3.3 | 1.02 ± 0.06 | -16.6 ± 0.2 | 8.0 ± 0.2 |
| ESO540-G030 | 0.50 ± 0.03 | 21.70 ± 0.4 | 1.17 ± 0.4 | 26.77 ± 9.3 | 0.01 | 35.2 ± 16.3 | 0.6 ± 0.2 | -14.7 ± 0.2 | 7.2 ± 0.2 |
| UGCA15 | 0.52 ± 0.03 | 21.51 ± 0.03 | 1.49 ± 0.07 | 54.51 ± 1.2 | 0.05 | 54.9 ± 2.1 | 0.89 ± 0.03 | -15.0 ± 0.2 | 7.3 ± 0.2 |
| ESO540-G032 | 0.48 ± 0.03 | 20.89 ± 3.1 | 0.90 ± 1.7 | 17.73 ± 19.2 | 0.15 | 36.0 ± 84.9 | 0.6 ± 1.1 | -14.7 ± 0.2 | 7.2 ± 0.2 |
| AM0106-382 | 1.0 ± 0.1 | 19.91 ± 0.4 | 0.56 ± 0.1 | 3.33 ± 2.3 | 0.13 | 27.2 ± 21.0 | 1.1 ± 0.8 | -16.4 ± 0.2 | 7.9 ± 0.2 |
| NGC0625 | 0.72 ± 0.03 | 17.20 ± 0.04 | 0.82 ± 0.1 | 23.38 ± 0.8 | 0.05 | 58.0 ± 10.5 | 1.1 ± 0.1 | -19.2 ± 0.2 | 9.0 ± 0.2 |
| SC42 | 0.04 ± 0.01 | 18.21 ± 0.6 | 0.43 ± 0.05 | 0.75 ± 0.5 | 0.04 | 22.5 ± 16.8 | 0.10 ± 0.03 | -10.6 ± 0.2 | 5.6 ± 0.2 |
| ESO245-G005 | 1.07 ± 0.08 | 20.95 ± 0.04 | 1.46 ± 0.09 | 61.74 ± 2.3 | 0.04 | 63.3 ± 3.6 | 1.36 ± 0.07 | -17.2 ± 0.2 | 8.2 ± 0.2 |
| ESO115-G021 | 0.76 ± 0.05 | 18.81 ± 0.1 | 0.95 ± 0.08 | 27.52 ± 3.6 | 0.09 | 50.3 ± 7.9 | 1.1 ± 0.1 | -17.7 ± 0.2 | 8.4 ± 0.2 |
| ESO154-G023 | 1.39 ± 0.08 | 19.85 ± 0.03 | 1.20 ± 0.03 | 85.02 ± 2.5 | 0.19 | 108.1 ± 3.9 | 3.00 ± 0.06 | -18.6 ± 0.2 | 8.8 ± 0.2 |
| NGC1313 | 2.0 ± 0.3 | 16.41 ± 0.2 | 0.46 ± 0.03 | 12.69 ± 3.6 | 0.86 | 260.6 ± 83.2 | 5.2 ± 0.7 | -22.3 ± 0.4 | 10.3 ± 0.2 |
| NGC1311 | 0.61 ± 0.04 | 17.70 ± 0.06 | 0.93 ± 0.03 | 19.30 ± 1.2 | 0.05 | 36.7 ± 2.6 | 0.97 ± 0.04 | -18.5 ± 0.2 | 8.7 ± 0.2 |
| AM0319-662 | 0.43 ± 0.02 | 22.19 ± 0.4 | 1.77 ± 0.8 | 29.05 ± 6.8 | 0.06 | 25.6 ± 8.7 | 0.5 ± 0.1 | -14.2 ± 0.2 | 7.0 ± 0.2 |
| IC1959 | 0.63 ± 0.02 | 18.46 ± 0.08 | 1.42 ± 0.06 | 32.04 ± 1.6 | 0.04 | 33.7 ± 1.9 | 1.04 ± 0.04 | -18.2 ± 0.2 | 8.6 ± 0.2 |
| AM0333-611 | 1.35 ± 0.08 | 20.69 ± 1.5 | 0.73 ± 0.3 | 8.58 ± 6.9 | 0.31 | 28.6 ± 28.4 | 1.8 ± 1.4 | -17.3 ± 0.2 | 8.3 ± 0.2 |
| IC2038 | 1.3 ± 0.1 | 17.62 ± 0.2 | 0.70 ± 0.05 | 6.32 ± 1.2 | 0.03 | 23.7 ± 5.0 | 1.9 ± 0.3 | -19.3 ± 0.2 | 9.1 ± 0.2 |
| IC2039 | 1.13 ± 0.05 | 15.04 ± 0.6 | 0.37 ± 0.03 | 0.25 ± 0.2 | 0.03 | 20.1 ± 12.9 | 1.6 ± 0.7 | -19.7 ± 0.2 | 9.2 ± 0.2 |
| NGC1705 | 0.37 ± 0.04 | 15.33 ± 0.4 | 0.44 ± 0.04 | 0.90 ± 0.4 | 0.15 | 23.7 ± 11.6 | 0.6 ± 0.2 | -18.5 ± 0.2 | 8.8 ± 0.2 |

Continued on next page

**Table 2.3 – continued from previous page**

| Name | $r_{eff}$ (kpc) | $\mu_0$ (mag arcsec$^{-2}$) | $n$ | $\alpha$ (arcsec) | $\Delta m$ (mag) | $R_{eff}$ (arcsec) | $R_{eff}$ (kpc) | $M_{H,0}$ (mag) | $\log_{10}(\mathcal{M}_*)$ ($\log_{10}(\mathcal{M}_\odot)$) |
|---|---|---|---|---|---|---|---|---|---|
| (1) | (2) | (3) | (4) | (5) | (6) | (7) | (8) | (9) | (10) |
| NGC1744 | 1.8 ± 0.1 | 17.86 ± 0.1 | 0.69 ± 0.05 | 21.97 ± 3.6 | 0.13 | 86.1 ± 16.7 | 3.3 ± 0.4 | -20.3 ± 0.2 | 9.5 ± 0.2 |
| AM0521-343 | 0.36 ± 0.01 | – | – | – | – | – | – | -15.9 ± 0.5 | 7.7 ± 0.3 |
| KKS2000-55 | 1.59 ± 0.04 | 18.05 ± 0.4 | 0.63 ± 0.09 | 11.36 ± 4.5 | 0.15 | 59.6 ± 27.1 | 2.9 ± 0.7 | -20.2 ± 0.2 | 9.4 ± 0.2 |
| ESO364-G029 | 1.30 ± 0.07 | 21.11 ± 0.05 | 1.78 ± 0.1 | 60.81 ± 2.2 | 0.02 | 53.3 ± 2.7 | 1.94 ± 0.07 | -17.5 ± 0.2 | 8.3 ± 0.2 |
| ESO121-G020 | 0.52 ± 0.04 | 20.82 ± 0.8 | 0.95 ± 0.4 | 12.22 ± 5.9 | 0.19 | 22.3 ± 14.0 | 0.7 ± 0.3 | -15.3 ± 0.2 | 7.4 ± 0.2 |
| ESO308-G022 | 0.92 ± 0.07 | 20.87 ± 0.3 | 0.71 ± 0.2 | 10.76 ± 5.2 | 0.53 | 38.8 ± 22.8 | 1.4 ± 0.5 | -16.7 ± 0.2 | 8.0 ± 0.2 |
| KKS2000-09 | 0.26 ± 0.03 | 14.12 ± 4.6 | 0.42 ± 0.2 | 0.28 ± 1.8 | 0.06 | 9.7 ± 63.4 | 0.3 ± 1.7 | -17.9 ± 0.2 | 8.5 ± 0.2 |
| Argo | 0.89 ± 0.04 | 21.87 ± 0.1 | 1.32 ± 0.2 | 48.77 ± 4.6 | 0.27 | 55.4 ± 7.7 | 1.3 ± 0.1 | -16.1 ± 0.2 | 7.8 ± 0.2 |
| ESO059-G001 | 0.76 ± 0.04 | 20.23 ± 0.2 | 1.33 ± 0.2 | 36.68 ± 6.2 | 0.1 | 41.3 ± 8.3 | 0.9 ± 0.2 | -17.2 ± 0.2 | 8.2 ± 0.2 |
| AM0737-691 | 2.5 ± 0.3 | 20.67 ± 0.2 | 1.07 ± 0.2 | 21.41 ± 3.9 | 0.1 | 32.0 ± 7.1 | 2.5 ± 0.6 | -19.0 ± 0.3 | 9.0 ± 0.2 |
| KK2000-25 | 0.03 ± 0.01 | 18.13 ± 0.08 | 1.12 ± 0.03 | 9.41 ± 0.5 | 0.03 | 13.1 ± 0.7 | 0.03 ± 0.01 | -11.9 ± 0.2 | 6.1 ± 0.2 |
| ESO006-G001 | 0.65 ± 0.04 | 19.20 ± 0.5 | 1.07 ± 0.2 | 16.11 ± 5.2 | 0.08 | 24.1 ± 8.9 | 0.8 ± 0.2 | -17.8 ± 0.2 | 8.5 ± 0.2 |
| UGCA148 | 0.90 ± 0.03 | 19.85 ± 0.07 | 1.37 ± 0.09 | 22.15 ± 1.3 | 0.05 | 24.2 ± 1.9 | 1.15 ± 0.07 | -18.0 ± 0.2 | 8.5 ± 0.2 |
| NGC2784 | 1.3 ± 0.1 | 15.26 ± 0.4 | 0.82 ± 0.1 | 26.85 ± 9.0 | 0.04 | 66.6 ± 24.4 | 3.2 ± 0.5 | -24.0 ± 0.2 | 10.9 ± 0.2 |
| KK98-73 | 0.62 ± 0.04 | 19.48 ± 0.3 | 0.95 ± 0.1 | 10.74 ± 2.2 | 0.36 | 19.6 ± 4.8 | 0.9 ± 0.1 | -17.4 ± 0.2 | 8.3 ± 0.2 |
| UGCA153 | 1.0 ± 0.1 | 20.93 ± 0.2 | 1.15 ± 0.1 | 33.31 ± 5.2 | 0.11 | 44.8 ± 8.5 | 1.5 ± 0.2 | -16.7 ± 0.3 | 8.0 ± 0.2 |
| NGC2835 | 3.5 ± 0.4 | 16.50 ± 0.04 | 0.52 ± 0.01 | 14.27 ± 0.8 | 0.54 | 160.0 ± 10.7 | 6.4 ± 0.2 | -23.1 ± 0.3 | 10.6 ± 0.2 |
| UGCA162 | 0.77 ± 0.05 | 20.22 ± 0.02 | 1.35 ± 0.02 | 47.70 ± 0.7 | 0.32 | 52.9 ± 1.0 | 2.00 ± 0.02 | -17.3 ± 0.2 | 8.3 ± 0.2 |
| ESO565-G003 | 0.60 ± 0.03 | 19.97 ± 0.5 | 1.01 ± 0.2 | 12.69 ± 4.1 | 0.05 | 20.8 ± 7.6 | 0.8 ± 0.2 | -16.7 ± 0.2 | 8.0 ± 0.2 |
| NGC2915 | 0.39 ± 0.02 | 15.97 ± 0.2 | 0.63 ± 0.03 | 5.21 ± 0.8 | 0.03 | 27.4 ± 4.8 | 0.50 ± 0.07 | -18.6 ± 0.2 | 8.8 ± 0.2 |
| NGC3115 | 1.3 ± 0.1 | 10.20 ± 0.4 | 0.31 ± 0.02 | 0.18 ± 0.1 | 0.14 | 62.1 ± 43.4 | 3.0 ± 0.9 | -24.4 ± 0.2 | 11.1 ± 0.2 |
| IC4662 | 0.39 ± 0.02 | 17.27 ± 0.2 | 0.94 ± 0.05 | 22.68 ± 2.9 | 0.03 | 42.3 ± 5.8 | 0.50 ± 0.06 | -18.3 ± 0.2 | 8.7 ± 0.2 |
| ESO461-G036 | 0.56 ± 0.08 | 21.16 ± 0.2 | 1.80 ± 0.4 | 21.07 ± 2.8 | 0.14 | 18.3 ± 3.4 | 0.7 ± 0.1 | -15.9 ± 0.3 | 7.7 ± 0.2 |
| DDO210 | 0.21 ± 0.02 | 22.07 ± 0.08 | 1.52 ± 0.2 | 64.49 ± 4.7 | 0.27 | 63.8 ± 6.4 | 0.29 ± 0.03 | -12.9 ± 0.2 | 6.5 ± 0.2 |

Continued on next page

**Table 2.3 – continued from previous page**

| Name | $r_{eff}$ (kpc) | $\mu_0$ (mag arcsec$^{-2}$) | $n$ | $\alpha$ (arcsec) | $\Delta m$ (mag) | $R_{eff}$ (arcsec) | $R_{eff}$ (kpc) | $M_{H,0}$ (mag) | $\log_{10}(\mathcal{M}_*)$ ($\log_{10}(\mathcal{M}_\odot)$) |
|---|---|---|---|---|---|---|---|---|---|
| (1) | (2) | (3) | (4) | (5) | (6) | (7) | (8) | (9) | (10) |
| IC5052 | 1.61 ± 0.06 | 18.07 ± 0.02 | 1.27 ± 0.02 | 88.82 ± 1.4 | 0.28 | 105.4 ± 2.1 | 3.08 ± 0.04 | -20.3 ± 0.2 | 9.5 ± 0.2 |
| IC5152 | 0.54 ± 0.03 | 17.65 ± 0.08 | 0.96 ± 0.04 | 35.44 ± 2.7 | 0.01 | 63.5 ± 5.5 | 0.64 ± 0.05 | -18.3 ± 0.2 | 8.7 ± 0.2 |
| ESO468-G020 | 0.41 ± 0.02 | 21.13 ± 0.07 | 1.28 ± 0.1 | 24.93 ± 1.9 | 0.13 | 29.3 ± 3.0 | 0.55 ± 0.04 | -14.9 ± 0.2 | 7.3 ± 0.2 |
| UGCA438 | 0.39 ± 0.03 | 20.49 ± 0.2 | 1.31 ± 0.08 | 38.34 ± 3.4 | 0.03 | 43.9 ± 4.4 | 0.47 ± 0.04 | -15.6 ± 0.2 | 7.6 ± 0.2 |
| IC5332 | 3.19 ± 0.08 | 16.92 ± 0.2 | 0.52 ± 0.04 | 8.51 ± 2.4 | 0.21 | 95.4 ± 30.5 | 4.4 ± 1.0 | -22.0 ± 0.2 | 10.1 ± 0.2 |
| ESO347-G017 | 1.00 ± 0.07 | 18.19 ± 0.4 | 0.74 ± 0.08 | 9.02 ± 2.9 | 0.22 | 29.0 ± 10.3 | 1.3 ± 0.4 | -18.3 ± 0.2 | 8.7 ± 0.2 |
| NGC7713 | 2.0 ± 0.1 | 16.98 ± 0.2 | 0.83 ± 0.06 | 24.46 ± 3.8 | 0.02 | 59.0 ± 10.6 | 2.7 ± 0.4 | -21.4 ± 0.2 | 9.9 ± 0.2 |
| UGCA442 | 0.67 ± 0.04 | 19.94 ± 0.03 | 1.42 ± 0.04 | 57.38 ± 1.5 | 0.44 | 60.4 ± 2.0 | 1.25 ± 0.03 | -17.3 ± 0.2 | 8.3 ± 0.2 |
| ESO348-G009 | 1.28 ± 0.07 | 21.26 ± 0.05 | 1.31 ± 0.07 | 44.50 ± 2.0 | 0.15 | 51.0 ± 3.1 | 2.14 ± 0.08 | -17.2 ± 0.2 | 8.2 ± 0.2 |
| NGC7793 | 1.7 ± 0.1 | 16.47 ± 0.08 | 0.62 ± 0.02 | 28.72 ± 3.0 | 0.46 | 159.4 ± 18.7 | 3.0 ± 0.2 | -21.9 ± 0.2 | 10.1 ± 0.2 |

### 2.4.1. Galactic extinction correction

The extinction correction used in our study is that of Schlegel et al. (1998). We prefer these IR emission maps over the older Burstein & Heiles (1978, 1982, 1984) models as the reddening is derived directly from dust emission rather than H I column densities and galaxy counts. The Schlegel et al. (1998) maps have a typical uncertainty of 16%. However, for low latitudes, $|b| < 5°$, most contaminating sources were not removed from the maps leading to larger errors for that part of the sky. This difficulty can not be circumvented by using the Burstein & Heiles maps as they do not include latitudes below $|b| < 10°$. Consequently, the reddening corrections applied to the two sample galaxies KK2000-25 and KKS2000-09 are less secure. This uncertainty will particularly affect the quoted $B$-band magnitudes. The $H$-band results will be affected to a lesser extent as the correction is of order one-tenth of that in the $B$-band.

Should one choose to use the Burstein & Heiles models the difference in our results is minimal. There are only two sample galaxies (KKS2000-09 and ESO461-G036) which have significantly different absolute $B$-band magnitudes. In these two cases we apply an average of the Burstein and Heiles and the Schlegel et al. corrections. The choice of the reddening estimate does not change the $H$-band results within the quoted errors.

### 2.4.2. The $H$-band mass-to-light ratio

For our analysis we will adopt a $H$-band mass-to-light ratio that is well supported by observations and theory. Assuming a typical 12 Gyr old, solar metallicity, stellar population with a constant star formation rate and a Salpeter initial mass function, the de Jong (1996) model yields a mass-to-light ratio of $\Upsilon_*^H = 1.0$. This is consistent with the empirically derived value of $\Upsilon_*^H = 0.9 \pm 0.6$ obtained for our sample by using each galaxy's $B - H$ colour (Tables 2.1 and 2.2) and adopting the colour-dependent stellar mass-to-light ratio relation from the Bell & de Jong (2001) galaxy evolution models. Finally, these two mass-to-light ratios are well in the range of $0.7 < \Upsilon_*^H < 1.3$ which is based on observed SDSS colours $0.1 < (g - r) < 1.1$ for 22,679 galaxies and 2MASS photometry (Bell et al., 2003). From these three independent values we derive the error weighted mean of $\Upsilon_*^H = 1.0 \pm 0.4$.

## 2.5. Are there any genuine young galaxies?

Observations for 11 galaxies were not included in our photometric study either because the galaxy remained invisible in the final mosaics despite our faint $H$-band surface brightness limit of $24 - 26$ mag arcsec$^{-2}$, or the galaxy was detected

but foreground stars interfered with the analysis. In this section, we discuss the four galaxies labelled as "no galaxy detected" in Table 2.4: AM0717-571, KK2000-04, KK2000-06 and NGC2784 DW1. While they remain as candidates for galaxies with a pure young stellar component, we show it is unlikely that this is the case. We also include KK2000-03 which had a marginal detection, and the galaxy pair HIZOAJ1616-55 and SJK98 J1616-55 which were not detected but we note that the images had serious foreground contamination.

A lower bound of the total apparent magnitude for these galaxies can be calculated. For that purpose, we consider a hypothetical galaxy with a constant star density equivalent to the survey's mean surface brightness limit of $\langle \mu_{0,lim} \rangle = 25\,\mathrm{mag\ arcsec^{-2}}$ out to a cutoff radius, $r_{cut}$, at which point the stellar density drops to zero. We set the cutoff radius, $r_{cut}$, to be 250 arcsec which is equivalent to the size of the largest galaxies in our sample. This yields the brightest apparent magnitude an undetected galaxy could possibly have:

$$m_{tot} > \mu_{0,lim} - 2.5\log_{10}(\pi r_{cut}^2) = 11.8\,\mathrm{mag}. \tag{2.5}$$

This lower bound is applicable to AM0717-571, KK2000-04, KK2000-06 and NGC2784 DW1 but not KK2000-03 which has a foreground star located directly in front of the galaxy (see discussion below), nor HIZOAJ1616-55 and SJK98 J1616-55 which have serious foreground contamination. A lower bound on the absolute magnitude and an upper bound on the stellar mass is calculated using distances from the literature (see Table 2.4 ).

## AM0717-571

Although AM0717-571 has appeared in several lists of nearby galaxies (eg. Karachentseva & Karachentsev, 1998; Whiting et al., 2002, 2007), this object was actually never followed-up in the optical or near-IR and consequently was never confirmed to be a galaxy. The only optical (*B*-band) image available comes from the Digital Sky Survey (DSS) and shows an object with a morphology resembling closely that of a Galactic nebula. An H I signal at the position of AM0717-571 was reported by HIPASS and included in the HIPASS Bright Galaxy Catalog (Koribalski et al., 2004). However, to understand this apparent detection one has to know that AM0717-571 has two neighboring galaxies, ESO123-G001 and ESO162-G017, located at an angular distance of only 20.7 and 22.4 arcmin respectively. These two galaxies have heliocentric velocities of 1160km $s^{-1}$and 1098km $s^{-1}$similar to and bracketing AM0717-571's listed velocity of 1148 km $s^{-1}$. The HIPASS spectra at the *RA, DEC* positions of ESO162-G017 and AM0717-571 are almost identical in velocity width and peak flux. The fact that our deep *H*-band image did not reveal any galaxy and considering the relatively large uncertainty of HIPASS coordinates due to the 15 armin beam size of the Parkes Radio Telescope, it is conceivable that the 21cm emission at 1148 km $s^{-1}$ detected

**Table 2.4** Galaxies not analysed further.

| Name | R.A. (J2000.0) | Decl. (J2000.0) | Reason | $m_H$ (mag) | $M_{H,0}$ (mag) | $\log_{10}(\mathcal{M}_*)$ $\log_{10}(\mathcal{M}_*)$ |
|---|---|---|---|---|---|---|
| (1) | (2) | (3) | (4) | (5) | (6) | (7) |
| KK2000-03 | 02:24:44.58 | -73:30:49.2 | A | – | – | – |
| KK2000-04 | 03:12:46.14 | -66:16:12.5 | B | > 11.8 | > −16.5 | < 7.0 |
| KK2000-06 | 03:14:26.14 | -66:23:27.9 | B | > 11.8 | > −16.5 | < 7.9 |
| ESO490-G017 | 06:37:57.09 | -26:00:03.1 | C | – | – | – |
| HIZSS003 | 07:00:29.3 | -04:12:30 | C | – | – | – |
| ESO558-PN011 | 07:06:56.80 | -22:02:26.0 | C | – | – | – |
| AM0717-571 | 07:18:37.90 | -57:24:46.5 | B | > 11.8 | > −18.7 | < 8.8 |
| NGC2784 DW1 | 09:12:18.5 | -24:12:41 | B | > 11.8 | > −18.3 | < 8.7 |
| SJK98 J1616-55 | 16:16:49.0 | -55:44:57 | D | – | – | – |
| HIZOAJ1616-55 | 16:18:46 | -55:37:30 | D | – | – | – |
| ESO594-G004 | 19:29:58.97 | -17:40:41.3 | C | – | – | – |

(A) marginal detection; (B) no galaxy detected; (C) foreground stars; (D) Galactic plane

by HIPASS is coming from the extended H I halos of ESO162-G017 and/or ESO123-G001. It has been pointed out by Koribalski et al. (2004) that larger offsets between the H I and the optical positions usually occur when multiple galaxies contribute to the signal or when the H I distribution is asymmetric or peculiar. A clarification of the true nature of AM0717-571 will require further investigations.

## HIZOAJ1616-55 and SJK98 J1616-55

HIZOAJ1616-55 (Juraszek et al. 2000; listed as HIZOAJ1618-55 in NED) and SJK98 J1616-55 have almost identical catalog positions and are close to the Galactic plane ($b = -3.8°$). Staveley-Smith et al. (1998) concluded from deep ATCA 21 cm mapping that these objects are likely part of a single or interacting pair of low-mass H I galaxies with a total H I mass of $8 \times 10^7 \mathcal{M}_\odot$. Their heliocentric velocities (402 km s$^{-1}$ and 430 km s$^{-1}$) are very similar to that of the Circinus galaxy (439 km s$^{-1}$; Jones et al. 1998) suggesting a possible physical connection to Circinus and the nearby Cen A group. However, no optical counterparts have been found to date and hence it is plausible that the H I detection originates from a compact high velocity cloud (Putman et al., 2002). To search for more evidence for either scenario we included HIZOAJ1616-55 and SJK98 J1616-55 in our imaging survey. The Galactic extinction in the $H$-band ($A_H = 0.4$ mag) is much lower than in the optical (eg. $A_B = 2.7$ mag) and hence increases the chances to detect the stellar components of these objects at low Galactic latitude. However, despite our deep imaging, no stellar counterpart to the H I was found and consequently the picture of high velocity cloud(s) seems more plausible.

## KK2000-03

KK2000-03, also known as PGC 9140, is well away from the Galactic plane at $l = 294.2$, $b = -42.0$ but remained almost invisible on our 1800 sec $H$-band image. Whiting et al. (2007) list the galaxy and report an $R$-band surface brightness of $23.7 \pm 0.2$ mag arcsec$^{-2}$. They calculate this as the average surface brightness for an area of roughly 1 arcmin in diameter, located such that it contains the brightest parts of the galaxy, and excludes stars (where possible). Assuming an $R-H$ colour of 1.10 for the sun (calculated using results from Colina et al., 1996) implies KK2000-03 should have an $H$-band surface brightness of 22.6 mag arcsec$^{-2}$, well above our detection limit. The DSS image shows that KK2000-03 is located directly behind a foreground star. Despite this contamination, KK2000-03 must have an unusual blue stellar population for it not to be detected more prominently in our survey.

## KK2000-04 and KK2000-06

Little is known about these two extremely low surface brightness irregular galaxies which were first mentioned in a catalogue of dwarf galaxy candidates by Karachentseva & Karachentsev (2000). The authors estimated their total $B$-band magnitudes from photographic plates as 17.8 and 17.0, respectively, and speculated that they may be companions of the barred spiral NGC 1313 ($v_\odot = 475$ km s$^{-1}$), another of our sample galaxies. We did not detect either KK2000-04 or KK2000-06 despite obtaining deep imaging data of fields with only low levels of foreground contamination. While KK2000-04 also remains undetected at 21 cm, the H I spectrum for KK2000-06 measured with the Effelsberg 100-m radio telescope (Huchtmeier et al., 2001) suggests a heliocentric velocity of ~2250 km s$^{-1}$. Therefore it is possible that KK2000-04 is a plate flaw and KK2000-06 is a distant galaxy unrelated to NGC1313.

## NGC2784 DW1

The extremely low surface brightness dwarf galaxy NGC2784 DW1 was first detected by Parodi et al. (2002). It is located between the S0 galaxy NGC2784 and the nucleated early-type dwarf KK98-73 on the sky and due to its morphology (dE), its size and location, Parodi et al. (2002) suggest it is likely to be a satellite of NGC2784. Karachentsev et al. (2004) give NGC2784 DW1 a membership distance and include it in the census of galaxies within 10 Mpc. However, it is important to note that no independent distance measurement has been obtained to date. Our deep near-IR observation detected the faint galaxy KK98-73, while NGC2784 DW1 is barely visible as expected from the recorded mean effective surface brightness of $\langle\mu\rangle_{eff} \approx 25$ mag arcsec$^{-2}$ and $r_{eff} \approx 20$ arcsec in the $B$-band.

## 2.6. Results

### 2.6.1. LSI survey versus 2MASS photometry

It is instructive to see how galaxies can change their appearance when going from 2MASS to the deeper LSI observations. For example, our image of the barred Sc galaxy NGC2835 (Fig. 2.12) reveals the rich near-IR morphology and extent of this spiral galaxy for the first time. The almost face-on view presents a well-ordered 4 or 5-arm spiral pattern outlined by the star-dominated Population II disk, which closely traces the gas-dominated Population I disk morphology observed in the *B*-band (Sandage & Bedke, 1994). The 2MASS image for the irregular Sculptor group galaxy ESO473-G024 shows qualitatively the limitation of that survey to study dwarf galaxies. With a central *H*-band surface brightness of $\approx 20.5\,\mathrm{mag\,arcsec^{-2}}$, ESO473-G024 remains effectively undetected in 2MASS (Fig. 2.12). Our image uncovers a smooth, dE-like morphology with little evidence of irregularity. This stands in stark contrast to the *B*-band image that is dominated by a number of prominent H II regions and dust features.

It has been previously pointed out by Andreon (2002) that the short integration time of 2MASS failed to detect most of the lower surface brightness (dwarf) galaxies and that, if they were detected, fluxes were underestimated by as much as 70 percent. To investigate this issue further, we plot in Figure 2.13 the difference between our total extrapolated apparent magnitudes ($m_{H,obs} - \Delta m$; Table 3, col. 2 and Table 4, col 6) and the total magnitudes from the 2MASS All-Sky Extended Source Catalog for 21 galaxies we have in common, as a function of mean effective surface brightness ($\langle \mu_H \rangle_{eff}$; Table 3, col. 4). LSI galaxies with a surface brightness fainter than $\mu_H = 18\,\mathrm{mag\,arcsec^{-2}}$ are affected at different levels with the missing flux in the range between 0.2 and 2.5 mag. Even in the cases of the luminous galaxies NGC2784 and NGC3115 our analysis finds that their 2MASS *H*-band magnitudes are 0.5 mag too faint.

To demonstrate that the disparity between the 2MASS and our *H*-band magnitudes is not caused by differences in the measuring procedure we analysed 2MASS images using our method. The photometric parameters listed in the 2MASS Extended Source Catalog, as well as the surface brightness profiles, were reproduced within the quoted uncertainties. It should be noted that the 2MASS Large Galaxy Atlas (Jarrett et al., 2003) has employed two different methods for recovering the flux below the sky background noise and that we have made the comparison to the magnitudes which were obtained by extrapolating the surface brightness profile. The 2MASS magnitudes which were obtained using Kron (1980) apertures are systematically fainter (see Figure 9 of Jarrett et al. 2003) and therefore the difference between our total apparent magnitudes and the 2MASS magnitudes obtained using Kron apertures is also larger.

The Extended Source Catalog is contaminated by a small (1% to 5%) number of

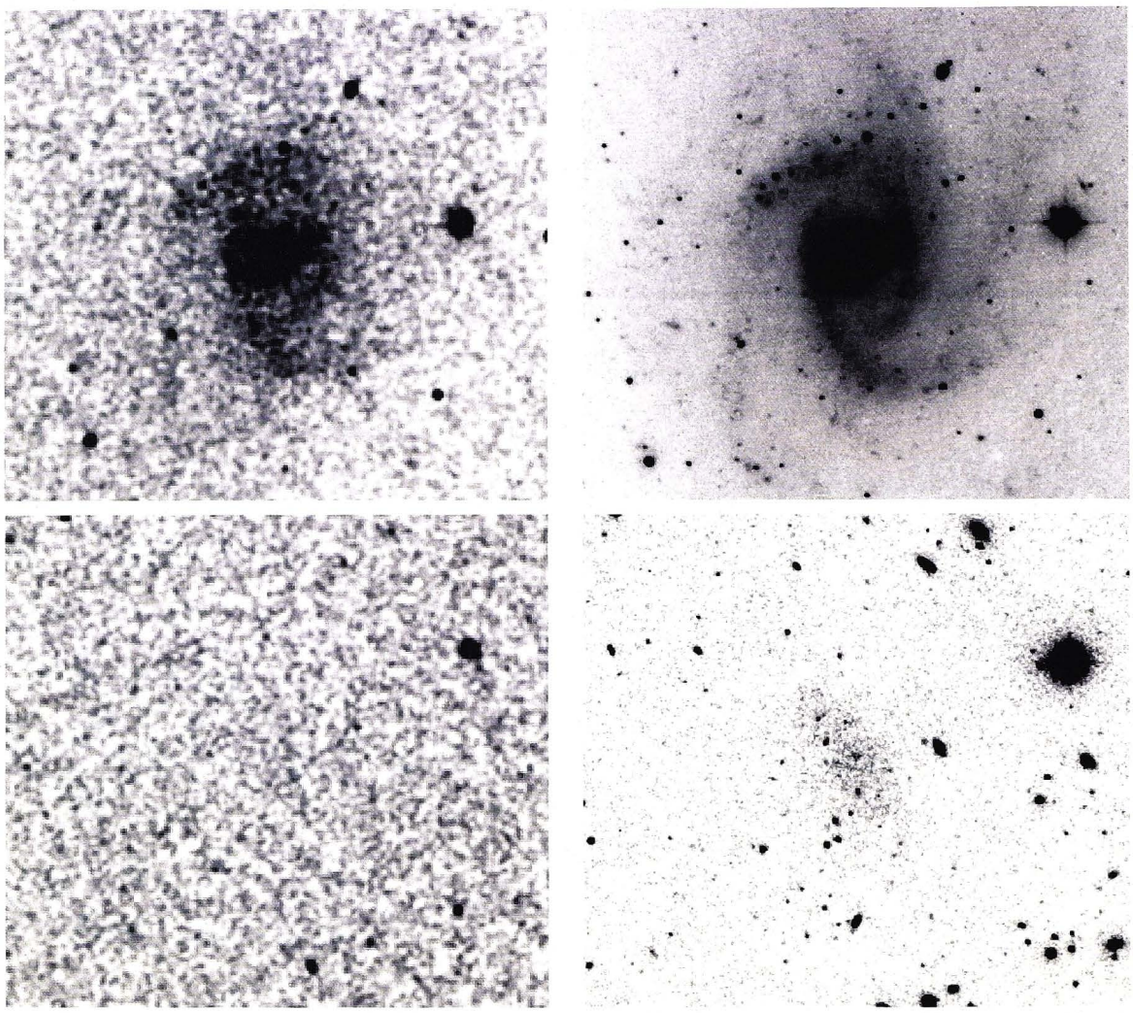

**Figure 2.12** The 2MASS (left panel) and the LSI (right panel) *H*-band images of the spiral galaxy NGC2835 ($V_{helio}$ = 886 km s$^{-1}$) and the dwarf irregular galaxy ESO473-G024 ($V_{helio}$ = 541 km s$^{-1}$) are shown in the upper and lower panels, respectively. The new LSI images probe to surface brightness levels ≈4 mag arcsec$^{-2}$ fainter than 2MASS. A complex morphology and additional spiral arms are detected in the case of NGC2835 whereas only the deeper LSI image detects a stellar component in the case of ESO473-G024.

artefacts which can significantly affect the photometry of real sources (Jarrett et al., 2000). Each of our galaxy images were visually inspected for artefacts which were effectively removed (unless documented otherwise). This is obviously an impractical approach for the much larger 2MASS dataset and Jarrett et al. (2000) notes that the pipeline is not 100% effective. It is conceivable that this accounts for a fraction of the discrepancy.

In summary, our finding is in good agreement with that of Andreon (2002) and emphasizes again that the 2MASS magnitudes are significantly fainter than those obtained from deeper near-IR imaging. As the mean effective surface brightness correlates with the luminosity of a galaxy (see section 2.6.3, Figure 2.17), serious selection biases must be expected, for instance, for the 2MASS-based *H*-band galaxy luminosity function at magnitudes fainter than $M_H = -20$ mag.

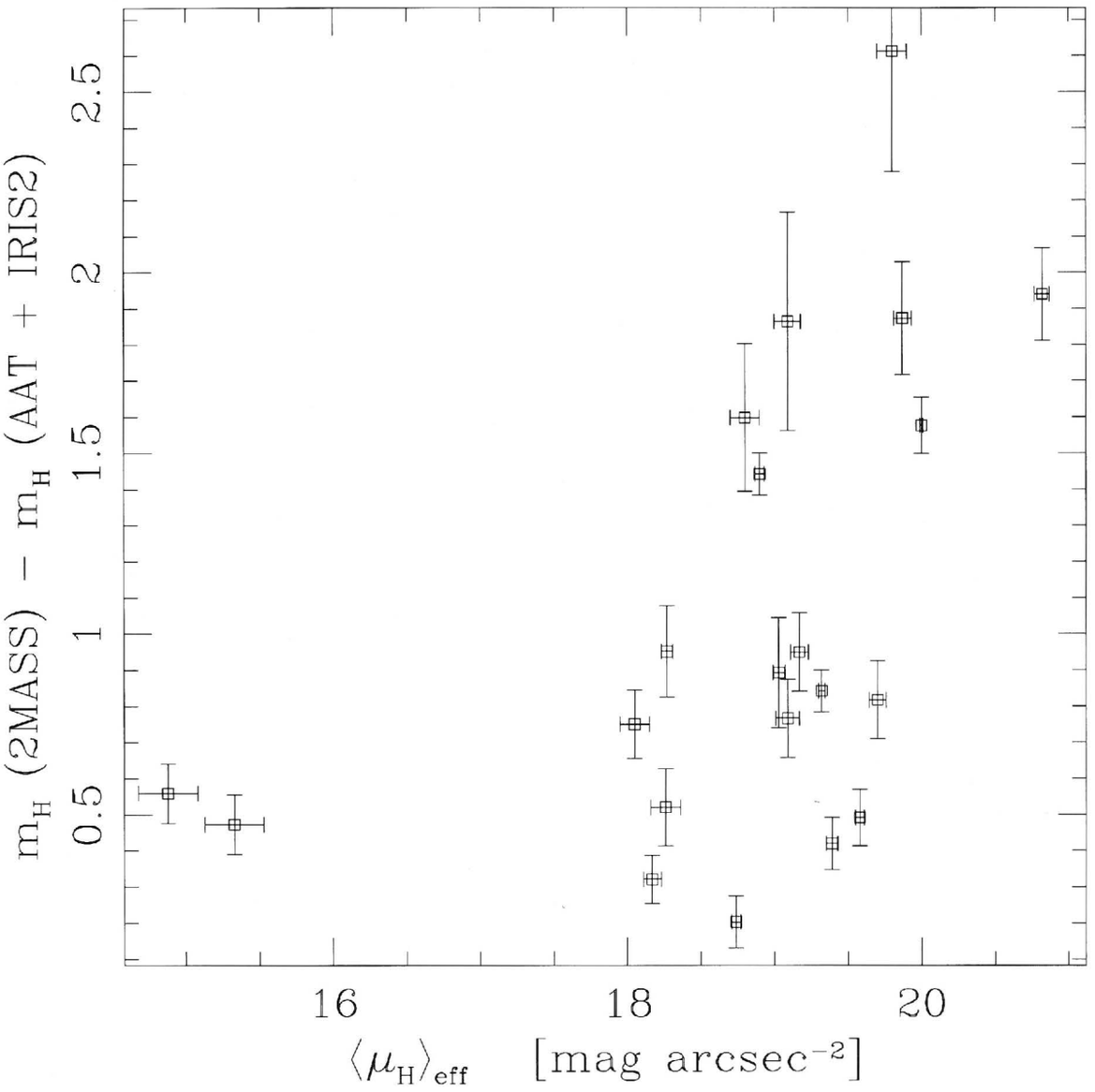


**Figure 2.13** 2MASS versus LSI magnitudes showing the systematic underestimation of galaxy fluxes by 2MASS for the galaxies that it did detect.

### 2.6.2. Optical - Near Infrared magnitude transformation

The $B - H$ colour of each galaxy is an indicator of the ratio of the population II to population I stars, as modulated by the effects of dust. A comparison of the absolute $B$- and $H$-band magnitude, corrected for Galactic extinction, is shown in Figure 2.14 for our sample galaxies. We also plot the Virgo cluster data from the Goldmine database (Gavazzi et al., 2003). The data of the Virgo galaxies were extinction-corrected using $A_B = 0.13$ mag and $A_H = 0.01$ mag. We have adopted the mean cluster distance of 15.8 Mpc (Jerjen et al., 2004) based on surface brightness fluctuation measurements of early-type galaxies. In addition to the Virgo cluster data, we have also included the data for 30 bright spiral

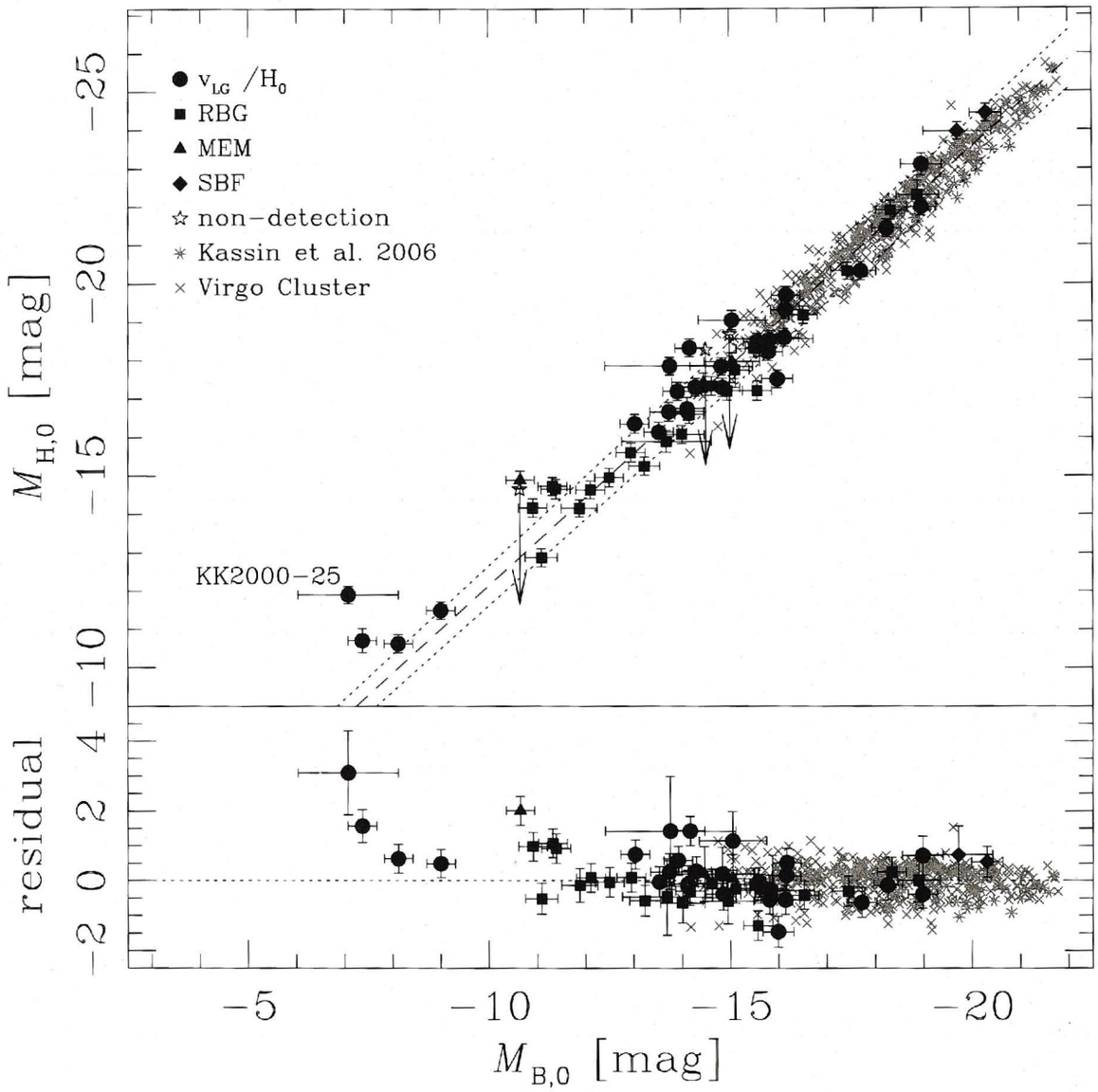


**Figure 2.14** Comparison of the integrated absolute $B$- and $H$-band magnitude. Plotted here is our new data with an indicator of the distance estimate method. Also plotted is the data of Kassin et al. (2006) and the Virgo cluster data from the Goldmine database (Gavazzi et al., 2003). Marked is the galaxy KK2000-25 which appears to be significantly under-luminous in the $B$-band. The dashed line is the $B-H$ mean colour for all galaxies in the Virgo Cluster sample and the dotted lines indicates data within 1 $\sigma$. The galaxies which were not detected have been given a lower bound magnitude estimate.

galaxies from Kassin et al. (2006) which were corrected for extinction (using Schlegel et al., 1998). By including the two additional data sets we are able to investigate the $B-H$ colour for late-type galaxies over a range of 15 magnitudes. Figure 2.14 shows that there is a tight correlation between the $B$- and $H$-band luminosity of a galaxy. This linear relation is

$$M_{H,0} = (1.14 \pm 0.02)M_{B,0} - (0.74 \pm 0.32) \tag{2.6}$$

which is a least squares fit to the Virgo cluster data. While the more luminous galaxies in our sample obey the relation closely, the residual plot suggests that the scatter marginally increases in the dwarf regime and possibly has a slight upwards trend to redder colours (average residual $\approx 1$ mag). The most deviant galaxy in our sample, KK2000-25, appears under-luminous in the $B$-band by 3 magnitudes. While we cannot exclude the possibility that this galaxy has had an unusual star formation history, we need to point out two things. Firstly, KK2000-25 is located almost in the Galactic plane ($b = 1.28°$) and thus has a large $B$-band extinction uncertainty. Secondly, the $B$-band magnitude for KK2000-25 was estimated visually from a photographic film (Huchtmeier et al., 2001). Consequently, the deviation from the line of best fit could be entirely due to a large uncertainty in the $B$-band magnitude. By excluding KK2000-25, there is no correlation between the residual in the $B - H$ plot and the galaxy distance, Galactic latitude or mean effective surface brightness (see Figure 2.15).

It is worth noticing that the least squares fit deviates from a line of unity slope. The gradient of $1.14 \pm 0.02$ implies that dwarf galaxies are in general bluer than the more luminous galaxies. It is well known that galaxy colour correlates with luminosity (eg, Tully et al., 1998; Hogg et al., 2002; Blanton et al., 2001, 2003).

Figure 2.14 gives a useful indication of the stellar population of galaxies. Galaxies which lie well below the line are bluer than most galaxies which suggests that they have a relatively young stellar population. Conversely, galaxies which lie well above the line are redder than expected indicating a larger old stellar population. The tight correlation (correlation coefficient = 0.97) between the $B$- and $H$-band luminosities comes somewhat as a surprise. A $B$-band light profile of a galaxy can be significantly attenuated and distorted by dust. Moreover, short-lived giant O and B stars contribute to the $B$-band emission and hence the profile can be distorted by transient star-formation events. The stellar mass of most galaxies is dominated by the older, low luminosity stellar population whose energy output peaks at near-IR wavelengths (Gavazzi et al., 1996b). Hence it has been argued that the near-IR is the optimal wavelength regime for investigations of structural properties (Driver, 2004). The tight correlation between the $B$- and $H$-bands, however, suggests that the advantages of the $H$-band may not be as significant as previously thought, at least for late-type giant galaxies. A detailed comparison of the observed scatter with the predictions from population synthesis models (eg, Bruzual & Charlot, 1993, 2003; Maraston, 1998; Li & Han, 2008) is beyond the scope of this paper because of the wide range of stellar compositions and star formation histories represented by our galaxy sample.

The $B - H$ colour for each galaxy can be compared with the morphological type (Figure 2.16). There we include the combined samples of Kassin et al. (2006) and the Virgo cluster data in the white boxes and the new LSI data is shown by the black boxes. The combined Virgo cluster and Kassin et al. (2006) sample is ten times the size of our sample but is dominated by giant, luminous galaxies.

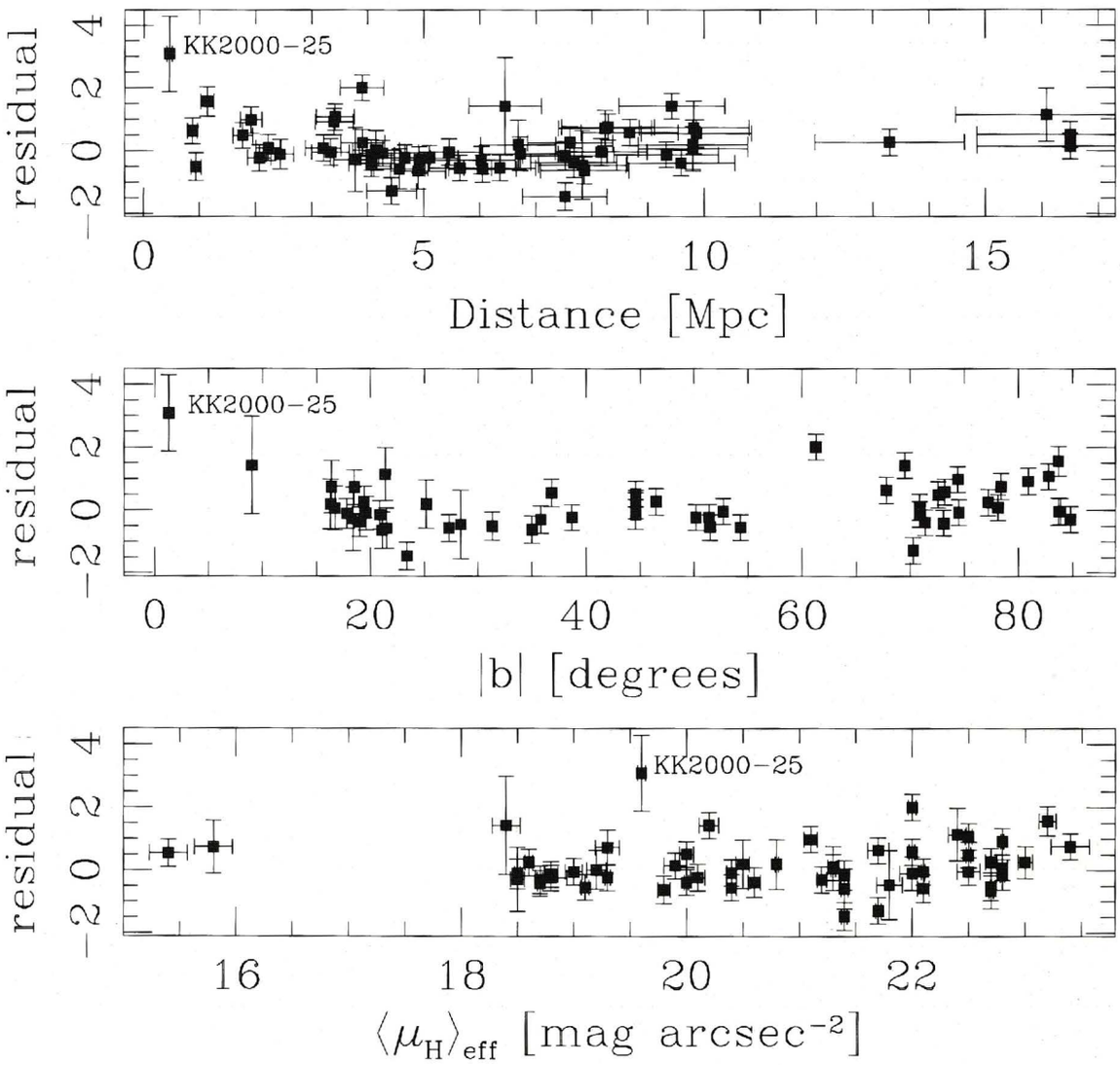


**Figure 2.15** The deviation of individual LSI galaxies from equation 2.6 as a function of distance [upper panel], Galactic latitude [middle panel] and mean effective surface brightness [lower panel]. The error in the distance is taken to be 10%. KK2000-25 is located at low Galactic latitude and significantly deviates from the relationship.

Our sample, in contrast, contains four times as many irregular dwarf galaxies. Therefore, when interpreting the colour vs morphology plot, it must be noted that our sample dominates the morphological bin of irregular galaxies and the literature data dominates the larger galaxies.

The comparison of morphology to the $B-H$ colour shows that the early-type galaxies are redder than the late-type, irregular and dwarf galaxies. A similiar study by Jarrett et al. (2003) for galaxies in the 2MASS Large Galaxy Atlas also showed this trend.

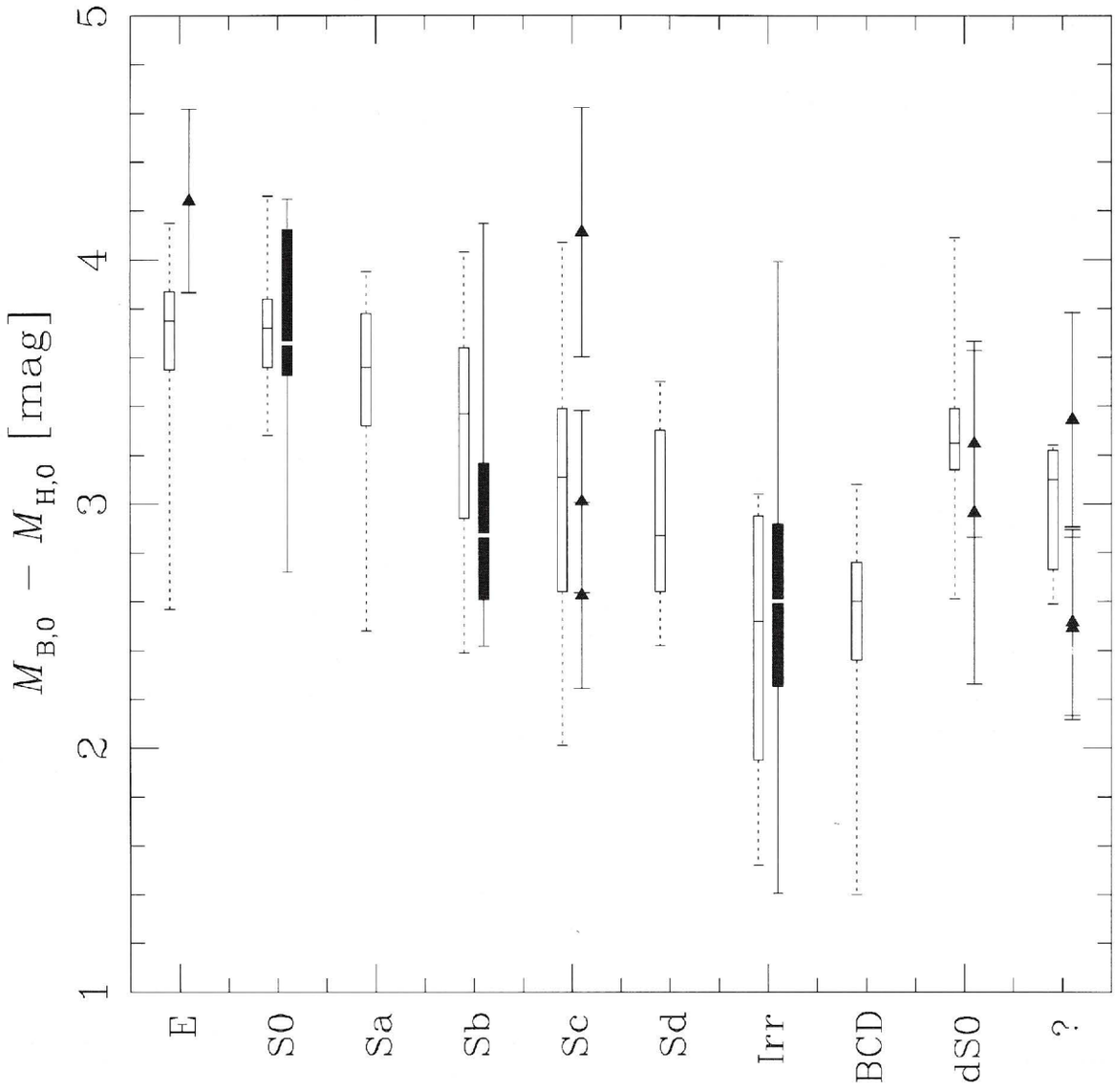


**Figure 2.16** Comparison of the integrated apparent $B-H$ colour and the morphological type. The black boxes show our data and the white boxes show the combined samples of Kassin et al. (2006) and the Virgo cluster data listed in the Goldmine database (Gavazzi et al., 2003). The boxes show the median values as well as the quartile range. The errorbars on the boxes show the maximum and minimum $B-H$ colour for each morphological type. For morphologies with insufficient data, the individual data points are displayed with their associated uncertainty.

### 2.6.3. Luminosity - Surface Brightness Relation

In Figure 2.17 we plot the mean effective surface brightness of our sample galaxies as a function of absolute magnitude. In addition to our $H$-band data, we include 560 late-type Virgo cluster galaxies (obtained from the Goldmine database; Gavazzi et al. 2003). The mean effective surface brightness for Virgo

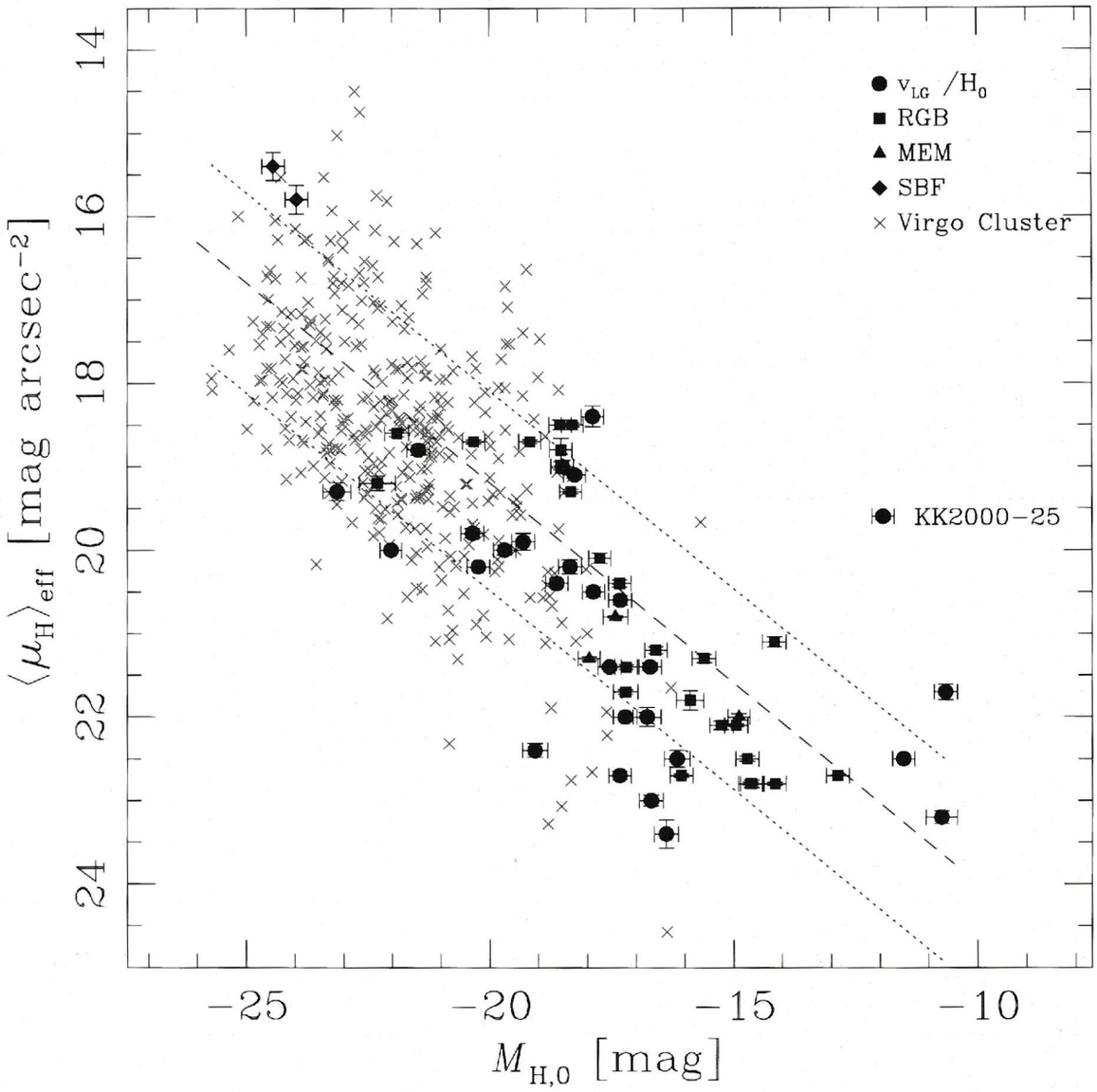


**Figure 2.17** Comparison of the mean effective surface brightness and the absolute magnitude for our sample galaxies. Symbol shapes indicate the distance estimation method used. Also plotted are 560 late-type galaxies in the Virgo cluster (Gavazzi et al., 2003). Marked is the galaxy KK2000-25 which deviates from the general trend probably caused by an incorrect distance estimate. The dashed line is the line of best fit for all galaxies and the dotted lines indicates data within $1\sigma$.

cluster galaxies was calculated as

$$\langle \mu_H \rangle_{eff} = M_H + 2.5 \log_{10}(\pi r_{eff}^2)$$

and the data was corrected for extinction using $A_H = 0.01$ mag. The morphologies of Virgo cluster galaxies included in the sample range from S0 to Sd, Irr and BCD (listed as types 1 to 18 in the Goldmine database).

As previously discussed in de Jong & Lacey (2000), the relationship between the two photometric parameters provides an important link to the underlying physical

parameters of a galaxy, namely its total mass $M_{tot}$ and total angular momentum. The total angular momentum of a galaxy, expressed as the dimensionless spin parameter $\lambda = J|E|^{1/2}M_{tot}^{-5/2}G^{-1}$ (Peebles, 1969), is related to the scale length of its disk (Fall & Efstathiou, 1980; Dalcanton et al., 1997; Mao et al., 1998). de Jong & Lacey (2000) showed that $\lambda$ can be transformed into observable quantities. The authors presented a model of a singular isothermal sphere with $E \propto M_{tot}V_c^2$ from the virial theorem and a perfect exponential disk with angular momentum $J_{disk} \propto M_{disk}r_{eff}V_c$ (assuming $V_{disk} = V_c$). They showed that if $J_{disk}/M_{disk} \propto J/M_{tot}$ and $M_{disk} \propto M_{tot}$ then $\lambda \propto r_{eff}V_c^2/M_{disk}$. Furthermore, using the relation $M_{tot} \propto V_c^3$ predicted for dark matter halos, de Jong and Lacey showed that $\lambda \propto r_{eff}L^{\Upsilon/3}$, where $\Upsilon$ is the mass-to-light ratio for the disk. This can be transformed into an expression between surface brightness and total magnitude by invoking

$$\Sigma_{eff} = L(2\pi r_{eff}^2)^{-1}$$

which results in:

$$\lambda \propto \Sigma_{eff}^{-1/2}L^{-\Upsilon/3+1/2}$$

Using the two identities $-2.5\log_{10}\Sigma_{eff} = \langle\mu_H\rangle_{eff} + c$ and $-2.5\log_{10}L = M + c'$ ($c$ and $c'$ being constants) we finally arrive at the theoretical luminosity –surface brightness relation:

$$\langle\mu\rangle_{eff} = (1 - 2\Upsilon/3)M + 5\log_{10}\lambda + C \tag{2.7}$$

Here, we can see that the gradient of the luminosity – surface brightness relation is a function of the galaxy mass-to-light ratio and that the dispersion in the empirical relation reflects the distribution of the spin parameter.

The empirical relation between the two observational quantities in Figure 2.17 for the late-type galaxies of the Virgo cluster sample is analytically best described by the linear equation:

$$\langle\mu_H\rangle_{eff} = a \cdot M_{H,0} + b \tag{2.8}$$

where $a$ is $0.47 \pm 0.08$, $0.44 \pm 0.06$ and $0.48 \pm 0.05$ for our LSI sample, the Virgo cluster sample and the combined LSI + Virgo samples respectively, and $b$ is $29.0 \pm 1.4$, $28.0 \pm 1.3$ and $28.8 \pm 1.1$. The uncertainty in $a$ and $b$ is the formal uncertainty in the linear fit plus the uncertainty due to the robustness of the sample obtained using bootstrap resampling. In Figure 2.17, the empirical relation between the mean effective surface brightness and the absolute magnitude is plotted for the combined LSI + Virgo cluster samples.

A comparison of the empirical result (see equation 2.8) with the theoretical prediction (equation 2.7) allows to estimate $\Upsilon_*^H$: $a = (1-2\Upsilon/3) \Rightarrow \Upsilon_*^H = 0.80 \pm 0.12$, $0.84 \pm 0.09$ and $0.78 \pm 0.08$ for our LSI sample, the Virgo cluster sample and the combined data sets respectively. These results are in excellent agreement with the value of $1.0 \pm 0.4$ adopted in section 2.4.2.

## 2.7. Interesting Galaxies

### KKS2000-09

KKS2000-09 has a morphological classification of a spiral "S". However, close inspection of our *H*-band image reveals that KKS2000-09 has a double nucleus and thus should be classified as a peculiar galaxy.

### HIZSS003

HIZSS003 is a H I source originally detected at 21 cm by the Dwingeloo obscured galaxies survey (Henning et al., 1998). It is located behind the zone of avoidance ($b = 0.09°$) in the outskirts of the LG at 1.7 Mpc (Silva et al., 2005). Our image is highly contaminated with foreground stars preventing further analysis. Begum et al. (2005) show that HIZSS003 is actually a galaxy pair (HIZSS003A and HIZSS003B). Our imaging shows that there is a resolved stellar overdensity associated with the H I peak (labelled HIZSS003A using the Begum et al. 2005 convention) as well as a stellar component associated with the peak of the narrowband $H_\alpha$ emission first detected by Massey et al. (2003) (labelled HIZSS003B by Begum et al. 2005).

### KK2000-25

The morphology of KK2000-25 is listed in NED as Irr. Our deep imaging (see Figure 2.4, third row, right panel) shows distinct spiral arms and that KK2000-25 should have a morphological classification of "Sb". This morphology is not consistent with its angular size given the listed distance of 0.5 Mpc. This distance estimate was obtained using a H I profile observed by Huchtmeier et al. (2001) and the spectrum given does not show a clear galaxy detection. Based on the updated morphological classification, KK2000-25 must be more distant than the estimate given.

The galaxy KK2000-25, although prominent when observed in the *H*-band, appears to be under-luminous in the *B*-band (see Figure 2.14). This galaxy, however, is located at a low Galactic latitude and hence the extinction correction will not be very reliable. An inaccurate extinction correction will affect the *B*-band magnitude significantly but will have minimal affect on the *H*-band magnitude. Hence it is possible that this galaxy does not obey the *H*-band to *B*-band transformation (equation 2.6) simply because the absolute *B*-band magnitude is incorrect. The discrepancy between the absolute *B*- and *H*-band for KK2000-25 is not due to the incorrect distance estimate.

## 2.8. Summary

We have presented the deepest $H$-band images available to date for 57 galaxies in the Local Sphere of Influence ($D < 10$ Mpc), obtained using the near-IR camera IRIS2 at the 3.9m Anglo-Australian Telescope. Of the 68 targets, 11 remained undetected or could not be usefully analysed due to contamination by foreground stars. The surface brightness limit reaches down to $\mu_{lim} < 26$ mag arcsec, 4 magnitudes fainter than 2MASS.

The images, cleaned from Galactic foreground contamination, reveal the morphology and extent of many of the galaxies for the first time. For 56 galaxies, we derive radial luminosity profiles, ellipticities, and position angles, together with global parameters such as total magnitude, mean effective surface brightness, half-light radius, Sérsic parameters, and stellar mass.

No genuine young galaxies have been found in this survey. Some sample galaxies were previously identified on $B$-band photographic plates but remain undetected in the near-IR. In each case there is a plausible alternative explanation for the non-detection:

- AM0717-571: DSS $B_J$-band morphology resembles that of a Galactic nebula, but true nature still remains unclear.
- HIZOAJ1616-55 and SJK98 J1616-55: possibly one or two high velocity clouds.
- KK2000-03: Superimposed star hampers analysis however the marginal detection in the H-band suggests an unusual blue galaxy.
- KK2000-04: Originally assumed to be a companion of NGC1313 however possibly a photographic plate flaw.
- KK2000-06: Originally assumed to be a companion of NGC1313. More likely a background galaxy at $\approx$2250 km s$^{-1}$.
- NGC2784 DW1: intrinsic extreme low surface brightness dwarf satellite of NGC2784.

We also detected a double nucleus in KKS2000-09 and propose to reclassify this system as a peculiar galaxy. KKS2000-25 was shown to have distinct spiral arms in the $H$-band and thus should be classified as "Sb". Morphology and angular size strongly suggest that this is a background galaxy beyond 10 Mpc.

We found compelling evidence that the short integration time of 2MASS resulted in serious underestimation of a galaxy's luminosity. The magnitudes of galaxies, with $H$-band surface brightnesses fainter than 18 mag arcsec$^{-2}$, obtained in our study are up to 2.5 mag brighter than those obtained by 2MASS. As the mean

effective surface brightness correlates with the luminosity of a galaxy, we expect serious selection biases for a 2MASS-based $H$-band galaxy luminosity function fainter than $M_H = -20$ mag.

There is a tight correlation (correlation coefficient = 0.97) between the $B$- and $H$-band magnitudes of a galaxy and this correlation has been demonstrated over a range of 15 magnitudes. The linear transformation between the $B$- and $H$-bands has a small scatter (0.3 mag) for bright galaxies. In the dwarf regime, there is a marginal increase in scatter and possibly a slight trend for galaxies to be redder (by approximately 1 magnitude) than indicated by the transformation found for bright galaxies.

The galaxy luminosity – mean effective surface brightness relation has been analysed to derive a semi-empirical stellar mass-to-light ratio of $\Upsilon_*^H = 0.78 \pm 0.08$ in the $H$-band.

All raw and reduced $H$-band images of the 57 program galaxies in this near-IR survey will be made publicly available and can be obtained via email request.

# CHAPTER 3

# The Local Volume HI Survey: Galaxy Kinematics

*To be submitted to MNRAS*
*Kirby, Koribalski, Jerjen, et al. 2010*

**Abstract:**
Here we present the results of a detailed kinematical analysis of 12 nearby galaxies from the 'Local Volume H I Survey' (LVHIS)[1]. For each galaxy we derive orientation parameters, and the H I rotation curve. Using the H I Parkes All-Sky Survey (HIPASS) and LVHIS, based on H I line data obtained with the Australia Telescope Compact Array (ATCA), we also compare the global galaxy properties, in particular the integrated H I flux density and velocity widths of the observed H I spectra. We show under which circumstances the latter accurately reflect the galaxy's rotation velocity which is a key ingredient to the (Baryonic) Tully Fisher relation.

## 3.1. Introduction

The kinematics of the gas and stars in galaxies are often very complex, reflecting both internal and external processes such as turbulence, infall/outflow, rotation, tidal interactions and ram pressure stripping. The rotational component, which

[1]A detailed description of the complete LVHIS survey is provided in this thesis in Appendix A. There we include the full LVHIS sample, observation method, data reduction techniques and data products for selected galaxies.

dominates in most spiral galaxies, provides a direct measure of the gravitational potential. In contrast, small dwarf galaxies often show similar rotational and non-rotational amplitudes (e.g., Begum et al. 2003). The rotation curve, i.e. the rotational velocity as a function of galaxy radius, gives an accurate estimate of the total galaxy mass out to the largest measured radial extent. When deriving a galaxy's rotation curve from the data, projection effects as well as the shape and orientation of the disk/orbits must be taken into account. In particular, the majority of spiral galaxies display mild or strong bars in the inner region and warps in the outer regions.

Rotation curves have long been used as a tool to study the bulk motion of the H I disk. Following several early studies of 21-cm (H I) rotation curves, e.g. by Rogstad & Shostak (1972) and Roberts & Rots (1973), Bosma (1981) carried out the first comprehensive analysis of relatively high resolution H I rotation curves of 35 galaxies with a range of morphological types. Begeman (1989) described a new method, the tilted-ring analysis, to derive rotation curves and demonstrated it for the extended H I disk of the spiral galaxy NGC 3198. This method is still the most commonly used for modelling mildly inclined galaxy disks.

The Local Volume (LV; $D < 10$ Mpc) is the ideal place to study the kinematics of galaxies. Approximately 550 galaxies are currently known to reside in this volume (Karachentsev et al., 2008), approximately 85% of which are dwarf galaxies (Karachentsev et al., 2004). Due to their proximity, independent distances are available for most LV galaxies, and they can be studied with high spatial resolution.

A large range of H I rotation curve studies already exist and more are under way. While we are working towards a large set of excellent galaxy rotation curves, each individual galaxy requires suitable data and a lot of time to model their kinematics and mass distribution. Dwarf galaxies are particularly difficult to model, because of their small size, low rotation velocity, non-rotational motions such as turbulence, infall/outflow, etc. as well as large neighbours. Côté et al. (2000) presented rotation curves for eight dwarf irregular galaxies located in the nearby Sculptor and Centaurus A groups, several of which are also discussed in this paper. Swaters et al. (2009) just published the H I rotation curves of 62 late-type dwarf galaxies based on data from the WHISP project (see Swaters et al. 2002) while Verheijen & Sancisi (2001) derived rotation curves for 43 spiral galaxies in the nearby Ursa Major cluster. Several high-resolution, high-sensitivity H I surveys of nearby galaxies are currently underway which together will provide a comprehensive picture of the local galaxy dynamics and mass distribution. Most notable are (1) 'The H I Nearby Galaxy Survey' (THINGS; Walter et al. 2008) which provides a detailed analysis of the rotation curves of 19 nearby galaxies (de Blok et al., 2008; Oh et al., 2008) and (2) the 'Faint Irregular GMRT Galaxies Survey' (FIGGS; Begum et al. 2008b) which provides detailed H I velocity fields (Begum et al., 2006) and rotational velocities (Begum et al. 2008a)

for a large number of dwarf galaxies. Most of the THINGS targets are well-resolved, large spiral galaxies, while the FIGGS targets are faint dwarf irregular galaxies observed with very high velocity and angular resolution. The 'Local Volume HI Survey' (LVHIS; Koribalski et al. 2010) will initially provide medium resolution (~ 60") H I data for a complete sample of ~70 southern galaxies (see Section 2) aimed at studying their large-scale gas distribution and kinematics. High resolution (10") data will be published after further data processing.

This paper is organised as follows. In Section 3.2 we describe the 12 nearby galaxies that were selected for the rotation curve analysis, followed by a brief outline of the radio observations and data reduction in Section 3.3. In Section 3.4 we discuss the galaxy properties as measured and derived from interferometric and single dish H I data. Rotation curves, $v(r)$, and disk orientation parameters are presented for each galaxy in Section 3.5. In Section 3.6 we compare the rotation curve and spectral properties of our sample galaxies. The kinematics of individual galaxies are presented in Section 3.7 and the Tully-Fisher relation discussed in Section 3.8. Finally the results are summarised in Section 3.9.

## 3.2. The Galaxy Sample

The 'Local Volume H I Survey' (LVHIS[2]; (Koribalski et al., 2010) is a large project which aims to provide H I distributions, H I velocity fields and 20-cm radio continuum maps for all galaxies within 10 Mpc. For observations with the Australia Telescope Compact Array (ATCA) we initially chose only those LV galaxies that are detected in the H I Parkes All-Sky Survey (HIPASS; Barnes et al. 2001; Koribalski et al. 2004) and reside south of approximately –30 degrees declination. For a brief overview of the LVHIS observations and data reduction see Section 3.3.

While we would like to derive rotation curves and mass models for all ~70 LVHIS galaxies observed with the ATCA, the typical angular resolution of the H I maps used here allows us to study only those galaxies with H I diameters larger than ~5'. Furthermore, a number of large, nearby galaxies have already been extensively studied and good rotation curves are available in the literature (see, e.g. Circinus: Jones et al. 1999, ESO215-G?009: Warren et al. 2004, ESO245-G005, ESO381-G020, ESO325-G011, ESO444-G084 and UGC442: Côté et al. 2000, M83: Tilanus & Allen 1993, NGC247: Carignan & Puche 1990b, NGC253: Puche et al. 1991a, NGC300: Puche et al. 1990, NGC625: Cannon et al. 2004, NGC1313: Ryder et al. 1995, NGC1512: Koribalski & López-Sánchez 2009, NGC1705: Meurer et al. 1998, NGC2188: Domgoergen et al. 1996, NGC2915: Bureau et al. 1999, NGC4945: Ott et al. 2001, NGC5102: van Woerden et al. 1993, NGC5128: Schiminovich et al. 1994, NGC5253: Kobulnicky & Skillman 1995, NGC6822: Weldrake et al. 2003,

[2]http://www.atnf.csiro.au/research/LVHIS/

NGC7793: Carignan & Puche 1990a). A tilted-ring analysis is most appropriate for galaxies with inclination angles of $i$ = 30 – 80 degrees. Edge-on galaxies ($i$ > 80 degrees require a different method (the envelope tracing method of Sofue 1996, 1997) to derive robust rotation curves as the observed line-of-sight crosses a large range of projected velocities. For nearly face-on galaxies, non-rotational and rotational motions in the line-of-sight can be of similar amplitude, leading to large uncertainties in the derived rotation curve (Lewis, 1975; Meyer et al., 2008). Following de Blok et al. (2008) we chose a lower limit of $i$ = 30 degrees. Using the above criteria, we select 12 LVHIS galaxies for our kinematical study.

In Figure 3.1 we show deep ($\mu_{lim}$ < 26 mag arcsec$^{-2}$) near-IR, $H$-band images, if available from Kirby et al. (2008), or $B$-band (optical) images of the selected galaxies. We prefer near-IR over optical images to reveal the full extent and shape of the stellar disk because (a) dust attenuation is minimal and (b) the observed light emission is not dominated by that of short-lived giant O and B stars. Deep $H$-band (1.65$\mu m$) images are, unfortunately, not yet available for AM0605-341, ESO174-G?001, ESO215-G?009, ESO325-G?011 and ESO381-G020, so $B$-band (468 nm) Digitised Sky Survey (DSS) images are displayed instead. Based on their stellar distribution we find that all 12 sample galaxies are dwarf irregular galaxies, some are of Magellanic type and some have central bars.

The basic optical properties of the sample galaxies are given in Table 3.1. The columns are organised as follows:

*Column* (1) – galaxy name.

*Columns* (2) and (3) – equatorial coordinations of the centre of the optical emission for the epoch of J2000, obtained from the ESO-LV catalog, (Lauberts & Valentijn, 1989) and the Arp & Madore (1987) catalog.

*Columns* (4) and (5) – distance to the galaxy and an indication of the method used: tip of the red giant branch (TRGB) or Hubble flow distance (H), $D = v_{LG}/H_0$, where $v_{LG}$ is the Local Group velocity calculated using the HIPASS derived heliocentric velocity (see Table 3.2) and coordinate transformation of Karachentsev & Makarov (1996). Here, $H_0$ = 73km s$^{-1}$ Mpc$^{-1}$ is adopted (Wilkinson Microwave Anisotropy Probe, WMAP; Spergel et al. 2007). An uncertainty of 10% is adopted (Karachentsev et al., 2006).

*Columns* (6) and (7) – the position angle and inclination of the outer isophotes. For the galaxies with $H$-band images available, the surface brightness at which these values were measured is typically 26 mag arcsec$^{-2}$. When DSS images were used, the surface brightness is higher. The position angle is listed taken in the anti-clockwise direction, between the north direction on the sky and the major axis. It is important to note that these parameters are defined by the optical morphology and may not be equivalent to the position angle and inclination defined kinematically.

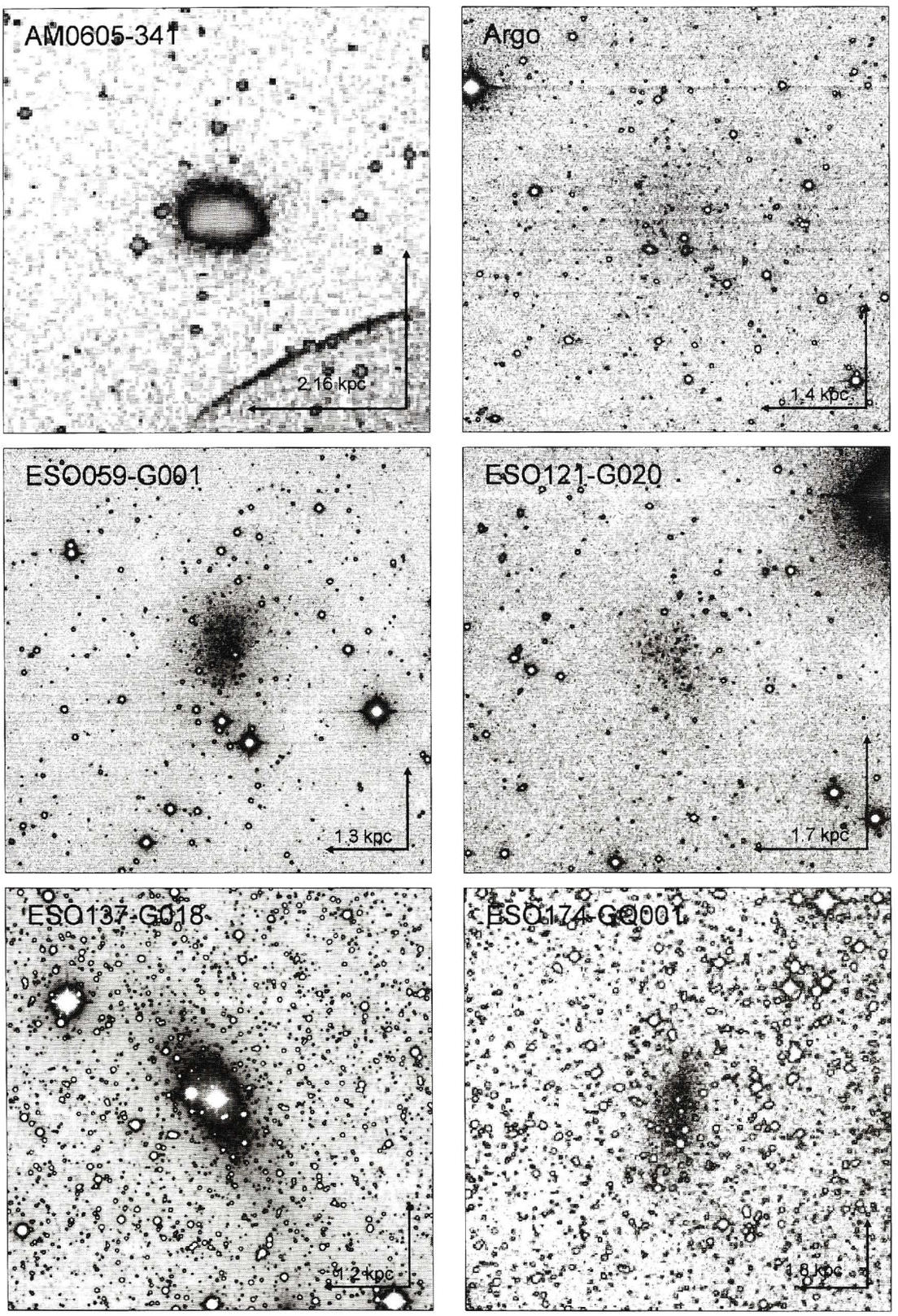


**Figure 3.1** Near-IR $H$-band image (Kirby et al., 2008), if available, for sample galaxies. For AM0605-341 and ESO174-G?001 $H$-band images are not available so the $B$-band (468 nm) DSS image is provided. Here, the scale represents 1 arcmin. The corresponding linear scale is also indicated. North is up and East is to the left. The intensity is represented by a grayscale, which goes from white (low intensity) to black (medium intensity) and then back to white (high intensity).

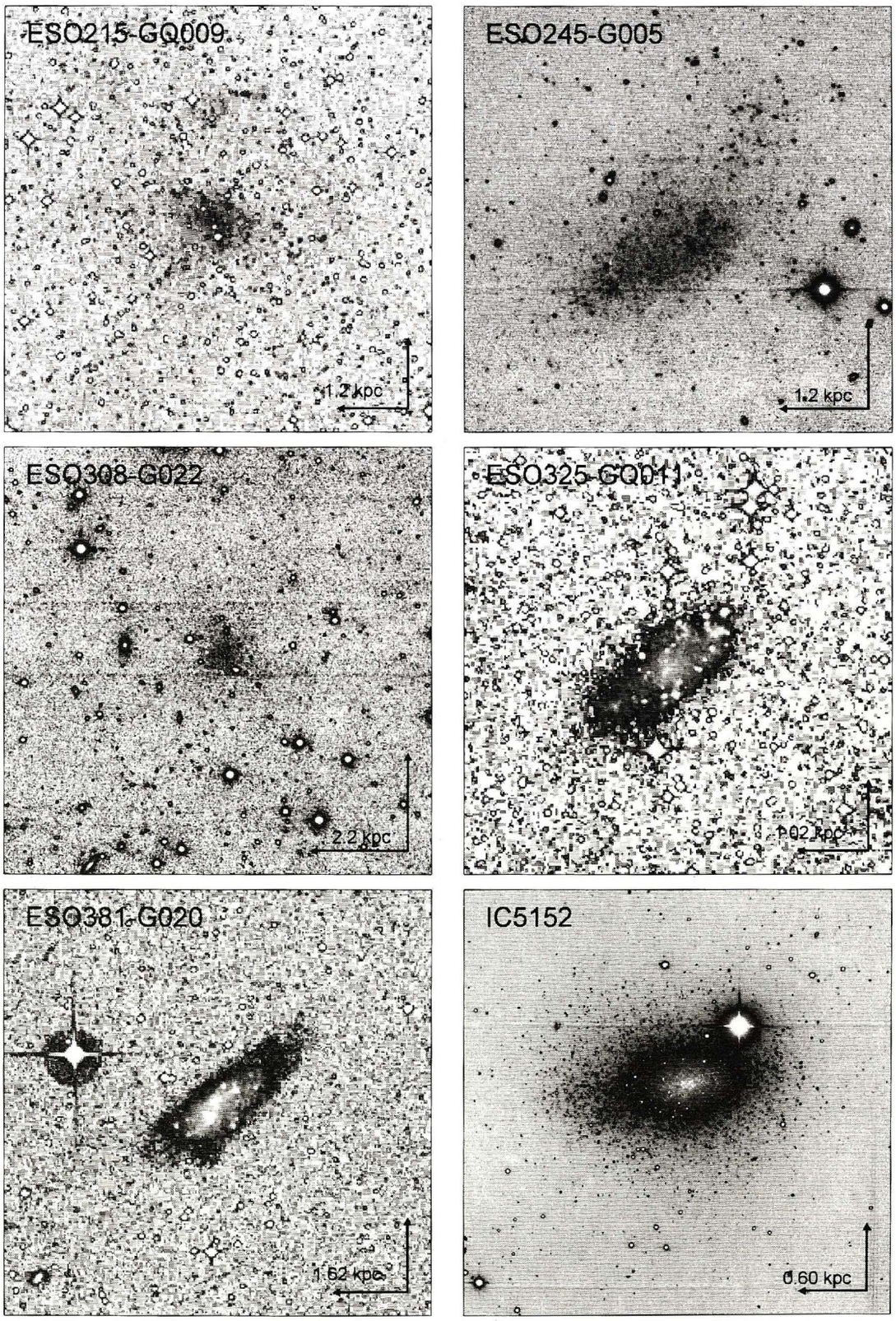


**Figure 3.2** Near-IR *H*-band image (Kirby et al., 2008), if available, for sample galaxies continued. For ESO215-G?009, ESO325-G?011 and ESO381-G020 *H*-band images are not available so the *B*-band (468 nm) DSS image is provided. Here, the scale represents 1 arcmin. The corresponding linear scale is also indicated. North is up and East is to the left. The intensity is represented by a grayscale, which goes from white (low intensity) to black (medium intensity) and then back to white (high intensity).

*Column* (8) – the total $B$-band magnitude and its source. An uncertainty of 0.2 mag is adopted.

*Column* (9) – the total $H$-band magnitude obtained from Kirby et al. (2008).

*Column* (10). - Reddening estimate, $E(B-V)$ from Schlegel et al. (1998). The associated error is 16%.

The basic H I properties for of our sample were established by HIPASS. In Table 3.2 we list:

*Column* (1) – galaxy name.

*Column* (2) – HIPASS name.

*Column* (3) – Integrated (spatially and spectrally) H I flux density, $F_{HI}$, and its uncertainty in Jansky kilometres per second.

*Column* (4) – H I heliocentric velocity, $v_{hel}$. This is the midpoint of the 50% level of peak flux (Koribalski et al., 2004).

*Column* (5) and (6) – The H I velocity line widths, $w_{50}$ and $w_{20}$, measured at the 50% and 20% level respectively.

*Column* (7) – Reference used.

*Column* (8) – The H I mass in solar units calculated as $M_{HI} = 2.36 \times 10^5 D^2 F_{HI}\ M_\odot$ (Roberts, 1975; Roberts & Haynes, 1994).

*Column* (9) – The H I mass-to-light ratio, $M_{HI}/L_{B,0}$, in solar units. Here $L_{B,0} = D^2 10^{10-0.4(m_B - A_B - M_{B,\odot})}\ L_{\odot,B}$ where $M_{B,\odot}$ is the absolute solar B magnitude taken as 5.48 (Bessell et al., 1998) and $A_B = 4.32 \cdot E(B-V)$ (Schlegel et al., 1998). The mass-to-light ratio is independent of the galaxy's distance.

**Table 3.1** Optical Properties

| Galaxy | R.A. (J2000) | Decl. (J2000) | Distance (Mpc) | Method | P.A. (degrees) | incl. (degrees) | $m_B$ (mag) | $m_H$ (mag) | $E(B-V)$ (mag) |
|---|---|---|---|---|---|---|---|---|---|
| (1) | (2) | (3) | (4) | (5) | (6) | (7) | (8) | (9) | (10) |
| AM0605-341 | 06h07m20.3s | -34d12m04s | 7.2 | H | 85[d] | 65[d] | 14.3[f] | – | 0.036 |
| AM0704-582 | 07h05m20.1s | -58d31m28s | 4.90 | TRGB[b] | 45[c] | 60[c] | 14.4[i] | 12.72 ± 0.08 | 0.119 |
| ESO059-G001 | 07h31m19.2s | -68d11m29s | 4.57 | TRGB[a] | 160[c] | 41[c] | 13.7[g] | 11.28 ± 0.06 | 0.147 |
| ESO121-G020 | 06h15m53.2s | -57d43m50s | 6.05 | TRGB[a] | 45[c] | 45[c] | 15.9[g] | 13.87 ± 0.09 | 0.040 |
| ESO137-G018 | 16h20m59.3s | -60d29m14s | 6.40 | TRGB[h] | 30[e] | 55[e] | 12.2[g] | – | 0.243 |
| ESO174-G?001 | 13h47m58.8s | -53d20m51s | 6.0 | H | 165[d] | 60[d] | 14.4[f] | – | 0.494 |
| ESO215-G?009 | 10h57m29.4s | -48d10m40s | 5.25 | TRGB[h] | – | – | 16.0[g] | – | 0.221 |
| ESO245-G005 | 01h45m04.7s | -43d35m47s | 4.43 | TRGB[b] | 127[c] | 52[c] | 12.8[g] | 11.10 ± 0.10 | 0.016 |
| ESO308-G022 | 06h39m33.1s | -40d43m13s | 7.6 | H | 130[c] | 37[c] | 16.2[g] | 13.40 ± 0.10 | 0.089 |
| ESO325-G?011 | 13h45m00.8s | -41d51m32s | 3.40 | TRGB[b] | 130[d] | 60[d] | 14.0[g] | – | 0.087 |
| ESO381-G020 | 12h46m00.4s | -33d50m17s | 5.44 | TRGB[h] | 130[d] | 40[d] | 14.2[g] | – | 0.065 |
| IC5152 | 22h02m41.3s | -51d17m53s | 2.07 | TRGB[b] | 95[c] | 50[c] | 11.1[g] | 8.26 ± 0.03 | 0.025 |

(a) Karachentsev et al. (2006), (b) Karachentsev et al. (2004), (c) Kirby et al. (2008), (d) measured independently using DSS image, (e) measured independently using a new Local Sphere of Influence Survey (Kirby et al., 2008) image. (f) Doyle et al. (2005), (g) ESO-LV catalog, Lauberts & Valentijn (1989), (h) Karachentsev et al. (2007), (i) Parodi et al. (2002)

**Table 3.2** Radio Properties from HIPASS

| Galaxy | HIPASS name | $F_{HI}$ (Jykm s$^{-1}$) | $v_{hel}$ (km s$^{-1}$) | $w_{50}$ (km s$^{-1}$) | $w_{20}$ (km s$^{-1}$) | Ref. | $M_{HI}$ ($10^8 M_\odot$) | $M_{HI}/L_{B,0}$ ($M_\odot/L_{\odot,B}$) |
|---|---|---|---|---|---|---|---|---|
| (1) | (2) | (3) | (4) | (5) | (6) | (7) | (8) | (9) |
| AM0605-341 | HIPASS J0607-34 | 9.0 ± 1.4 | 765 ± 6 | 123 | 168 | 1 | 1.1 ± 0.2 | 0.6 ± 0.1 |
| AM0704-582 | HIPASS J0705-58 | 34.8 ± 4.4 | 564 ± 2 | 68 | 84 | 2 | 2.0 ± 0.4 | 1.9 ± 0.4 |
| ESO059-G001 | HIPASS J0731-68 | 17.7 ± 2.5 | 530 ± 3 | 82 | 104 | 2 | 0.9 ± 0.2 | 0.5 ± 0.1 |
| ESO121-G020* | HIPASS J0615-57 | 14.1 ± 2.9 | 577 ± 5 | 65 | 96 | 2 | 1.2 ± 0.3 | 4.1 ± 1.0 |
| ESO137-G018 | HIPASS J1620-60 | 37.4 ± 4.9 | 605 ± 3 | 139 | 155 | 2 | 3.6 ± 0.7 | 0.16 ± 0.03 |
| ESO174-G?001 | HIPASS J1348-53 | 55.1 ± 5.9 | 688 ± 3 | 71 | 103 | 2 | 4.7 ± 0.8 | 0.7 ± 0.1 |
| ESO215-G?009 | HIPASS J1057-48 | 104.4 ± 11.5 | 598 ± 2 | 67 | 83 | 2 | 6.8 ± 1.2 | 16.8 ± 3.0 |
| ESO245-G005 | HIPASS J0145-43 | 81.0 ± 9.1 | 391 ± 2 | 60 | 85 | 2 | 3.9 ± 0.7 | 1.5 ± 0.3 |
| ESO308-G022 | HIPASS J0639-40 | 3.8 ± 1.0 | 822 ± 5 | 52 | 74 | 1 | 0.5 ± 0.2 | 1.2 ± 0.4 |
| ESO325-G?011 | HIPASS J1345-41 | 26.6 ± 3.7 | 545 ± 2 | 59 | 75 | 2 | 0.7 ± 0.1 | 1.1 ± 0.2 |
| ESO381-G020 | HIPASS J1246-33 | 30.9 ± 3.7 | 589 ± 2 | 83 | 100 | 2 | 2.2 ± 0.4 | 1.8 ± 0.3 |
| IC5152 | HIPASS J2202-51 | 97.2 ± 9.5 | 122 ± 2 | 84 | 100 | 2 | 1.0 ± 0.2 | 0.4 ± 0.1 |

(*) Warren et al. (2006) identified a nearby companion, ATCA J061608-574552, which is not resolved from ESO121-G020 by HIPASS. (1) Meyer et al. (2004), (2) Koribalski et al. (2004)

## 3.3. Observations and Data Reduction

A detailed description of the LVHIS project, including observations, data reduction and analysis as well as first results is the subject of an upcoming paper (Koribalski et al., 2010).

The H I line observations analysed in this paper were obtained with the Australia Telescope Compact Array (ATCA) as part of the LVHIS project. The data was taken between January 2005 and January 2009 using three arrays, EW352/EW367-m, 750-m, and 1.5-km (~12-h each), to ensure excellent *uv*-coverage and sensitivity to large-scale structure. Each sample galaxy was observed for a full synthesis (12-h) in each of the three arrays, unless equivalent archival observations were available. In addition, all other available archival data were used where available, including the ATCA observations in the 6km array for ESO215-G?009 (no 1.5-km were taken for this galaxy).

The first frequency band was centred on 1418 MHz with a bandwidth of 8 MHz, divided into 512 channels. This gives a channel width of 3.3km $s^{-1}$ and a velocity resolution of 4km $s^{-1}$. The ATCA primary beam is 33.6′ at 1418 MHz.

Data reduction was carried out with the MIRIAD (Multichannel Image Reconstruction, Image Analysis and Display) software package using standard procedures. Here we use the H I moment maps made using 'natural' weighting of the *uv*-data in the velocity range covered by the H I emission using steps of 4km $s^{-1}$. To obtain low-resolution maps we excluded the longest baselines, to the distant antenna six. The average synthesized beam size is 45 arcseconds.

## 3.4. Galaxy Spectra

The H I line spectra for the selected LVHIS data were obtained using the *mbspect* task in miriad. For each galaxy, the spectrum was integrated over the coordinates with detected H I emission (defined by the region of emission in the first moment map) for the entire range of observed velocities. In Figure 3.3, the LVHIS spectrum for each sample galaxy is provided (solid line) with its HIPASS spectrum for comparison (dotted line).

The HIPASS spectrum was extracted from the HIPASS datacubes. We derive the spectral parameters to ensure that an accurate comparison can be made between the HIPASS and the LVHIS data. For each galaxy we derived the HIPASS spectrum as both a point source and an extended source. The point source spectrum was extracted by considering data in a region of size 20′ × 20′, centered on the source, with each pixel weighted according to the expected beam response. The extended source spectrum was extracted for regions of consecutive sizes 24′ × 24′, 28′ × 28′, 32′ × 32′, etc, with the flux directly summed

within the region. Sources with increased flux in the extended source spectrum, were visually inspected to find the optimal spectrum, whereby the total flux was obtained with the highest signal to noise (ie, the smallest region which encapsulated the entire galaxy). Sources with no significant increase of flux in the extended source fit were considered to be point sources in HIPASS.

Various quantities have been obtained to describe the spectral properties of each galaxy. A first-order polynomial was fitted to the continuum and subtracted from each spectrum. The H I peak and integrated flux densities, the systemic velocity and the velocity widths were then computed with *mbspect*. The spectral properties for the sample galaxies obtained from the LVHIS data are listed in Table 3.3. The columns are organised as follows:

*Column* (1) – galaxy name.

*Column* (2) – the H I peak flux density, $S_{\rm peak}$ with its uncertainty given by $\sigma(S_{\rm peak})^2 = {\rm rms}^2 + (0.05S_{\rm peak})^2$, following that described in Koribalski et al. (2004) and Barnes et al. (2001).

*Column* (3) – Integrated (spatially and spectrally) H I flux density, $F_{HI}$, and its uncertainty in Jansky kilometres per second. The uncertainty has been calculated as $\sigma(F_{HI}) = 4\sigma(S_{\rm peak})/S_{\rm peak}(S_{\rm peak}F_{HI}\Delta v)^{1/2}$ (Koribalski et al., 2004; Fouque et al., 1990), where $\Delta v$ = 4km s$^{-1}$ is the velocity resolution of LVHIS.

*Column* (4) – the H I heliocentric velocity, $v_{hel}$ which has been measured as the midpoint of the 50% level of peak flux density. The uncertainty in $v_{hel}$ was calculated as $\sigma(v_{hel}) = 3\sigma(S_{\rm peak})/S_{\rm peak}(P\delta v)^{1/2}$, where $P = 0.5(w_{20} - w_{50})$ is a measure of the steepness of the profile edges (Koribalski et al., 2004; Fouque et al., 1990).

*Column* (5) and (6) – The velocity line widths, $w_{50}$ and $w_{20}$ which are the widths of the H I line profile measured at the 50% and 20% level of peak flux density respectively. The uncertainties are calculated as $\sigma(w_{50}) = 2\sigma(v_{hel})$ and $\sigma(w_{20}) = 3\sigma(v_{hel})$ following that of Schneider et al. (1986) (using the same definition as Koribalski et al., 2004).

*Column* (7) – The H I mass in solar units calculated as $M_{HI} = 2.36 \times 10^5 D^2 F_{HI} M_\odot$ (Roberts, 1975; Roberts & Haynes, 1994).

*Column* (8) – The radial extent of the observed H I compared to the stellar component given as $r_{HI}/r_{opt}$. This value was estimated by comparing the outermost isophote of the optical data (Figures 3.1 and 3.2) with the radial extent of the H I imaging. Therefore it should be noted that this value is dependent on the surface brightness limit of the optical imaging.

*Column* (9) – The ratio of the flux detected by LVHIS to the flux detected by HIPASS.

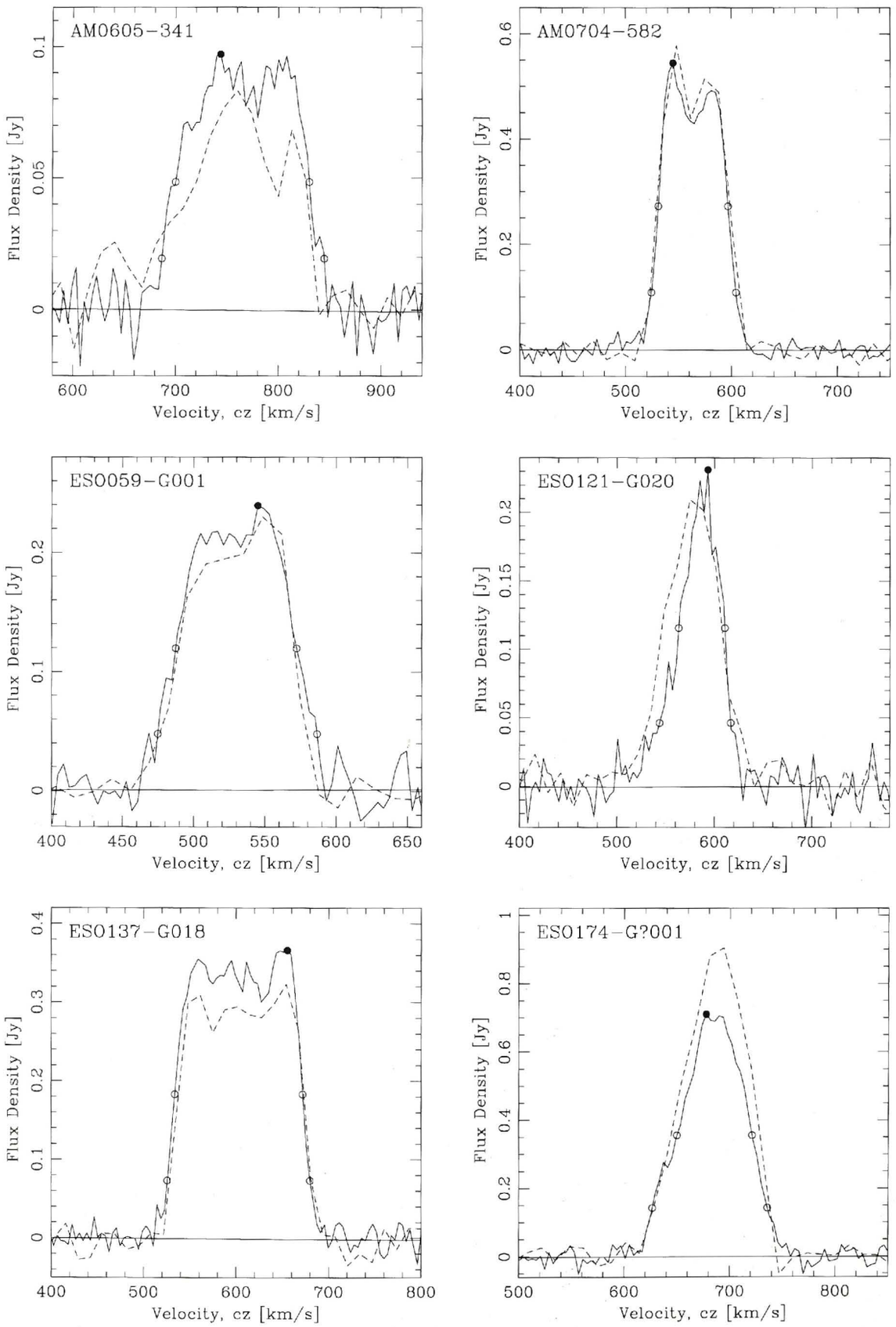


**Figure 3.3** The global HI line spectrum as obtained from LVHIS (solid line) and HIPASS (dashed line). The solid dot indicates the peak flux, and the open circles show the points used to measure the H I velocity line widths at the 50% and 20% peak flux density levels. The zero baseline is shown for the LVHIS data only.

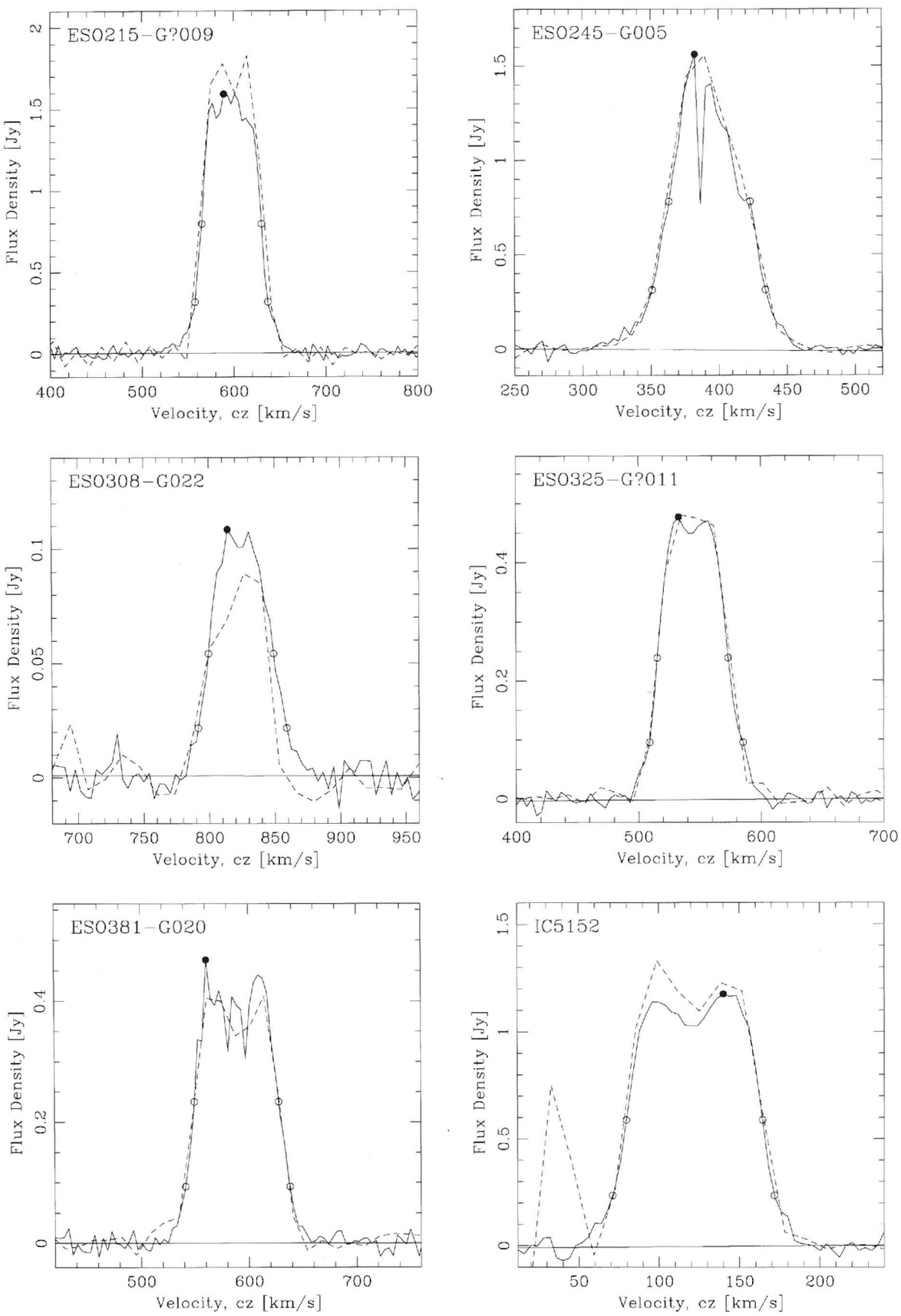


**Figure 3.4** The global HI line spectrum as obtained from LVHIS (solid line) and HIPASS (dashed line) continued. The solid dot indicates the peak flux, and the open circles show the points used to measure the H I velocity line widths at the 50% and 20% peak flux density levels. The zero baseline is shown for the LVHIS data only.

**Table 3.3** Measured ATCA H I Properties

| Galaxy | $S_{peak}$ (mJy) | $F_{HI}$ (Jykm s$^{-1}$) | $v_{hel}$ (km s$^{-1}$) | $w_{50}$ (km s$^{-1}$) | $w_{20}$ (km s$^{-1}$) | $M_{HI}$ ($10^8 M_\odot$) | $r_{HI}/r_{opt}$ | $\frac{F_{HI}(LVHIS)}{F_{HI}(HIPASS)}$ |
|---|---|---|---|---|---|---|---|---|
| (1) | (2) | (3) | (4) | (5) | (6) | (7) | (8) | (9) |
| AM0605-341 | 97 ± 5 | 11.7 ± 1.2 | 765 ± 3 | 130 ± 6 | 158 ± 9 | 1.4 ± 0.3 | 3.5 | 1.3 ± 0.2 |
| AM0704-582 | 545 ± 27 | 33.2 ± 1.5 | 564 ± 1 | 66 ± 1 | 80 ± 2 | 1.9 ± 0.3 | 4.0 | 1.0 ± 0.1 |
| ESO059-G001 | 239 ± 12 | 19.6 ± 2.2 | 530 ± 3 | 85 ± 6 | 112 ± 9 | 1.0 ± 0.2 | 2.0 | 1.1 ± 0.2 |
| ESO121-G020 | 231 ± 12 | 10.0 ± 1.2 | 587 ± 2 | 47 ± 4 | 73 ± 6 | 0.9 ± 0.2 | 2.0 | 0.7 ± 0.2 |
| ESO137-G018 | 366 ± 18 | 47.8 ± 1.5 | 603 ± 1 | 138 ± 2 | 154 ± 2 | 4.6 ± 0.7 | 3.0 | 1.3 ± 0.2 |
| ESO174-G?001 | 710 ± 36 | 48.8 ± 2.6 | 686 ± 1 | 71 ± 3 | 109 ± 4 | 4.1 ± 0.6 | 3.0 | 0.9 ± 0.1 |
| ESO215-G?009 | 1591 ± 80 | 100.9 ± 3.1 | 598 ± 1 | 65 ± 1 | 79 ± 1 | 6.6 ± 0.9 | 4.5 | 1.0 ± 0.1 |
| ESO245-G005 | 1561 ± 78 | 81.6 ± 2.6 | 393 ± 1 | 60 ± 1 | 83 ± 2 | 3.8 ± 0.5 | 2.0 | 1.0 ± 0.1 |
| ESO308-G022 | 109 ± 6 | 5.3 ± 0.8 | 824 ± 2 | 50 ± 5 | 67 ± 7 | 0.7 ± 0.1 | 2.5 | 1.4 ± 0.4 |
| ESO325-G?011 | 477 ± 24 | 27.1 ± 0.9 | 544 ± 1 | 58 ± 1 | 76 ± 2 | 0.7 ± 0.1 | 1.5 | 1.0 ± 0.1 |
| ESO381-G020 | 468 ± 23 | 33.4 ± 1.7 | 589 ± 1 | 78 ± 2 | 97 ± 3 | 2.3 ± 0.4 | 2.0 | 1.1 ± 0.1 |
| IC5152 | 1175 ± 59 | 96.4 ± 3.0 | 122 ± 1 | 85 ± 1 | 101 ± 2 | 1.0 ± 0.1 | 1.5 | 1.0 ± 0.1 |

### 3.4.1. A Comparison with HIPASS

Interferometric measurements can underestimate the total flux because of the lack of *uv*- sampling at small spatial frequencies resulting from the minimum antenna separation. Due to the missing short baselines any extended, diffuse H I emission may not have been observed by LVHIS. Thus, it is imperative that a comparison to single dish observations is made. In Figure 3.5 we show the comparison between the H I velocity line widths obtained by LVHIS and the HIPASS Bright Galaxy Catalogue (Koribalski et al., 2004). The uncertainty in the line width is calculated as $\sigma(w_{50}) = 2\sigma(v_{hel})$ and $\sigma(w_{20}) = 3\sigma(v_{hel})$. The H I line widths have been corrected for instrumental broadening using the method of Bottinelli et al. (1990). This correction is based on comparing line widths at different resolutions and is given by the linear relations:

$$w_{20,corr} = w_{20} - 0.55R \quad (3.1)$$

$$w_{50,corr} = w_{50} - 0.13R \quad (3.2)$$

where $w_{20}$ is the observed line width and $w_{20,corr}$ is the line width corrected for the instrumental resolution $R$ in km s$^{-1}$. The velocity resolution of LVHIS is 4 km s$^{-1}$ compared to the 18 km s$^{-1}$ resolution HIPASS. The average rms for the LVHIS data is 1.5 mJy compared to 13 mJy for HIPASS, thus the uncertainty in the LVHIS measurements is much lower.

The HIPASS measurement of the H I line width of ESO121-G020 (96km s$^{-1}$ at the 20% level of peak flux density) is significantly larger than the LVHIS measurement ($73 \pm 6$km s$^{-1}$). Warren et al. (2006) identified a nearby companion ATCA J061608-574552 at a projected distance of 3 arcmin from ESO121-G020. HIPASS measured these two galaxies as a single point source because the intrinsic size is much smaller than the angular resolution of 15.5 arcmin. The ATCA observations of ESO121-G020 have an angular resolution of 40 arcsec and easily resolve the galaxy pair. Thus, the HIPASS spectrum is broadened by the companion galaxy whereas the ATCA spectrum is not.

The mean difference between the HIPASS and LVHIS H I velocity line widths for all sample galaxies excluding ESO121-G020 is $-2.0 \pm 3.1$ km s$^{-1}$and $-6.1 \pm 6.2$ km s$^{-1}$(or $-0.6 \pm 5.9$ km s$^{-1}$and $-4.6 \pm 8.0$ km s$^{-1}$including ESO121-G020) at the 50% and 20% levels of peak flux density respectively. HIPASS measurements of the H I line width have a median uncertainty of 8 km s$^{-1}$ and 12 km s$^{-1}$ for $w_{50}$ and $w_{20}$ respectively. We conclude that the two HI surveys obtained consistent measurements of the H I velocity line widths, however the agreement is clearly better for $w_{50}$. We note that the use of the Verheijen & Sancisi (2001) method to correct for instrumental broadening does not change the overall results.

The HIPASS spectrum of IC5152 is contaminated by H I emission from Galactic high velocity clouds at a velocity of 33 km s$^{-1}$ with a peak flux of 0.7 Jy. Fortunately this does not overlap with the velocity range of IC5152 and does not effect

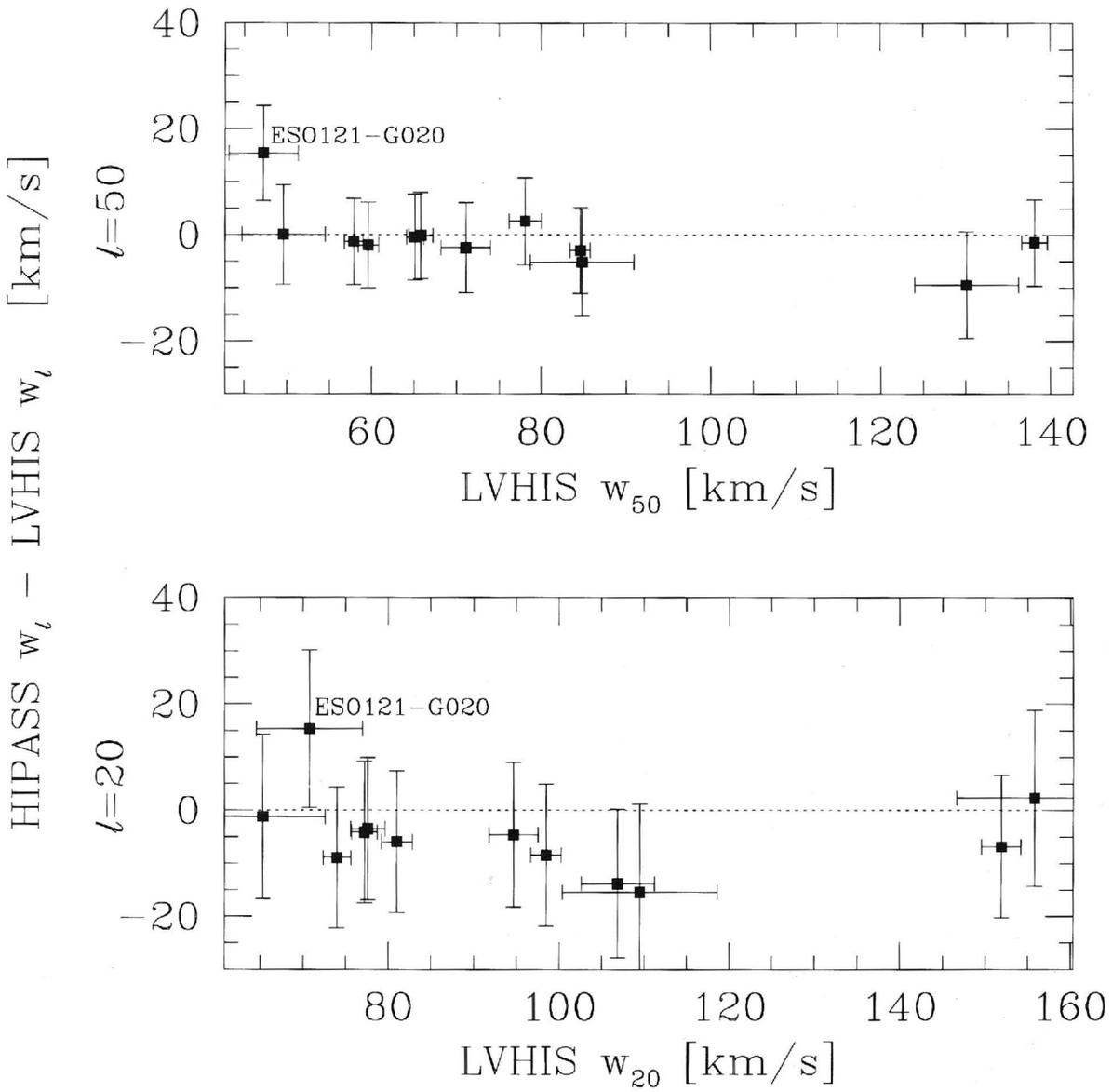


**Figure 3.5** Comparison between the derived H I velocity line widths from the LVHIS galaxies and the offset from the H I velocity line widths measured by HIPASS, corrected for instrumental broadening.

the HIPASS measurements. This is resolved and excluded from the spectrum in the LVHIS observations. The LVHIS spectrum of ESO245-G005 shows a strong H I absorption line at a redshift of 386 km $s^{-1}$. Similarly, the LVHIS spectrum of ESO381-G020 shows two weak absorption lines at 581 km $s^{-1}$ and 597 km $s^{-1}$. LVHIS measured the integrated flux density of ESO174-G?001 11% lower than HIPASS. This indicates that the interferometer filtered out the more extended, diffuse H I emission due to the missing short baselines but the flux was observed by the single dish observations of HIPASS. Note that although LVHIS measured the integrated flux density of AM0605-341 and ESO137-G018 to be higher than HIPASS, in both cases it appears to be due to uncertainty in the HIPASS baseline.

## 3.5. Rotation Curves

### 3.5.1. Fitting Procedure

The rotation curves were derived by fitting a tilted ring model to the LVHIS intensity weighted mean velocity fields. We utilised the tilted ring fitting algorithm, ROTCUR, which is incorportated in the Groningen Image Processing System (GIPSY; van der Hulst et al. 1992; Vogelaar & Terlouw 2001). The width of each tilted ring was set to 2/3 that of the synthesised beam (following that adopted by Verheijen & Sancisi 2001) with an average value of 30 arcseconds.

First, the systemic velocity and the dynamic centre of the galaxy were determined by fitting one large ring that encompasses all of the data. All data points within the ring were given equal consideration, i.e., were uniformly weighted. The uncertainty in the systemic velocity and the dynamic centre was estimated by fitting multiple tilted rings to the data and taken to be the range in the values obtained. Once the systemic velocity and dynamic centre were determined, they were kept at that value for the rest of the analysis.

Next, the kinematical position angle and inclination of the galaxy's H I disk was obtained. The data was weighted by $|\cos\theta|$, where $\theta$ is the angle from the semi-major axis of the galaxy. Hence data near the semi major axis is given the most consideration whereas data near the semi-minor axis is given the least consideration to avoid large deprojection errors. The position angle was fixed first, either to the average value for all tilted rings if appropriate, or to a general trend, if it was found to vary systematically as a function of radius. Once the position angle was fixed, the inclination was investigated. The inclination could sometimes be highly variable. Hence at this step, the inclination would either be obtained via the titled ring model, or the inclination was set such that the model has the same semi-major/semi-minor axis ratio as the observed distribution of the H I gas. We indicate in the results when the titled ring model failed and the inclination is obtained to reproduce the galaxy's axis ratio. The uncertainty in the position angle and inclination was estimated from the range in values obtained for the multiple rings fitted.

Finally, the rotation curve was obtained by fitting a final tilted ring model to the $|\cos\theta|$ weighted data with systemic velocity, dynamic centre, position angle and inclination fixed to the values obtained in the previous steps. The rotation curve for the receding and approaching sides of a galaxy were obtained separately by fixing the dynamic centre and the systemic velocity to that found when analysising the whole galaxy, and obtaining the position angle and inclination separately for each side.

To accurately obtain a true measure of the rotational velocity, the effect of pressure on the rotation curve needs to be considered (ie., an asymmetric drift correction). However, this is only important if the rotational velocity is comparable to the

velocity dispersion (Begum & Chengalur, 2003), which is not the case for our sample galaxies. Swaters et al. (2009) calculated the correction required for a sample of similar galaxies and showed that the correction is typically smaller than 3 km $s^{-1}$; less than the uncertainties in our derived velocities. Therefore we have not corrected the rotation curves for asymmetric drift.

Any deviations from the method stated above will be noted in the detailed discussion for each galaxy.

### 3.5.2. Rotation Curve Results

The rotation curve parameters obtained by the titled ring analysis for each galaxy are listed in Table 3.4. There we list:

*Column* (1). – galaxy name.

*Column* (2). – beam size, in arcsec.

*Columns* (3), (4) and (5). – equatorial coordinates with uncertainty for the dynamic centre for the epoch of J2000.

*Column* (6). – the systemic velocity.

*Column* (7). – the position angle, taken in anti-clockwise direction, between the north direction on the sky and the major axis of the receding half of the galaxy. Here if two values are given, then the position angle was found to vary as a function of radius, with the inner position angle given by the first value and the outer position angle given by the second.

*Column* (8). – the inclination of the tilted ring model. Here, for galaxies where the tilted ring model failed to obtain a solution for the inclination, the value was chosen such that the physical dimensions of the tilted ring model matched the observed distribution of the H I gas. This is indicated by listing the value obtained in parentheses.

*Column* (9). – the maximum rotational velocity obtained via the tilted ring model. The uncertainties, if given, represent the difference between the maximum rotational velocity obtained by fitting the tilted ring model to the entire galaxy and the maximum rotational velocity obtained by fitting the tilted ring model to the approaching and receding sides.

*Column* (10). – the rotational velocity at which the flat part of the rotation curve is obtained. Note that this value may be lower than the maximum rotational velocity as it is taken as the average of the flat part of the rotation curve (if sufficient data points are available).

**Table 3.4** Rotation Curve Results

| Galaxy | Beam (arcsec) | centre R.A. (J2000) | centre Decl. (J2000) | Δcentre (arcsec) | $v_{sys}$[a] (km s$^{-1}$) | P.A.[a] (degrees) | $i$[a] (degrees) | $v_{max}$[b] (km s$^{-1}$) | $v_{flat}$ (km s$^{-1}$) |
|---|---|---|---|---|---|---|---|---|---|
| (1) | (2) | (3) | (4) | (5) | (6) | (7) | (8) | (9) | (10) |
| AM0605-341 | 80 × 52 | 06h07m20.2s | -34d12m22s | 7.5 | 757 ± 2 | 274 ± 5 | (50) | 85 | A |
| AM0704-582 | 59 × 53 | 07h05m18.0s | -58d31m10s | 10.5 | 564 ± 3 | 276 ± 2 | (35) | 57 | A |
| ESO059-G001 | 51 × 47 | 07h31m18.6s | -68d11m17s | 8 | 527 ± 2 | 329 – 319 | 45 ± 10 | $61.8^{+16}_{-2}$ | B |
| ESO121-G020 | 40 × 37 | 06h15m54s* | -57d43m32s* | – | 584 ± 1 | 265 ± 5 | (40) | 48.7 | A |
| ESO137-G018 | 57 × 49 | 16h20m58.5s | -60d29m23s | 19.5 | 601 ± 2 | 33 – 28 | 50 ± 6 | $80.1^{+1.2}_{-1.3}$ | 80 ± 2 |
| ESO174-G?001 | 61 × 50 | 13h47m57.4s | -53d21m08s | 10 | 682 ± 5 | 233 – 202 | 40 ± 5 | $66^{+7.4}_{-2.1}$ | 65 ± 9 |
| ESO215-G?009 | 47 × 41 | 10h57m31.0s | -48d10m45s | 30 | 598 ± 3 | 123 – 116 | 35 ± 3 | $53.8^{+6.0}_{-5.2}$ | 54 ± 5 |
| ESO245-G005 | 71 × 48 | 01h45m06.7s | -43d36m5s | 20 | 395 ± 3 | 84 – 102 | 36 ± 6 | 47 | 47 |
| ESO308-G022 | 65 × 46 | 06h39m33.0s | -40d43m12s | 7 | 823 ± 1 | 82 ± 2 | (40) | 40 | A |
| ESO325-G?011 | 62 × 43 | 13h45m01.8s | -41d51m50s | 15 | 546 ± 5 | 302 ± 4 | 42 ± 10 | $46.0^{+3.9}_{-2.9}$ | A – B |
| ESO381-G020 | 80 × 49 | 12h46m00.0s | -33d50m11s | 10 | 587 ± 2 | 295 – 314 | 55 ± 10 | 46.7 | – |
| IC5152 | 47 × 40 | 22h02m42.3s | -51d17m 50s | 16 | 121 ± 2 | 271 – 198 | 49 ± 6 | $59.5^{+6.3}_{-5.7}$ | A – B |

(a) value for tilted ring model fitted to both approaching and receding sides, inclinations given in parenthesis indicate that the tilted ring analysis failed and the H I dimensions were used constrain this parameter; (b) the uncertainty in the measurement represents the tilted ring model for the approaching and receding sides; (A) the flat part of the rotation curve is not reached; (B) the rotation curve appears to be flattening at the outermost radii with measured rotational velocity; (*) the dynamic centre could not be fixed using the tilted ring analysis and was set to the optical centre.

The derived tilted ring models are best compared visually to the observed rotation field of the galaxy. In Figures 3.6 to 3.8, we present the observed velocity field (the first moment map), the model velocity field (the tilted ring model) and the residual field (the difference between the observed field and the model). In Figures 3.9 and 3.10 the derived rotation curve for each of the sample galaxies is presented. The derived rotation curve is presented with the solid line representing the tilted ring model fitted to the entire galaxy and the dashed lines represent the approaching and receding sides. In Figure 3.11 we show the rotation curve of all sample galaxies overlaid for comparison.

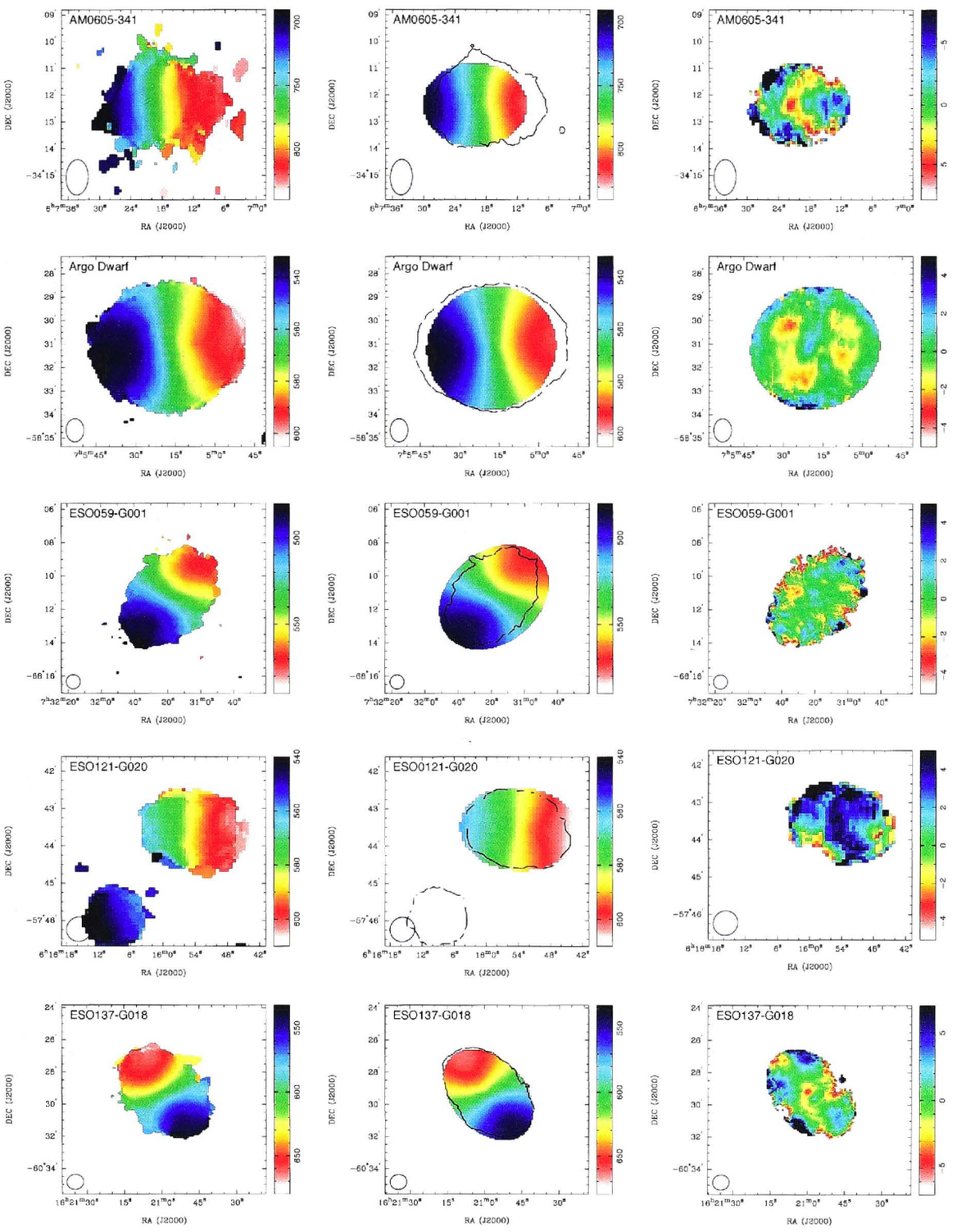


**Figure 3.6** From left to right: the HI velocity field, the derived tilted ring model, the difference between the observed velocity field and the model velocity field, and the derived rotation curve. Note that the scale on the colour bar for the residual map varies between galaxies.

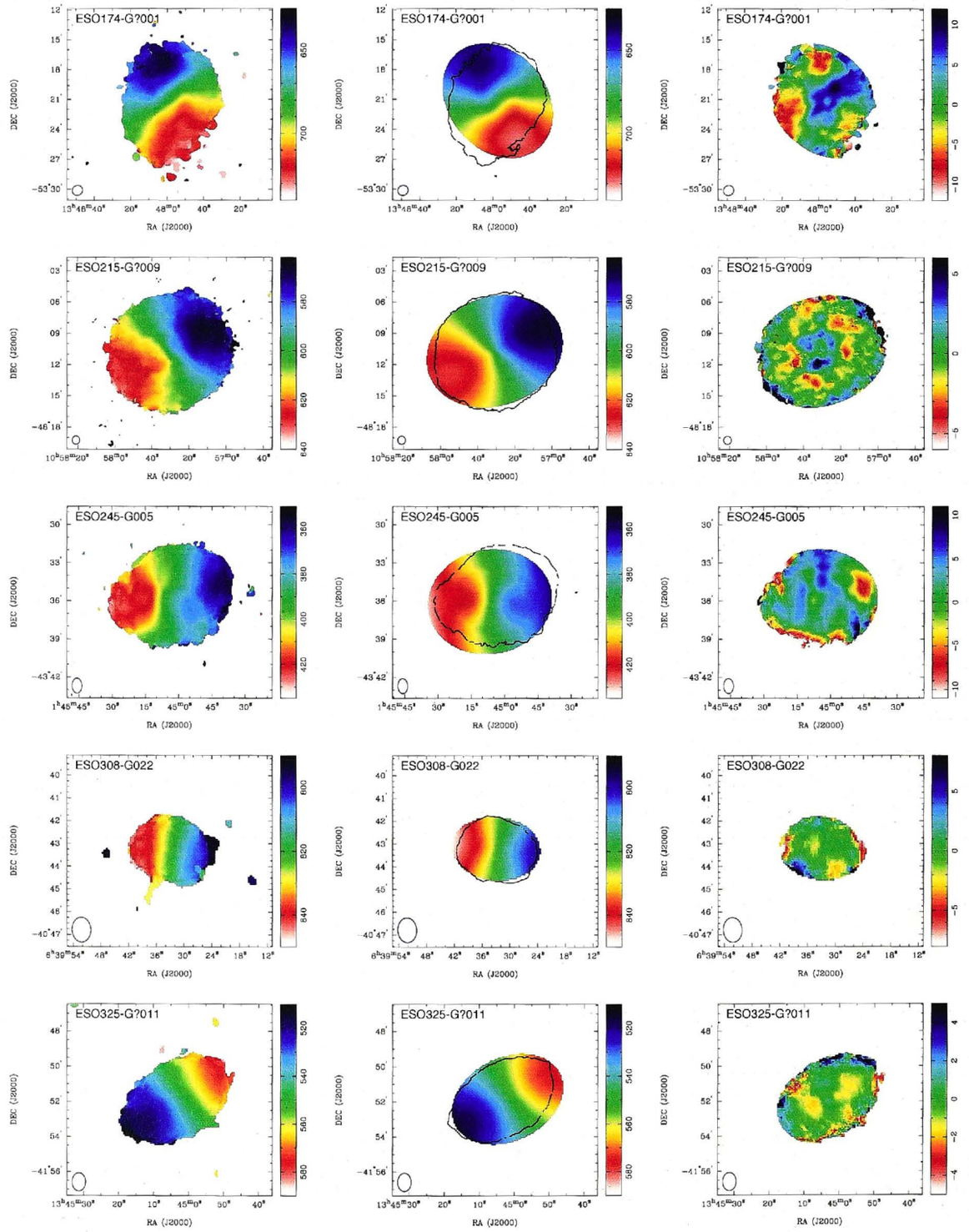


**Figure 3.7** From left to right: the HI velocity field, the derived tilted ring model, the difference between the observed velocity field and the model velocity field, and the derived rotation curve. Note that the scale on the colour bar for the residual map varies between galaxies.

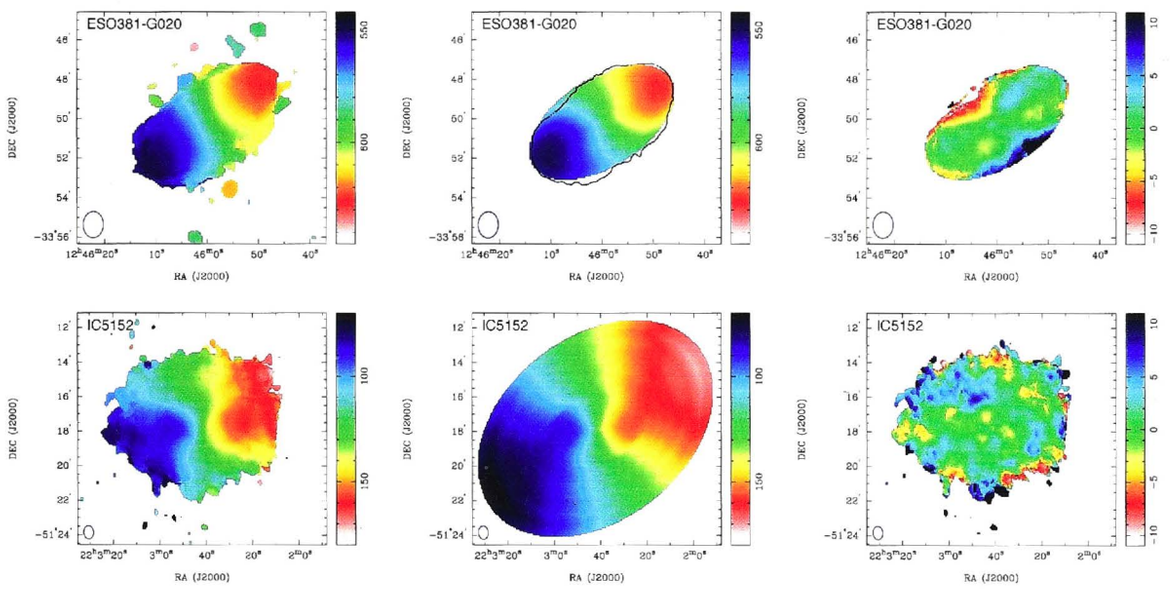


**Figure 3.8** From left to right: the HI velocity field, the derived tilted ring model, the difference between the observed velocity field and the model velocity field, and the derived rotation curve. Note that the scale on the colour bar for the residual map varies between galaxies. For IC5152, the large model is needed to fully encompass all the available data; see section 3.7.12 for a detailed discussion.

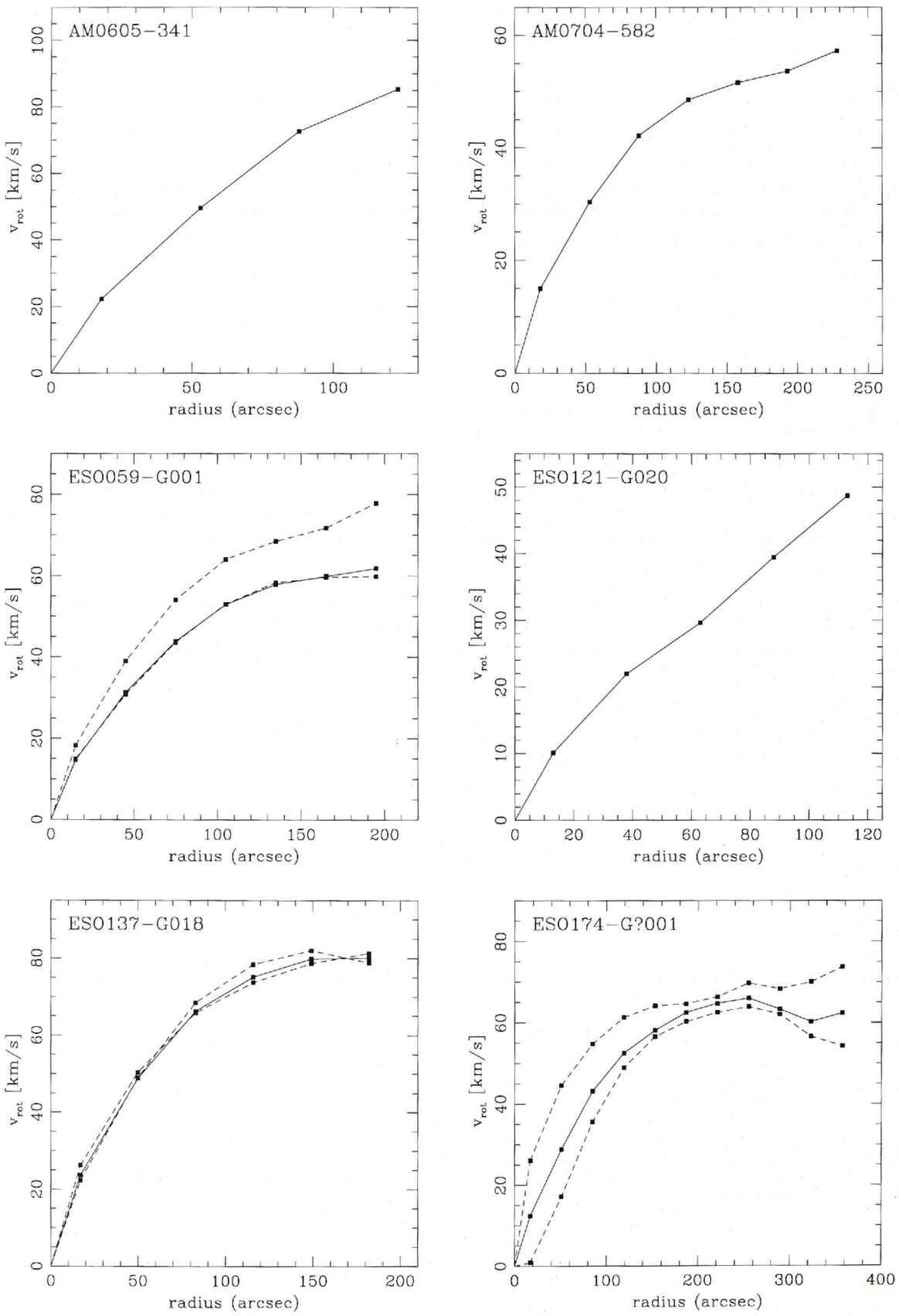


**Figure 3.9** The derived rotation curve for sample galaxies. The solid line represents the titled ring model fitted to the entire galaxy. Dashed lines are provided for some galaxies and represent the approaching and receding sides if they could be derived.

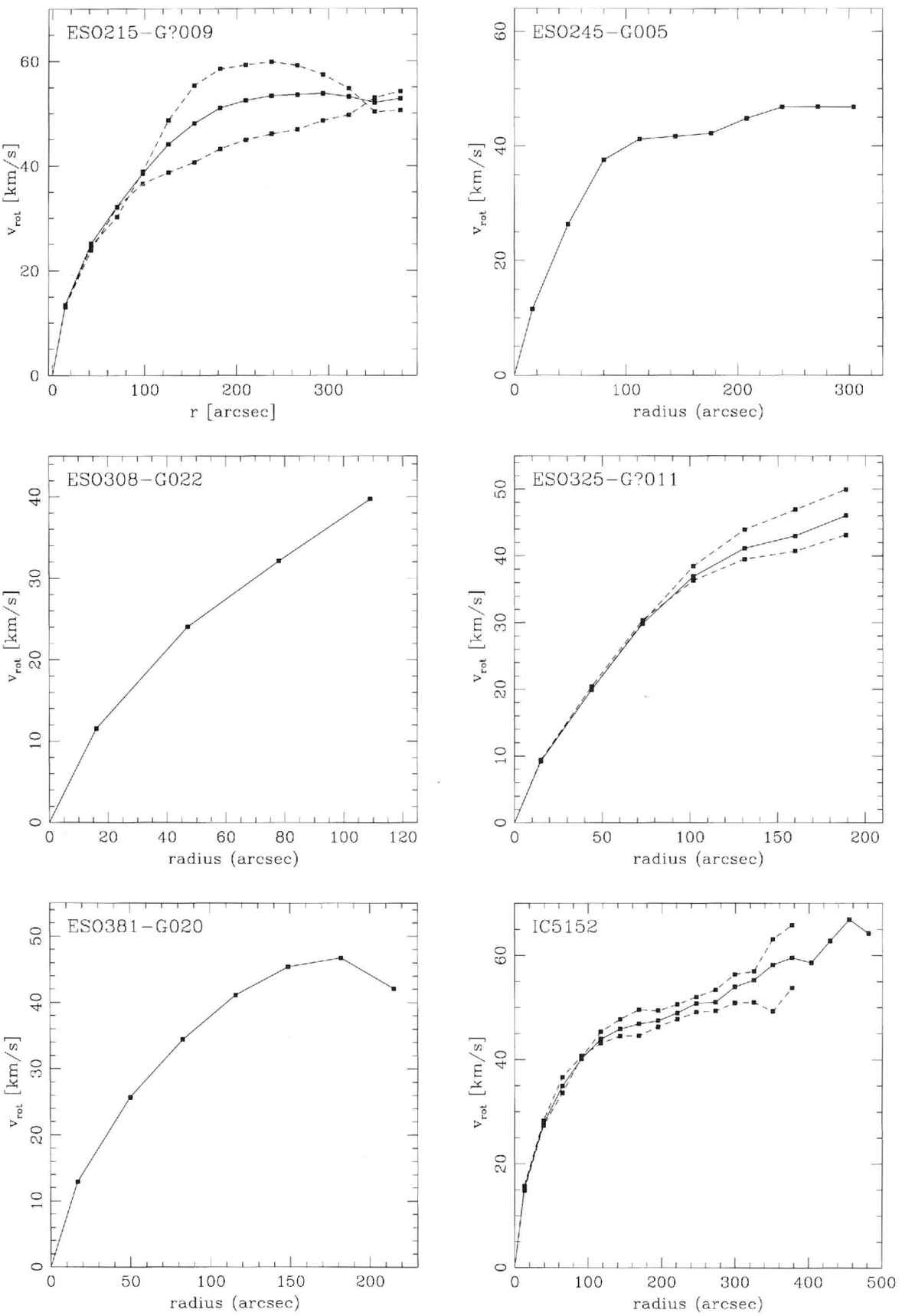


**Figure 3.10** The derived rotation curve for sample galaxies. The solid line represents the titled ring model fitted to the entire galaxy. Dashed lines are provided for some galaxies and represent the approaching and receding sides if they could be derived.

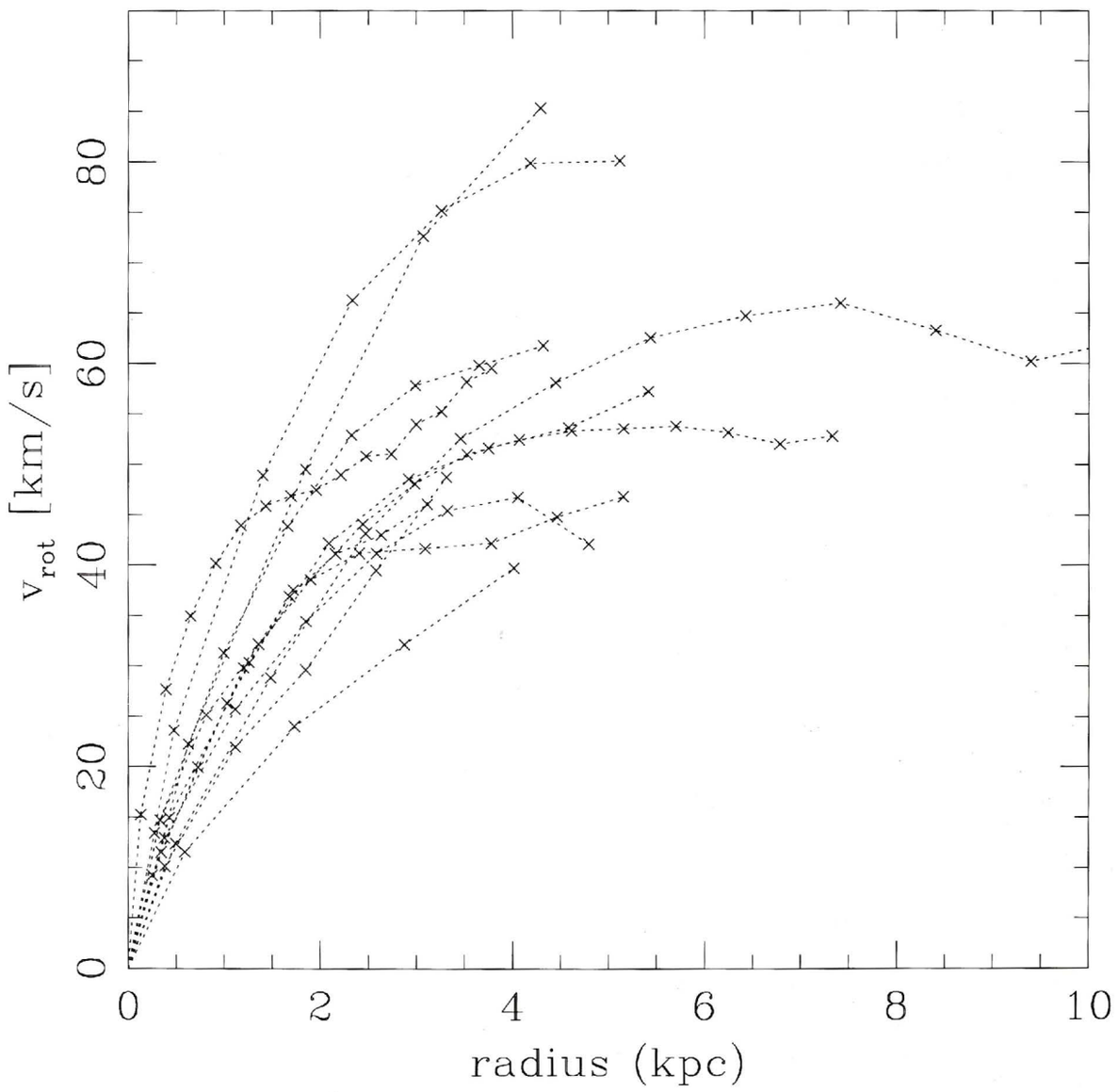


**Figure 3.11** The derived rotation curve for sample galaxies overlaid for comparison. Here, only the average rotation curve for each galaxy is presented. The rotation curves for the individual approaching and receding sides are omitted.

## 3.6. Analysis

### 3.6.1. The kinematic systemic velocity of LVHIS galaxies.

The heliocentric velocity quoted throughout the literature (eg, values taken from the Nasa Extragalactic Database, NED) for nearby galaxies is the central velocity of the H I spectrum, typically measured at the 50% level of peak flux. This is not the same as the systemic velocity derived from detailed studies of the kinematics of these galaxies. The two quantities are fundamentally different. For example, a spectrum with a classic, symmetrical, double horn profile will likely have the centre of the spectrum coincide with the true systemic velocity. However in galaxies with an asymmetric spectral profile, this may not be the case if there is inflowing gas or if their dynamic centre is not aligned with the centre of the gas distribution (axisymmetric or peculiar HI distributions). In Figure 3.12 we show the comparison between our derived systemic velocity (i.e., the centre of the tilted ring model, given in Table 3.4) and the centre of the H I spectrum where the latter is defined as the midpoint of the 50% level of the peak flux (Koribalski et al., 2004). The vertical errorbars are calculated as the sum in quadrature of the uncertainties in the derived systemic velocity and the HIPASS heliocentric velocity.

It can be seen in Figure 3.12 that the heliocentric velocities measured as the midpoint of the HIPASS spectrum are similar to the true systemic velocities measured as the centre of the tilted ring model for the sample galaxies. The two furthest outliers are ESO121-G020 and AM0605-341. The HIPASS measurement of the heliocentric velocity for ESO121-G020 is incorrect due to the inclusion of an unresolved nearby companion (Warren et al., 2006) as mentioned before. The offset of the galaxy AM0605-341 is due to the dynamic centre being offset from the centre of the H I distribution. This galaxy has an extension of redshifted atomic hydrogen, thus the heliocentric velocity measured as centre of the HIPASS spectrum is larger than the true systemic velocity. The distribution of the H I gas in AM0605-341 is discussed in further detail in section 3.7.1. Figure 3.12 shows that there is no significant difference between the centre of the H I line profile and the systemic velocity defined as the centre of the tilted ring model.

### 3.6.2. Measuring rotation velocities from H I line profiles

Information on the rotational velocities of disk galaxies are of great importance for the study of their evolution and the reconstruction of the underlying dark matter potential (see for example Bosma 1978; Rubin et al. 1978 and Bosma 1981). Key areas of research in this context are the classical and baryonic Tully-Fisher relations, two empirical relations between the luminous or baryonic mass of a spiral galaxy and its peak rotation velocity (for recent studies see Pfenniger &

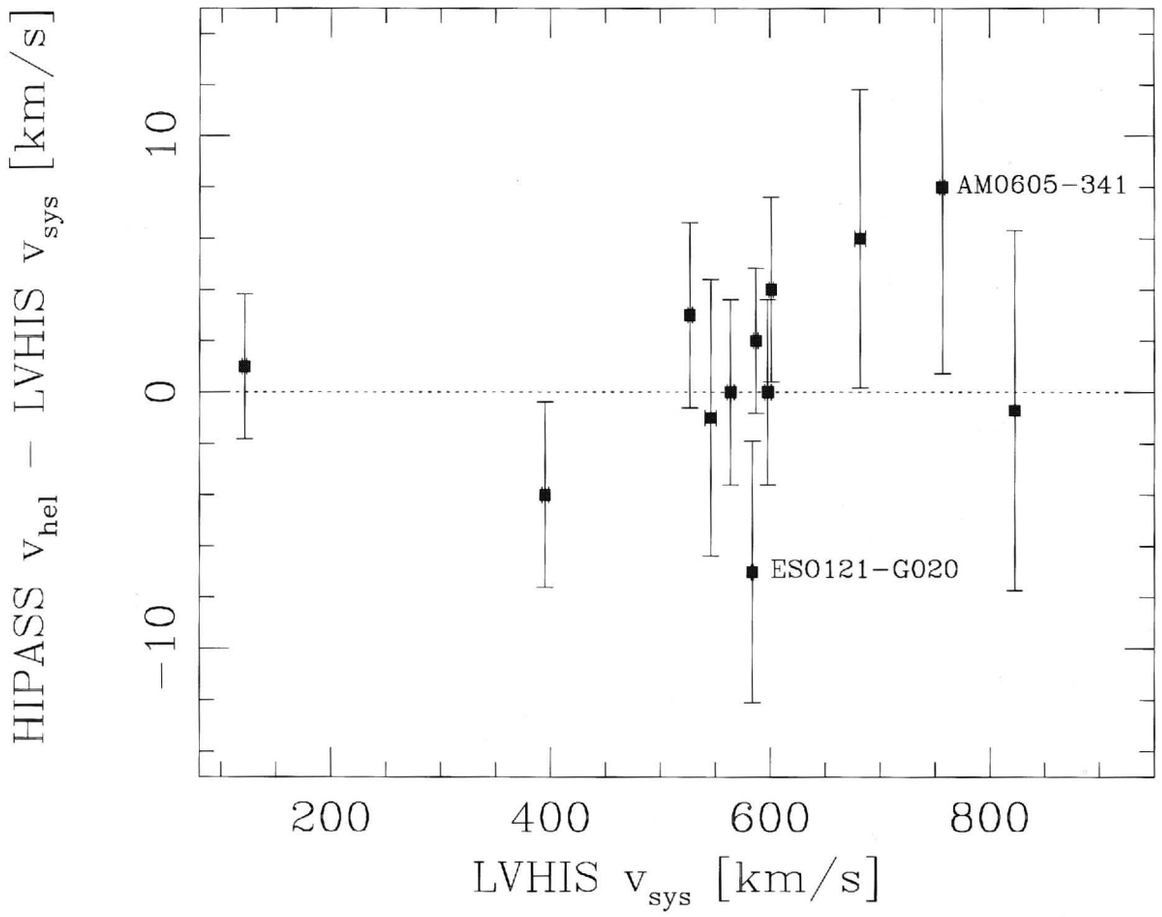


**Figure 3.12** Comparison between the derived systemic velocity from the LVHIS galaxies (the centre of the tilted ring model) and the offset from the heliocentric velocity measured by HIPASS (the midpoint of the H I line profile).

Revaz 2005; Begum et al. 2008a; Trachternach et al. 2009 and Stark et al. 2009). These relations can be used to measure distances, constrain properties of dark matter and study galaxy evolution as a function of redshift (Combes, 2009).

Due to observational limitations (ie, insufficient angular resolution) the width of the H I line profile is often used as a proxy for the rotational velocity of a spiral galaxy. Obtaining an integrated H I spectrum is a relatively straightforward process and requires minimal observing time and data analysis. Consequently, H I line profiles have been systematically measured by various HI surveys over the last decade, continuously building up a valuable database for measuring rotational velocities of galaxies in large numbers. For example, the HIPASS Survey (Barnes et al., 2001) mapped the entire southern sky ($\delta < 2°$) over a velocity range of $-1280\text{km s}^{-1} < cz < 12,700\text{km s}^{-1}$. Most galaxies are point sources in HIPASS with intrinsic sizes less than the 15.5 arcmin angular resolution (Koribalski et al., 2004), therefore the H I line width is the only measure of their rotation. This approach stands in contrast to the deep H I synthesis imaging with high resolution and good sensitivity where the data acquisition and analysis are

considerably more complex and time consuming. If the relation between H I line width and rotational velocity of the galaxy can be put on a firm ground not only could telescope time be saved but also kinematic results from 21cm observations of unresolved high redshift galaxies would be considered more reliable.

In Fig. 3.13 we show the relationship between the H I line width measured at the 50 percent ($w_{50}$, top panel) and 20 percent ($w_{20}$, bottom panel) level of peak flux density and the maximum rotational velocity, where "maximum" refers to the velocity we measured at the largest radius for each sample galaxy. We plot the line widths measured from the LVHIS spectrum (see Table 3.3) against the maximum rotational velocity obtained by the titled ring analysis (see Table 3.4). The H I line width has been corrected for instrumental broadening using the Bottinelli et al. (1990) method and de-projected adopting the inclination from our tilted ring analysis (see Table 3.4). The scatter in the data is approximately 10 km s$^{-1}$ which implies that the H I line width can not be used as a proxy for the rotational velocity if an accuracy of greater than this value is required.

In Fig. 3.13 we also show the weighted least squares fits to the data as dashed lines which are described by:

$$w_{50} = (1.1 \pm 0.2) \cdot 2v_{max} \sin i - (4.7 \pm 14.6) \quad (3.3)$$

$$w_{20} = (1.1 \pm 0.2) \cdot 2v_{max} \sin i + (9.3 \pm 15.3) \quad (3.4)$$

The slope and y-intercept of the two relations are fully consistent within the measured uncertainties, with a one-to-one relationship between the line width and the rotational velocity (ie., a slope of unity and a y-intercept = 0). The line widths measured at the 20% and the 50% level of peak flux density are highly correlated to the rotational velocity (correlation coefficient = 0.97 and 0.98, respectively).

From the tight correlations in eqns. 3.3 and 3.4 we conclude that $w_{20}$ and $w_{50}$ both are highly suitable quantities to infer the rotational velocity in the velocity range $50 < v < 150$ km s$^{-1}$. Previous studies (Corbelli & Schneider, 1997; Meyer et al., 2008) were suggesting that $w_{50}$ is the optimal quantity. This preference is not surprising as the HIPASS data on which the Meyer et al. 2008 study was based on had a much lower signal-to-noise than our data (average rms noise of 13mJy compared to 1.5mJy for our sample). Using $w_{50}$ naturally is less affected by the noise in the radio continuum. The Corbelli & Schneider (1997) study also recommended adopting the $w_{50}$ to minimize the effects of warped outer disks, a feature that was not observed in our sample.

The rotational velocity can be retrieved from the H I line widths by using equations 3.3 or 3.4 but this simple approach does not take into account possible turbulent motions within the disk, which are particularly important when studying dwarf galaxies where the maximum rotation velocities have comparable amplitudes (Patterson & Thuan, 1996). A physical model that addresses this issue was put forward by Tully & Fouque (1985). Gaussian random motions are

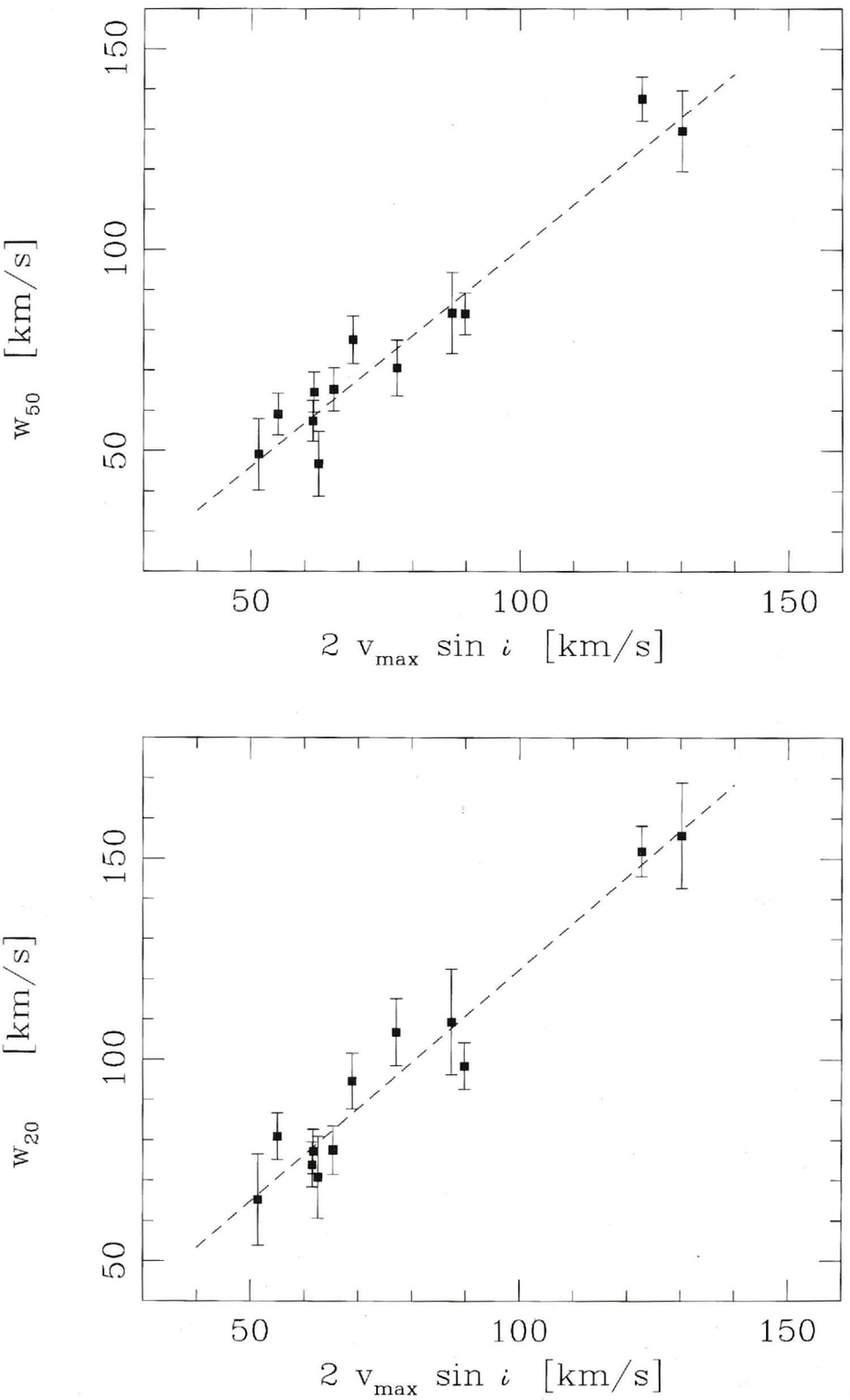


**Figure 3.13** Comparison between the derived rotational velocity using the tilted ring analysis and the H I line width measured at the 50% [top panel] and 20% [bottom panel] level of peak flux denisty. The measured H I line width has been de-projected using the inclination values from our tilted ring analysis.

subtracted linearly for fast rotators and in quadrature for dwarf galaxies using the equation:

$$\begin{aligned} v_{max}^2 &= w_l^2 + w_{t,l}^2 \left[1 - 2e^{-(w_l/w_{c,l})^2}\right] \\ &\quad -2w_l w_{t,l} \left[1 - e^{-(w_l/w_{c,l})^2}\right] \end{aligned} \tag{3.5}$$

where $l$ is the 20% or 50% level of peak flux density, $w_{t,l}$ characterises the amount of profile broadening caused by random motions and $w_{c,l}$ is chosen to give a smooth transition between the boxy shaped HI profiles of large spiral galaxies and the Gaussian profiles of dwarf galaxies. We follow Verheijen & Sancisi (2001) and adopt the values $w_{c,50} = 100\,\mathrm{km\ s^{-1}}$ and $w_{c,20} = 120\,\mathrm{km\ s^{-1}}$. Using our sample we find that the optimal values which allow an accurate retrieval of the maximum rotational velocity from the line widths to be:

$$\begin{aligned} w_{t,50} &= 2 \pm 14\ \mathrm{km\ s^{-1}} \\ w_{t,20} &= 34 \pm 10\ \mathrm{km\ s^{-1}} \end{aligned}$$

Our value of $w_{t,20}$ is slightly larger than $w_{t,20} = 22\,\mathrm{km\ s^{-1}}$ obtained by Verheijen & Sancisi (2001). However, given that no uncertainties were quoted and the large scatter in the data (approximately 50km $\mathrm{s^{-1}}$) in their plot of global profile width versus rotational velocity (see their Figure 2), it is reasonable to say that the two studies are in agreement. Our value for $w_{t,50} = 2 \pm 14\,\mathrm{km\ s^{-1}}$ is in good agreement with their value of $w_{t,50} = 5\,\mathrm{km\ s^{-1}}$ within the measured uncertainties. The two improved equations of the Tully & Fouque (1985) model with the newly derived parameters are:

$$\begin{aligned} v_{max}^2 &= w_{50,corr}^2 + (2 \pm 14)^2 \left[1 - 2e^{-(w_{50,corr}/100)^2}\right] \\ &\quad -w_{50,corr}(4 \pm 28) \left[1 - e^{-(w_{50,corr}/100)^2}\right] \end{aligned} \tag{3.6}$$

$$\begin{aligned} v_{max}^2 &= w_{20,corr}^2 + (34 \pm 10)^2 \left[1 - 2e^{-(w_{20,corr}/120)^2}\right] \\ &\quad -w_{20,corr}(68 \pm 20) \left[1 - e^{-(w_{20,corr}/120)^2}\right] \end{aligned} \tag{3.7}$$

This analysis has demonstrated that it is indeed possible to estimate the disk rotation velocity from the H I line width measurements either using the simple model given by equations 3.3 and 3.4 or equations 3.6 and 3.7 when broadening by turbulent motions is a concern. However, there is considerable scatter in Figure 3.13 making resolved observations essential if an accuracy of greater than $\sim 10\,\mathrm{km\ s^{-1}}$ in the rotational velocity measurement is required. It is important to note that the rotational velocity derived is not necessarily the peak velocity of the galaxy disk because HI observations for low surface brightness dwarf galaxies often lack the sensitivity to trace the H I emission in the low column density regime, typically a few galactic-disk scale radii where the rotation curve becomes flat. Finally, the above discussion regarding the calculation of the

rotational velocity from the H I line width is valid for galaxies in the nearby Universe. Measurements for galaxies at higher redshifts require an extra line width correction to take into account relativistic broadening of the H I profile using the standard factor of $(1 + z)$.

## 3.7. Individual Galaxies

### 3.7.1. AM0605-341

AM0605-341 is a nearby ($D = 7.2$ Mpc) magellanic type spiral galaxy (see Figure 3.1). It has a structureless stellar disk and a very bright bar (Matthews & Gallagher, 1997), possibly with a starburst nucleus (Matthews & Gallagher, 2002). This galaxy forms a small ensemble with the late-type spiral NGC2188 (separation of 35.6 arcmin and 18km $s^{-1}$) and the irregular galaxy ESO364-G?029 (separation of 70.2 arcmin and 22km $s^{-1}$).

The small angular diameter of AM0605-341 ($\sim$ 4 arcmin) makes resolved H I imaging extremely difficult to obtain. Previous H I observations (Gallagher et al., 1995; Matthews et al., 1998; Meyer et al., 2004) have been from single dish telescopes and were able to measure only a point source spectrum. Our H I synthesis imaging of AM0605-341 thus reveals the atomic hydrogen distribution for the first time.

We find an asymmetric H I distribution with respect to the optical and dynamic centres (see Figure 3.6). There is an extension of redshifted H I located to the west of the galaxy. This is opposite to the direction of NGC2188 (located to the east of AM0605-341). Domgoergen et al. (1996) have already noticed that NGC2188 shows a similar extension directly opposite to AM0605-341. These authors suggested that the extension observed in NGC2188 is unlikely to be due to some interaction. However, they identify only ESO364-G?029 as a potential disturber although they do point out that an interaction with an unknown neighbour was possible. We propose that the extensions of NGC2188 and AM0605-341 are of tidal origin due to their interaction. The angular distance of the two galaxies is 77 kpc.

There is no distortion to the AM0605-341 velocity field indicating a bar feature. However the bright bar observed by (Matthews & Gallagher, 1997) is smaller than the synthesized beam, so the non-detection in the H I is to be expected.

We derive a H I rotation model in Figure 3.6. Because of the galaxy's small angular size, the inclination measurement did not converge using a tilted ring model. Thus a value was chosen such that the model had the same semi-major and minor dimensions as the observed H I distribution. This corresponds to an inclination of 50 degrees which was adopted to derive the AM0605-341 rotation curve. Setting the inclination to slightly higher or lower values ($\pm$10 degrees)

does not significantly increase the residual difference between the observed H I velocity field and the model due to the degeneracy between the rotational velocity and the inclination (Begeman, 1989). Also, the chosen inclination is higher than the optical inclination of 26 degrees from Matthews & Gallagher (2002). A rotation curve could not be obtained separately for the approaching and receding sides of the galaxy.

A $H_\alpha$ position velocity curve was measured for AM0605-341 out to $r = 20''$ by Matthews & Gallagher (2002) who concluded that the galaxy must have extended H I and reach its maximum rotational velocity well outside its stellar disk. Our result, with the rotation curve still increasing at the observed H I column density limit ($r = 120''$), is in good agreement with the Matthews & Gallagher result.

### 3.7.2. AM0704-582/ Argo

The near-IR image of the Argo dwarf (Figure 3.1, top panel, second to left) shows a very low surface brightness galaxy with no visible structures such as a bar or spiral features. The optical emission appears very extended and has almost no compact region (Parodi et al., 2002). The galaxy is extremely isolated in space with a tidal index of -2 using the Karachentsev & Makarov (1999) measure of interaction. The atomic hydrogen emission of this galaxy has been observed previously by HIPASS (Koribalski et al., 2004) and a point source spectrum was obtained. Here we present the first resolved H I synthesis imaging of the Argo Dwarf.

Our H I map reveals a regular velocity field. We also see that the peak integrated density is offset from the centre of the H I emission. The stellar component is located at the centre of the H I emission which is also the location of the dynamic centre as derived by our rotation curve analysis.

The orientation parameters of the H I disk are inconsistent with orientation parameters for the stellar disk in the literature, but this is due to the large uncertainty in the optical measurements rather than a detection of a warp. The position angle of the H I disk derived by rotation curve fitting was effectively constant as a function of radius and determined at 276±2 degrees. This is different to the values of 225 degrees (Kirby et al., 2008) and 354 degrees (Parodi et al., 2002) however due to the extreme low surface brightness of the optical emission, these values have considerable uncertainty. Hence deeper optical imaging is required to determine whether the optical position angle and H I position angle are aligned. We found that the inclination could not be determined using the tilted ring analysis. Thus the inclination was chosen so that the model had the same semimajor and semiminor dimensions as the observed HI distribution. This yielded an inclination of 35 degrees which was used to derive the rotation curve. Once again, it should be noted that the inclination and the rotational velocity are degenerate parameters (Begeman, 1989), therefore changing the inclination

does not significantly change the residual difference between the observed H I velocity field and the model. Kirby et al. (2008) measured the inclination of the outermost isophote to be 65 degrees by fitting ellipses as a function of radii, however once again, it should be noted that due to the extreme low surface brightness, this value has considerable uncertainty.

The kinematic model obtained by rotation curve analysis is in good agreement with the observed velocity field. The typical differences between the observations and the model are less than 4km $s^{-1}$. A rotation curve could not be obtained separately for the approaching and receding sides of the galaxy.

### 3.7.3. ESO059-G001

ESO059-G001 is an isolated low-surface brightness dwarf irregular galaxy 4.57 Mpc away from the Milky Way (Karachentsev et al., 2006). The galaxy has a tidal index of −1.5 using the Karachentsev & Makarov (1999) measure of interaction. Parodi et al. (2002) found rudiments of spiral arms in their *B*-band imaging which were subsequently confirmed by ACS-HST imaging (Karachentsev et al., 2006). Helmboldt et al. (2004, 2005) reported two HII regions and a total H$\alpha$ flux of $\log(F_{H\alpha}) = -12.19\,\mathrm{ergs\,s^{-1}\,cm^{-2}}$.

An H I point source spectrum was initially obtained by HIPASS (Koribalski et al., 2004) while our resolved H I synthesis image of ESO059-G001 reveals details of the atomic hydrogen distribution for the first time. The galaxy shows a regularly rotating H I velocity field. The kinematic model obtained by the rotation curve analysis is in excellent agreement with the observed velocity field with a typical residual less than 4km $s^{-1}$. We found that the inclination varied between 35 and 55 degrees with no clear trend. Thus the inclination was set to 45 degrees. We also note that this average value optimised the dimensions of the model compared to the observed H I distribution. The receding side has a similar rotation curve as the overall rotation curve (with a model position angle of 326 ± 6 degrees and an inclination of 45 ± 10 degrees) whereas the approaching side was found to have a 25 percent higher rotation at the largest radius (with a model position angle of 324 ± 4 degrees and an inclination of 35 ± 10 degrees).

### 3.7.4. ESO121-G020

ESO121-G020 is a dwarf irregular galaxy located 6.05 Mpc from the Milky Way. The galaxy is about 2.6 mag fainter in the near-IR than ESO059-G001. It has a small companion, ATCA J061608-574552, located approximately 3′ to the south east. Warren et al. (2006) detected neither an H I nor a stellar bridge between the two galaxies.

The galaxy ESO121-G020 was analysed using new LVHIS data and ATCA archival data that was originally obtained by Warren et al. (2006). The combined data set

easily resolves the two galaxies in angular and velocity space. A slight distortion is observed in the southeastern region of the velocity field most likely caused by the companion, however the strength of this feature is low compared to the overall bulk rotation. The companion galaxy was masked from the data during the kinematic analysis of ESO121-G020.

The dynamic centre could not be obtained with the help of a tilted ring model and was thus assumed to be the optical centre. This assumption was justified by the observation that the dynamic centres for all galaxies in our sample agree with the optical centres as defined by the outermost isophotes (see Trachternach et al. 2008 for similar result). In contrast to the Warren et al. (2006) kinematic model, the inclination value was statistically unstable. The value of $78 \pm 5$ used by Warren et al. implies that the galaxy would be almost edge-on which is clearly not the case (see Figure 3.6). This discrepancy was investigated more closely and we concluded that the high inclination obtained by Warren et al. was in fact the result of fitting a small number of data points rather than a genuine better fit. The HI image had very low resolution and the fitting routine tended to higher inclination values to reduce the number of data points used in the fitting process. While the residuals were lower, this was a direct consequence of comparing fewer data points, not that the obtained model was intrinsically more accurate. We choose to model ESO121-G020 by keeping the inclination fixed at 40 degrees which results in a model with the same semimajor and semiminor dimensions as the observed HI distribution.

The overestimation of the inclination in the Warren et al. result has a direct effect on some of the values quoted in their paper. We measure a rotation velocity of 36km $s^{-1}$ at the maximum radius of 80 arcsec compared to their value of 21km $s^{-1}$. At our outermost radius (113 arcsec) we measure a rotation velocity of 49km $s^{-1}$ with the rotation curve still rising. These new parameters and the improved TRGB distance measurement (Karachentsev et al., 2006) imply that the lower limit for the dynamical mass is $1.7 \times 10^9$ $M_\odot$ ($M = v^2 r G^{-1}$). Using the Warren et al. (2006) total *B*-band luminosity of $(2.39 \pm 0.13) \times 10^7$ $L_\odot$, we get a lower limit for the dynamical mass-to-light ratio of $\sim 70$ $M_\odot/L_\odot$ suggesting that this galaxy is a dark matter dominated object. Other low luminosity dwarf galaxies are known to have mass-to-light ratios similar to this and higher (see for example ESO215-G?009 which has a dynamical mass-to-light ratio of $200 \pm 110$ $M_\odot/L_\odot$, Warren et al. 2004)

The incorrect inclination obtained by Warren et al. (2006) highlights the need for visual inspection of the model rotation field compared to the observed rotation field. This is particularly important for upcoming surveys in the Square Kilometre Array (SKA) era, where due to the sheer volume of data automated pipelines will be employed to do rotation curve fitting.

### 3.7.5. ESO137-G018

ESO137-G018 is an isolated late-type galaxy of type Sm or Im located behind the Galactic plane ($b = -7.4°$). It has several bright superimposing foreground stars (Figure 3.1) and hence the optical properties are poorly constrained. The current distance estimate ($D = 6.4$ Mpc) is based on the TRGB magnitude (Karachentsev et al., 2007).

The only previously available H I observations of ESO137-G018 were obtained by HIPASS (Koribalski et al., 2004) which measured point source spectrum. Our H I synthesis observations show that the integrated density field is very symmetric about the major and minor axes of the galaxy. The velocity field resembles an undisturbed, regularly rotating system. The kinematic model obtained by rotation curve analysis is in good agreement with the observed velocity field. The typical velocity residuals are less than 5km $s^{-1}$. Our rotation curve shows that the H I is tracing the galaxy out to the radius at which the peak rotation velocity at $80 \pm 2$km $s^{-1}$ is reached.

We find that the position angle of ESO137-G018 decreases from 33 to 28 degrees, but the inclination is steady at $50 \pm 6$ degrees. The position angle on the approaching and receding sides are well constrained at $30 \pm 2$ and $33 \pm 2$ degrees, respectively. The inclination on the approaching and receding sides are $50 \pm 7$ and $48 \pm 4$ degrees, respectively. Thus the approaching and receding sides of ESO137-G018 exhibit similar kinematic behaviour.

### 3.7.6. ESO174-G?001

ESO174-G?001 is a nearby ($D = 6$ Mpc) low-surface brightness (LSB) galaxy located near the Galactic plane ($b = 8.6°$). The galaxy is a member of the Centaurus A Group (Banks et al., 1999) and has poorly constrained optical properties. The optical image of ESO174-G?001 shows a uniform and elongated distribution of stars[3].

Previous H I studies of this galaxy (Banks et al., 1999; Huchtmeier et al., 2001; Koribalski et al., 2004) have been from single dish telescopes and were only able to measure a point source spectrum. Here we present the first resolved H I imaging of ESO174-G?001. We observe a disturbed H I velocity field (Figure 3.7). The kinematic major axis of ESO174-G?001 is not perpendicular to the kinematic minor axis indicating that the gas is moving in elliptical orbits in the plane of the galaxy (Bosma, 1978; Simon et al., 2003). Thus it was to be expected that the tilted ring model will not accurately reproduce the observed velocity field. It should be noted that a tilted ring model was fitted to a galaxy showing

[3]Note that the optical image currently available in NED is incorrect. The optical image available is that of ESO174-G001 (not ESO174-G?001) which has the coordinates 13h33m19.7s, −53d21m17s.

non-circular motions, which means that the derived rotational velocity is likely to have been underestimated (Rhee et al., 2004; Oh et al., 2008). While a rotation curve could be derived, the residual between the observed velocity field and the model velocity field in some areas was up 11km $s^{-1}$, almost 3 times higher than the velocity resolution. The flat part of the rotation curve was reached.

The rotation curve was derived for the approaching and receding sides of the galaxy. It was found that the position angle decreased from 233 to 202 degrees as a function of radius both for the individual sides and for the galaxy as a whole. The position angle of the H I is not aligned with the position angle of the stellar component (165 degrees). The inclination was found to be $40 \pm 5$ degrees overall or $46 \pm 7$ and $40 \pm 5$ degrees on the approaching and receding sides, respectively, which is lower than the inclination of the stellar component (60 degrees).

### 3.7.7. ESO215-G?009

ESO215-G?009 is a LSB galaxy located near the Galactic plane. Warren et al. (2004) have studied the optical and H I properties of this galaxy extensively and we refer the reader to their study. They found that ESO215-G?009 has a H I mass-to-light ratio of $22 \pm 4$ $M_{\odot}/L_{\odot,B}$, the highest known for any galaxy. We modeled the kinematics using a tilted ring analysis and our results are generally consistent with those of Warren et al. (2004).

It is interesting to note that although the velocity field of ESO215-G?009 was reasonably well modeled, the ellipticity of the model does not agree well with the observed H I distribution. The highly circular gas distribution suggests that the galaxy must have an inclination of approximately 20 degrees but this is inconsistent with the high line-of-sight rotation ($w_{20} = 79 \pm 1$km $s^{-1}$) and the derived inclination of the model ($35 \pm 3$ degrees). This may well be evidence that the assumption of the gas being located in an infinitely thin disk is incorrect. Such extraplanar H I was first observed in NGC891 (Swaters et al., 1997) and has since been observed in other nearby galaxies (Boomsma et al., 2005; Hess et al., 2009). Any extension of gas along the vertical component of the disk will naturally result in an increase of the observed semi-minor axis and could explain the highly circular observed distribution of H I gas in ESO215-G?009.

### 3.7.8. ESO245-G005

ESO245-G005 is a barred magellanic galaxy located 4.4 Mpc away from the Milky Way. It has a star formation rate of $0.02 M_{\odot}\,\mathrm{yr}^{-1}$ (Oey et al., 2007). Côté et al. (2000) suggest that due to a strong abundance oxygen gradient along the bar (oxygen abundance changes by a factor of three; Miller 1996), either an H I cloud of a different metallicity has been accreted or that the whole object is the product of a recent merger. Côté et al. (2000) have obtained H I synthesis imaging and

observed a very peculiar velocity field. Despite the indications that ESO245-G005 has had past interactions, no shock waves are detected through the study of its diffuse ionised gas (Hidalgo-Gámez, 2006).

Our H I imaging shows that the integrated density field has several regions of peak flux density. The velocity field is disturbed. A kinematic model was derived by tilted ring analysis but the residual between the observed velocity field and the model velocity field in some areas was up 10km $s^{-1}$.

We find evidence that ESO245-G005 has a warp in its outer regions. At a radius of $r \approx 200$ arcsec there is a rise in inclination and an associated change in the position angle. The detection of a warp gives further support to the Côté et al. (2000) hypothesis that ESO245-G005 has undergone recent accretion (Ostriker & Binney, 1989; Jiang & Binney, 1999).

The H I position angle was found to be steady at 84 degrees in the inner portion of the galaxy ($r < 200$ arcsec) then increased to 102 degrees in the outer regions. This is not aligned with the position angle of the stellar disk (127 degrees; Kirby et al. 2008). The H I inclination was modeled $36 \pm 6$ degrees which is also not aligned with the inclination of the stellar disk (52 degrees; Kirby et al. 2008). The H I inclination increases and becomes highly variable in the outer parts ($56 \pm 12$ degrees for $r > 200$ arcsec). Due to this variability, the entire galaxy was modelled using the inclination derived for the inner region. Kinematic modelling could not be achieved for the approaching and receding sides separately.

The H I kinematics of ESO245-G005 has been studied previously by Côté et al. (2000) whose results differ somewhat from those presented here. Côté et al. (2000) observed a similar trend in position angle however chose to model the position angle as a constant value of $88 \pm 8$ degrees. They find a higher inclination of $54 \pm 10$ degrees which is similar to that which we obtain for the inclination at larger radii.

### 3.7.9. ESO308-G022

ESO308-G022 is a dwarf irregular galaxy located ~ 7.6 Mpc away from the Milky Way. The deep near-IR image (see Figure 3.1) shows an extended stellar distribution with no visible structures such as a bar or spiral features. The optical image of Parodi et al. (2002) shows an extended and diffuse galaxy with a few regions of brighter emission.

The new LVHIS H I synthesis imaging of ESO308-G002 reveals the atomic hydrogen distribution for the first time. Previous H I observations (Matthews et al., 1995; Huchtmeier et al., 2000; Meyer et al., 2004) of this galaxy have been obtained by single dish telescopes and were only able to measure a point-source spectrum. Our H I imaging is able to resolve ESO308-G002 despite its small angular diameter (~ 4 arcmin).

The kinematic model obtained by rotation curve analysis is in good agreement with the observed velocity field. The typical differences between the observations and the model are less than 6km $s^{-1}$. A rotation curve could not be obtained separately for the approaching and receding sides of the galaxy. The rotation curve does not flatten at the last points measured suggesting that the H I is not tracing the galaxy out to the radius at which the maximum rotation velocity is reached.

Due to the small angular diameter of ESO308-G022 our observations have low resolution and the inclination could not be determined using a tilted ring model. Thus it was chosen such that the model had the same semi-major and semi-minor dimensions as the observed HI distribution (40 degrees). The position angle was found to be constant at 82 ± 2 degrees. This is inconsistent with measurements of the position angle of the stellar disk (130 and 160 degrees by Kirby et al. 2008 and Parodi et al. 2002 respectively). However, the alignment parameters for the stellar component have considerable uncertainty as the galaxy has very low surface brightness. Therefore, deeper near-IR or optical imaging is required before the alignment between the stellar and H I disks can be confirmed.

### 3.7.10. ESO325-G?011

ESO325-G?011 is a dwarf irregular galaxy and a member of the Centaurus A Group. It has a TRGB distance of 3.4 Mpc which is consistent with its group membership (Karachentsev et al., 2002a). The optical image shows that the stellar distribution is asymmetric; the central area of highest surface brightness is offset from the centre defined by the outer isophotes.

The atomic hydrogen of this galaxy has been observed on numerous occasions with both single dish telescopes (Longmore et al. 1982; Huchtmeier & Richter 1986; Côté et al. 1997; Banks et al. 1999; Koribalski et al. 2004) and with H I synthesis imaging (Côté et al., 2000). While the Côté et al. (2000) imaging was able to resolve the atomic hydrogen distribution of ESO325-G?011, their data had significantly lower sensitivity with an rms noise of 4.6 mJy $beam^{-1}$ than the LVHIS value of 1.3 mJy $beam^{-1}$.

Our H I imaging shows that the integrated density is asymmetric with the peak flux density offset from the centre of the H I emission. The position of the peak integrated density is located at the position of the optical core. ESO325-G?011 has an extremely regular velocity field. The kinematic model obtained by the rotation curve analysis is in excellent agreement with the observed velocity field. The typical differences between the observations and the model are less than 2km $s^{-1}$, the lowest for all galaxies in our sample.

We find that the optical position angle is aligned with the H I position angle. The H I inclination (42 ± 10 degrees) is lower than that of the stellar component (60 degrees), but the optical inclination was obtained from a DSS image and

thus deeper imaging is required. Kinematic modelling has been done previously by Côté et al. (2000) who used a slightly higher inclination ($52 \pm 5$ degrees) for their models. This value is consistent within the uncertainties with the value used here. We also note that Côté et al. (2000) fitted 4 tilted rings to their HI data and only the inner two agree with the value adopted in their model. The outer two tilted rings have inclinations similar to the value we measure.

### 3.7.11. ESO381-G020

ESO381-G020 is a dwarf irregular galaxy located at 5.4 Mpc (Karachentsev et al., 2007) and a member of the Centaurus A Group. The optical image shows a very asymmetric stellar distribution, similar to that of ESO325-G?011.

Previous HI studies of this galaxy have been carried out using single dish telescopes (Longmore et al., 1982; Huchtmeier & Richter, 1986; Côté et al., 1997; Banks et al., 1999; Koribalski et al., 2004) as well as with synthesis imaging (Côté et al., 2000). The kinematics of this galaxy have previously been studied by Côté et al. (2000) using their synthesis imaging. Their observations have higher angular resolution ($13 \times 13$ arcsec compared to $80 \times 49$ arcsec) but slightly lower sensitivity (rms noise of 1.7 mJy beam$^{-1}$ compared to 1.3 mJy beam$^{-1}$). The Côté et al. (2000) study allows a useful comparison to ensure that our analysis provides consistent results with those of others.

The observed HI velocity field is somewhat disturbed with the contours of constant velocity appearing asymmetric about the major axis. While a kinematic model could be derived, the residual between the observed velocity field and the model velocity field in some areas was up 10km s$^{-1}$.

The HI position angle was found to increase steadily from 295 to 314 degrees as a function of radius. The latter value is consistent with the position angle of 310 degrees derived from the outer isophotes of the stellar light. The inclination obtained by tilted ring analysis ($55 \pm 10$ degrees) is higher than the inclination of the stellar component (40 degrees). The kinematic study of this galaxy by Côté et al. (2000) obtained similar results. They modelled ESO381-G020 with a position angle of $311 \pm 1$ degrees and an inclination of $57 \pm 6$ degrees. Their position angle is an average of the values obtained by their tilted ring analysis (with actual values ranging from 305 to 313 degrees).

### 3.7.12. IC5152

IC5152 is a nearby irregular galaxy that was originally considered a Local Group (LG) candidate (Yahil et al., 1977). However current distance estimates place it at 2.1 Mpc (Karachentsev et al., 2004), beyond the edge of the LG. Due to its close proximity to the Milky Way, it is often included in studies of the LG dynamics

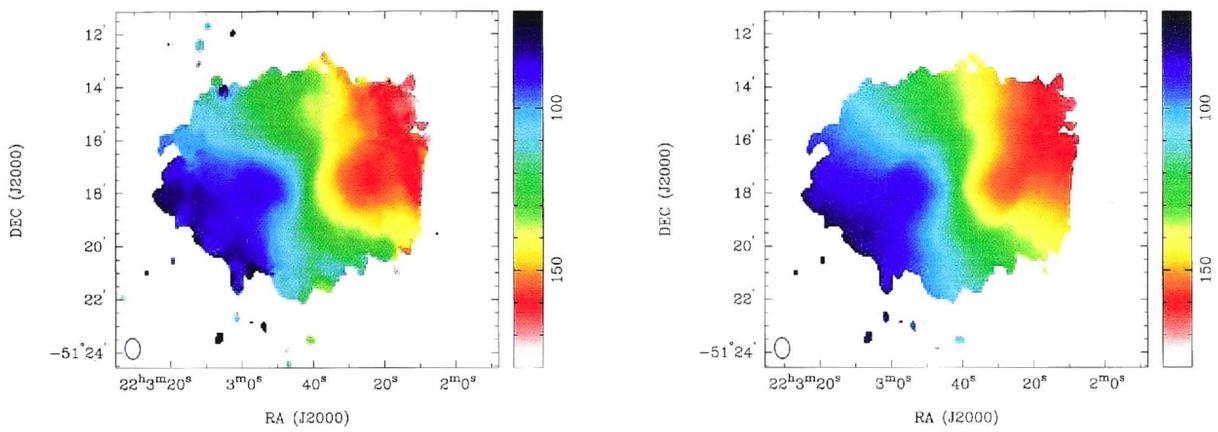


**Figure 3.14** [Left] The observed H I velocity field of the Local Group irregular galaxy IC5152. [Right] The model velocity field masked using the region defined by the observed velocity field.

and evolution (see for example Chernin et al. 2004; Sawa & Fujimoto 2005; Pasetto & Chiosi 2007), hence requires accurate mass modelling. The near-IR image (see Figure 3.1) shows a well resolved galaxy with a fairly bright centre. The central region of IC5152 is an active site of star formation (Zijlstra & Minniti, 1999) and several H II regions have been studied (Hidalgo-Gámez & Olofsson, 2002; Lee et al., 2003). IC5152 has many blue stars and dusty patches (Karachentsev et al., 2002b). The north west corner has a very bright superimposed star. Deep CO emission maps have been obtained but no emission was detected ($4\sigma$ upper limit of 0.03 K km $s^{-1}$) despite the presence of large amounts of neutral gas (Buyle et al., 2006).

The H I line profile of IC5152 has been studied previously using single dish telescopes (Huchtmeier & Richter, 1986; Becker et al., 1988; Koribalski et al., 2004). H I synthesis imaging has also been obtained but only the integrated intensity map has been published (Buyle et al., 2006).

The H I velocity field shows a twisting of the contours of constant velocity. The kinematic model obtained by rotation curve analysis is presented in Figure 3.7. At first glance, the model velocity field and the observed velocity field appear inconsistent as the physical dimensions are different. This occurs because the inclination and position angle obtained by tilted ring analysis implies a model that extends past beyond the observed H I in the north west and south east regions of the galaxy. However, if the model velocity field is masked by region defined in the observed velocity field, the agreement appears to be excellent, particularly given the distortion in the observed field (see Figure 3.14). The typical differences between the observations and the model are less than 5km $s^{-1}$ with maximum deviations less than 10km $s^{-1}$. The physical motivation which allows for masking of the model is that the masked H I gas is thought to be present but below the observed column density limit.

The inclination of IC5152 is found to be constant as a function of radius at $49 \pm 6$ degrees which is consistent with the inclination of the stellar disk (50 degrees; Kirby et al. 2008). The H I position angle (increasing from 271 to 298 degrees) is also consistent with the inclination of the stellar disk (275 degrees; Kirby et al. 2008).

## 3.8. The Tully-Fisher Relation

The classical and baryonic Tully-Fisher relations are empirical relations between the luminous or baryonic mass of a spiral galaxy and its peak rotation velocity (for recent studies see Pfenniger & Revaz 2005; Begum et al. 2008a; Trachternach et al. 2009 and Stark et al. 2009). These relations can be used to measure distances, constrain properties of dark matter and study galaxy evolution as a function of redshift (Combes, 2009) indicating the importance of accurately determining the empirical relationship, particularly in the dwarf regime. In Figure 3.15 we show the classical [upper panel] and baryonic [lower panel] Tully-Fisher plots for our sample galaxies in the black squares.

The classical Tully-Fisher relation shows the absolute $B$-band magnitude (calculated using the apparent magnitudes, $m_B$, and the distances listed in Table 3.1) plotted against the maximum rotational velocity of a galaxy obtained by rotation curve analysis (Table 3.4). The $B$-band magnitudes have been corrected for Galactic extinction using Schlegel et al. (1998). Also plotted are the samples of Sakai et al. (2000) which contains many bright spiral galaxies and of Begum et al. (2008a) which contains many faint dwarf galaxies. These are indicated by open circles and crosses respectively. Sakai et al. (2000) provide H I line widths which are used to obtain the rotational velocity by correcting for inclination and broadening due to turbulent motions (using equation 3.7). We determine the classical Tully-Fisher relation by a weighted least squares fit to be:

$$M_{B,0} = (-7.29 \pm 0.33) \log(2v_{max}) - (1.40 \pm 0.71) \tag{3.8}$$

The baryonic Tully-Fisher relation (lower panel of Figure 3.15) shows the total baryonic mass plotted against the maximum rotational velocity of a galaxy obtained by rotation curve analysis for our sample (black squares), the Begum et al. sample (open circles) and the Sakai et al. sample (crosses). Once again, the rotational velocity for the Sakai et al. (2000) sample was obtained by correcting the H I linewidth for inclination and turbulent broadening (equation 3.7). We determine the baryonic Tully-Fisher relation by a weighted least squares fit to Figure 3.15 (right panel) as:

$$\log(M_{bary}) = (2.51 \pm 0.11) \log(2v_{max}) - (3.94 \pm 0.23) \tag{3.9}$$

The total baryonic, $\log(M_{bary})$, mass was calculated as $\log(M_* + 1.4 M_{HI})$. Since we have no direct measurement of the mass-to-light ratio for our sample galaxies,

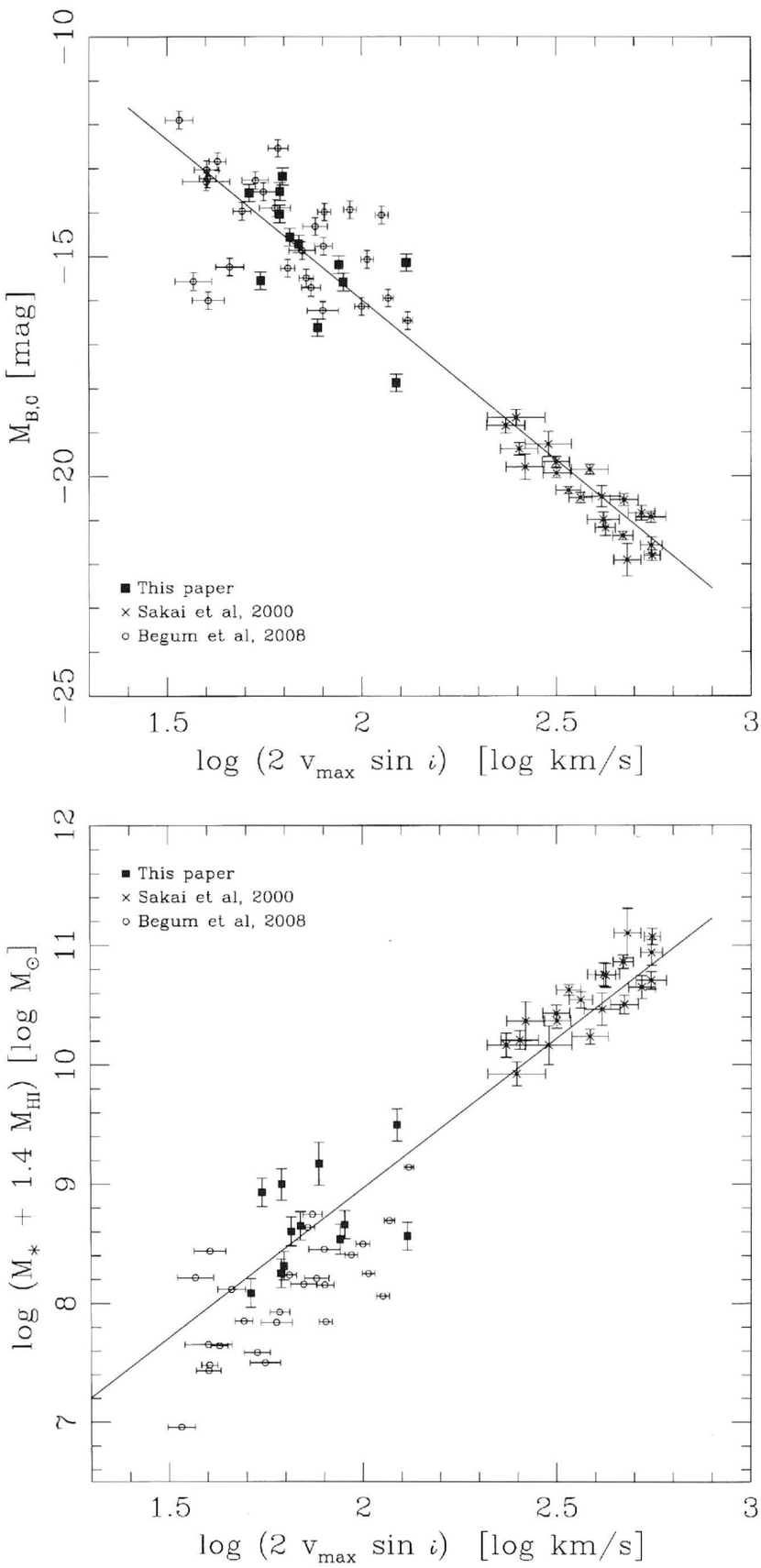


**Figure 3.15** The classical [upper panel] and baryonic [lower panel] Tully-Fisher relations. Here we compare our sample to the bright galaxy sample of Sakai et al. (2000) and the faint galaxy sample of Begum et al. (2008). The solid line is a weighted least squares fit to the data

we estimate the stellar mass from the $B$-band luminosity using the moderate ratio $M_*/L_B = 1.2 M_\odot/L_{\odot,B}$ (Bell & de Jong 2001). The baryonic mass includes the total gas mass which we obtain using the conversion factor $M_{gas}/M_{HI} = 1.4$ (following McGaugh et al. 2000, Geha et al. 2006 and Warren et al. 2007). This takes into account primordial helium and metals but does not include molecular hydrogen. Dwarf galaxies are thought not to contain large amounts of molecular hydrogen (Taylor et al., 1998; Leroy et al., 2005). While the bright galaxies of the Sakai et al. (2000) sample will have significant amounts, the baryonic mass of these systems is dominated by the stellar component and the uncertainty in the mass-to-light ratio is likely to contribute a larger error than ignoring the molecular hydrogen (Begum et al., 2008a). We note that Pfenniger & Revaz (2005) suggested that the conversion factor could be as high as 2.98. This result, however, is based on a slight reduction to the scatter of their baryonic Tully-Fisher relation rather than any observational or theoretical evidence. Begum et al. (2008a) confirmed that the conversion factor is poorly constrained by the baryonic Tully-Fisher relation and showed that any value between $\sim 2$ and 29 leads to significant tightening of the relation.

The tight correlation between the H I line width and the true rotational velocity obtained by tilted ring analysis (see Figure 3.13) provides a degree of confidence in studies which utilise the H I line widths as a measure of rotation for Tully-Fisher investigations (see Meyer et al. 2008 for a recent example). However, we note that obtaining accurate distance estimates rather than using the midpoint of the H I line profile is imperative as both the classical and baryonic Tully-Fisher relation depend on this measurement (through the derivation of the absolute magnitude and the stellar and H I mass). Also of note is the fact that 5 galaxies (AM0605-341, ESO174-G?001, ESO245-G?009, ESO325-G?011 and ESO381-G020) in our sample were found to have an inclination of their H I disk different to the measured optical inclination (by more than 5 degrees). When deprojecting the observed rotational velocity obtained from an H I line width, it is the inclination of the H I disk which should be used.

## 3.9. Conclusion

We have presented a kinematic study of 12 galaxies in the Local Volume ($D < 10$ Mpc). The data was obtained using the ATCA as part of the LVHIS Survey. For six galaxies in our sample (AM0605-341, Argo Dwarf, ESO059-G001, ESO137-G018, ESO174-G?001, ESO308-G022) we have presented the only resolved H I imaging available to date, revealing the atomic hydrogen distribution for the first time.

The global H I line spectra are presented and compared to those obtained by HIPASS. The spectrum of ESO245-G005 shows a strong H I absorption line at a redshift of 386km s$^{-1}$. The spectrum of ESO381-G020 shows two weak absorption

lines at 581km $s^{-1}$ and 597km $s^{-1}$. The comparision to the single-dish spectra of HIPASS shows that the new H I synthesis observations of IC5152 are missing flux due to missing short baselines in the interferometer. The H I line widths obtained by HIPASS and LVHIS are consistent within the experimental uncertainties.

Rotation curve analysis has been carried out for all sample galaxies by applying a tilted ring model to the observed velocity field. The best fitting rotation curve parameters are provided.

We show that the H I line width can be used to derive the rotational velocity of galaxies in the velocity range $50 < v < 150$km $s^{-1}$ using the newly updated Tully & Fouque (1985) model:

$$\begin{aligned} v_{max}^2 &= w_{50,corr}^2 + (2 \pm 14)^2 \left[1 - 2e^{-(w_{50,corr}/100)^2}\right] \\ &\quad -w_{50,corr}(4 \pm 28) \left[1 - e^{-(w_{50,corr}/100)^2}\right] \\ v_{max}^2 &= w_{20,corr}^2 + (34 \pm 10)^2 \left[1 - 2e^{-(w_{20,corr}/120)^2}\right] \\ &\quad -w_{20,corr}(68 \pm 20) \left[1 - e^{-(w_{20,corr}/120)^2}\right], \end{aligned}$$

however resolved observations are essential if an accuracy greater than approximately 10 km $s^{-1}$ is required.

AM0605-341 was found to have an extension of redshifted H I located to its west. We propose that this is due to a tidal interaction with its nearby neighbour NGC2188, which has previously been found to have a similar tidal extension.

ESO121-G020 was found to have a much lower inclination (40 degrees) than the current value available in the literature (78 degrees; Warren et al. 2006). We derive the new lower limit for its dynamical mass as $1.7 \times 10^9$ $M_\odot$.

It was observed that the observed ellipticity of ESO215-G?009 is inconsistent with its kinematic inclination ($35 \pm 3$ degrees). The observed H I distribution is highly circular implying that the galaxy is nearly face-on. This may be evidence that the assumption of the gas being located in an infinitely thin disk is incorrect.

We find evidence that ESO245-G005 has a warp in its outer disk, located at an angular radius of 200 arcsec. This lends support to the Côté et al. (2000) hypothesis that ESO245-G005 has undergone recent accretion.

The classical and baryonic Tully-Fisher relations are found to be:

$M_{B,0} = (-7.29 \pm 0.33) \log(2v_{max}) - (1.40 \pm 0.71)$
$\log(M_{bary}) = (2.51 \pm 0.11) \log(2v_{max}) - (3.94 \pm 0.23)$

# CHAPTER 4

# The Maximum Baryonic Content of a Galaxy

*To be submitted to the Astrophysical Journal*
*Kirby & Jerjen 2010*

**Abstract:**
Near-IR flux and 21cm emission data for 1394 nearby ($z \approx 0$), gas-rich galaxies are analysed to examine the relation between the processed (stars) and unprocessed (atomic hydrogen) baryons in these systems. We show that there is an upper limit for the total H I mass a galaxy can have. While this mass limit systematically increases with the galaxy's stellar mass, the $\mathcal{M}_{\rm H\,I}/\mathcal{M}_*$ mass ratio decreases more rapidly, leading to a progressively larger population of star-dominated galaxies. The transition is complete at $10^{10}M_\odot$ beyond which all galaxies are star-dominated. We further investigate the relation between the stellar and baryonic mass of a galaxy and find that the stellar mass fraction $\mathcal{M}_*/\mathcal{M}_{bary}$ has a lower limit for a given baryonic mass. The fraction steadily increases over the $8 < \log(\mathcal{M}_{bary}) < 12$ mass range after which it reaches unity, suggesting that $\approx 10^{12}M_\odot$ must be close to the maximum initial mass of the gas reservoir of a protogalaxy. This empirical value is in excellent agreement with the mass limit that has been reported for elliptical galaxies by Rocca-Volmerange et al. (2004) and the critical mass of self-gravitating clouds regulated by cooling.

## 4.1. Introduction

The majority of baryonic mass in galaxies consists of two distinct, albeit intimately related constituents; stars and neutral hydrogen gas. Although many nearby galaxies have been studied in great details (e.g. THINGS, Walter et al. 2008; LVHIS, Koribalski et al. 2010), a complete and coherent understanding of the physical processes that regulate star formation has not yet been achieved. The star formation rate measures how quickly a galaxy evolves through progressively converting gas into stars thereby enlarging the stellar content that leads to the baryonic mixtures we observe in galaxies today. This rate is highly variable over the cosmological timescale. It depends on the local gas conditions of the disk, foremost the amount, distribution and dynamic properties (Schmidt, 1959; Toomre, 1964; Kennicutt, 1989; Jimenez et al., 1997; Martin & Kennicutt, 2001; Verde et al., 2002) and can temporarily reach a hundred solar masses per year (Mobasher et al., 2009). Another important factor is the galaxy environment (Gómez et al., 2003).

It has long been speculated that highly unevolved HI-rich galaxies with extreme low star densities (optical surface brightness) or even HI protogalaxies still exist in large numbers at the present epoch but are generally absent in galaxy surveys due to observational selection bias (Disney, 1976; Disney & Phillipps, 1987). However, Taylor & Webster (2005) have argued on theoretical grounds that there is a minimum global star formation rate for a galaxy with a given H I mass. This result is consistent with the non-detection of any convincing isolated extragalactic H I cloud unaccompanied by a stellar counterpart (Minchin et al., 2003; Doyle et al., 2005; Bekki et al., 2005). While a number of objects with no optical counterparts has been detected at 21 cm over the years they can always be associated with another galaxy or a group where ram pressure stripping is at work, e.g. high-velocity clouds in the Milky Way (Wakker & van Woerden, 1997), HIPASS J1712-64 (Kilborn et al., 2000), HIJASS J1021+6842 in the M81 Group (Boyce et al., 2001), an intergalactic gas cloud in the NGC2442 Group (Ryder et al., 2001), and VIRGOHI 21 in the Virgo cluster (Minchin et al., 2005, 2007). Recently, Thilker et al. (2009) used the Galaxy Evolution Explorer (GALEX) to detect pockets of star formation in the best example of a pure HI cloud, the Leo Ring (Schneider et al., 1983).

When restricting the view on isolated HI detections, even in such extreme cases like ESO215-G?009, a galaxy with a current star formation rate of $2.5 \times 10^{-3} M_{\odot}$ and 95 percent of baryons still in form of HI gas (Warren et al., 2004), the stellar component of the galaxy has sufficiently built-up to be optically visible at the current epoch. A first systematic analysis of nearby galaxies with tentatively high HI mass-to-light ratios by Warren et al. (2006) reached the conclusion that galaxies in which the stellar component makes up less than a few percent of the total baryonic mass are rare objects.

The main aim of this paper is to assess the status quo of galaxy evolution by investigating the baryon mixture of current-day galaxies of different morphological types. The required data of the sample galaxies is described in section 4.2. In section 4.3 we examine how well gas and stellar masses correlate in these galaxies. This is further analysed in section 4.4, where we investigate the $\mathcal{M}_{HI}/L$ which provides a measure of the integral evolutionary status of a galaxy. We further examine the relationship between the stellar mass fraction and the total baryonic mass of the sample galaxies in section 4.5. The results are summarised in section 4.7.

## 4.2. The Data Sources

### 4.2.1. The Local Sphere of Influence (LSI) Survey

Kirby et al. (2008) obtained deep near-IR $H$-band ($1.65\mu m$) surface photometry for 57 galaxies. Galaxies were drawn from the low density environments of the Local Sphere of Influence (LSI, $d_{MW} < 10\,\mathrm{Mpc}$). Approximately 60 percent of the sample are low surface brightness, late-type dwarf galaxies that remained undetected in the Two Micron All-Sky Survey (2MASS, Skrutskie et al., 2006).

The H I masses for the sample galaxies were taken from the HIPASS Bright Galaxy Catalog (BGC, Koribalski et al., 2004). This catalogue contains HI data for the 1000 H I brightest galaxies in the southern sky as obtained from the blind H I Parkes All-Sky Survey (HIPASS, Staveley-Smith et al. 1996, Barnes et al., 2001, Meyer et al. 2004). For the few LSI galaxies not listed in the BGC, we visually inspected the original HIPASS data cubes for a 21cm emission line signal and calculated the neutral hydrogen mass by following the same procedure employed to establish the BGC parameters (B. Koribalski, priv. comm.). It should be noted that we excluded the three dwarf galaxies SC18, SC24 and SC42 (Côté et al. 1997) in the Sculptor group from our analysis due to strong confusion with Galactic H I in position as well as velocity space (see Fig. 4.1)[1].

Galaxy distances were taken from a number of sources (Karachentsev et al. 2004, 2006; Seth et al. 2005) based on a range of distance indicators. A total of 44 LSI galaxies were unambiguously detected in both the $H$-band and the HI. Their parameters including stellar and gas properties have been compiled in Table 4.1.

[1]SC18, SC24 and SC42 are discussed in further detail in Appendix B of this thesis.

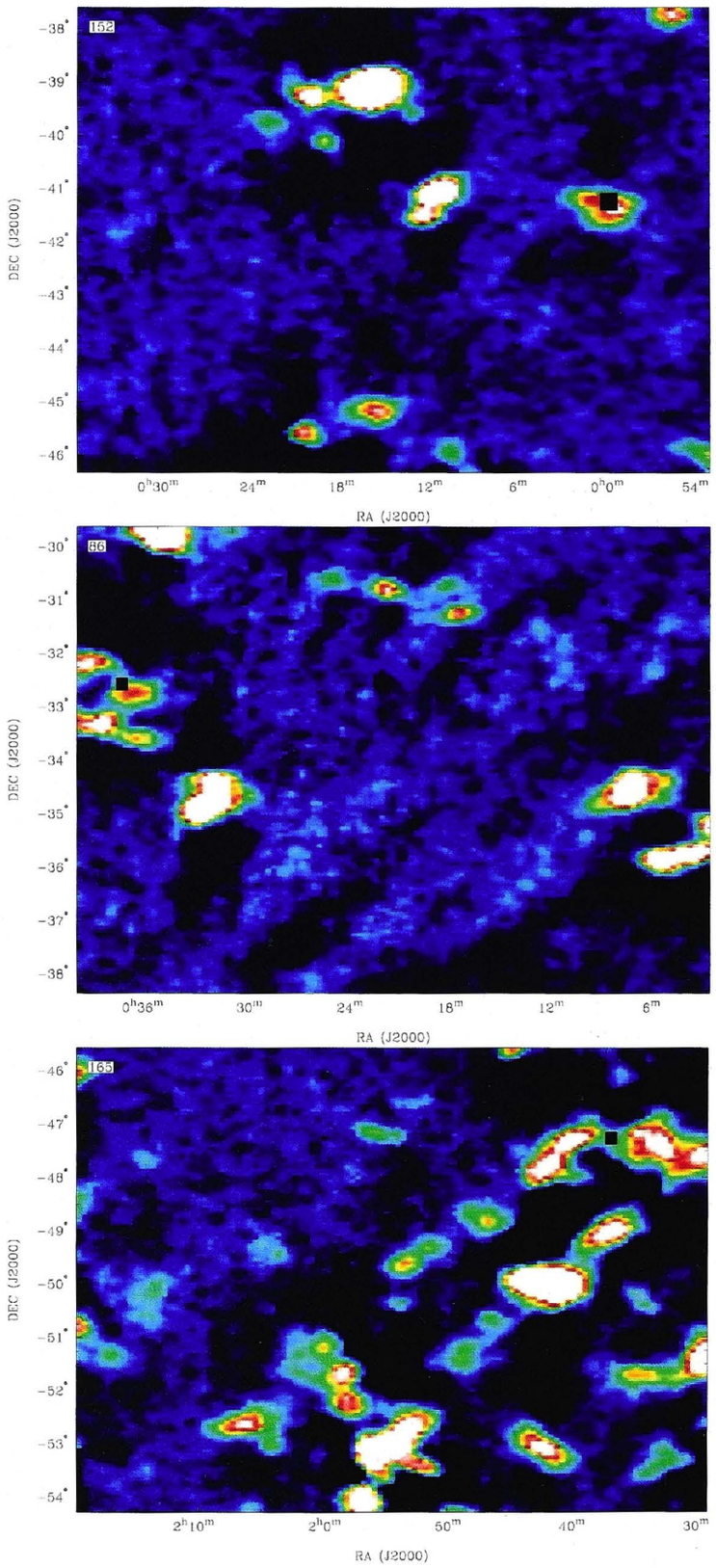


**Figure 4.1** The HI line emission in the proximity of the Sculptor dwarf galaxies SC18 (top), SC24 (middle), and SC42 (bottom). Here we show the HIPASS data cube sliced at the listed distance of the galaxies with the black square indicating the optical center of the galaxy. The intensity of the HI emission is represented by the colour scale going from black (low intensity) to white (high intensity).

**Table 4.1** Properties of Local Sphere of Influence Galaxies

| Name | $D$ (Mpc) | Method* | $\log_{10}(\mathcal{M}_*)$ ($\log_{10}(\mathcal{M}_\odot)$) | $F_{\rm H\,I}$ (Jy·km s$^{-1}$) | $\log_{10}(\mathcal{M}_{\rm H\,I})$ ($\log_{10}(\mathcal{M}_\odot)$) |
|---|---|---|---|---|---|
| (1) | (2) | (3) | (4) | (5) | (6) |
| AM0106-382 | 8.4 | H | 7.89 ± 0.05 | 3.5 ± 0.9[d] | 7.8 ± 0.1 |
| AM0319-662 | 4.07 | RGB[a] | 7.00 ± 0.02 | 21.7 ± 4.2[d] | 7.93 ± 0.08 |
| AM0333-611 | 13.5 | H | 8.27 ± 0.04 | 4.9 ± 2.1[d] | 8.3 ± 0.2 |
| AM0521-343 | 10.5 | H | 7.7 ± 0.2 | 4.7 ± 3.1[d] | 8.1 ± 0.3 |
| Argo | 4.9 | RGB[a] | 7.77 ± 0.03 | 34.8 ± 4.4[e] | 8.30 ± 0.05 |
| DDO210 | 0.94 | RGB[a] | 6.49 ± 0.04 | 11.2 ± 2.4[e] | 6.37 ± 0.09 |
| ESO059-G001 | 4.57 | RGB[b] | 8.22 ± 0.03 | 17.7 ± 2.5[e] | 7.94 ± 0.06 |
| ESO115-G021 | 4.66 | RGB[a] | 8.44 ± 0.03 | 97.6 ± 8.2[e] | 8.70 ± 0.04 |
| ESO121-G020 | 6.05 | RGB[b] | 7.44 ± 0.04 | 14.1 ± 2.9[e] | 8.09 ± 0.09 |
| ESO154-G023 | 5.7 | H | 8.79 ± 0.03 | 139.2 ± 11.6[e] | 9.03 ± 0.04 |
| ESO245-G005 | 4.43 | RGB[a] | 8.22 ± 0.05 | 81.0 ± 9.1[e] | 8.57 ± 0.05 |
| ESO308-G022 | 7.7 | H | 8.02 ± 0.04 | 3.2 ± 2.9[d] | 7.7 ± 0.4 |
| ESO347-G017 | 9.6 | H | 8.68 ± 0.03 | 8.4 ± 1.7[e] | 8.26 ± 0.09 |
| ESO348-G009 | 8.8 | H | 8.23 ± 0.04 | 13.4 ± 2.2[e] | 8.39 ± 0.07 |
| ESO349-G031 | 3.21 | RGB[b] | 7.19 ± 0.03 | 5.8 ± 1.6[e] | 7.1 ± 0.1 |
| ESO364-G029 | 7.6 | H | 8.35 ± 0.03 | 17.6 ± 2.5[e] | 8.38 ± 0.06 |
| ESO461-G036 | 7.83 | RGB[b] | 7.70 ± 0.07 | 7.2 ± 1.8[d] | 8.0 ± 0.1 |
| ESO473-G024 | 8.3 | H | 7.80 ± 0.06 | 7.2 ± 1.8[e] | 8.1 ± 0.1 |
| ESO565-G003 | 7.6 | H | 8.02 ± 0.03 | 2.0 ± 1.9[d] | 7.4 ± 0.4 |
| IC1574 | 4.92 | RGB[a] | 7.98 ± 0.04 | 5.4 ± 1.5[e] | 7.5 ± 0.1 |
| IC1959 | 6.4 | H | 8.64 ± 0.02 | 27.2 ± 3.2[e] | 8.43 ± 0.05 |
| IC4662 | 2.44 | RGB[b] | 8.66 ± 0.02 | 130 ± 12[e] | 8.26 ± 0.04 |
| IC5052 | 6.03 | RGB[c] | 9.47 ± 0.02 | 101.7 ± 7.6[e] | 8.94 ± 0.03 |
| IC5152 | 2.07 | RGB[a] | 8.67 ± 0.02 | 97.2 ± 9.5[e] | 7.99 ± 0.04 |
| IC5332 | 9.7 | H | 10.15 ± 0.02 | 159.2 ± 13.9[e] | 9.55 ± 0.04 |
| KKS2000-09** | 6.5 | H | 8.49 ± 0.03 | 31.4 ± 6.9[e] | 8.5 ± 0.1 |
| KKS2000-55** | 10.2 | H | 9.43 ± 0.02 | 54.3 ± 5.1[e] | 9.13 ± 0.04 |
| NGC0625 | 4.07 | RGB[a] | 9.01 ± 0.02 | 30.9 ± 3.6[e] | 8.08 ± 0.05 |
| NGC1311 | 5.5 | H | 8.74 ± 0.03 | 14.6 ± 3.2[e] | 8.0 ± 0.1 |
| NGC1313 | 4.15 | RGB[a] | 10.3 ± 0.1 | 462.7 ± 32.6[e] | 9.27 ± 0.03 |
| NGC1705 | 5.1 | RGB[a] | 8.75 ± 0.03 | 15.4 ± 2.6[e] | 7.98 ± 0.07 |
| NGC1744 | 8.0 | H | 9.48 ± 0.04 | 144.3 ± 10.1[e] | 9.34 ± 0.03 |
| NGC2835 | 8.3 | H | 10.59 ± 0.08 | 127.8 ± 9.6[e] | 9.32 ± 0.03 |
| NGC2915 | 3.78 | RGB[a] | 8.76 ± 0.03 | 108.4 ± 13.9[e] | 8.56 ± 0.06 |
| NGC7713 | 9.5 | H | 9.92 ± 0.03 | 58.6 ± 5.1[e] | 9.09 ± 0.04 |
| NGC7793 | 3.91 | RGB[a] | 10.10 ± 0.05 | 278.5 ± 20.4[e] | 9.00 ± 0.03 |
| UGCA15 | 3.34 | RGB[a] | 7.32 ± 0.04 | 13.4 ± 2.5[e] | 7.55 ± 0.08 |

Continued on next page

**Table 4.1 – continued from previous page**

| Name (1) | $D$ (Mpc) (2) | Method* (3) | $\log_{10}(\mathcal{M}_*)$ ($\log_{10}(\mathcal{M}_\odot)$) (4) | $F_{\rm H\,I}$ (Jy·km s$^{-1}$) (5) | $\log_{10}(\mathcal{M}_{\rm H\,I})$ ($\log_{10}(\mathcal{M}_\odot)$) (6) |
|---|---|---|---|---|---|
| UGCA148 | 9.8 | MEM[a] | 8.53 ± 0.03 | 1.9 ± 1.6[d] | 7.6 ± 0.4 |
| UGCA153 | 6.8 | H | 8.05 ± 0.07 | 13.4 ± 2.5[e] | 8.17 ± 0.08 |
| UGCA162 | 7.8 | H | 8.27 ± 0.04 | 32.9 ± 3.5[e] | 8.67 ± 0.05 |
| UGCA442 | 4.27 | RGB[a] | 8.27 ± 0.03 | 50.1 ± 5.3[e] | 8.33 ± 0.05 |

(*) Distance indicators: RGB = tip of the red giant branch method, H = Hubble flow distance, MEM = group membership
(a) Karachentsev et al. 2004; (b) Karachentsev et al. 2006; (c) Seth et al. 2005 (d) calculated using original HICAT data cubes (private communication with B. Koribalski); (e) obtained from the HIPASS Bright Galaxy Catalogue, (Koribalski et al. 2004);
(**) We use KK2000 to indicate that the original listing of this galaxy was in the Karachentseva & Karachentsev (2000) paper and KKS2000 to indicate that it was originally listed in the Karachentsev et al. (2000) paper. This is consistent with the names listed in NED.

### 4.2.2. The Goldmine Virgo Cluster data

Stellar systems residing in high density environments are represented in our study by 507 galaxies from the Virgo cluster. This galaxy sample contains all morphological types and is taken from the Goldmine Database (Gavazzi et al., 2003) that provides the $H$-band magnitude, the H I mass and the distance (amongst other parameters) for each galaxy. The Goldmine Database lists galaxy distances that are either derived from the mean Virgo cluster redshift or from an individual redshift measurement. However, to avoid an artificial depth (finger of God) effect due to substantial peculiar velocities in the cluster, we adopted for all sample galaxies the same distance, the mean cluster distance of 16 ± 1.6 Mpc (Jerjen et al., 2004) based on surface brightness fluctuations in early-type Virgo dwarfs. The $H$-band data for the galaxies were formally corrected for Galactic extinction by applying a mean $A_H$ = 0.01 mag (Schlegel et al., 1998).

### 4.2.3. The Bouchard et al. Sample

Bouchard et al. (2007) studied 18 dwarf galaxies with early and transition-type morphology in the Centaurus A group less luminous than $M_B = -14$, taken from the catalogues of Côté et al. (1997); Jerjen et al. (2000); Karachentseva & Karachentsev (1998) and Karachentsev et al. (2007). They obtained both single

dish and synthesis H I observations for them using the 64m Parkes Telescope and the Australia Telescope Compact Array (ATCA), respectively. They measured H I masses for five galaxies and provided upper limits for the remaining 13. We use their H I data, distances as well as the quoted *B*-band magnitudes. The latter values were then corrected for extinction (Schlegel et al., 1998) and converted into *H*-band magnitudes by making use of the tight B-band to H-band relation discussed in (Kirby et al., 2008):

$$M_H = 1.14 M_B - 0.74. \tag{4.1}$$

### 4.2.4. The Local Group Dwarf Galaxies Sample

A comprehensive parameter list for 36 Local Group galaxies were compiled by Mateo (1998, and references therein). Almost all galaxies have absolute *B*-band magnitudes and accurate distances based on either one or more high precision distance indicators, including Cepheid variables, tip magnitude of the RGB stars, RR Lyr stars, and the luminosity of the horizontal branch. After correcting the *B*-band magnitude for Galactic extinction we derived the corresponding *H*-band magnitude using equation (4.1). The integrated neutral hydrogen masses were taken from the most recent HI study by Grcevich & Putman (2009).

### 4.2.5. The Warren et al. Sample

A sample of gas-rich late-type galaxies which predominately reside in low density environments was obtained from Warren et al. (2006). This sample consists of 789 galaxies that were detected during the HIPASS Survey and are listed in the BGC with photographic *B*-band magnitudes extracted from the Lyon-Meudon Extragalactic Database (LEDA, Paturel et al., 1997, and references therein; now moved to HYPERLEDA). All galaxies have absolute *B*-band magnitudes brighter than $M_B = -11.4$ and 90 percent are brighter than $-15.7$. While the uncertainties in the photographic photometry for these galaxies are generally large (see Warren et al. 2006 for a comprehensive discussion), it should be noted that a subset of 38 low luminosity galaxies were reobserved at the Australian National University 2.3 m telescope to obtain accurate *BVRI* CCD photometry (Warren et al., 2007). Again, we corrected the *B*-band magnitudes for extinction and converted to *H*-band magnitudes using equation (4.1). The galaxy distances were calculated from the Local Group velocities listed in the BGC by adopting a Hubble constant of $H_o = 75\,\mathrm{km\,s^{-1}\,Mpc^{-1}}$, except for nine galaxies with known large peculiar velocities. For those galaxies we adopted the independent distance measurements listed in the BGC (see Koribalski et al. 2004, and references therein). The galaxies in this sample have Local Group velocities ranging from 150 km s$^{-1}$ to 7413 km s$^{-1}$.

## 4.3. Sharing the Baryons

The total apparent H-band magnitudes, $m_H$, were converted into luminosities using the standard equation

$$L_H = 10^{0.4(M_{H,\odot} - m_H + 5\log D + 25 + A_H)},$$

where $M_{H,\odot} = 3.35$ mag is the $H$-band luminosity of the sun (Colina et al., 1996) and $A_H$ is the Galactic extinction (Schlegel et al., 1998) in the direction of the target galaxy. The uncertainty in $M_{H,0}$ largely depended on the accuracy of the distance measurement. The stellar mass was calculated adopting a $H$-band mass-to-light ratio of $\Upsilon_*^H = 1.0 \pm 0.4$, a value that is broadly consistent with observations and theory (de Jong 1996, Bell et al. 2003, Kirby et al. 2008). In Figure 4.2 we compare the HI mass to the stellar mass for the combined sample of 1394 galaxies. Different morphological types of galaxies occupy different parts of the parameter space. The early and transition type dwarfs from Bouchard et al. (2007) are found in the bottom left corner of the plot; that is, the sample only contains low mass galaxies which have very little or no HI gas. Non-detections are associated with upper limits in HI mass, and are marked with downward arrows. The Local Group dwarfs occupy the same part of the diagram as the Bouchard et al. sample which is not surprising given the many early-type systems. The LG galaxies also extends to higher HI values due to the late-type dwarfs in the sample. The LSI field galaxies sample is dominated by late-type dwarfs and lies above the Bouchard et al. sample. It has a much larger spread in stellar masses than galaxies found in the Local Group. Similarly, the field galaxy sample of Warren et al. (2006) contains objects with higher HI values and occupies a similar parameter space to the LSI sample. The Warren et al. sample is dominated by high HI mass spiral and irregular galaxies and consequently occupies the upper right corner of the parameter space. Finally, the Virgo cluster galaxies are predominately dwarf ellipticals, ellipticals, and spiral galaxies. This sample is located below the Warren et al. sample, reflecting the systematically lower HI mass content in cluster galaxies. This result emphasises that the relation between the stellar and gas mass of a galaxy depends on the morphological type and on the environment.

Fig. 4.2 highlights the large range over six orders of magnitudes in both neutral hydrogen ($10^5$ to $10^{10.5} M_\odot$) and stellar masses ($10^5$ to $10^{11.5} M_\odot$) of nearby galaxies. A ridge line defined by the distribution of late-type galaxies with stellar masses larger than $10^7 M_\odot$ strongly suggests that there is an upper limit to the amount of HI gas a galaxy can have for a given stellar mass, or in other words a minimum stellar mass for a given HI mass in a galaxy. Binning the data in the $6.5 < \log M_\odot < 11.5$ interval using a 1 dex bin size gives the 97th upper percentiles shown as triangles, ie. 97 percent of all galaxies in the bin are below the triangle. The dashed line represents the least squares fit to the HI upper bounds as a function of stellar mass. It is best described by the equation

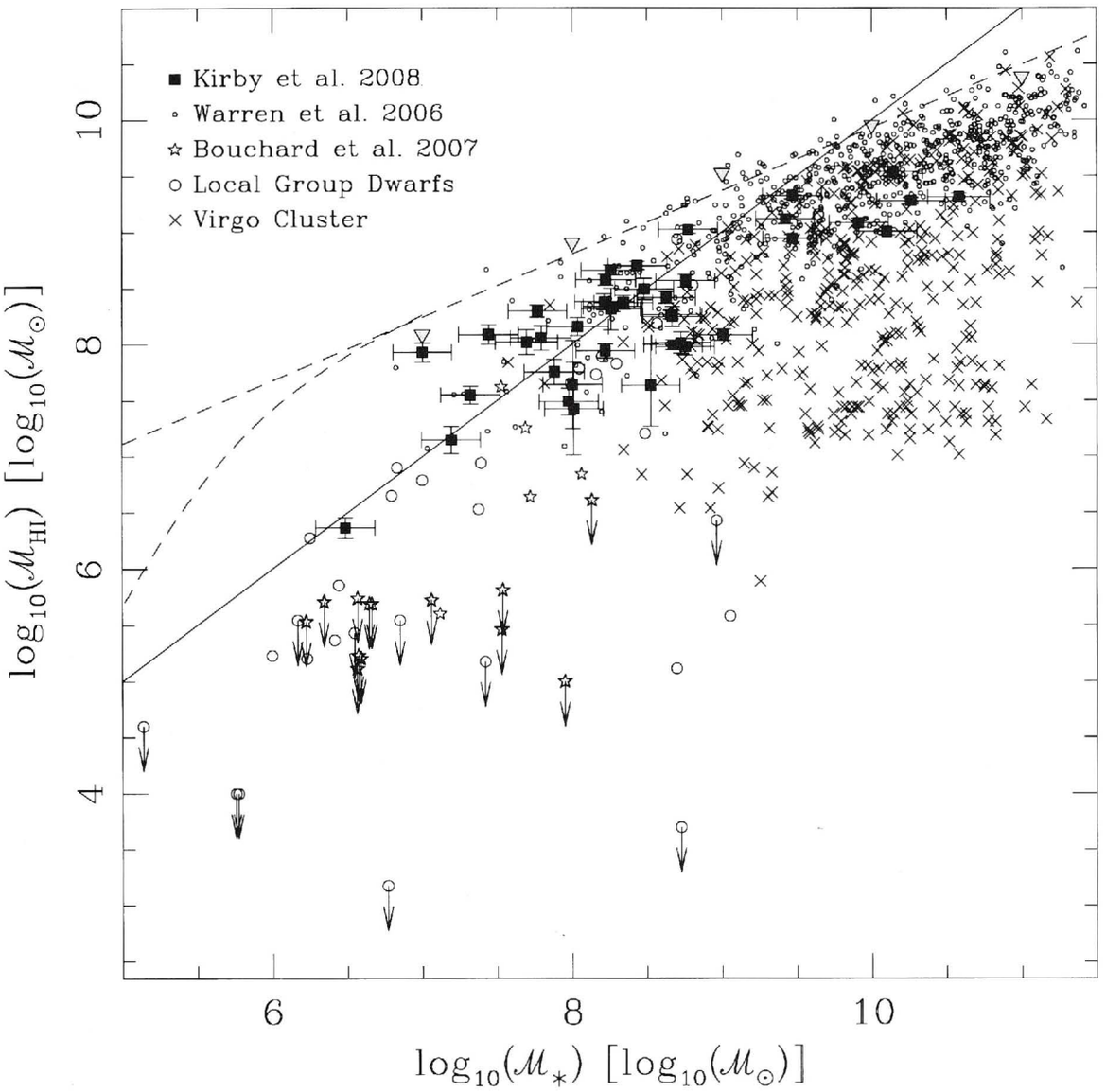


**Figure 4.2** A direct comparison of the H I mass and the stellar mass of 1394 galaxies in the local universe showing the five sub-samples as well as the derived upper bound (dashed line). The bifurcation of the dashed line indicates the potential position of the upper bound for low mass systems. The solid line indicates the position of galaxies which have 50% of their baryonic mass as stars and 50% as gas.

$$\log(\mathcal{M}_{HI})_{max} = 0.55 \log \mathcal{M}_* + 4.1. \quad (4.2)$$

Below $\log \mathcal{M}_* \approx 7$ there is a kink in the distribution with a sharp downturn as indicated by the dashed line. Less massive dwarf galaxies with a few times $10^6\,M_\odot$ total baryonic mass seem to lose their gas more easily. Grcevich & Putman (2009) also found a lower HI mass limit of $10^5\,M_\odot$ (with a $10^4\,M_\odot$ detection limit) for Local Group dwarf galaxies outside the gravitational influence of the Milky Way and the Andromeda galaxy. No HI was detected in the numerous newly

discovered satellites of the Milky Way and M31. This picture is consistent with the finding that galaxies without HI do exist (eg, many of the galaxies in the Mateo 1998 and Bouchard et al. 2007 samples), but there are no isolated extragalactic H I galaxies known to date, ie self-gravitating systems entirely made of gas without any signs of stars or star formation (de Blok et al., 2002; Minchin et al., 2003; Doyle et al., 2005; Bekki et al., 2005; Bailin & Ford, 2007).

It is important to note that the sample of low HI mass dwarf galaxies as shown in Fig.4.2 is currently limited to the immediate vicinity of the MW and M31 due to the detection sensitivity. Future blind HI surveys like WALLABY (Koribalski et al.) and MeerKATNGS (de Blok et al.) will probe significantly deeper into the low column density and low HI mass regimes to address the question of what is the baryonic mixture of spatially isolated gas-rich (dwarf) galaxies. As the H I mass-to-light ratio of galaxies seems to increase with isolation (e.g. Warren et al. 2007) it is conceivable that larger samples of such systems once found will follow more closely the trend outlined by the massive galaxies.

The fact that equation 4.2 has a slope of 0.55, shallower than unity, means that galaxies close to the ridge line have increasingly larger stellar mass fractions when going to larger baryonic masses. The solid line in Figure 4.2 is the $M_{HI} = M_*$ line that separates the gas-dominated (above) from the star-dominated (below) galaxies. It intercepts the upper bound line at $\log M_\odot \approx 10$ meaning that a galaxy with $10^{10} M_\odot$ or more total stellar mass is always star-dominated. This result is consistent with the "downsizing" picture of galaxy formation, where the star formation rate changes from high to low-mass systems with decreasing redshift (Cowie et al., 1996; Juneau et al., 2005; Mobasher et al., 2009).

An interesting test for N-body and hydrodynamical simulations that include star formation and chemical evolution will be to reproduce the upper envelope in Figure 4.2. Recently a number of simulations with enough dynamic range to resolve both a galaxy and its satellites have become available (for example, Klypin et al., 1999; Moore et al., 1999; Libeskind et al., 2007; Sales et al., 2007b,a). In this context, it is worth noticing that when two galaxies, both of which lie on or near the upper envelope are passively merged, the resulting galaxy would contain more atomic hydrogen than the "allowed" maximum (by Figure 4.2 or equation 4.2) for its combined stellar mass. Consequently, the slope of the upper envelope holds valuable statistical information about the minimum amount of star formation that is triggered during merger events. The largest separation from the permitted region occurs when the two galaxies are twins in terms of their HI and stellar masses. In that case, the discrepancy is 0.12 dex which can only be compensated by converting at least 32 percent of the combined HI mass into stars (adopting a gas-star conversion of unity).

When HI will be probed more systematically in galaxies at higher redshifts it will be interesting to see how the slope in the H I mass - stellar mass plot correlates with the star formation history over cosmic times.

## 4.4. H I Mass-to-Light Ratio of Galaxies

Depending on the conditions in a galaxy and its environment, star formation may occur either stochastically, through accumulation and condensation of neutral hydrogen gas or triggered through the compression of gas by tidal interactions between galaxies (Alonso et al., 2004; Perez et al., 2006), shock fronts created by recently formed massive stars (e.g. Elmegreen & Lada, 1977; Elmegreen, 1998; Deharveng et al., 2003; Hosokawa & Inutsuka, 2005), and supernova feedback into the interstellar medium. However, the conditions under which those processes regulate the birth of stars are not well understood. While studying the color-magnitude diagram of the underlying stellar population can provide detailed insight into the evolution of an individual galaxy through its star formation history (Tosi et al., 1991; Yuk & Lee, 2007), the H I mass-to-light ratio ($\mathcal{M}_{HI}/L$), particularly in the near-IR such as the H-band where light traces mass, offers an observational quantity that describes the integral evolutionary status of a galaxy by comparing the available amounts of unprocessed to processed baryons (hydrogen gas versus stars). For our statistical study we calculated this parameter for the combined galaxy sample and plotted it in Figure 4.3 as a function of absolute H-band magnitude or stellar mass. The five samples populate different areas of Figure 4.3, similar to that shown in Figure 4.2. Here we see that the field and late-type galaxies (from Warren et al. 2006 and Kirby et al. 2008) have higher mass-to-light ratios than the galaxies in the Virgo cluster, Local Group, and the early-type galaxies (from the Goldmine Database, Mateo 1998 and Bouchard et al. 2007). This emphasises that the star formation and/or gas removal efficiency in galaxies depends heavily on the environment.

Warren et al. (2006) found empirical evidence for an upper envelope to a galaxy's H I mass-to-light ratio at a given luminosity. The existence of this envelope implies that a galaxy will form a minimum amount of stars, at a level that depends on the galaxy's initial baryonic mass. The empirical upper envelope hypothesis has since been tested by Begum et al. (2008a) using the Faint Irregular Galaxies GMRT Survey (FIGGS) sample. This survey specifically targeted low luminous, gas-rich, dwarf irregular galaxies to test the boundary. None of the studied systems were found to have H I mass-to-light ratios above the Warren et al. (2006) upper envelope. This upper envelope hypothesis is supported theoretically by Taylor & Webster (2005) who found that a minimum amount of star formation is required in a disk for gravothermal stability. The hypothesis predicts that no future surveys of the local universe will find galaxies with H I mass-to-light ratios higher than the upper envelope for their given luminosity. In Figure 4.3, the dotted line is the upper envelope as determined by Warren et al. (2006) transformed to the $H$-band employing equation 4.1. The solid line is our improved estimate of the upper envelope best described by the analytical line:

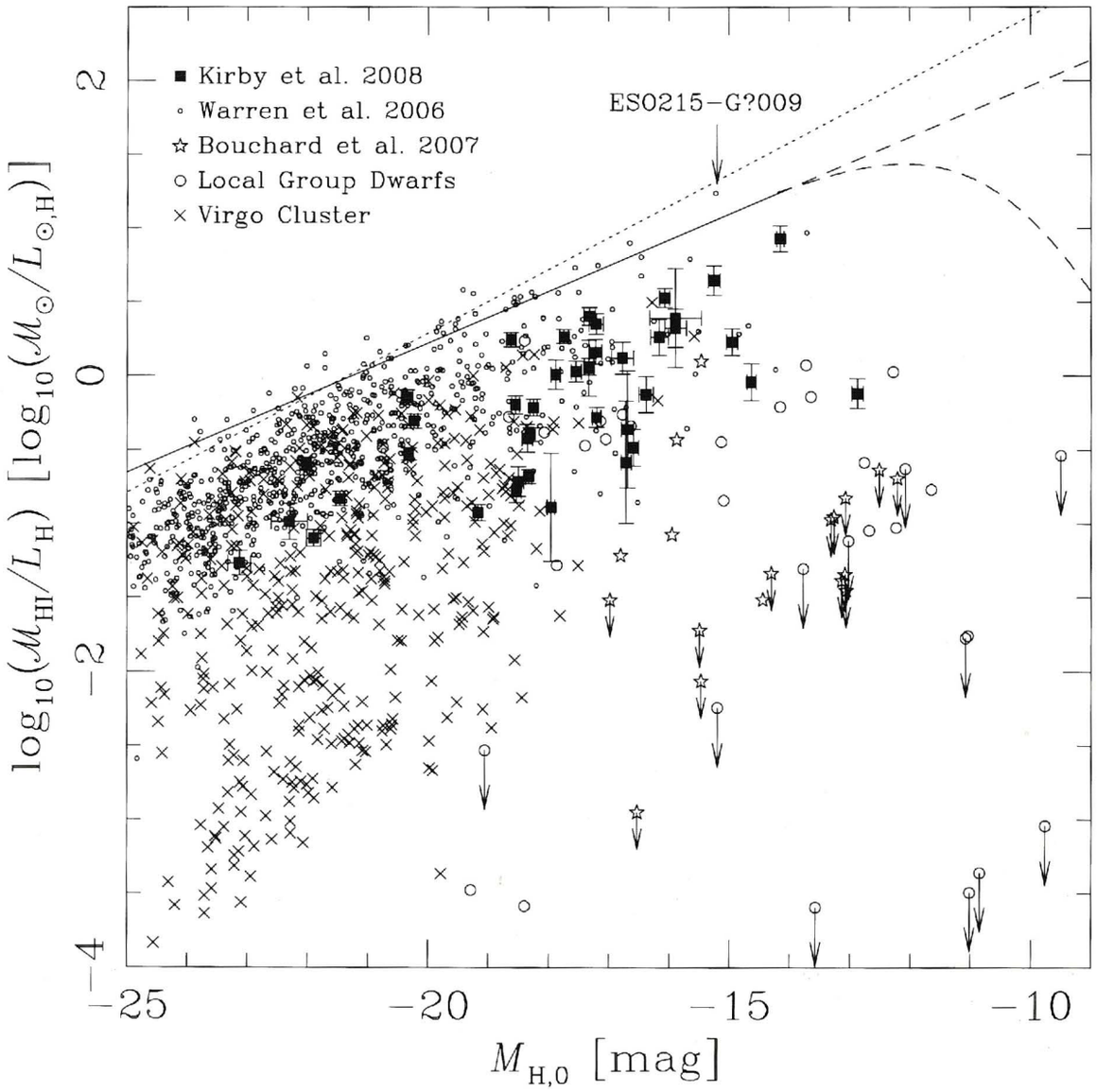


**Figure 4.3** The H I mass-to-light ratio ($\mathcal{M}_{HI}/L_H$) vs absolute H magnitude. The dotted line is the upper envelope of Warren et al. (2007) and the dashed line is the new upper envelope derived by us. We also highlight the position of the galaxy ESO215-G?009 which has the highest H I mass-to-light ratio known to date.

$$\log(\mathcal{M}_{HI}/L_H)_{max} = 0.17M_{H,0} + 3.71 \tag{4.3}$$

This equation for the upper envelope was derived by converting equation 4.2 into an expression for the mass-to-light ratio as a function of the *H*-band magnitude. Note that because equation 4.2 was derived for $6.5 < \log \mathcal{M}_\odot < 11.5$, the upper envelope for the mass-to-light ratio as a function of luminosity is only valid in the range $-25.4 < M_{H,0} < -12.9$. As for Figure 4.2, we also plot the upper bound for fainter objects as both a continuation of the linear equation, and for the case of a drop off in the H I mass for low mass systems.

The galaxy with the highest HI mass-to-light ratio currently known, ESO215-G?009 (Warren et al., 2004), is labeled in the graph. It has a present day star formation rate of $2.5 \times 10^{-3}\ M_\odot\ yr^{-1}$, as estimates from the 20cm continuum, and still hold 95 percent of its baryons in form of HI gas. The results from the Warren et al. (2006) investigation of galaxies with high HI mass-to-light ratios suggests that galaxies in which the stellar component is only a small fraction of the total baryonic content are genuinely rare objects.

To estimate the average star formation rate $\langle SFR \rangle$ over a time period $t$ as a function of total baryonic mass $\mathcal{M}_{bary} = \mathcal{M}_* + 1.4\,\mathcal{M}_{HI}$ and the HI mass-to-stellar mass ratio of a galaxy one can write:

$$\frac{\mathcal{M}_{HI}}{\mathcal{M}_*} = \frac{\mathcal{M}_{bary} - \mathcal{M}_*}{1.4\mathcal{M}_*} = \frac{\mathcal{M}_{bary}}{1.4t \cdot \langle SFR \rangle} - 0.71$$

$$\frac{\mathcal{M}_{bary}}{1.4t(\frac{\mathcal{M}_{HI}}{\mathcal{M}_*} + 0.71)} = \langle SFR \rangle$$

For example, a galaxy with a total baryonic mass of $2.4{\times}10^{10}\ M_\odot$ and $\mathcal{M}_{HI}/\mathcal{M}_* = 1$ has an average SFR of $0.56\ M_\odot\ yr^{-1}$ over a Hubble time ($1.4 \cdot 10^{10}\ yr$). In contrast, the most gas-dominated galaxies in our sample (e.g. $\mathcal{M}_* = 10^7, \mathcal{M}_{HI} = 10^8$) have an average SFR of $7 \times 10^{-4}\ M_\odot\ yr^{-1}$. While the interpretation of these numbers in absolute terms may be limited due to the oversimplified assumptions, the more robust ratio suggests that decreasing the total baryonic mass by a factor of 100, from a few $10^{10}$ to $10^8\ M_\odot$, reduces the average star formation rate in a galaxy by $\approx 1000$, which is essentially due to the increase in $\mathcal{M}_{HI}/L_H$ by a factor of 10. It will be interesting to see if direct star formation indicators like $H_\alpha$ emission in galaxies or systematic 20 cm continuum surveys can confirm these statistical results.

From the above estimates it becomes obvious that galaxies with a high $\mathcal{M}_{HI}/L_H$ are not missing the baryons to create stars, but are under-luminous because they lack either the internal or external stimulation for star formation (Warren et al., 2006). Such optically elusive galaxies started to emerge with recent blind HI surveys like HIPASS that only became feasible in recent years. These gas-dominated galaxies are often referenced as solutions to reconciling the faint-end of the galaxy luminosity function with the predicted cold dark matter halo mass function. Therefore, understanding how galaxies can maintain such low star formation is crucial for gaining a complete picture of galaxy formation and evolution. Hence the numbers and properties of galaxies with high mass-to-light ratios is currently a topic of much interest. Our work complements the work of Geha et al. (2006); Warren et al. (2006) showing that galaxies with high mass-to-light ratios must be low surface brightness, late-type dwarfs residing in spatial isolation.

## 4.5. The Stellar Mass fraction and maximum baryonic mass in Gas-rich galaxies

In Figure 4.4 we show a comparison between the stellar mass fraction or the star formation efficiency integrated over a Hubble time and the total baryonic mass in our sample galaxies. We calculate the total baryonic mass as

$$\mathcal{M}_{\rm baryonic} = \mathcal{M}_* + 1.4\mathcal{M}_{HI}. \quad (4.4)$$

This definition is consistent with that used by McGaugh et al. (2000); Geha et al. (2006) and Warren et al. (2007). We do note that Pfenniger & Revaz (2005) stated that the conversion factor for $\mathcal{M}_{gas}/\mathcal{M}_{HI}$ could be as large as 2.98. This result, however, is based on the assumption that the conversion factor is the sole parameter responsible for the observed scatter in the baryonic Tully-Fisher relation. The reduction in the rms of a linear least-squares fit to the baryonic Tully-Fisher relation between their optimal value of 2.98 and a highly unlikely value of 11.5 (where the gas content galaxies contains 10.5 times the amount of metals and molecular hydrogen than atomic hydrogen) is one percent. Begum et al. (2008a) further confirmed that this method of tightening the baryonic Tully-Fisher relation does not provide sufficient accuracy for measuring the $\mathcal{M}_{gas}/\mathcal{M}_{HI}$ conversion factor.

The solid line in Fig.4.4 was derived again by converting equation 4.2. Since equation 4.2 was derived for $6.5 < \log \mathcal{M}_\odot < 11.5$, the line that represents here the minimum stellar mass fraction as a function of total baryonic mass is only valid for $8.4 < \mathcal{M}_{bary} < 11.3 M_\odot$. Following this line, which is defined by the gas-rich field galaxies, to increasing baryonic masses we notice that the minimum stellar mass fraction goes to unity as the total baryonic mass approaches $\approx 10^{12}\mathcal{M}_*$. This suggests that there is an upper limit to the total baryonic mass a late-type galaxy can have. This upper limit is in excellent agreement with the observed upper limit for our early-type Virgo galaxy sample and the results found by Rocca-Volmerange et al. (2004). In the latter study, the apparent $K$ magnitudes of a sample of high redshift galaxies ($0.01 < z < 4$) were used to measure the maximum total baryonic mass of galaxies. Most striking is that the uniformity of the galaxy mass limit, $\mathcal{M}_{bar,max} = 10^{12} M_\odot$ seems independent of redshift. This result is also supported by the theoretical value discussed by Rees & Ostriker (1977) who estimated the critical mass of fragmentation for a self-gravitating cloud. Further theoretical support is provided by Silk (1977) who showed that HI clouds in the mass range $10^{8.5} - 10^{12.5} M_\odot$ will cool and collapse and eventually fragment, whereas more massive clouds will be unable to cool at all, or they will form galaxies at a reduced rate.

We notice that the VIRGOHI 21 candidate (Minchin et al. 2007) with a total HI and baryonic mass of $3 \times 10^7\, M_\odot$ lies on the x-axis at that mass.

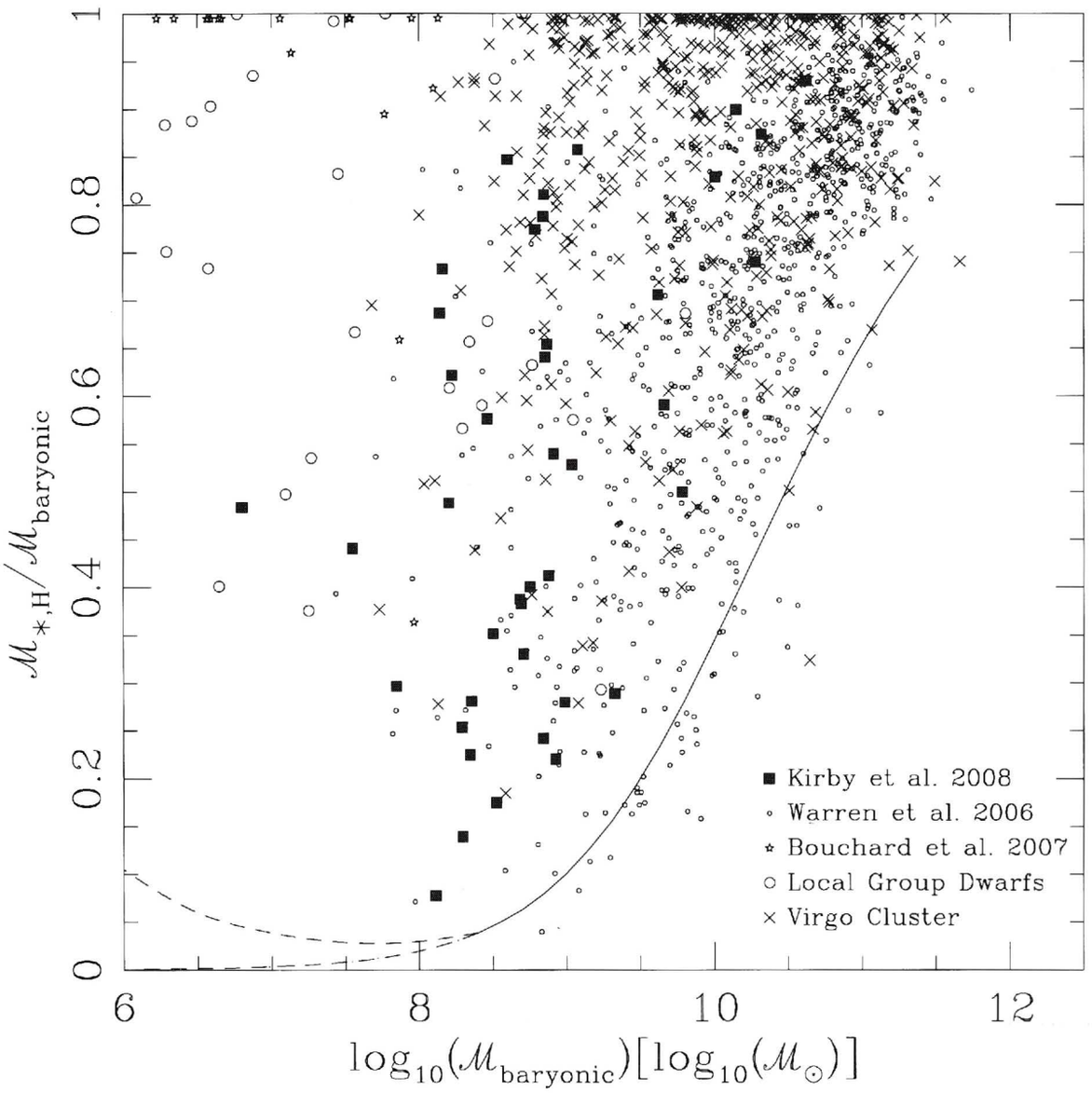


**Figure 4.4** The stellar fraction of the baryonic mass vs. the total baryonic mass. The solid line is the upper envelope of the H I mass-to-light ratio for a given luminosity (equation 4.3) and the dashed lines show possible extensions to lower mass systems.

The possible extension of the minimum mass fraction lower bound to smaller masses plotted in Figure 4.4 as the dashed lines is poorly defined due to small numbers. It could continue to fall to zero as the total baryonic mass decreases. This is equivalent to a linear extension of equation 4.2 (shown as the straight line in Figures 4.2 and 4.3). Alternatively, in section 4.3, it was speculated that the upper bound to the amount of H I gas for a given stellar mass would drop off at lower masses (shown as the curved line in Figures 4.2 and 4.3). For this second case, the minimum mass fraction will curve upwards at lower masses. This scenario currently finds strong support by the large number of faint dwarf galaxies discovered around the Milky Way and Andromeda that have small

numbers of stars but no evidence of H I (see Grcevich & Putman 2009, and references therein).

The average SFR of gas-rich galaxies over a Hubble time is thought to be suppressed as they lack either the internal or external stimulation for star formation. However, we note that Pflamm-Altenburg & Kroupa (2009) have argued that using an integrated galactic stellar initial mass function (IGIMF; Kroupa & Weidner 2003), the gas depletion timescale is constant for all galaxies (approximately 3 Gyr) and that dwarf galaxies do not have lower star formation efficiencies. This alternative hypothesis is not inconsistent with our results if and only if dwarf galaxies have only recently begun forming stars and thus have not depleted their H I gas; a situation which is supported by downsizing.

## 4.6. Discussion

The proposal of an upper envelope demands that there are no selection effects which influence the results. The original upper envelope of Warren et al. (2007) was based on the H I mass-to-light ratio. In our H I mass-to-light ratio versus absolute *H*-band magnitude (Figure 4.3), there are some obvious selection effects influencing our sample. In such a sample there is always a bias towards galaxies with lower absolute magnitude. Smaller galaxies are more difficult to detect and hence there are galaxies missing with the higher absolute magnitudes (particularly for $M_{H,0} > -15$). However, unless these have exceptionally high H I mass-to-light ratios, they will fall below the upper envelope.

A much more serious possible selection effect to consider is whether there are any bright galaxies with high $M_{HI}/L_H$ which have not been included in the sample. For a galaxy to exist with such properties and remain undetected, then it must be very massive (to have such a low absolute magnitude) yet also very low surface brightness (to remain optically undetected) and also have very low H I column density (to remain undetected in the radio).

Undetected galaxies with low H I column density have been searched by the HIDEEP project Minchin et al. (2003). HIDEEP was an extragalactic blind survey for very low column density neutral hydrogen. Minchin et al. (2003) were able to reach an H I column density limit of $4.2 \times 10^{18}$ cm$^{-2}$ yet found no galaxies with a column density less than $N_{HI} = 10^{20.65 \pm 0.38}$ which is at least an order of magnitude above sensitivity limit. Moreover, of their newly detected H I sources, there was not a single source without an optical counterpart. This suggests that there are no large gas rich, low surface brightness galaxies. It should be noted when applying the result of Minchin et al. (2003) that a galaxy which fills the beam at the peak flux survey limit has the lowest detectable H I column density. If such a galaxy is located at a greater distance then it would not be detected. This means that the result only applies to nearby, large, gas rich, low surface

brightness galaxies. A clear illustration of this selection effect is shown in Figure 1 of the Minchin et al. (2003) paper. Further discussion into possible physical explanations for HIDEEP's result are given by Disney & Minchin (2003).

The only known candidate for a galaxy which potentially violates the upper envelope hypothesis is the low surface brightness galaxy Malin 1 (Bothun et al. 1987). This was noted by Warren et al. (2007) in their original study. However, they noted that the nature of Malin 1 is still poorly understood. Various studies (Bothun et al. 1987; Impey & Bothun 1989; Pickering et al. 1997) have obtained HI mass-to-light ratios between 0.1 and 6 which for an absolute magnitude of $M_H = -25.36 \pm 0.4$ mag, could be on either side of the envelope. They also noted that upcoming results (F. Briggs, private communication) indicate that Malin 1 is actually a member of a small galaxy group, imposing further uncertainty on the origin of Malin 1's HI mass. New observations by Moore & Parker (2006) have also shown that the stellar disk extends out to at least $124\,h_{75}$ kpc, much further than that of previous observations $80\,h_{75}$ kpc; Pickering et al. 1997). An analysis of HST images by Barth (2007) has also confirmed that Malin 1 contains a normal stellar disk that was not previously recognised. Therefore, while Malin 1 remains an unusual galaxy, it appears to be a normal early type, barred spiral embedded in a huge, low surface brightness stellar and HI disk. Moreover, the discovery of the extended stellar disk indicates that the HI mass-to-light ratio is lower than previous estimates, supporting the hypothesis that no galaxies lie above the upper envelope.

## 4.7. Summary

We have presented a study of 1394 nearby galaxies with near-IR ($H$-band) and 21cm data available in the literature and investigated the relation between the atomic hydrogen and the stellar components of a galaxy.

The distribution of late-type galaxies with stellar masses larger than $10^7 M_\odot$ strongly suggests that there is an upper limit to the amount of H I gas a galaxy can have for a given stellar mass. The upper bound is defined exclusively by late type galaxies.

Gas-rich galaxies have increasingly larger stellar mass fractions when going to larger baryonic masses. A galaxy with $10^{10} M_\odot$ or more total stellar mass is always star-dominated. This result is consistent with the "downsizing" picture of galaxy formation, where the star formation rate changes from high to low-mass systems with decreasing redshift.

The star formation efficiency integrated over a Hubble time is higher for galaxies with larger baryonic masses. Decreasing the total baryonic mass by a factor of 100 reduces the average star formation rate by approximately 1000.

The maximum total baryonic mass of a galaxy (both observational and theoretical) corresponds to the mass of a galaxy which has converted all of its gas into stars. Our empirical results strongly suggest an upper baryonic mass limit of $10^{12} \mathcal{M}_{\odot}$.

# CHAPTER 5

# Summary

## 5.1. Summary

In this thesis, an investigation into the baryonic components of nearby galaxies was presented. Chapter 2 outlined an ultra-deep near-IR, *H*-band study of 57 galaxies which focused on the stellar component of these galaxies. In Chapter 3, a 21 cm line survey of nearby galaxies was described and the kinematic properties of 12 of these galaxies was examined. There, the gaseous component of the galaxies was the primary scientific focus. The relation between the two baryonic components, the stellar and the gaseous, was investigated in Chapter 4. Here we summarise our findings and look at how further studies can extend our knowledge of stellar and gas properties of nearby galaxies.

### 5.1.1. The Stellar Properties of Local Volume Galaxies

The near-IR is the best wavelength to study the stellar component of nearby galaxies as the attenuation and distortion of light profiles due to internal and Galactic dust is minimal. Moreover, the near-IR traces the quiescent old stellar component and is not distorted by transient star-formation events. Bouchard et al. (2009) investigated the environmental influence on the evolution of local galaxies and cited our *H*-band study as advocacy for using the near-IR rather than optical wavelengths as a better tracer of the stellar mass.

We have presented the deepest *H*-band images available to date for 57 galaxies in the Local Sphere of Influence ($D < 10$ Mpc). The surface brightness limit reaches down to $\mu_{lim} < 26$ mag arcsec, 4 magnitudes fainter than 2MASS. The images, cleaned from Galactic foreground contamination, reveal the morphology and extent of many of the galaxies for the first time.

For 56 galaxies, we derive radial luminosity profiles, ellipticities, and position angles, together with global parameters such as total magnitude, mean effective surface brightness, half-light radius, Sérsic parameters, and stellar mass. The absolute $H$-band magnitudes for 8 of these galaxies have since been used by Pflamm-Altenburg & Kroupa (2009) to obtain their $B-H$ colour. The Sérsic parameters that best describe the observed surface brightness profile of ESO059-G001 have been used by van Eymeren et al. (2009). The kinematics of this irregular galaxy were analysed in detail as part of an investigation into the cusp-core discrepancy between the observed mass distribution of galaxies and the predictions of cold dark matter simulations. Additionally they decompose the H I rotation curve into different mass components using our $H$-band Sérsic parameters.

No genuine young galaxies (ie., those forming stars for the first time) were found in our $H$-band survey. Some sample galaxies were previously identified on $B$-band photographic plates but remain undetected in the near-IR. In each case there was a plausible alternative explanation for the non-detection:

- AM0717-571: DSS $B_J$-band morphology resembles that of a Galactic nebula, but true nature still remains unclear.
- HIZOAJ1616-55 and SJK98 J1616-55: possibly one or two high velocity clouds.
- KK2000-03: Superimposed star hampers analysis however the marginal detection in the H-band suggests an unusual blue galaxy.
- KK2000-04: Originally assumed to be a companion of NGC1313 however possibly a photographic plate flaw.
- KK2000-06: Originally assumed to be a companion of NGC1313. More likely a background galaxy at $\approx$2250 km s$^{-1}$.
- NGC2784 DW1: intrinsic extreme low surface brightness dwarf satellite of NGC2784.

We found that there is a tight correlation between the $B$- and $H$-band magnitudes of a galaxy and this correlation has been demonstrated over a range of 15 magnitudes. The linear transformation between the $B$- and $H$-bands has a small scatter (0.3 mag) for bright galaxies and is described by the equation:

$$M_{H,0} = (1.14 \pm 0.02)M_{B,0} - (0.74 \pm 0.32)$$

In the dwarf regime, there is a marginal increase in scatter and possibly a slight trend for galaxies to be redder (by approximately 1 magnitude) than indicated by the transformation found for bright galaxies. This new transformation between

the total $B$- and $H$-band magnitudes of a galaxy has been used by Pflamm-Altenburg & Kroupa (2009) in a study of galaxy star formation rates to obtain the $B-H$ colour of galaxies with only $B$-band imaging available to date.

We derive the $H$-band mass-to-light ratio to be $\Upsilon_*^H = 1.0 \pm 0.4$ in section 2.4.2 using three independent methods. This analysis has been used by Ramya et al. (2009) while studying star formation properties of blue compact dwarf galaxies to obtain stellar masses for their sample galaxies. We also used the galaxy luminosity – mean effective surface brightness relation to derive a semi-empirical stellar mass-to-light ratio of $\Upsilon_*^H = 0.78 \pm 0.08$.

We found that the short integration time of 2MASS resulted in serious underestimation of a galaxy's luminosity. The magnitudes of galaxies, with $H$-band surface brightnesses fainter than 18 mag arcsec$^{-2}$, obtained in our study are up to 2.5 mag brighter than those obtained by 2MASS. This has since been used to discuss the bias in the sample selection of van Driel et al. (2009). As the mean effective surface brightness correlates with the luminosity of a galaxy, we expect serious selection biases for a 2MASS-based $H$-band galaxy luminosity function fainter than $M_H = -20$ mag. This result has been confirmed by Dale et al. (2009) as part of the Local Volume Legacy program, who likewise find that the fainter sources in the 2MASS Extended Source Catalog have their global fluxes underestimated. Dale et al. (2009) show (see Figure 5 of their paper) the ratio of the 'true' flux to the 2MASS flux, and include our $H$-band magnitudes demonstrating the consistency between our results.

### 5.1.2. The Gas Properties of Local Volume Galaxies

In this thesis, the first results from the Local Volume H I Survey (LVHIS) have been presented. LVHIS is a new deep H I line and 20 cm continuum survey of all nearby, gas rich galaxies, which provides the perfect complement to our deep near-IR survey. This survey includes approximately 2200 hours of new observations at the Australia Telescope Compact Array as well as complementary archival data. For all program galaxies H I distribution, mean velocity field and velocity dispersion maps have been made as well as channel maps and spectra of the H I emission. For many galaxies in the sample, the new LVHIS observations are the only resolved imaging available to date which reveal the H I distribution and galaxy kinematics for the first time.

We have presented a kinematical study of 12 galaxies in the Local Volume ($D < 10$ Mpc). Rotation curve analysis has been carried out for all sample galaxies by applying a tilted ring model to the observed velocity field. The best fitting rotation curve parameters are provided. Our rotation curve results for ESO059-G001 and ESO215-G?009 have since been confirmed by van Eymeren et al. (2009).

Out of the 12 galaxies analysed, we highlight four as having interesting kinematical results:

- AM0605-341 was found to have an extension of redshifted H I located to its east. We propose that this is due to a tidal interaction with its nearby neighbour NGC2188, which has previously been found to have a similar tidal extension.
- ESO121-G020 was found to have a much lower inclination (40 degrees) than the current value available in the literature (78 degrees; Warren et al. 2006) and have highlighted the need for visual inspection of the model velocity field. We derive the new lower limit for its dynamical mass as $1.7 \times 10^9$ $M_\odot$.
- We observed that the observed ellipticity of ESO215-G?009 is inconsistent with its kinematical inclination ($35 \pm 3$ degrees). The observed H I distribution is highly circular implying that the galaxy is nearly face-on. This may be evidence that the assumption of the gas being located in an infinitely thin disk is incorrect.
- We find evidence that ESO245-G005 has a warp in its outer disk, located at an angular radius of 200 arcsec. This lends support to the Côté et al. (2000) hypothesis that ESO245-G005 has undergone recent accretion.

We show that the H I line width can be used to accurately derive the true rotational velocity of galaxies in the velocity range $50 < v < 150$km s$^{-1}$ using the newly updated Tully & Fouque (1985) model:

$$\begin{aligned} v_{max}^2 &= w_{50,corr}^2 + (2 \pm 14)^2 \left[1 - 2e^{-(w_{50,corr}/100)^2}\right] \\ &\quad -w_{50,corr}(4 \pm 28)\left[1 - e^{-(w_{50,corr}/100)^2}\right] \\ v_{max}^2 &= w_{20,corr}^2 + (34 \pm 10)^2 \left[1 - 2e^{-(w_{20,corr}/120)^2}\right] \\ &\quad -w_{20,corr}(68 \pm 20)\left[1 - e^{-(w_{20,corr}/120)^2}\right] \end{aligned}$$

The classical and baryonic Tully-Fisher relations are found to be:

$$M_{B,0} = (-7.29 \pm 0.33)\log(2v_{max}) - (1.40 \pm 0.71)$$
$$\log(M_{baryonic}) = (2.51 \pm 0.11)\log(2v_{max}) - (3.94 \pm 0.23)$$

### 5.1.3. The Connection Between the Stellar and Gas Components

We have presented a study of 1394 nearby galaxies with near-IR ($H$-band) and 21 cm data available in the literature and investigated the relation between the atomic hydrogen and the stellar components of a galaxy.

The distribution of late-type galaxies with stellar masses larger than $10^7 M_\odot$ strongly suggests that there is an upper limit to the amount of H I gas a galaxy can have for a given stellar mass which is described by the equation:

$$\log (\mathcal{M}_{HI})_{max} = 0.55 \log \mathcal{M}_* + 4.1.$$

The upper bound is defined exclusively by late type galaxies. We also confirm that the Warren et al. (2006, 2007) hypothesis of an upper envelope for the H I mass-to-light ratio, $\mathcal{M}_{HI}/L$, with our larger sample which includes galaxies of all morphological types. We obtain an improved estimate of the upper envelope best described by the analytical line:

$$\log (\mathcal{M}_{HI}/L_H)_{max} = 0.17 M_{H,0} + 3.71$$

Gas-rich galaxies have increasingly larger stellar mass fractions when going to larger baryonic masses. A galaxy with $10^{10} M_\odot$ or more total stellar mass is always star-dominated. This result is consistent with the "downsizing" picture of galaxy formation, where the star formation rate changes from high to low-mass systems with decreasing redshift.

The star formation efficiency integrated over a Hubble time is higher for galaxies with larger baryonic masses. Decreasing the total baryonic mass by a factor of 100 reduces the average star formation rate by approximately 1000.

The maximum total baryonic mass of a galaxy (both observational and theoretical) corresponds to the mass of a galaxy which has converted all of its gas into stars. Our empirical results strongly suggest an upper baryonic mass limit of $10^{12} M_\odot$, a value for which observational and theoretical support is available (Rocca-Volmerange et al., 2004; Rees & Ostriker, 1977; Silk, 1977).

## 5.2. Future Work

This thesis has presented two new deep imaging data sets; the LSI *H*-band survey and the LVHIS 21 cm line survey. These data sets provide a wealth of information, the analysis of which has only just begun. There are many scientific investigations which could be undertaken using these data sets, however, here we discuss those most relevant to this study.

No genuine young galaxies were found in our deep *H*-band survey. While some sample galaxies which were previously identified on *B*-band photographic plates remain undetected in the near-IR, in each case there was a plausible alternative explanation for the non-detection. Previous studies of BCD galaxies, which were thought to be primeval galaxies forming their first stars, have also revealed the presence of an older stellar population (Schulte-Ladbeck et al. 1998, 2000, 2001; Aloisi et al. 2005, 2007; Corbin et al. 2008). This naturally leads

to the question of whether genuinely young galaxys exist. The "downsizing" picture of galaxy formation, where the star formation rate changes from high to low-mass systems with decreasing redshift (Cowie et al., 1996; Juneau et al., 2005; Mobasher et al., 2009), indicates that the nearby universe may have dwarf galaxies which are forming stars for the first time. This is further supported by the constant gas depletion timescale presented by Pflamm-Altenburg & Kroupa (2009) which requires that some dwarf galaxies have only recently begun forming stars otherwise all dwarfs would have depleted their H I gas. Continuation of the LSI survey to include all nearby ($D < 10$ Mpc) galaxies would allow for a complete distance limited search for genuine young galaxies. The LSI survey collaboration already has plans to continue the southern hemisphere observations using the 1.4 m IRSF telescope in Sutherland, South Africa. There are also plans for a northern hemisphere extension using the UK InfraRed Telescope (UKIRT).

The relationship between the two baryonic components is complex, because these components are intimately connected. Star formation reduces the gaseous component and increases the stellar component, whereas supernovae return the stellar mass back. We have 20 cm continuum data as part of the LVHIS survey which can be used to derive accurate star formation rates or upper limits for our sample galaxies (see Condon 1992 for a review of radio emission as a dust insensitive tracer of star formation). It is important to note that the star formation rates obtained from the 20 cm continuum flux will need to be compared with the star formation rates estimated from SINGS (Kennicutt et al. 2003) and the radio-infrared correlation confirmed on all scales. An empirical exploration of the multi-dimensional parameter space (stellar mass, gas mass, baryonic mass, dynamical mass, star formation rate, etc) using a complete, volume limited sample, over as broad a mass range as possible ($10^4 - 10^{11} M_\odot$), will provide a deeper understanding of the processes that govern galaxy formation and evolution.

Over the next decade there will be a revolution in observational astronomy with many new instruments and telescopes becoming available. The SkyMapper Telescope will conduct a multi-colour, multi-epoch survey of the southern hemisphere known as the Southern Sky Survey. Part of this will include the Stromlo Missing Satellites Survey (Jerjen 2010) which will be the deepest, most extended, optical search for Milky Way satellites ever done. Extensive follow up observations of newly detected Local Volume galaxies with optical, infrared, and radio telescopes will provide an unprecedented physical understanding of dwarf galaxies and address fundamental questions in near-field cosmology.

A new near-IR northern hemisphere blind survey is to be carried out using the Visible and Infrared Survey Telescope for Astronomy (VISTA) which will provide near-IR images approximately 4 magnitudes fainter than 2MASS. The VISTA Hemisphere Survey (VHS; PI: Richard McMahon) will allow many of the results presented in Chapter 2 to be confirmed for large numbers of galaxies.

For example, the systematic underestimation of galaxy fluxes by 2MASS will be calibrated. Our new optical – near-IR ($B$ and $H$-band) transformation will be populated with large numbers of dwarf galaxies which will allow for a statistically significant investigation into the flaring out in the dwarf regime. The luminosity – surface brightness relation will also benefit from the vastly increased sample size and provide semi-empirical mass-to-light ratios for the VHS observing bands.

There are currently several new H I surveys being undertaken with the ALFA (Arecibo L-band Feed Array) multibeam system on the Arecibo Telescope. The Arecibo Legacy Fast ALFA (ALFALFA[1]; Giovanelli et al. 2005) survey is a blind extragalactic HI survey which will detect more than 25,000 extragalactic HI line sources out to z 0.06 and has a flux sensitivity approximately 8 times that of HIPASS. The Arecibo Galaxy Environment Survey (AGES; Auld et al. 2006; Cortese et al. 2008) is an intermediate depth (integration time of 300 s/beam) HI survey with the ALFA multibeam instrument studying galaxies from the Local Void through isolated galaxies, galaxy pairs and galaxy groups to the Virgo Cluster. There is also a zone of avoidance (ZOA) survey studying galaxies hidden behind the Milky Way (?) and an ultra deep survey been carried out (?).

A new 21 cm complement to the upcoming optical and near-IR surveys is the Widefield ASKAP L-band Legacy All-sky Blind surveY (WALLABY, PI: Baerbel Koribalski) using ASKAP, the Australian Square Kilometre Array Pathfinder, which is a next generation radio telescope expected to be fully operational by 2013. WALLABY will have a flux sensitivity some 20 times better than HIPASS and detect dwarf galaxies ($M_{HI}$ = $10^8$ $M_\odot$) out to a distance of approximately 60 Mpc. It aims to examine the H I properties and large-scale distribution of about 500,000 galaxies out to a redshift of 0.26 in order to study galaxy formation, the missing satellite problem, galaxy evolution, galaxy mergers, the H I mass function, cool gas at low redshift, gas-rich galaxies, and the nature of the cosmic web.

The combination of the SkyMapper Southern Sky Survey and WALLABY will provide a tremendous database for continuing the exploration of the stellar and gas content of nearby galaxies. In particular, it will allow us to hunt for the elusive "dark" galaxies and those with high H I mass-to-light ratios. The increased sample size will allow an investigation of the H I and stellar content in the dwarf regime and answer the question of whether the upper limit to a galaxy's H I mass continues linearly with stellar mass or whether it drops off more steeply. Finally, one can not ignore the potential for fortuitous discoveries which could revolutionise the current understanding galaxy evolution. Thus we conclude with the outlook that the future for near-field studies of the formation and evolution of galaxies has never been more promising.

[1]see for example Zitrin & Brosch (2008); Kent et al. (2009); Kniazev et al. (2009); Grossi et al. (2009) for some of the first results from this survey.

# APPENDIX A

# The Local Volume HI Survey

The Local Volume H I Survey[1] (LVHIS; Koribalski et al. 2010) obtained deep H I line and 20cm continuum observations for all nearby, gas rich galaxies. The scientific motivation for this large survey was to obtain a high quality data set for a complete, distance limited sample to determine the true Tully-Fisher relation, investigate local galaxy environments, obtain accurate star formation rates, determine the H I mass function and derive H I rotation curves. As part of this thesis approximately 470 hours (out of the total 2200 hours) of observing for the LVHIS survey was carried out. Also, included was a contribution to the general survey data reduction and imaging effort. The focus of this thesis is to derive good rotation curves for a suitable sub-set of LVHIS galaxies using their HI velocity fields, which will be discussed in Chapter 3. In this chapter we outline the observations and the data reduction process for the LVHIS data.

## A.1. Observations

The LVHIS sample is a subset of the galaxies known to reside in the Local Volume (Karachentsev et al. 2008 and references therein). All galaxies are located less than 10 Mpc away from the Milky Way. To ensure an H I detection, only galaxies which were detected by the H I Parkes All-Sky Survey (HIPASS; Barnes et al. 2001) were included. The LVHIS survey was carried out using the Australia Telescope Compact Array (ATCA) at the Paul Wild Observatory outside Narrabri, New South Wales, Australia, between January 2005 and January 2009. The ATCA is a radio interferometer with an array of six 22-metre dishes, five of which can move along a 3 km east-west track and the adjoining 214 m northern spur. The sixth antenna is stationary and is located 3 km to the west of the east-west track. The longest possible baseline of the ATCA is therefore 6 km. A declination limit

[1]LVHIS website: http://www.atnf.csiro.au/research/LVHIS/

of -30 degrees was chosen for all observations with the ATCA as for higher declinations the beam shape becomes highly elongated and gives poor resolution in the north-south direction.

Each galaxy was observed for $3 \times 12$ hours using the EW352/367, 750 and 1.5 arrays. If equivalent archival H I (and 20cm continuum) data was available, these would be utilised. Additionally, $\sim$ 10 large galaxies were observed using the ultra compact H75 array configuration, which has two of the antennas on the northern spur, ensuring that the more extended, diffuse H I emission is detected. A total of $\sim$ 2200 hours of new observations were required with the ATCA.

The LVHIS sample is listed in Tables A.1 to A.3. In Table A.1, published archival data included in the LVHIS sample is listed, with an indication of the reference used. In Table A.2, unpublished ATCA archival data is listed with an indication of the project ID and the array configurations of the available data. Finally, in Table A.3, the LVHIS galaxies which required new observations with the ATCA are listed.

**Table A.1** LVHIS galaxies with data obtained from published H I studies.

| HIPASS Name | Galaxy Name | $D^*$ [Mpc] | $v_{LG}^{**}$ [km s$^{-1}$] | H I data reference |
|---|---|---|---|---|
| HIPASS J0135-41 | NGC 625 | 4.07 | 309 | Cannon et al. (2004) |
| HIPASS J0317-66 | NGC 1313 | 4.15 | 262 | Ryder et al. (1995) |
| HIPASS J0454-53 | NGC 1705 | 5.10 | 401 | Meurer et al. (1998) |
| HIPASS J0926-76 | NGC 2915 | 3.78 | 204 | Meurer et al. (1996) |
| | cont ... | | | Bureau et al. (1999) |
| HIPASS J1057-48 | ESO215-G?009 | 5.25 | 312 | Warren et al. (2004) |
| HIPASS J1118-32 | NGC 3621 | 6.70 | 466 | Walsh (1997) |
| HIPASS J1305-49 | NGC 4945 | 3.82 | 325 | Ott et al. (2001) |
| HIPASS J1413-65 | Circinus | 2.82 | 209 | Jones et al. (1999) |
| HIPASS J0015-39 | NGC 0055 | 1.8 | 95 | Puche et al. (1991b) |
| HIPASS J0054-37 | NGC 0300 | 2.15 | 98 | Puche et al. (1990) |
| HIPASS J1324-42 | NGC 5128 | 3.66 | 338 | Schiminovich et al. (1994) |
| HIPASS J2357-32 | NGC 7793 | 3.91 | 232 | Carignan & Puche (1990a) |
| HIPASS J0047-25 | NGC 0253 | 3.94 | 254 | Boomsma et al. (2005) |
| HIPASS J0047-20 | NGC 0247 | 3.65 | 187 | Carignan & Puche (1990b) |

(*) Listed independent distances, D, are Karachentsev et al. (2004 and references therein) and Karachentsev et al. (2006); (**) the Local Group velocity, $v_{LG}$ are from the HIPASS Bright Galaxy Catalog (Koribalski et al., 2004) if available or the HIPASS Catalog Meyer et al. (2004).

**Table A.2** LVHIS galaxies with data obtained from unpublished or ongoing ATCA H I studies.

| HIPASS Name | Galaxy Name | $D$ [Mpc] | $v_{LG}$ [km s$^{-1}$] | project ID (arrays) |
|---|---|---|---|---|
| HIPASS J0256-54 | ESO154-G023 | 5.55 | 399 | CX062 (EW367) |
| HIPASS J0605-33 | ESO364-G?029 | | 549 | C661 (375,750C,750e) |

Continued on next page

**Table A.2 – continued from previous page**

| HIPASS Name | Galaxy Name | $D$ [Mpc] | $v_{LG}$ [km s$^{-1}$] | ATCA project ID (arrays) |
|---|---|---|---|---|
| HIPASS J0615-57 | ESO121-G020 | 6.05 | 311 | C1046 (EW352,750D,1.5B) |
| HIPASS J1327-41 | ESO324-G024 | 3.73 | 302 | C598 (375,750D) |
| HIPASS J1337-42 | NGC 5237 | 3.33 | 150 | C598 (375,750D) |
| HIPASS J1341-29 | NGC 5264 | 4.53 | 300 | C598 (375,750D) |
| HIPASS J1349-36 | ESO383-G087 | 3.45 | 137 | C598 (375,750D) |
| HIPASS J1403-41 | NGC 5408 | 4.81 | 314 | C598 (375,750D) |
| HIPASS J1305-40 | CEN06 | 5.89 | 392 | C1133 (750D) |
| HIPASS J1443-44 | ESO272-G025 | | 429 | C1133 (EW352) |
| HIPASS J1337-42 | NGC 5237 | 3.33 | 150 | C765 (1.5C,1.5D) |
| HIPASS J1321-31 | – | 5.22 | 375 | C970 (750D,1.5D) |
| HIPASS J1337-39 | – | 4.90 | 287 | C970 (750D,1.5D) |
| HIPASS J1219-79 | IC 3104 | 2.27 | 184 | C1128 (750D,1.5B) |
| HIPASS J1247-77 | – | 3.16 | 169 | C1128 (750D,1.5B) |
| HIPASS J1747-64 | IC 4662 | 2.44 | 153 | C1128 (750D,1.5B) |
| HIPASS J2202-51 | IC 5152 | 2.07 | 69 | C1253 (EW367,750A) |
| HIPASS J2326-32 | UGCA438 | 2.23 | (82) | C1253 (EW367,750A,1.5D) |

See Table A.1 for distance and velocity references. We note that in HIPASS the galaxy UGCA438 is confused with Galactic H I gas and the Local Group velocity, $v_{LG}$ is marked in parenthesis to highlight this.

**Table A.3** The LVHIS sample.

| HIPASS Name | Galaxy Name | $D$ [Mpc] | $v_{LG}$ [km s$^{-1}$] | ATCA configuration | | | |
|---|---|---|---|---|---|---|---|
| HIPASS J0008-34 | ESO349-G031 | 3.21 | 212 | EW352 | 750B | 1.5A | |
| HIPASS J0145-43 | ESO245-G005 | 4.43 | 290 | EW352 | 750D | 1.5C | |
| HIPASS J0237-61 | ESO115-G021 | 4.66 | 333 | EW352 | 750D | 1.5C | H75 |
| HIPASS J0256-54 | ESO154-G023 | 5.55 | 399 | EW367 | 750D | 1.5C | H75 |
| HIPASS J0258-49 | ESO199-G007 | | 479 | EW352 | 750B | 1.5C | |
| HIPASS J0320-52 | NGC 1311 | 5.20 | 387 | EW352 | 750B | 1.5C | |
| HIPASS J0321-66 | AM0319-662 | 4.07 | 479 | EW367 | 750D | 1.5C | |
| HIPASS J0333-50 | IC 1959 | 6.02 | 456 | EW352 | 750B,D | 1.5C | |
| HIPASS J0457-42 | ESO252-IG001 | | 440 | EW352 | 750D | 1.5C | |
| HIPASS J0605-33 | ESO364-G?029 | | 549 | *375* | *750C* | *750e* | |
| HIPASS J0607-34 | AM0605-341 | | 515 | EW352 | 750D | 1.5C | |
| HIPASS J0610-34 | NGC 2188 | | 505 | EW352 | 750D | 1.5C | |
| HIPASS J0615-57 | ESO121-G020 | 6.05 | 311 | *EW352* | *750D* | *1.5B* | |
| HIPASS J0639-40 | ESO308-G022 | | 551 | EW367 | 750B | 1.5C | |
| HIPASS J0705-58 | AM0704-582 | 4.90 | 284 | EW352 | 750C | 1.5A | |
| HIPASS J0731-68 | ESO059-G001 | 4.57 | 255 | EW352 | 750C | 1.5B | |
| HIPASS J1043-37 | ESO376-G016 | | 386 | EW352 | 750D | 1.5B | |
| HIPASS J1047-38 | ESO318-G013 | | 428 | EW352 | 750C | 1.5B | |
| HIPASS J1131-31 | – | | 465 | EW352 | 750C | 1.5B | |
| HIPASS J1132-32 | – | | 424 | EW352 | 750C | 1.5B | |
| HIPASS J1137-39 | ESO320-G014 | 5.65 | 362 | EW352 | 750C | 1.5B | |
| HIPASS J1154-33 | ESO379-G007 | 5.22 | 391 | EW367 | 750A | 1.5B | *GMRT* |

Continued on next page

**Table A.3 – continued from previous page**

| HIPASS Name | Galaxy Name | $D$ [Mpc] | $v_{LG}$ [km s$^{-1}$] | ATCA configuration | | | |
|---|---|---|---|---|---|---|---|
| HIPASS J1204-35 | ESO379-G024 | | 356 | EW352 | 750A | 1.5B | |
| HIPASS J1214-38 | ESO321-G014 | 3.19 | 361 | EW352 | 750A | 1.5B | *GMRT* |
| HIPASS J1219-79 | IC 3104 | 2.27 | 184 | EW367 | *750D* | *1.5B* | |
| HIPASS J1244-35 | ESO381-G018 | 5.33 | 367 | EW352 | 750A | 1.5B | |
| HIPASS J1246-33 | ESO381-G020 | 5.47 | 366 | EW352 | 750A | 1.5B | |
| HIPASS J1247-77 | – | 3.16 | 169 | EW367 | *750D* | *1.5B* | |
| HIPASS J1305-40 | CEN06 | 5.89 | 392 | EW367 | *750D* | 1.5B | |
| HIPASS J1310-46A | ESO269-G058 | 3.70 | 167 | EW352 | 750A | 1.5D | |
| HIPASS J1321-31 | – | 5.22 | 375 | EW367 | 750D | 1.5D | |
| HIPASS J1321-36 | NGC 5102 | 3.40 | 260 | EW367 | 750D,*D* | 1.5B | H75 |
| HIPASS J1324-30 | AM1321-304 | 4.63 | 264 | EW367 | 750A | 1.5B | *GMRT* |
| HIPASS J1326-30A | IC4247 | 4.97 | 195 | EW367 | 750A | 1.5B | |
| HIPASS J1327-41 | ESO324-G024 | 3.73 | 302 | *375* | *750D* | 1.5B | |
| HIPASS J1336-29 | UGCA365 | 5.15 | 360 | EW367 | *M83 mosaic* | | *GMRT* |
| HIPASS J1339-31 | NGC 5253 | 4.00 | 223 | EW367 | 750A | 1.5A | H75 |
| HIPASS J1340-28 | IC4316 | 4.41 | 382 | EW367 | 750A | 1.5B | *GMRT* |
| HIPASS J1341-29 | NGC 5264 | 4.53 | 300 | *375* | *750D* | 1.5A | |
| HIPASS J1345-41 | ESO325-G?011 | 3.40 | 340 | EW367 | 750A,D | 1.5B,C | |
| HIPASS J1349-36 | ESO383-G087 | 3.45 | 137 | *375* | *750D* | 1.5A | |
| HIPASS J1403-41 | NGC 5408 | 4.81 | 314 | *375* | *750D* | 1.5A | |
| HIPASS J1428-46 | UKS1424-460 | 3.58 | 202 | EW367 | 750A | 1.5D | *GMRT* |
| HIPASS J1434-49 | ESO222-G010 | | 431 | EW367 | 750A | 1.5D | |
| HIPASS J1441-62 | – | | 461 | EW367 | 750A | 1.5D | |
| HIPASS J1443-44 | ESO272-G025 | | 429 | *EW352* | 750A | 1.5D | |
| HIPASS J1501-48 | ESO223-G009 | 6.17 | 414 | EW367 | 750A | 1.5D | |
| HIPASS J1514-46 | ESO274-G001 | 3.02 | 360 | EW367 | 750A | 1.5D | H75 |
| HIPASS J1526-51 | – | | 438 | EW367 | 750A | 1.5D | |
| HIPASS J1620-60 | ESO137-G018 | 6.34 | 439 | EW367 | 750A | 1.5D | |
| HIPASS J1747-64 | IC 4662 | 2.44 | 153 | EW367 | 750A | 1.5D | |
| HIPASS J1337-39 | – | 4.90 | 287 | EW367 | *750D* | *1.5D* | |
| HIPASS J1337-42 | NGC 5237 | 3.33 | 150 | *375* | *750D* | *1.5C,D* | |
| HIPASS J1348-37 | – | 5.70 | 360 | EW352 | 750A,E | 1.5B | |
| HIPASS J1348-53 | ESO174-G?001 | | 466 | EW352 | 750A,B | 1.5B | |
| HIPASS J1351-47 | – | 5.32 | 291 | EW367 | 750A,B | 1.5B | |
| HIPASS J1802-39 | – | | 505 | EW367 | 750B | – | |
| HIPASS J2003-31 | ESO461-G036 | 7.83 | 471 | EW367 | 750B | 1.5A | *GMRT* |
| HIPASS J2052-69 | IC 5052 | 6.03 | 445 | EW367 | 750B | 1.5B | H75 |
| HIPASS J2202-51 | IC 5152 | 2.07 | 69 | *EW367* | *750A* | 1.5B | H75 |
| HIPASS J2326-32 | UGCA438 | 2.23 | (82) | *EW367* | *750A* | *1.5D* | |
| HIPASS J2343-31 | UGCA442 | 4.27 | 282 | EW367 | 750B | 1.5C | H75 |
| HIPASS J2352-52 | ESO149-G003 | 6.4 | 491 | EW352 | 750B | 1.5C | |

See Table A.1 for distance and velocity references. *Italicised* ATCA configurations indicate the data was from archival observations, with the rest coming from new observations as part of the LVHIS survey.

The combined data from the 3 array configurations has 45 baselines (or 30 if excluding the distant sixth antenna, CA06). The combined data from the three array configurations results in an angular resolution of 35 arcsec and sensitivity

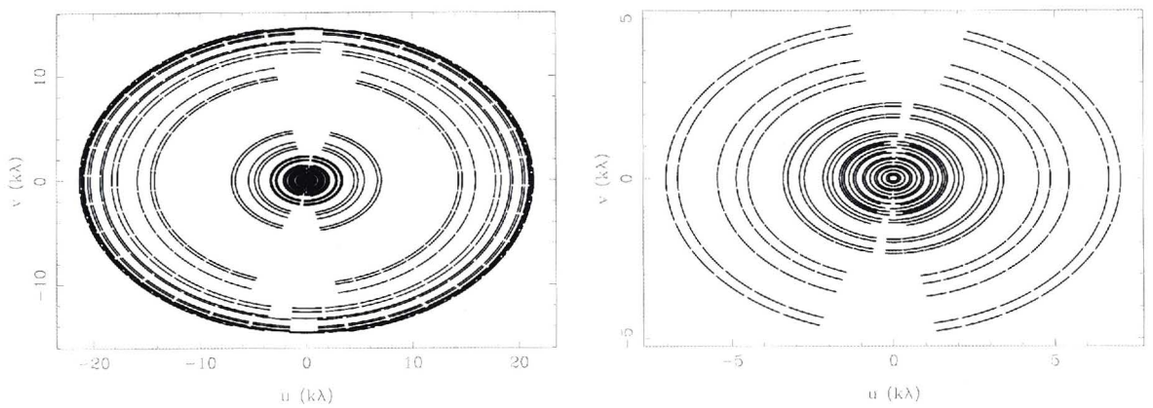


**Figure A.1** Typical *uv*-coverage of LVHIS data. The data shown is for the combined array configurations of ESO245-G005 with all antennas [left] and excluding the distant sixth antenna [right].

to large scale structures up to ~ 12 arcmin. When H I emission can be detected on the 6 km baselines, the maximum angular resolution is 9 arcsec. Therefore, good *uv*-coverage is obtained for observations of nearby gas rich galaxies. The typical coverage of the *uv*-plane is shown in Figure A.1 for the galaxy ESO245-G005. Here the coverage is shown both including [left] and excluding the distant sixth antenna [right].

The H I line observations were obtained with the band centred at a frequency of 1418 MHz, with a bandwidth of 8 MHz. The bandwidth was divided into 512 channels resulting in a channel width of 3.3 km $s^{-1}$ and a velocity resolution of 4 km $s^{-1}$. The ATCA primary beam is 33.6 arcmin at 1418 MHz. The 20 cm continuum observations were obtained with the band centred at 1384 MHz and with a bandwidth of 128 MHz. The primary flux calibrator used was PKS 1934-638.

## A.2. Data Reduction

The data reduction was carried out with the MIRIAD (Multichannel Image Reconstruction, Image Analysis and Display) software package using standard procedures. Channels with Galactic H I emission were discarded and then both the H I and 20 cm data were flux and phase calibrated. After subtracting the narrowband 20 cm continuum from the pure H I emission, the data was Fourier transformed using a channel width of 4 km $s^{-1}$. Maps were created with 'natural' and 'robust' weighting of the *uv*-data as well as both including and excluding the distant sixth antenna. The data was cleaned and restored with a synthesised beam and a primary beam correction applied. The data reduction process for the broadband 20 cm continuum data was similar.

The reduced data cubes were utilised to make H I 0th, 1st and 2nd moment maps

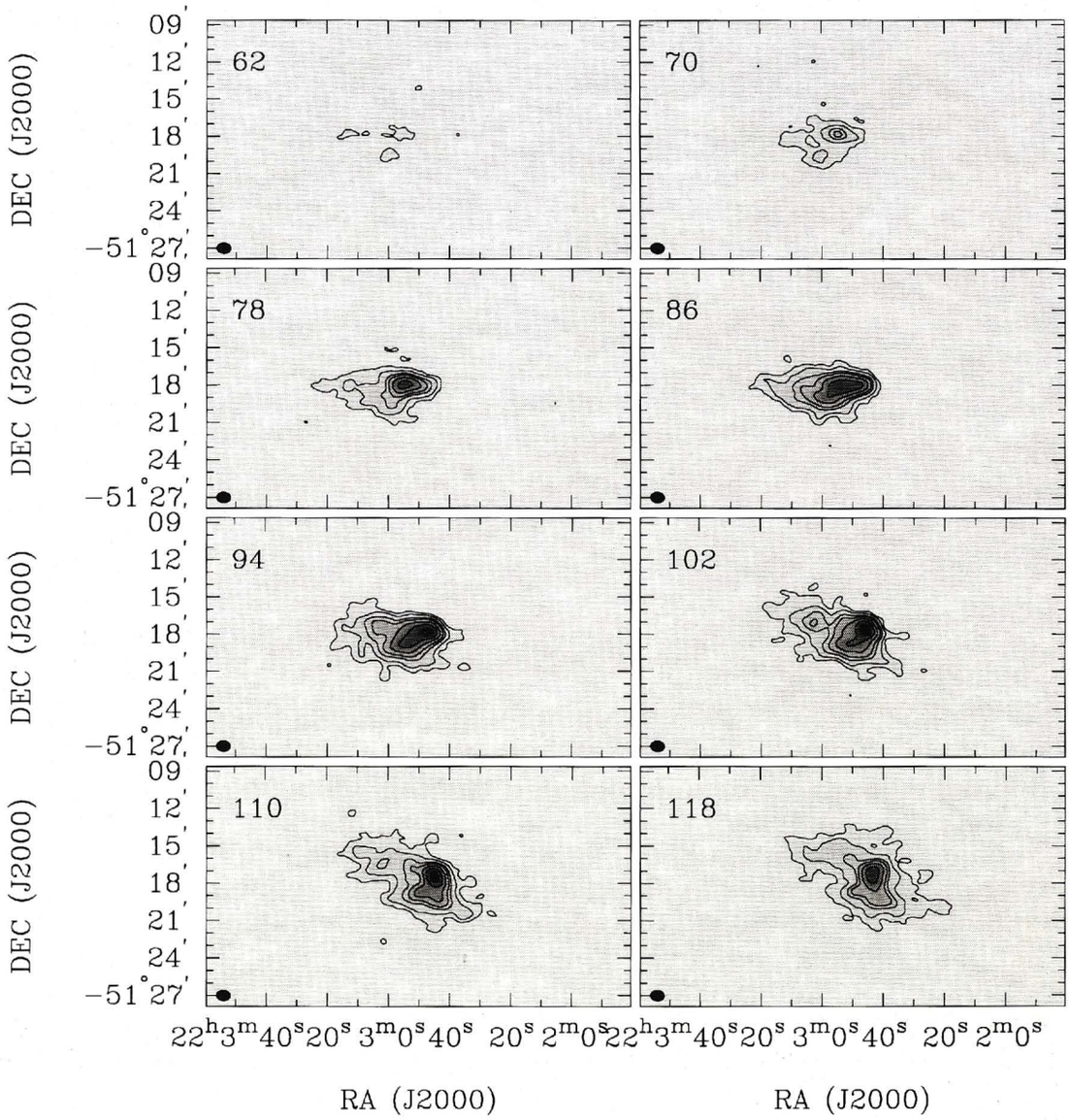


**Figure A.2** Example LVHIS channel maps shown for the galaxy IC5152. We show channels smoothed to a velocity resolution of 8 km $s^{-1}$ with the central heliocentric velocity for each panel given in the top left corner. Here the contour levels are 5, 10, 20, 30, 50 and 80 mJy $beam^{-1}$. The grey scale ranges from -10 to 120 mJy $beam^{-1}$. The synthesised beam (46.7 arcsec x 39.6 arcsec) is displayed in the bottom left corner of each panel. Figure continued on next page.

(H I distribution, mean velocity field and velocity dispersion maps respectively), as well as channel maps of the H I emission for all galaxies. In Figures A.3 to A.4 we show example maps for the galaxy IC5152.

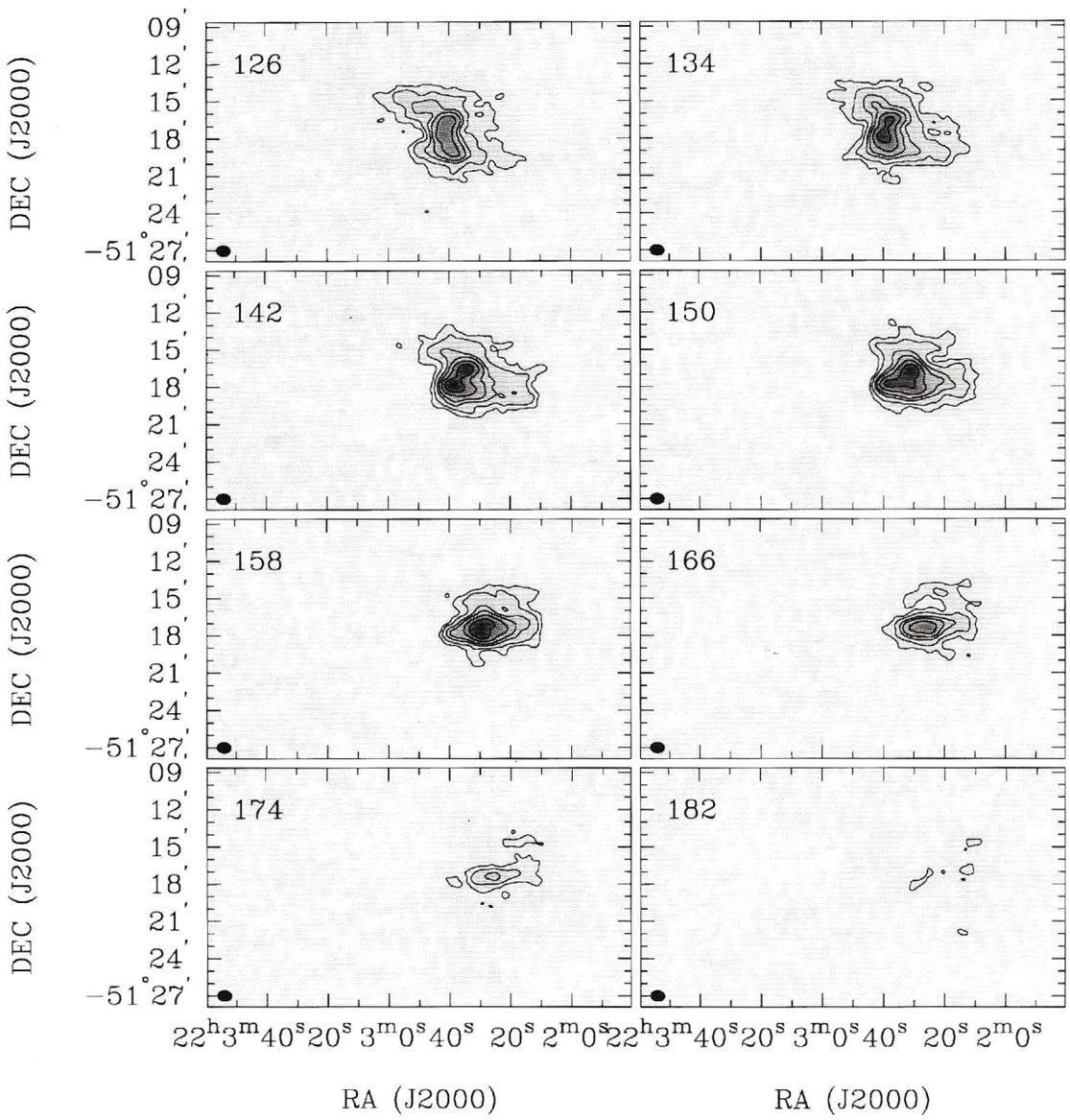


**Figure A.3** Example LVHIS channel maps shown for the galaxy IC5152 continued. We show channels smoothed to a velocity resolution of 8 km $s^{-1}$ with the central heliocentric velocity for each panel given in the top left corner. Here the contour levels are 5, 10, 20, 30, 50 and 80 mJy $beam^{-1}$. The grey scale ranges from -10 to 120 mJy $beam^{-1}$. The synthesised beam (46.7 arcsec x 39.6 arcsec) is displayed in the bottom left corner of each panel.

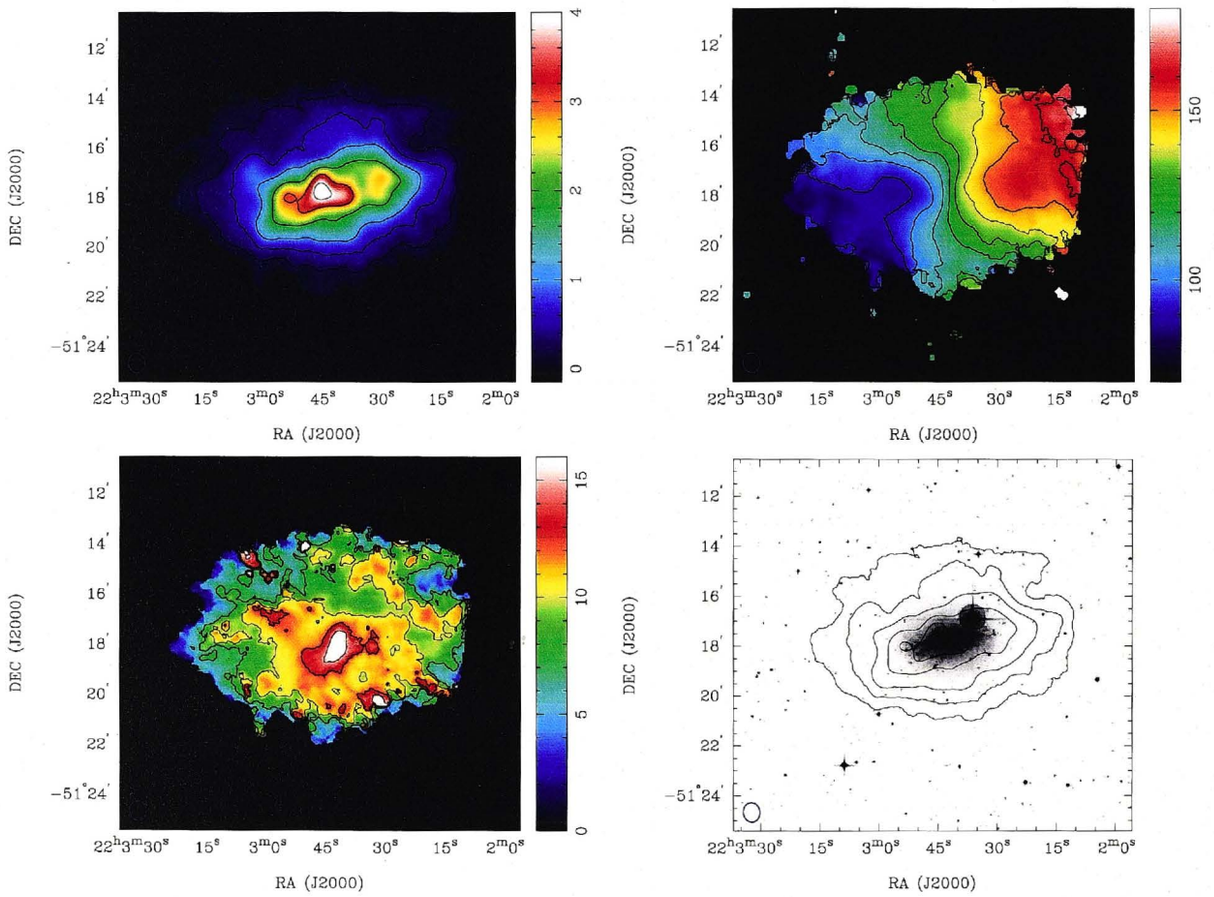


**Figure A.4** Example LVHIS H I moment maps shown for the galaxy IC5152. [top left] The integrated H I intensity distribution with contour levels at 0.5, 1, 2, 3 and 4 Jy km $s^{-1}$. [top right] The mean H I velocity field. The contour levels range from 90 to 180 km $s^{-1}$ in step sizes of 10 km $s^{-1}$. [bottom left] The H I velocity dispersion. The contour levels are 7.5, 10, 12.5 and 15 km $s^{-1}$. [bottom right] The levels as described for the top left overlaid on the optical Digitized Sky Survey *B*-band image. The synthesised beam (46.7 arcsec x 39.6 arcsec) is displayed in the bottom left corner of each panel.

# APPENDIX B

# The 'SC' Galaxies

## B.1. SC18

SC18 was first discovered by Côté et al. (1997) by visually scanning ESO/SRC *J*-band films to find dwarf candidates. It has the (J2000) right ascension and declination of 00h 00m 59.1s, -41d 09m 20s. H I line observations were carried out at the Parkes telescope by Côté et al. who found an H I detection at the coordinates of SC18 with a heliocentric velocity of 151 km $s^{-1}$, an integrated flux of 4.6 Jy km $s^{-1}$ and a line width of 46 km $s^{-1}$. From this measurement, it was concluded that SC18 was a nearby galaxy ($v_{\odot}$ = 151 km $s^{-1}$ indicates a Hubble distance of 1.8 Mpc) with a H I mass of $6.8 \times 10^6$ $M_{\odot}$. Follow up observations of SC18 were obtained in the *R*-band using the 2.5m Isaac Newton Telescope (INT) by Whiting et al. (2002) who concluded from their imaging that the galaxy was likely to be member of the Sculptor Group. Narrowband $H_{\alpha}$ imaging was obtained by Skillman et al. (2003) who detected a flux of $5.3 \times 10^{-15}$ ergs $cm^{-2}$ $s^{-1}$ and calculated the star formation rate as $2.4 \times 10^{-5}$ $M_{\odot}$ $yr^{-1}$.

SC18 was included in the Karachentsev et al. (2004) "Catalog of Neighbouring Galaxies" and therefore became a target for the LSI survey (see Chapter 2). The LSI *H*-band image of SC18 was obtained in October 2004 and is shown in the left panel of Figure B.1. There we see a low surface brightness galaxy with an extended, diffuse stellar component. The stars are not resolved despite the nearby distance implied by the H I line detection of Côté et al. (1997). SC18 was measured to have a total apparent *H*-band magnitude of $14.94 \pm 0.05$ mag making it the faintest galaxy observed during our program. Assuming that $D$ = 1.8 Mpc, this is equivalent to an absolute *H*-band magnitude of $-11.5 \pm 0.2$ mag or a total stellar mass of $7.9 \times 10^5$ $M_{\odot}$.

In Figure B.1 (right panel) we show the HIPASS H I line spectrum at the coordinates of SC18. The line spectrum was extracted using the procedure outlined

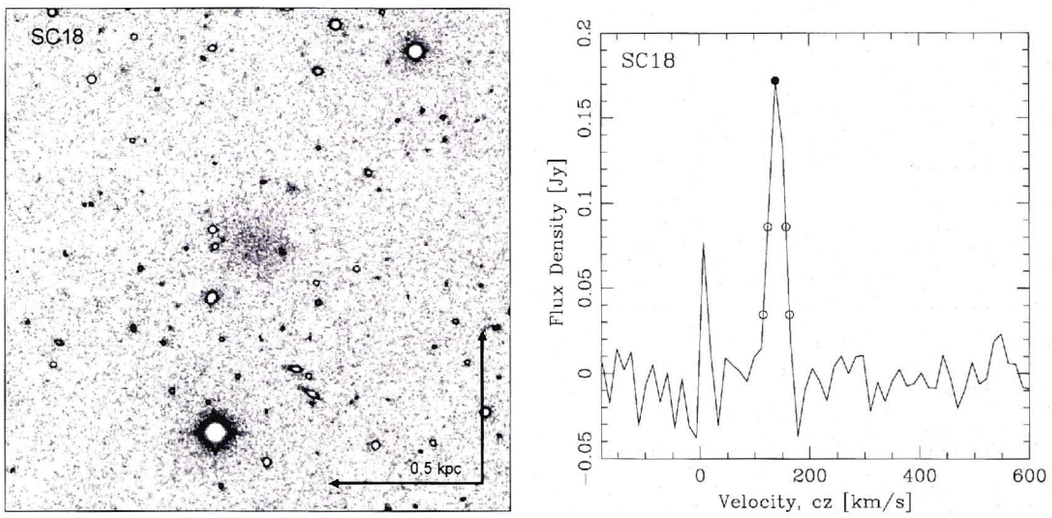


**Figure B.1** [Left] The LSI *H*-band image of SC18. Here, the scale represents 1 arcmin. The corresponding linear scale is also indicated. North is up and East is to the left. The intensity is represented by a grayscale, which goes from white (low intensity) to black (medium intensity) and then back to white (high intensity). [Right] The global H I line spectrum obtained by HIPASS. The solid dot indicates the peak flux, and the open circles show the 50% and 20% peak flux density levels.

in Section 3.4. There is a clear detection of H I emission at the velocity stated by Côté et al. (1997). However, in Figure B.2, we show the general field around SC18 which highlights the fact that the region is dominated by high velocity cloud emission and that no detection of SC18 can be confirmed.

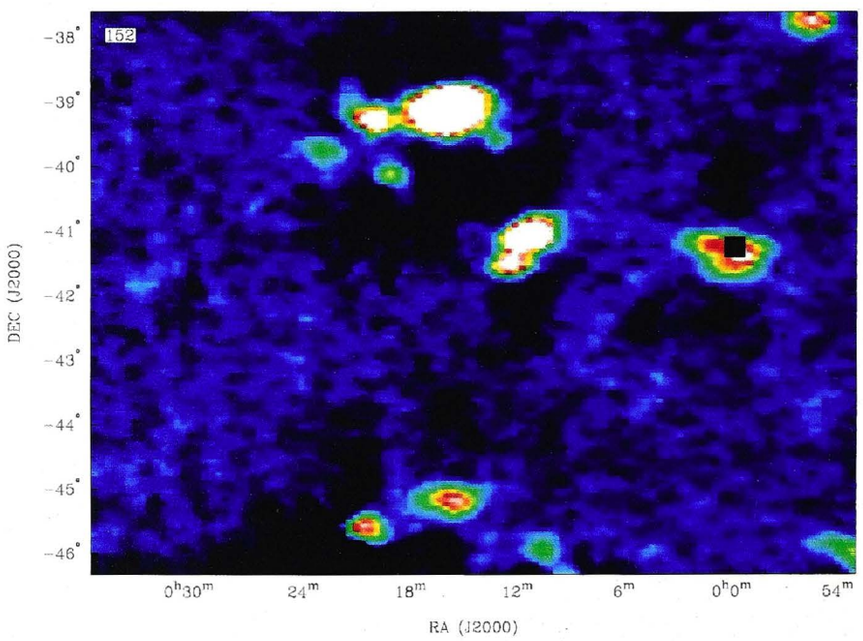


**Figure B.2** The H I line emission in the proximity of SC18. Here we show the HIPASS datacube sliced at the listed distance of the galaxy with the black square at the coordinates 00h 00m 59.1s, -41d 09m 20s indicating the position of the *H*-band imaging. The intensity of the H I emission is represented by the colour scale going from black (low intensity) to white (high intensity).

Therefore, we conclude that to date, no accurate distance estimate of SC18 has been obtained and the galaxy is likely to be more distant than is currently quoted in the literature. Thus we exclude SC18 from the the analysis in Chapter 4.

## B.2. SC24

The galaxy SC24 was first proposed as a nearby dwarf candidate by Roukema & Peterson (1995) who listed it as object 410.01. It was identified by visual inspection of photographic plates. Subsequently, Côté et al. (1997) stated it was confirmed it was a member of Sculptor Group after H I observations carried out with the Parkes telescope revealed emission at its listed coordinates (J2000: 00h 36m 38.3s, -32d 34m 25.2s). Côté et al. (1997) identified H I emission at a heliocentric velocity of 79 km $s^{-1}$, with an integrated flux of 11.8 Jy km $s^{-1}$ and a velocity width of 55 km $s^{-1}$. The H I emission at 79 km $s^{-1}$ provides current (Hubble) distance estimate for SC24 as 1.1 Mpc and indicates a H I mass of $1.7 \times 10^7$ $M_\odot$. Whiting et al. (2002) targeted SC24 for *R*-band imaging with the INT and also concluded the galaxy was probably in the Sculptor Group. Skillman et al. (2003) obtained narrowband $H_\alpha$ imaging and detected a flux of $0.8 \times 10^{-15}$ ergs $cm^{-2}$ $s^{-1}$ and calculated a star formation rate as $2.1 \times 10^{-6}$ $M_\odot$ $yr^{-1}$. Skillman et al. (2003) also inspected the HIPASS detection and revised the H I line emission to be at a velocity of 80 km $s^{-1}$ and with a width of 21 km $s^{-1}$.

SC24 was included in the Karachentsev et al. (2004) "Catalog of Neighbouring Galaxies" and hence was targeted as part of the LSI survey (see Chapter 2). The LSI *H*-band image of SC24 is shown in of Figure B.3 (left panel). There we see a low surface brightness galaxy with an extended, diffuse stellar component similar to that of SC18. SC24 has an *H*-band apparent magnitude of $14.8 \pm 0.2$ mag which, assuming $D = 1.1$ Mpc, is equivalent to an absolute *H*-band magnitude of $10.7 \pm 0.3$ mag or a stellar mass of $4.0 \times 10^5$ $M_\odot$.

In Figure B.3 (right panel) we show the HIPASS spectrum at the coordinates of SC24 which was extracted using the procedure outlined in Section 3.4. There we see H I emission at the heliocentric velocity identified by Côté et al. (1997). However, Begum & Chengalur (2005) have stated that the previous H I detections are likely to be of the Magellanic stream which HIPASS observed in the direction of SC24 and at the proposed radial velocity of the galaxy (Putman et al., 2003). In Figure B.4, we show the general field around SC24 which highlights the fact that the region is dominated by high velocity cloud emission. Therefore, we find supporting evidence for the Begum & Chengalur (2005) hypothesis that SC24 is likely to be a more distant galaxy and we exclude SC24 from the the analysis in Chapter 4.

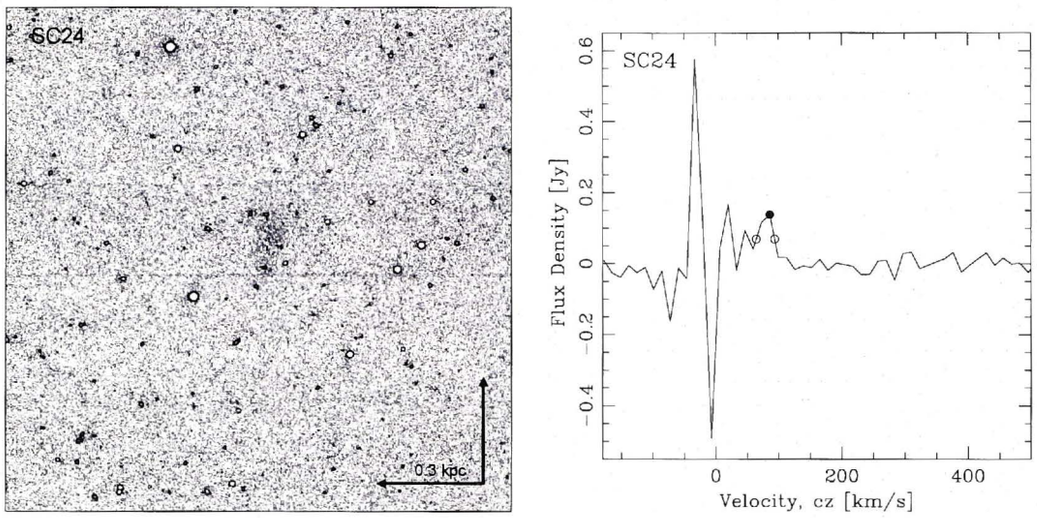


**Figure B.3** [Left] The LSI *H*-band image of SC24. Here, the scale represents 1 arcmin. The corresponding linear scale is also indicated. North is up and East is to the left. The intensity is represented by a grayscale, which goes from white (low intensity) to black (medium intensity) and then back to white (high intensity). [Right] The global H I line spectrum obtained by HIPASS. The solid dot indicates the peak flux, and the open circles show the 50% peak flux density level.

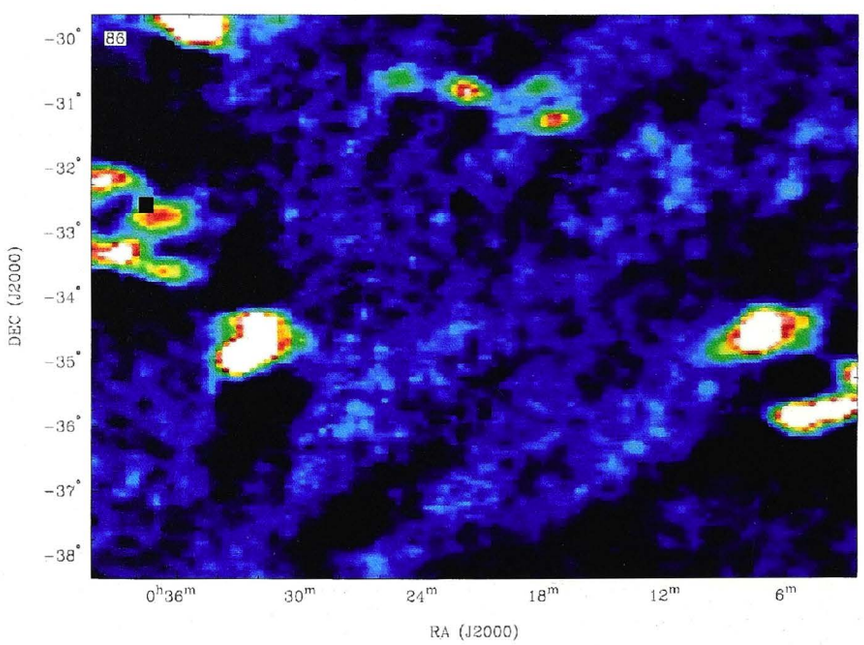


**Figure B.4** The H I line emission in the proximity of SC24. Here we show the HIPASS datacube sliced at the listed distance of the galaxy with the black square at the coordinates 00h 36m 38.3s, -32d 34m 25.2s indicating the position of the *H*-band imaging. The intensity of the H I emission is represented by the colour scale going from black (low intensity) to white (high intensity).

## B.3. SC42

The galaxy SC42 was first discovered by Côté et al. (1997) by visual scanning of ESO/SRC *J*-band films. They obtained H I observations with the Parkes telescope and detected H I emission at the coordinates of SC42. The emission had a redshift of 162 km $s^{-1}$ (equivalent to a Hubble distance of 0.9 Mpc), an integrated flux of 8 Jy km $s^{-1}$ and a velocity width of 64 km $s^{-1}$. Côté et al. (1997) calculated an H I mass of $1.7 \times 10^7$ $M_\odot$.

The Karachentsev et al. (2004) catalogue included SC42 as a Local Volume galaxy and hence it was targeted as part of the LSI survey (see Chapter 2). In Figure B.5 (left panel) we show the LSI *H*-band imaging of SC42. There we can see a region with very low surface brightness emission which has a very bright central core. This morphology is more consistent with background E/S0 galaxy than that of a nearby dwarf irregular galaxy.

In Figure B.5 (right panel) we show the HIPASS spectrum of SC42 which was extracted using the procedures discussed in Section 3.4. We clearly detect the nearby H I emission at the coordinates of SC42 which was identified by Côté et al. (1997). However, similar to SC18 and SC24, we argue that this emission is that of high velocity clouds. In Figure B.6 we show the extended HIPASS field around SC42 which shows that the region is dominated by high velocity cloud emission and that no clear detection of SC42 is made. On this basis, we exclude SC42 from the the analysis in Chapter 4.

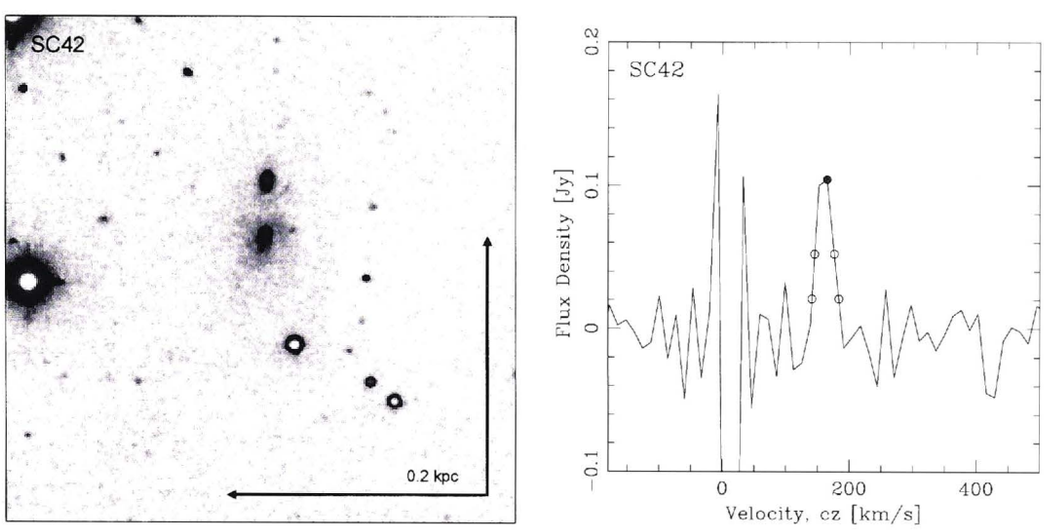


**Figure B.5** [Left] The LSI *H*-band image of SC24. Here, the scale represents 1 arcmin. The corresponding linear scale is also indicated. North is up and East is to the left. The intensity is represented by a grayscale, which goes from white (low intensity) to black (medium intensity) and then back to white (high intensity). [Right] The global H I line spectrum obtained by HIPASS. The solid dot indicates the peak flux, and the open circles show the 50% and 20% peak flux density levels.

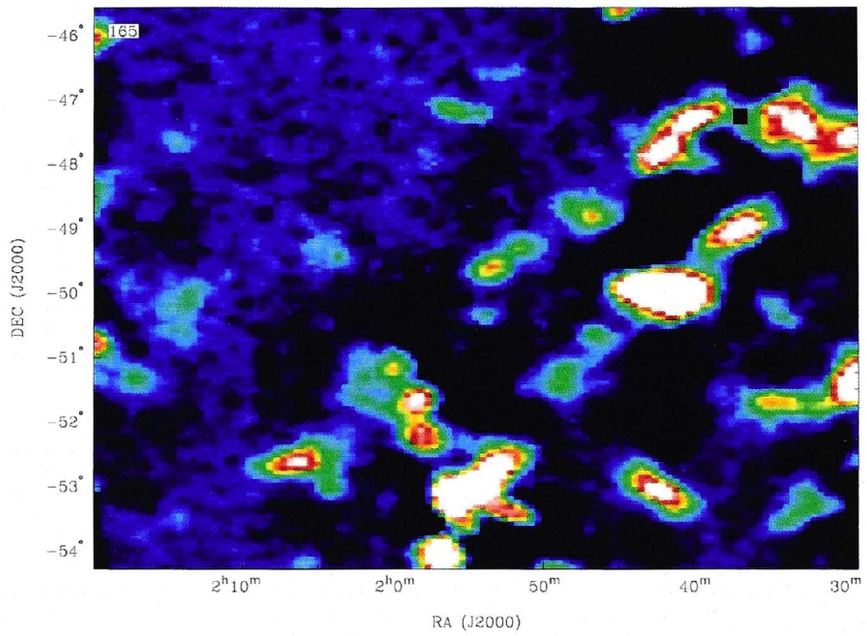


**Figure B.6** The H I line emission in the proximity of SC42. Here we show the HIPASS datacube sliced at the listed distance of the galaxy with the black square at the coordinates 01h 39m 15.9s, -47d 17 m51.4s indicating the position of the *H*-band imaging. The intensity of the H I emission is represented by the colour scale going from black (low intensity) to white (high intensity).

## B.4. Summary

SC18, SC24 and SC42 are three galaxies in the LSI survey which have their distance estimates obtained from the heliocentric velocity of H I emission identified at their coordinates. In all three cases, we show that the H I emission is occurs in a region dominated by high velocity clouds and that no clear detection has been made. Thus, all three have unreliable distance estimates and have been excluded from further analysis in Chapter 4.

# BIBLIOGRAPHY


Aloisi, A., Clementini, G., Tosi, M., et al. 2007, ApJ, 667, L151

Aloisi, A., van der Marel, R. P., Mack, J., et al. 2005, ApJ, 631, L45

Alonso, M. S., Tissera, P. B., Coldwell, G., & Lambas, D. G. 2004, MNRAS, 352, 1081

Andreon, S. 2002, A&A, 382, 495

Armandroff, T. E., Davies, J. E., & Jacoby, G. H. 1998, AJ, 116, 2287

Armandroff, T. E., Jacoby, G. H., & Davies, J. E. 1999, AJ, 118, 1220

Arp, H. C. & Madore, B. 1987, A catalogue of southern peculiar galaxies and associations (Cambridge ; New York : Cambridge University Press, 1987.)

Auld, R., Minchin, R. F., Davies, J. I., et al. 2006, MNRAS, 371, 1617

Bailin, J. & Ford, A. 2007, MNRAS, 375, L41

Banks, G. D., Disney, M. J., Knezek, P. M., et al. 1999, ApJ, 524, 612

Barnes, D. G., Staveley-Smith, L., de Blok, W. J. G., et al. 2001, MNRAS, 322, 486

Barth, A. J. 2007, AJ, 133, 1085

Becker, R., Mebold, U., Reif, K., & van Woerden, H. 1988, A&A, 203, 21

Begeman, K. G. 1989, A&A, 223, 47

Begum, A. & Chengalur, J. N. 2003, A&A, 409, 879

Begum, A. & Chengalur, J. N. 2005, MNRAS, 362, 609

Begum, A., Chengalur, J. N., Karachentsev, I. D., Kaisin, S. S., & Sharina, M. E. 2006, MNRAS, 365, 1220

Begum, A., Chengalur, J. N., Karachentsev, I. D., & Sharina, M. E. 2005, MNRAS, 359, L53

Begum, A., Chengalur, J. N., Karachentsev, I. D., & Sharina, M. E. 2008a, MNRAS, 386, 138

Begum, A., Chengalur, J. N., Karachentsev, I. D., Sharina, M. E., & Kaisin, S. S. 2008b, MNRAS, 386, 1667

Bekki, K., Koribalski, B. S., & Kilborn, V. A. 2005, MNRAS, 363, L21

Bell, E. F. & de Jong, R. S. 2001, ApJ, 550, 212

Bell, E. F., McIntosh, D. H., Katz, N., & Weinberg, M. D. 2003, ApJS, 149, 289

Belokurov, V., Zucker, D. B., Evans, N. W., et al. 2007, ApJ, 654, 897

Belokurov, V., Zucker, D. B., Evans, N. W., et al. 2006, ApJ, 647, L111

Bessell, M. S., Castelli, F., & Plez, B. 1998, A&A, 333, 231

Blanton, M. R., Dalcanton, J., Eisenstein, D., et al. 2001, AJ, 121, 2358

Blanton, M. R., Hogg, D. W., Bahcall, N. A., et al. 2003, ApJ, 594, 186

Boomsma, R., Oosterloo, T. A., Fraternali, F., van der Hulst, J. M., & Sancisi, R. 2005, A&A, 431, 65

Boselli, A., Gavazzi, G., Franzetti, P., Pierini, D., & Scodeggio, M. 2000, A&AS, 142, 73

Bosma, A. 1978, PhD thesis, PhD Thesis, Groningen Univ., (1978)

Bosma, A. 1981, AJ, 86, 1825

Bothun, G. D., Impey, C. D., Malin, D. F., & Mould, J. R. 1987, AJ, 94, 23

Bottinelli, L., Gouguenheim, L., Fouque, P., & Paturel, G. 1990, A&AS, 82, 391

Bouchard, A., Da Costa, G. S., & Jerjen, H. 2009, AJ, 137, 3038

Bouchard, A., Jerjen, H., Da Costa, G. S., & Ott, J. 2007, AJ, 133, 261

Boyce, P. J., Minchin, R. F., Kilborn, V. A., et al. 2001, ApJ, 560, L127

Broeils, A. H. & Rhee, M. 1997, A&A, 324, 877

Broeils, A. H. & van Woerden, H. 1994, A&AS, 107, 129

Bruzual, G. & Charlot, S. 1993, ApJ, 405, 538

Bruzual, G. & Charlot, S. 2003, MNRAS, 344, 1000

Bureau, M., Freeman, K. C., Pfitzner, D. W., & Meurer, G. R. 1999, AJ, 118, 2158

Burstein, D. & Heiles, C. 1978, ApJ, 225, 40

Burstein, D. & Heiles, C. 1982, AJ, 87, 1165

Burstein, D. & Heiles, C. 1984, ApJS, 54, 33

Buyle, P., Michielsen, D., de Rijcke, S., Ott, J., & Dejonghe, H. 2006, MNRAS, 373, 793

Cannon, J. M., McClure-Griffiths, N. M., Skillman, E. D., & Côté, S. 2004, ApJ, 607, 274

Carignan, C. & Puche, D. 1990a, AJ, 100, 394

Carignan, C. & Puche, D. 1990b, AJ, 100, 641

Carrasco, E. R., Mendes de Oliveira, C., Infante, L., & Bolte, M. 2001, AJ, 121, 148

Chernin, A. D., Karachentsev, I. D., Valtonen, M. J., et al. 2004, A&A, 415, 19

Colina, L., Bohlin, R. C., & Castelli, F. 1996, AJ, 112, 307

Combes, F. 2009, A&A, 500, 119

Condon, J. J. 1992, ARA&A, 30, 575

Corbelli, E. & Schneider, S. E. 1997, ApJ, 479, 244

Corbin, M. R., Kim, H., Jansen, R. A., Windhorst, R. A., & Fernandes, R. C. 2008, ApJ, 675, 194

Cortese, L., Minchin, R. F., Auld, R. R., et al. 2008, MNRAS, 383, 1519

Côté, S., Carignan, C., & Freeman, K. C. 2000, AJ, 120, 3027

Côté, S., Freeman, K. C., Carignan, C., & Quinn, P. J. 1997, AJ, 114, 1313

Cowie, L. L., Songaila, A., Hu, E. M., & Cohen, J. G. 1996, AJ, 112, 839

Dalcanton, J. J., Spergel, D. N., & Summers, F. J. 1997, ApJ, 482, 659

Dale, D. A., Cohen, S. A., Johnson, L. C., et al. 2009, ApJ, 703, 517

de Blok, W. J. G., Walter, F., Brinks, E., et al. 2008, AJ, 136, 2648

de Blok, W. J. G., Zwaan, M. A., Dijkstra, M., Briggs, F. H., & Freeman, K. C. 2002, A&A, 382, 43

de Jong, R. S. 1996, A&A, 313, 377

de Jong, R. S. & Lacey, C. 2000, ApJ, 545, 781

Deharveng, L., Lefloch, B., Zavagno, A., et al. 2003, A&A, 408, L25

Disney, M. & Phillipps, S. 1987, Nature, 329, 203

Disney, M. J. 1976, Nature, 263, 573

Disney, M. J. & Minchin, R. F. 2003, in Astrophysics and Space Science Library, Vol. 281, The IGM/Galaxy Connection. The Distribution of Baryons at z=0, ed. J. L. Rosenberg & M. E. Putman, 305–+

Domgoergen, H., Dahlem, M., & Dettmar, R.-J. 1996, A&A, 313, 96

Donley, J. L., Staveley-Smith, L., Kraan-Korteweg, R. C., et al. 2005, AJ, 129, 220

Doyle, M. T., Drinkwater, M. J., Rohde, D. J., et al. 2005, MNRAS, 361, 34

Driver, S. 2004, Publications of the Astronomical Society of Australia, 21, 344

Driver, S. P., Popescu, C. C., Tuffs, R. J., et al. 2007, MNRAS, 379, 1022

Elmegreen, B. G. 1998, in Astronomical Society of the Pacific Conference Series, Vol. 148, Origins, ed. C. E. Woodward, J. M. Shull, & H. A. Thronson, Jr., 150–+

Elmegreen, B. G. & Lada, C. J. 1977, ApJ, 214, 725

Engelbracht, C. W., Kennicutt, R. C., Calzetti, D., & SINGS Team. 2005, in Bulletin of the American Astronomical Society, Vol. 37, Bulletin of the American Astronomical Society, 1254–+

Ewen, H. I. & Purcell, E. M. 1951, Nature, 168, 356

Fall, S. M. & Efstathiou, G. 1980, MNRAS, 193, 189

Fouque, P., Durand, N., Bottinelli, L., Gouguenheim, L., & Paturel, G. 1990, A&AS, 86, 473

Freudling, W., Staveley-Smith, L., Calabretta, M., et al. 2005, in Bulletin of the American Astronomical Society, Vol. 37, Bulletin of the American Astronomical Society, 1316–+

Gallagher, III, J. S., Littleton, J. E., & Matthews, L. D. 1995, AJ, 109, 2003

Gavazzi, G., Boselli, A., Donati, A., Franzetti, P., & Scodeggio, M. 2003, A&A, 400, 451

Gavazzi, G., Franzetti, P., Scodeggio, M., et al. 2000, A&AS, 142, 65

Gavazzi, G., Pierini, D., Baffa, C., et al. 1996a, A&AS, 120, 521

Gavazzi, G., Pierini, D., & Boselli, A. 1996b, A&A, 312, 397

Gavazzi, G., Pierini, D., Boselli, A., & Tuffs, R. 1996c, A&AS, 120, 489

Geha, M., Blanton, M. R., Masjedi, M., & West, A. A. 2006, ApJ, 653, 240

Giovanelli, R., Haynes, M. P., Kent, B. R., et al. 2005, AJ, 130, 2598

Gómez, P. L., Nichol, R. C., Miller, C. J., et al. 2003, ApJ, 584, 210

Grcevich, J. & Putman, M. E. 2009, ApJ, 696, 385

Grebel, E. K. & Gallagher, III, J. S. 2004, ApJ, 610, L89

Grossi, M., di Serego Alighieri, S., Giovanardi, C., et al. 2009, A&A, 498, 407

Helmboldt, J. F., Walterbos, R. A. M., Bothun, G. D., & O'Neil, K. 2005, ApJ, 630, 824

Helmboldt, J. F., Walterbos, R. A. M., Bothun, G. D., O'Neil, K., & de Blok, W. J. G. 2004, ApJ, 613, 914

Henning, P. A., Kraan-Korteweg, R. C., Rivers, A. J., et al. 1998, AJ, 115, 584

Henning, P. A., Staveley-Smith, L., Ekers, R. D., et al. 2000, AJ, 119, 2686

Hess, K. M., Pisano, D. J., Wilcots, E. M., & Chengalur, J. N. 2009, ApJ, 699, 76

Hidalgo-Gámez, A. M. 2006, AJ, 131, 2078

Hidalgo-Gámez, A. M. & Olofsson, K. 2002, A&A, 389, 836

Hogg, D. W., Blanton, M., Strateva, I., et al. 2002, AJ, 124, 646

Hosokawa, T. & Inutsuka, S.-i. 2005, ApJ, 623, 917

Hubble, E. P. 1936, Yale University Press

Huchtmeier, W. K., Karachentsev, I. D., & Karachentseva, V. E. 1997, A&A, 322, 375

Huchtmeier, W. K., Karachentsev, I. D., & Karachentseva, V. E. 2001, A&A, 377, 801

Huchtmeier, W. K., Karachentsev, I. D., Karachentseva, V. E., & Ehle, M. 2000, A&AS, 141, 469

Huchtmeier, W. K., Lercher, G., Seeberger, R., Saurer, W., & Weinberger, R. 1995, A&A, 293, L33

Huchtmeier, W. K. & Richter, O. G. 1986, A&AS, 63, 323

Hunter, D. A., Brinks, E., Elmegreen, B., et al. 2007, in Bulletin of the American Astronomical Society, Vol. 38, Bulletin of the American Astronomical Society, 895–+

Ibata, R. A., Gilmore, G., & Irwin, M. J. 1994, Nature, 370, 194

Impey, C. & Bothun, G. 1989, ApJ, 341, 89

Jarrett, T. H. 2000, PASP, 112, 1008

Jarrett, T. H., Chester, T., Cutri, R., et al. 2000, AJ, 119, 2498

Jarrett, T. H., Chester, T., Cutri, R., Schneider, S. E., & Huchra, J. P. 2003, AJ, 125, 525

Jerjen, H. 2010, Advances in Astronomy, 2010, 2

Jerjen, H., Binggeli, B., & Barazza, F. D. 2004, AJ, 127, 771

Jerjen, H., Binggeli, B., & Freeman, K. C. 2000, AJ, 119, 593

Jerjen, H., Freeman, K. C., & Binggeli, B. 1998, AJ, 116, 2873

Jerjen, H., Rekola, R., Takalo, L., Coleman, M., & Valtonen, M. 2001, A&A, 380, 90

Jiang, I.-G. & Binney, J. 1999, MNRAS, 303, L7

Jimenez, R., Heavens, A. F., Hawkins, M. R. S., & Padoan, P. 1997, MNRAS, 292, L5

Jones, K. L., Koribalski, B. S., Elmouttie, M., & Haynes, R. F. 1999, MNRAS, 302, 649

Juneau, S., Glazebrook, K., Crampton, D., et al. 2005, ApJ, 619, L135

Juraszek, S. J., Staveley-Smith, L., Kraan-Korteweg, R. C., et al. 2000, AJ, 119, 1627

Karachentsev, I. D., Dolphin, A., Tully, R. B., et al. 2006, AJ, 131, 1361

Karachentsev, I. D., Karachentseva, V., Huchtmeier, W., et al. 2008, in Galaxies in the Local Volume, ed. B. S. Koribalski & H. Jerjen, 21–30

Karachentsev, I. D., Karachentseva, V. E., & Huchtmeier, W. K. 2001, A&A, 366, 428

Karachentsev, I. D., Karachentseva, V. E., Huchtmeier, W. K., & Makarov, D. I. 2004, AJ, 127, 2031

Karachentsev, I. D., Karachentseva, V. E., Suchkov, A. A., & Grebel, E. K. 2000, A&AS, 145, 415

Karachentsev, I. D. & Makarov, D. A. 1996, AJ, 111, 794

Karachentsev, I. D. & Makarov, D. I. 1999, in IAU Symposium, Vol. 186, Galaxy Interactions at Low and High Redshift, ed. J. E. Barnes & D. B. Sanders, 109–+

Karachentsev, I. D., Sharina, M. E., Dolphin, A. E., et al. 2002a, A&A, 385, 21

Karachentsev, I. D., Sharina, M. E., Makarov, D. I., et al. 2002b, A&A, 389, 812

Karachentsev, I. D., Tully, R. B., Dolphin, A., et al. 2007, AJ, 133, 504

Karachentseva, V. E. & Karachentsev, I. D. 1998, A&AS, 127, 409

Karachentseva, V. E. & Karachentsev, I. D. 2000, A&AS, 146, 359

Karachentseva, V. E., Karachentsev, I. D., & Richter, G. M. 1999, A&AS, 135, 221

Kassin, S. A., de Jong, R. S., & Pogge, R. W. 2006, ApJS, 162, 80

Kennicutt, Jr., R. C. 1989, ApJ, 344, 685

Kennicutt, Jr., R. C., Armus, L., Bendo, G., et al. 2003, PASP, 115, 928

Kent, B. R., Spekkens, K., Giovanelli, R., et al. 2009, ApJ, 691, 1595

Kilborn, V. A. 2002, in Astronomical Society of the Pacific Conference Series, Vol. 276, Seeing Through the Dust: The Detection of HI and the Exploration of the ISM in Galaxies, ed. A. R. Taylor, T. L. Landecker, & A. G. Willis, 80–+

Kilborn, V. A., Staveley-Smith, L., Marquarding, M., et al. 2000, AJ, 120, 1342

Kilborn, V. A., Webster, R. L., Staveley-Smith, L., et al. 2002, AJ, 124, 690

Kirby, E. M. & Jerjen, H. 2010, ApJ

Kirby, E. M., Jerjen, H., Ryder, S. D., & Driver, S. P. 2008, AJ, 136, 1866

Kirby, E. M., Koribalski, B. S., Jerjen, H., et al. 2010, MNRAS

Klypin, A., Gottlöber, S., Kravtsov, A. V., & Khokhlov, A. M. 1999, ApJ, 516, 530

Kniazev, A. Y., Brosch, N., Hoffman, G. L., et al. 2009, MNRAS, 400, 2054

Kobulnicky, H. A. & Skillman, E. D. 1995, ApJ, 454, L121+

Koribalski, B. S. 2007, in Galaxies in the Local Volume, ed. B. S. Koribalski & H. Jerjen

Koribalski, B. S. & Jerjen, H., eds. 2008, Galaxies in the Local Volume (Springer)

Koribalski, B. S. & López-Sánchez, Á. R. 2009, MNRAS, 400, 1749

Koribalski, B. S., Staveley-Smith, L., Kilborn, V. A., et al. 2004, AJ, 128, 16

Koribalski, B. S. et al. 2010, MNRAS, in prep

Kraan-Korteweg, R. C., Loan, A. J., Burton, W. B., et al. 1994, Nature, 372, 77

Kraan-Korteweg, R. C. & Tammann, G. A. 1979, Astronomische Nachrichten, 300, 181

Kron, R. G. 1980, ApJS, 43, 305

Kroupa, P. & Weidner, C. 2003, ApJ, 598, 1076

Lauberts, A. & Valentijn, E. A. 1989, The surface photometry catalogue of the ESO-Uppsala galaxies (Garching: European Southern Observatory, |c1989)

Lee, H., Grebel, E. K., & Hodge, P. W. 2003, A&A, 401, 141

Leroy, A., Bolatto, A. D., Simon, J. D., & Blitz, L. 2005, ApJ, 625, 763

Lewis, B. M. 1975, A&A, 44, 147

Li, Z. & Han, Z. 2008, MNRAS, 387, 105

Libeskind, N. I., Cole, S., Frenk, C. S., Okamoto, T., & Jenkins, A. 2007, MNRAS, 374, 16

Longmore, A. J., Hawarden, T. G., Goss, W. M., Mebold, U., & Webster, B. L. 1982, MNRAS, 200, 325

Maddox, S. J., Efstathiou, G., Sutherland, W. J., & Loveday, J. 1990, MNRAS, 243, 692

Makarov, D. I., Karachentsev, I. D., & Burenkov, A. N. 2003, A&A, 405, 951

Makarova, L. N., Karachentsev, I. D., Grebel, E. K., et al. 2005, A&A, 433, 751

Mao, S., Mo, H. J., & White, S. D. M. 1998, MNRAS, 297, L71

Maraston, C. 1998, MNRAS, 300, 872

Martin, C. L. & Kennicutt, Jr., R. C. 2001, ApJ, 555, 301

Martin, N. F., Ibata, R. A., Bellazzini, M., et al. 2004, MNRAS, 348, 12

Massey, P., Henning, P. A., & Kraan-Korteweg, R. C. 2003, AJ, 126, 2362

Mateo, M. L. 1998, ARA&A, 36, 435

Matthews, L. D. & Gallagher, III, J. S. 1997, AJ, 114, 1899

Matthews, L. D. & Gallagher, III, J. S. 2002, ApJS, 141, 429

Matthews, L. D., Gallagher, III, J. S., & Littleton, J. E. 1995, AJ, 110, 581

Matthews, L. D., van Driel, W., & Gallagher, III, J. S. 1998, AJ, 116, 1169

McCall, M. L. & Buta, R. J. 1995, AJ, 109, 2460

McCall, M. L. & Buta, R. J. 1997, AJ, 113, 981

McGaugh, S. S., Schombert, J. M., Bothun, G. D., & de Blok, W. J. G. 2000, ApJ, 533, L99

Meurer, G. R., Carignan, C., Beaulieu, S. F., & Freeman, K. C. 1996, AJ, 111, 1551

Meurer, G. R., Staveley-Smith, L., & Killeen, N. E. B. 1998, MNRAS, 300, 705

Meyer, M. J., Zwaan, M. A., Webster, R. L., Schneider, S., & Staveley-Smith, L. 2008, MNRAS, 391, 1712

Meyer, M. J., Zwaan, M. A., Webster, R. L., et al. 2004, MNRAS, 350, 1195

Miller, B. W. 1996, AJ, 112, 991

Minchin, R., Davies, J., Disney, M., et al. 2005, ApJ, 622, L21

Minchin, R., Davies, J., Disney, M., et al. 2007, ApJ, 670, 1056

Minchin, R. F., Disney, M. J., Boyce, P. J., et al. 2003, MNRAS, 346, 787

Mobasher, B., Dahlen, T., Hopkins, A., et al. 2009, ApJ, 690, 1074

Moore, B., Ghigna, S., Governato, F., et al. 1999, ApJ, 524, L19

Moore, L. & Parker, Q. A. 2006, Publications of the Astronomical Society of Australia, 23, 165

Neugebauer, G. & Leighton, R. B. 1969, NASA Special Publication, 3047

Oey, M. S., Meurer, G. R., Yelda, S., et al. 2007, ApJ, 661, 801

Oh, S.-H., de Blok, W. J. G., Walter, F., Brinks, E., & Kennicutt, R. C. 2008, AJ, 136, 2761

Ostriker, E. C. & Binney, J. J. 1989, MNRAS, 237, 785

Ott, J., Warren, S., Stilp, A., et al. 2010, in American Astronomical Society Meeting Abstracts, Vol. 215, American Astronomical Society Meeting Abstracts, 202.03–+

Ott, M., Whiteoak, J. B., Henkel, C., & Wielebinski, R. 2001, A&A, 372, 463

Parodi, B. R., Barazza, F. D., & Binggeli, B. 2002, A&A, 388, 29

Pasetto, S. & Chiosi, C. 2007, A&A, 463, 427

Patterson, R. J. & Thuan, T. X. 1996, ApJS, 107, 103

Paturel, G., Andernach, H., Bottinelli, L., et al. 1997, A&AS, 124, 109

Peebles, P. J. E. 1969, ApJ, 155, 393

Perez, M. J., Tissera, P. B., Lambas, D. G., & Scannapieco, C. 2006, A&A, 449, 23

Perryman, M. A. C., de Boer, K. S., Gilmore, G., et al. 2001, A&A, 369, 339

Pfenniger, D. & Revaz, Y. 2005, A&A, 431, 511

Pflamm-Altenburg, J. & Kroupa, P. 2009, ApJ, 706, 516

Pickering, T. E., Impey, C. D., van Gorkom, J. H., & Bothun, G. D. 1997, AJ, 114, 1858

Puche, D., Carignan, C., & Bosma, A. 1990, AJ, 100, 1468

Puche, D., Carignan, C., & van Gorkom, J. H. 1991a, AJ, 101, 456

Puche, D., Carignan, C., & Wainscoat, R. J. 1991b, AJ, 101, 447

Putman, M. E., de Heij, V., Staveley-Smith, L., et al. 2002, AJ, 123, 873

Putman, M. E., Staveley-Smith, L., Freeman, K. C., Gibson, B. K., & Barnes, D. G. 2003, ApJ, 586, 170

Ramya, S., Sahu, D. K., & Prabhu, T. P. 2009, MNRAS, 396, 97

Rees, M. J. & Ostriker, J. P. 1977, MNRAS, 179, 541

Rhee, G., Valenzuela, O., Klypin, A., Holtzman, J., & Moorthy, B. 2004, ApJ, 617, 1059

Roberts, M. S. 1975, in Galaxies and the Universe, ed. A. Sandage, M. Sandage, & J. Kristian (the University of Chicago Press), 309–+

Roberts, M. S. & Haynes, M. P. 1994, ARA&A, 32, 115

Roberts, M. S. & Rots, A. H. 1973, A&A, 26, 483

Rocca-Volmerange, B., Le Borgne, D., De Breuck, C., Fioc, M., & Moy, E. 2004, A&A, 415, 931

Rogstad, D. H. & Shostak, G. S. 1972, ApJ, 176, 315

Rosenberg, J. L. & Schneider, S. E. 2000, in Astronomical Society of the Pacific Conference Series, Vol. 218, Mapping the Hidden Universe: The Universe behind the Mily Way - The Universe in HI, ed. R. C. Kraan-Korteweg, P. A. Henning, & H. Andernach, 223–+

Roukema, B. F. & Peterson, B. A. 1995, A&AS, 109, 511

Rubin, V. C., Thonnard, N., & Ford, Jr., W. K. 1978, ApJ, 225, L107

Ryder, S. 2007, Anglo-Australian Observatory Epping Newsletter, 111, 25

Ryder, S. D., Koribalski, B., Staveley-Smith, L., et al. 2001, ApJ, 555, 232

Ryder, S. D., Staveley-Smith, L., Malin, D., & Walsh, W. 1995, AJ, 109, 1592

Sakai, S., Mould, J. R., Hughes, S. M. G., et al. 2000, ApJ, 529, 698

Sakamoto, T. & Hasegawa, T. 2006, ApJ, 653, L29

Sales, L. V., Navarro, J. F., Abadi, M. G., & Steinmetz, M. 2007a, MNRAS, 379, 1475

Sales, L. V., Navarro, J. F., Abadi, M. G., & Steinmetz, M. 2007b, MNRAS, 379, 1464

Salpeter, E. E. & Hoffman, G. L. 1996, ApJ, 465, 595

Sandage, A. 1961, The Hubble atlas of galaxies (Washington: Carnegie Institution, 1961)

Sandage, A. & Bedke, J. 1994, The Carnegie atlas of galaxies (Washington, DC: Carnegie Institution of Washington with The Flintridge Foundation, |c1994)

Sandage, A. & Binggeli, B. 1984, AJ, 89, 919

Sawa, T. & Fujimoto, M. 2005, PASJ, 57, 429

Schiminovich, D., van Gorkom, J. H., van der Hulst, J. M., & Kasow, S. 1994, ApJ, 423, L101+

Schlegel, D. J., Finkbeiner, D. P., & Davis, M. 1998, ApJ, 500, 525

Schmidt, K.-H. & Boller, T. 1992, Astronomische Nachrichten, 313, 329

Schmidt, M. 1959, ApJ, 129, 243

Schneider, S. E., Helou, G., Salpeter, E. E., & Terzian, Y. 1983, ApJ, 273, L1

Schneider, S. E., Helou, G., Salpeter, E. E., & Terzian, Y. 1986, AJ, 92, 742

Schulte-Ladbeck, R. E., Crone, M. M., & Hopp, U. 1998, ApJ, 493, L23+

Schulte-Ladbeck, R. E., Hopp, U., Greggio, L., & Crone, M. M. 2000, AJ, 120, 1713

Schulte-Ladbeck, R. E., Hopp, U., Greggio, L., Crone, M. M., & Drozdovsky, I. O. 2001, AJ, 121, 3007

Seth, A. C., Dalcanton, J. J., & de Jong, R. S. 2005, AJ, 129, 1331

Silk, J. 1977, ApJ, 211, 638

Silva, D. R., Massey, P., DeGioia-Eastwood, K., & Henning, P. A. 2005, ApJ, 623, 148

Simon, J. D., Bolatto, A. D., Leroy, A., & Blitz, L. 2003, ApJ, 596, 957

Skillman, E. D., Côté, S., & Miller, B. W. 2003, AJ, 125, 610

Skrutskie, M. F., Cutri, R. M., Stiening, R., et al. 2006, AJ, 131, 1163

Sofue, Y. 1996, ApJ, 458, 120

Sofue, Y. 1997, PASJ, 49, 17

Sorar, E. 1994, PhD thesis, Pittsburgh Univ.

Spergel, D. N., Bean, R., Doré, O., et al. 2007, ApJS, 170, 377

Springob, C. M., Henning, P. A., Catinella, B., et al. 2008, in IAU Symposium, Vol. 244, IAU Symposium, ed. J. Davies & M. Disney, 383–384

Stark, D. V., McGaugh, S. S., & Swaters, R. A. 2009, AJ, 138, 392

Staveley-Smith, L., Juraszek, S., Koribalski, B. S., et al. 1998, AJ, 116, 2717

Staveley-Smith, L., Wilson, W. E., Bird, T. S., et al. 1996, Publications of the Astronomical Society of Australia, 13, 243

Steinmetz, M., Zwitter, T., Siebert, A., et al. 2006, AJ, 132, 1645

Swaters, R. A., Sancisi, R., van Albada, T. S., & van der Hulst, J. M. 2009, A&A, 493, 871

Swaters, R. A., Sancisi, R., & van der Hulst, J. M. 1997, ApJ, 491, 140

Swaters, R. A., van Albada, T. S., van der Hulst, J. M., & Sancisi, R. 2002, A&A, 390, 829

Taylor, C. L., Kobulnicky, H. A., & Skillman, E. D. 1998, AJ, 116, 2746

Taylor, E. N. & Webster, R. L. 2005, ApJ, 634, 1067

Thilker, D. A., Donovan, J., Schiminovich, D., et al. 2009, Nature, 457, 990

Thuan, T. X. & Izotov, Y. I. 1997, ApJ, 489, 623

Tilanus, R. P. J. & Allen, R. J. 1993, A&A, 274, 707

Tinney, C. G. et al. 2004, Ground-based Instrumentation for Astronomy, ed. Moorwood, A. F. M., Masanori, I. (Proceedings of the SPIE), 998

Tolstoy, E. 1999, Ap&SS, 265, 199

Tonry, J. L., Dressler, A., Blakeslee, J. P., et al. 2001, ApJ, 546, 681

Toomre, A. 1964, ApJ, 139, 1217

Tosi, M., Greggio, L., Marconi, G., & Focardi, P. 1991, AJ, 102, 951

Trachternach, C., de Blok, W. J. G., McGaugh, S. S., van der Hulst, J. M., & Dettmar, R. 2009, A&A, 505, 577

Trachternach, C., de Blok, W. J. G., Walter, F., Brinks, E., & Kennicutt, R. C. 2008, AJ, 136, 2720

Tully, R. B. & Fouque, P. 1985, ApJS, 58, 67

Tully, R. B., Pierce, M. J., Huang, J.-S., et al. 1998, AJ, 115, 2264

Vader, J. P. & Chaboyer, B. 1994, AJ, 108, 1209

Vaduvescu, O. & McCall, M. L. 2004, PASP, 116, 640

van der Hulst, J. M., Terlouw, J. P., Begeman, K. G., Zwitser, W., & Roelfsema, P. R. 1992, in Astronomical Society of the Pacific Conference Series, Vol. 25, Astronomical Data Analysis Software and Systems I, ed. D. M. Worrall, C. Biemesderfer, & J. Barnes, 131–+

van der Hulst, J. M., van Albada, T. S., & Sancisi, R. 2001, in Astronomical Society of the Pacific Conference Series, Vol. 240, Gas and Galaxy Evolution, ed. J. E. Hibbard, M. Rupen, & J. H. van Gorkom, 451–+

van Driel, W., Schneider, S. E., Kraan-Korteweg, R. C., & Monnier Ragaigne, D. 2009, A&A, 505, 29

van Eymeren, J., Trachternach, C., Koribalski, B. S., & Dettmar, R. 2009, A&A, 505, 1

van Woerden, H., van Driel, W., Braun, R., & Rots, A. H. 1993, A&A, 269, 15

Verde, L., Oh, S. P., & Jimenez, R. 2002, MNRAS, 336, 541

Verheijen, M. A. W. & Sancisi, R. 2001, A&A, 370, 765

Vogelaar, M. G. R. & Terlouw, J. P. 2001, in Astronomical Society of the Pacific Conference Series, Vol. 238, Astronomical Data Analysis Software and Systems X, ed. F. R. Harnden, Jr., F. A. Primini, & H. E. Payne, 358–+

Wakker, B. P. & van Woerden, H. 1997, ARA&A, 35, 217

Walsh, S. M., Jerjen, H., & Willman, B. 2007, ApJ, 662, L83

Walsh, W. 1997, PhD Thesis, University of NSW

Walter, F., Brinks, E., de Blok, E., et al. 2005, in Bulletin of the American Astronomical Society, Vol. 37, Bulletin of the American Astronomical Society, 1258–+

Walter, F., Brinks, E., de Blok, W. J. G., et al. 2008, AJ, 136, 2563

Warren, B. E., Jerjen, H., & Koribalski, B. S. 2004, AJ, 128, 1152

Warren, B. E., Jerjen, H., & Koribalski, B. S. 2006, AJ, 131, 2056

Warren, B. E., Jerjen, H., & Koribalski, B. S. 2007, AJ, 134, 1849

Weldrake, D. T. F., de Blok, W. J. G., & Walter, F. 2003, MNRAS, 340, 12

Whiting, A. B., Hau, G. K. T., & Irwin, M. 2002, ApJS, 141, 123

Whiting, A. B., Hau, G. K. T., Irwin, M., & Verdugo, M. 2007, AJ, 133, 715

Willman, B., Blanton, M. R., West, A. A., et al. 2005a, AJ, 129, 2692

Willman, B., Dalcanton, J. J., Martinez-Delgado, D., et al. 2005b, ApJ, 626, L85

Yahil, A., Tammann, G. A., & Sandage, A. 1977, ApJ, 217, 903

York, D. G., Adelman, J., Anderson, Jr., J. E., et al. 2000, AJ, 120, 1579

Yuk, I.-S. & Lee, M. G. 2007, ApJ, 668, 876

Zijlstra, A. A. & Minniti, D. 1999, AJ, 117, 1743

Zitrin, A. & Brosch, N. 2008, MNRAS, 390, 408

Zucker, D. B., Belokurov, V., Evans, N. W., et al. 2006, ApJ, 643, L103

Zwaan, M. A., Briggs, F. H., Sprayberry, D., & Sorar, E. 1997, ApJ, 490, 173